Chair of Process Technology and Industrial Environmental Protection

Doctoral Thesis

Experimental investigation of the reverse water gas shift reaction to develop a concept study for a power-to-liquid process

Dipl.-Ing. Dipl.-Wirt.-Ing. (FH) Christoph Markowitsch, BSc

July 2024

MONTANUNIVERSITÄT LEOBEN
www.unileoben.ac.at

AFFIDAVIT

I declare on oath that I wrote this thesis independently, did not use any sources and aids other than those specified, have fully and truthfully reported the use of generative methods and models of artificial intelligence, and did not otherwise use any other unauthorized aids.

I declare that I have read, understood and complied with the "Good Scientific Practice" of the Montanuniversität Leoben.

Furthermore, I declare that the electronic and printed versions of the submitted thesis are identical in form and content.

Date 24.06.2024

Signature Author
Christoph Markowitsch

Abstract

Power-to-liquid (PtL) technologies will be an integral part of the energy transition, allowing CO_2 to be reused as a resource and thus avoiding the further use of fossil fuels. Notably, the cement industry currently employs limestone as a raw material, which in turn leads to the emission of process-related CO_2 during decarbonization in the clinker production process. This study investigates the utilization of CO_2 and its catalytic conversion into valuable polyolefins through the identification of suitable process routes (Fischer-Tropsch and methanol synthesis). The techo-economic assessment reveals that the PtL process utilizing the reverse water-gas shift (rWGS) reaction for synthesis gas production, the Fischer-Tropsch synthesis, and a steam cracker technology for producing lower olefins is the most cost-effective and technically feasible process, yielding in costs of 14.92 € kg^{-1} product. A sensitivity analysis indicates the enormous reliance, particularly on electricity and chemical process investment, as well as significant expenses associated with future electrolysis cell manufacturing costs.

The rWGS reaction, which is still in the early stages of technological development, is necessary for the production of synthesis gas demanded as feed gas for the Fischer-Tropsch reactor. The present study compares the simulated and experimental results of the conversion of CO_2 with hydrogen via rWGS, utilizing a Ni/Al_2O_3 catalyst, two perovskite catalysts, and the support material Al_2O_3 in an experimental test rig. The Ni/Al_2O_3 catalyst generates a considerable amount of methane under low temperatures (< 750 °C) and ambient pressure, and this is heightened by elevating the pressure (reaching up to 28.3 vol.-% CH_4 at 550 °C and 8 bara). The perovskite catalysts indicate low methane formation from 550 °C on, and this further increases to a maximum of 2.7 vol.-% CH_4 in the product gas at the same temperature and a pressure of 8 bara.

In the concluding section of this work, the use of perovskite catalysts in the PtL process chains is investigated, specifically in Fischer-Tropsch synthesis incl. product separation and the rWGS reactor as pre-conversion unit. A comparison of the performance of perovskite catalysts with Ni/Al_2O_3 catalysts is executed based on ASPEN simulations. Depending on the technical evaluation of liquid product quantity, PtL efficiency, carbon efficiency, and carbon deposition, the use of a perovskite catalyst is superior to the Ni/Al_2O_3 catalyst in all key figures. However, an additional reforming step of the recycled gas streams from the Fischer-Tropsch reactor and an additional CO_2 and H_2 separation unit is required.

Acknowledgment

The last four years at Montanuniversität Leoben have flown by and have helped me progress both personally and academically. My special thanks go to my doctoral supervisor and head of department Prof. Dr. Markus Lehner. He has supported me in all my matters, given me every opportunity for further training in my professional and private life. I would especially like to thank him for appreciating my skills in the field of process engineering and for the opportunity to spend time abroad as a visiting researcher at the University of Wisconsin-Madison in the USA in 2023. The exchange of knowledge and the research activities in the field of "Sustainable Aviation Fuels" under the supervision of my visiting professor George W. Huber and my colleague Javier have awakened my interest in new fields of research and confirmed the diversity of process engineering.

It was a pleasure for me to work with the C2PAT team and I would also like to thank them for their financial support. Dr. Joseph Kitzweger offered me the opportunity to introduce myself as a doctoral student to Prof. Lehner during my diploma thesis, executed at the cement plant in Mannersdorf. I was then able to contribute my knowledge and ambition to the industrial consortium led by Dr. Joseph Kitzweger, Dr. Sorin Ivanovici, Ing. Wolfgang Haider and Dipl.-Ing. Michael Unfried.

Scientific questions were often discussed with Dipl.-Chem. Markus Maly, whom I am very grateful for the valuable discussions and his experience in the chemical industry.

I would also like to thank my colleagues at the chair for their consistently reliable and constructive cooperation. Colleagues have become friends. I would especially like to thank Katrin, Simon, Marion, Nina, Hanna, Sarah and Florian, who have supported me in all my challenges.

Finally, I would like to thank the most important people in my life. My family - father Markus, mother Petra, my siblings Andreas and Julia, my grandparents Gertraud, Renate and Matthias - they are always behind me and support me in all my decisions, whether professional or personal. Being abroad has shown me once again how important family and friends are and how much they are appreciated when they are not around me.

Contents

Chapter 1

Introduction

1.1 Motivation

In the course of this research study, the importance of developing and researching climate-neutral technologies for the production of sustainable products (e.g. polyolefins, fuels) was highlighted. Global warming is causing natural disasters scattered all over the world with increasing frequency and intensity of floodings, droughts, wildfires or storms [1]. The greenhouse gas emissions increased from annually emitted 22 to over 34 billion tons (CO_2 equivalent) within the last 30 years, which also leads to a global temperature increase [2]. To counteract this trend and take action, 196 parties signed the Paris Agreement in 2015, in which they committed to limit the global temperature increase to a maximum of 2 °C compared to the pre-industrial level in the year of 1990. The parties also agreed on a more ambitious target, to not exceed a temperature increase of 1.5 °C. Nowadays, a level of 1.1 °C is already reached, and the appropriate reduction scenario would demand a peak of greenhouse gas emissions in 2025 to accomplish the target of 1.5 °C [3], [4].

Austria's national intention is to achieve climate neutrality until 2040, which is a tough ambition as current greenhouse gas emissions measure up to about 80 million tons (CO_2 equivalent). This is equal to 0.1 % of the worldwide emissions. The national emissions in 2021 can be divided into the sections energy and industry (37.0 wt.-% of ETS (emission trading system) certified and 7.4 wt.-% of non-certified emissions), traffic (27.8 wt.-%), buildings and construction industry (11.7 wt.-%), agriculture (10.6 wt.-%) and the rest accounted to waste management and fluorinated gases. As it is reported in "Austria's National Inventory Report 2022", the major emissions stem from the energy and industry section, with a total of 44.7 wt.-% [5]. This specific section can be further divided into the industry section, whereas the steel (9,393 kt CO_2 or 12.8 wt.-% of total emissions in 2020) and cement production (1,821 kt CO_2 or 2.5 wt.-% of total greenhouse gas emissions in 2020) count for the two

significant emitters. As a part of emission reduction, production processes must be adapted to achieve low emission manufacturing. This idea can be incorporated in the iron production industry, as the traditional and conventional route with coke operated blast furnaces is replaced by a new technology to reduce iron ore, for instance with hydrogen or by molten oxide electrolysis. These technologies are partially available and there is a strategy to replace these blast furnaces in Austria by innovative technology in the near future [6]. In contrast to the steel industry, where the CO_2 emissions are merely technology related, the cement industry is faced with the problem, that around two thirds of the CO_2 emissions stem from the calcination of the limestone. These emissions are also designated as process-related emissions [7]. Hence, new technologies must be developed and implemented in the existing process to get rid of those unavoidable CO_2 emissions. So-called carbon capture and utilization plants could provide a solution, where, on the one hand, CO_2 is extracted from an exhaust gas stream (e.g., from a cement plant) to reduce the CO_2 emissions into the atmosphere. On the other hand, CO_2 could be concentrated and converted to valuable products in downstream processes. Circular economy is nowadays in everybody's mind and should play an important role in reducing the demand for fossil resources (e.g., for chemical, fuel or polyolefin production). The "Austrian Association of Cement Industry" revealed a roadmap for the cement industry to reduce CO_2 emissions, where the major contribution with a reduction potential of 44 % is attributed to the "Carbon Capture and Utilization and/or Storage (CCU/S)" section [8].

Carbon capture and utilization plants are developed to produce valuable products out of CO_2 and hydrogen. There are several power-to-liquid (PtL) studies, which deal with the production of methanol or electrified fuels (e-fuels), whereas the optimization towards high kerosene or jet fuel yields is mainly addressed in recent publications [9]–[15]. König conducted a study for jet fuel production, in which in a first step, synthesis gas (syngas, a mixture of carbon monoxide and hydrogen) is produced out of CO_2 and H_2 in a reverse water-gas shift (rWGS) reactor. The rWGS reactor operates at temperatures of 900 °C and 25 bara. This process step is mandatory, as the conventional downstream Fischer-Tropsch (FT) synthesis demands syngas as feedstock. A product separation unit contains a couple of flash drums, to separate the Fischer-Tropsch product (syncrude) into the desired boiling cuts. The wax fraction is subjected to a further process step, where the hydrocracking of long chain hydrocarbons increases the desired jet fuel yield [13]. Adelung et al. also simulated a PtL process, with the aim to produce jet fuel as the main product. They also included an rWGS reactor and a Fischer-Tropsch synthesis, to produce the syncrude for the jet fuel carbon range. The study reveals optimal operation conditions for the rWGS (825 °C and 5 bara) to obtain high process efficiencies [16]. In both studies, the rWGS reactor is implemented as an equilibrium reactor which considers all input species (e.g., CO_2, H_2, CH_4 in case of a recycle stream) and calculates the output composition according to the principle of minimizing the Gibbs free enthalpy for a specified temperature and pressure. Validation is pending for this

assumption.

Apart from the PtL processes to produce alternative fuels, there are comparatively few studies on the production of polyolefins, with CO_2 as a feedstock [17]. The process route for polyolefin production can, on the one hand include a Fischer-Tropsch syncrude as intermediate, which is further converted in a steam or hydrocracker to lower olefins, or on the other hand consider a methanol production process with a downstream methanol-to-propylene (MtP) plant [18]. Here again, the Fischer-Tropsch synthesis requires the rWGS reactor for syngas production, but the methanol synthesis can be used with or without this pre-conversion unit [19]. In the study of Ghosh et al., the rWGS reactor is simulated as an equilibrium reactor at a temperature of 500 °C and around 11 bara, with conversion yields according to Joo et al. [19], [20]. The downstream processes to lower olefins or polyolefins are not conducted in their studies.

The "Carbon to Product Austria (C2PAT)" project investigates various PtL process routes and pursues the conversion of the CO_2 emissions of an existing cement plant into polyolefins. C2PAT is founded of Austrian's leading companies in the field of cement production (Holcim Ltd.), electricity generation (Verbund AG) and chemicals production (OMV AG and Borealis AG). The CO_2 emissions shall be captured and used for the production of polyolefins to close the carbon circle and serve as a flagship project for the circular economy [21]. It is worth mentioning here, that, although Austria can contribute only a small part to the global emission reduction, the research and development of carbon capture and utilization projects could bring national economic benefits, also in terms of knowledge advantage.

1.2 Objectives of this study

The cement industry is a sector, which emits hard to abate and process-related CO_2. The use of this emitted species as a carbon source in the chemical industry to produce valuable products would favor greenhouse gas reduction and reduce consumption of fossil resources. The objective of this work is divided into three sections: a theoretical work of comparing different power-to-liquid processes to produce polyolefins out of CO_2, an experimental study of the rWGS reaction to validate the product gas composition for specific temperature, pressure and specific gas velocity ranges, as well as the influence of various commercial and development stage catalyst materials. The final part is the processing of the results obtained in the overall process simulations and the proposal of the best process route from a techno-economic point of view.

In the first part of the study, the potential for carbon capture and utilization processes and technologies should be identified, which are suitable for the integration in a cement factory and which are able to deal with the exhaust gas compounds from the clinker production process. The previously mentioned process units, such as the rWGS reactor, the Fischer-Tropsch or methanol synthesis should be defined and considered as conversion processes. As hydrogen is required for these PtL processes, various electrolysis' technologies (low and high temperature facilities) should also be taken into account. The processes should be mapped in a flow sheet simulation using the software ASPEN Plus V12.1 [22] to obtain the respective mass and energy balances. Key performance indicators (KPIs), such as the power-to-liquid efficiency, carbon efficiency and economic considerations like net production costs are defined, in order to obtain a meaningful and reasonable comparison of the process routes. The conclusion of this chapter should consist of a definition of the most appropriate technologies used for an optimal PtL process route, considering all techo-economic aspects.

The second part of the study includes the experimental work on the reverse water-gas shift reaction. As the rWGS reaction is mostly implemented as an equilibrium reactor in the flow sheet simulations, this study is intended to provide additional insight into the practical implementation of an rWGS reactor. Therefore, the endothermic reaction should be examined in a laboratory scale reactor and the design of the test rig should be elaborated within this study. The impact of the operation conditions, such as variation of temperature, pressure, or the gas hourly space velocity (GHSV) and the impact of various catalyst materials (especially nickel and perovskite-based materials) on the product composition should be investigated and discussed. These experimental results should validate the theoretical assumption of the implementation of a Gibbs reactor as rWGS unit in the flow sheet simulations.

Finally, the findings from the experimental perovskite catalyst are transferred to an ASPEN Plus simulation. In the flow sheet simulations, the impact of the implementation of the perovskite catalyst instead of a nickel-based catalyst needs to be addressed and a comparison of various possible process setups should be executed to obtain the advantages and disadvantage of implementing the newly investigated perovskite catalyst. The comparison of process indicators (product quantity, PtL, carbon efficiency and carbon decomposition) is intended to provide an initial indication of whether the integration of perovskite catalysts is viable for future PtL investigations and whether further development of perovskite catalysts should be pursued.

Summarizing the previous tasks, the following essential research questions are defined:

1. How should a PtL process for the production of polyolefins from cement plant off-gas be designed in order to obtain an optimal, efficient and cost-effective plant from a techno-economic point of view?

2. The hypothesis of implementing a Gibbs reactor in the flow sheet simulations must be confirmed by experimental tests. Is this assumption validated by the experimental investigation of nickel- and perovskite-based materials?

3. Which influence has the perovskite catalyst compared to the nickel-based catalyst on the KPIs, in particular on the efficiencies in the overall process, and is it worthwhile to conduct further research in the field of perovskite catalyst materials?

1.3 Structure of this thesis

The first part of the study involves a theoretical analysis and techno-economic evaluation of power-to-liquid processes for polyolefin production, in detail described in chapter 2. The fundamental parameters for the operation conditions (e.g., temperature, pressure) for the main process units, especially the rWGS reactor, are elaborated and a detailed analysis of the entire process chains is conducted in ASPEN Plus V12.1 [22]. Different rWGS and electrolysis operation strategies, as well as various recycle combinations are considered in the technological evaluation, to achieve high desired product yields regarding syncrude and downstream lower olefins. The PtL, global and carbon efficiencies are defined for a reasonable comparison, where all energy (electrical, thermal and product energy) streams are considered. The assessment of the techno-economic analysis is summarized at the end of this chapter.

In chapter 3, the experimental tests of the reverse water-gas shift reaction are explained. Starting with the structure and the flow sheet development of the test rig, this chapter also deals with the design of the experiments, the execution of the tests and the evaluation and analysis of the results. The main influencing parameters on the conversion yields in the rWGS reaction are evaluated, based on the operating temperature, pressure and GHSV, as well as the catalyst material used. In the summary of this chapter, the operating window (e.g., reliance on temperature and pressure) of the rWGS reaction is given to validate the operating conditions and the implementation of a Gibbs reactor supposed in the theoretical study.

In chapter 4, the experimental results from chapter 3 are implemented in an ASPEN Plus simulation, where a process route development of a Fischer-Tropsch synthesis with a rWGS reactor is executed and the process parameters (product quantity, PtL and carbon efficiency) with the integration of a perovskite catalyst in the rWGS reactor are compared with the previously investigated Ni/Al_2O_3 catalyst in chapter 2. Finally, this chapter shows whether the perovskite catalyst in Fischer-Tropsch PtL process chains has advantages over using a Ni/Al_2O_3 catalyst.

The cumulative thesis merges the results of the theoretical and experimental studies in the conclusion chapter 5. An outlook on further investigation in the field of CCU flow sheet simulations and the experimental tests of the rWGS reaction is also given in chapter 6. The publications on which this work is based on are appended to the conclusion and outlook chapters. The most relevant publications, including conference papers and peer-reviewed articles, are listed in Table 1.1. The publications and dissemination additionally executed during this work are presented in chapter 7.

Table 1.1: List of conference papers and the peer-reviewed manuscripts refereed to in this study

Publication number	**Title**	**Journal or conference**	**Citation**
Publication 1	Evaluation of process structures and reactor technologies of an integrated power-to-liquid plant at a cement factory	*Peer-reviewed journal* Published in Journal of CO_2 Utilization	[23]
Publication 2	Comparison and techno-economic evaluation of process routes for lower olefin production via Fischer–Tropsch and methanol synthesis	*Peer-reviewed journal* Published in International Journal of Greenhouse Gas Control	[24]
Publication 3	Impact of the Operation Conditions on the Reverse-Water-Gas Shift Reaction	*Conference paper* EURECA Pro 2022	[25]
Publication 4	Process intensification of the rWGS reaction by perovskite-based catalyst	Submitted for review	

Chapter 2

Techno-economic assessment of the power-to-liquid processes

In the first stage of each project realization, a feasibility study is conducted to get an idea of a process structure and to define the most appropriate process design according to key performance indicators from a technical (e.g., power-to-liquid efficiencies, product quantities) and economical perspective (e.g., investment and operating costs or net production costs). In this study, a carbon capture and utilization plant is designed at a pilot scale, which should capture 10,000 tons of CO_2 annually from the waste gas of a cement plant. The highly concentrated CO_2 should be further converted into a liquid intermediate product (such as methanol or syncrude), which can then be processed downstream into chemicals serving as feedstock for polyolefin production.

2.1 Overview of possible process routes for polyolefin production

The possible process routes are depicted in the following Figure 2.1 [24]. Carbon dioxide is in all process routes captured from the cement plant (1) with an amine scrubber unit (2). Hydrogen is produced via a low (5) or high (4) temperature water electrolysis, which is fed with purified water (3) and powered by green electricity (3) from the grid. The production of polyolefins can be performed via the intermediate methanol synthesis, where a distinction is made between direct hydrogenation of CO_2 (8) and the conventional methanol synthesis (9), the latter utilizes syngas. Syngas is produced by feeding an rWGS reactor (6) with hydrogen and CO_2 or directly from water and CO_2 in a solid oxide electrolysis (Co-SOEC, 7). The Co-SOEC is an electrolysis setup which combines the hydrogen production and rWGS reaction to produce directly syngas. This technology does not follow the heterogeneous catalysis approach

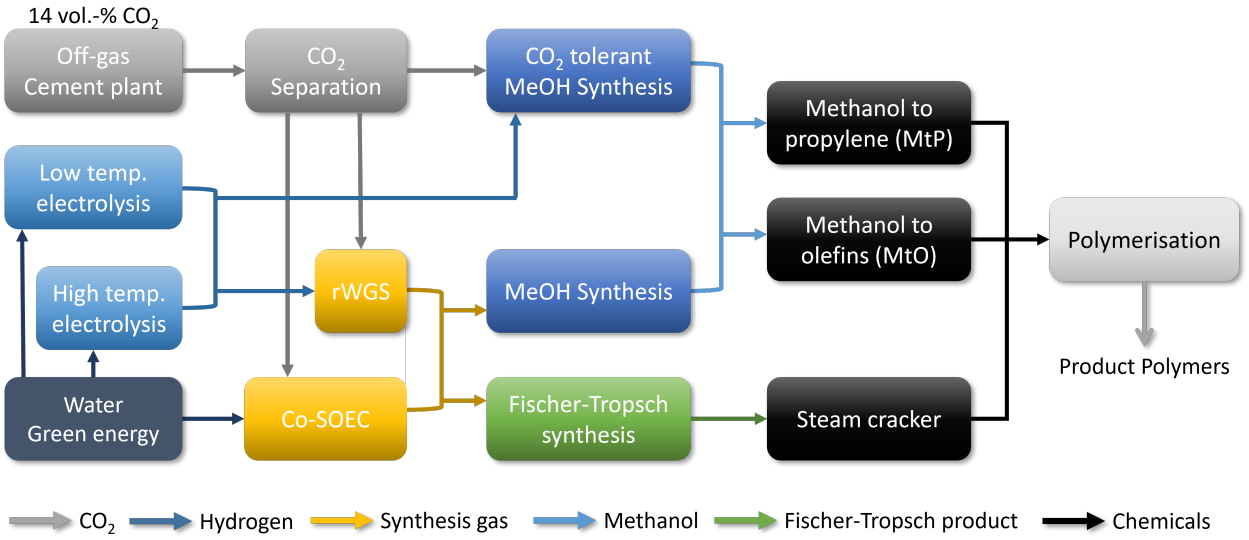

Figure 2.1: Block flow diagram of possible CO_2 conversion routes to produce polyolefins

and is therefore not in the scope of this study. Methanol as intermediate product is converted in either a methanol-to-propylene (MtP, 10) or methanol-to-olefin (MtO, 11) unit to the desired lower olefin feedstock for polymerization process (14). The second possible technology is the Fischer-Tropsch synthesis (12), which is also operated with syngas, supplied from (6) and (7). The Fischer-Tropsch product, also called syncrude (consisting of liquid, mostly paraffinic hydrocarbons at atmospheric pressure) is then converted in a steam cracker (13) to mainly lower olefins which are again a feedstock for the polymerization unit (14).

As the plant is designed in pilot scale on the site of a cement factory and close to a refinery, all existing facilities should be taken into account to be able to deduce whether the investment or operating costs can be reduced, or synergy effects can be used (e.g. steam generation, cooling facilities). Figure 2.2 shows the possible process routes which are considered in this study [24]. The various colors describe the existing (blue) or new planned infrastructure or utilities (green). Within the scope of this study is the CO_2 separation unit, the electrolysis and the conversion of CO_2 to lower olefins. The amine scrubber unit is designed once, as the CO_2 capture quantity is fixed with 10,000 tons per year. Process route 1 describes the pathway through Fischer-Tropsch synthesis with pre-conversion of CO_2 and H_2 in a rWGS reactor to syngas and a subsequent steam cracker. A distinction is made in the steam cracker utility, as it is firstly assumed as a new facility located at the site of the cement plant, but also as existing infrastructure in the refinery. The impact of synergies on the economic assessment (e.g., additional investment costs) between existing and new facilities should be addressed here.

Process route 2 involves conventional methanol synthesis operated with synthesis gas. Therefore, synthesis gas is produced from CO_2 and H_2 in the first step, which is used as feed

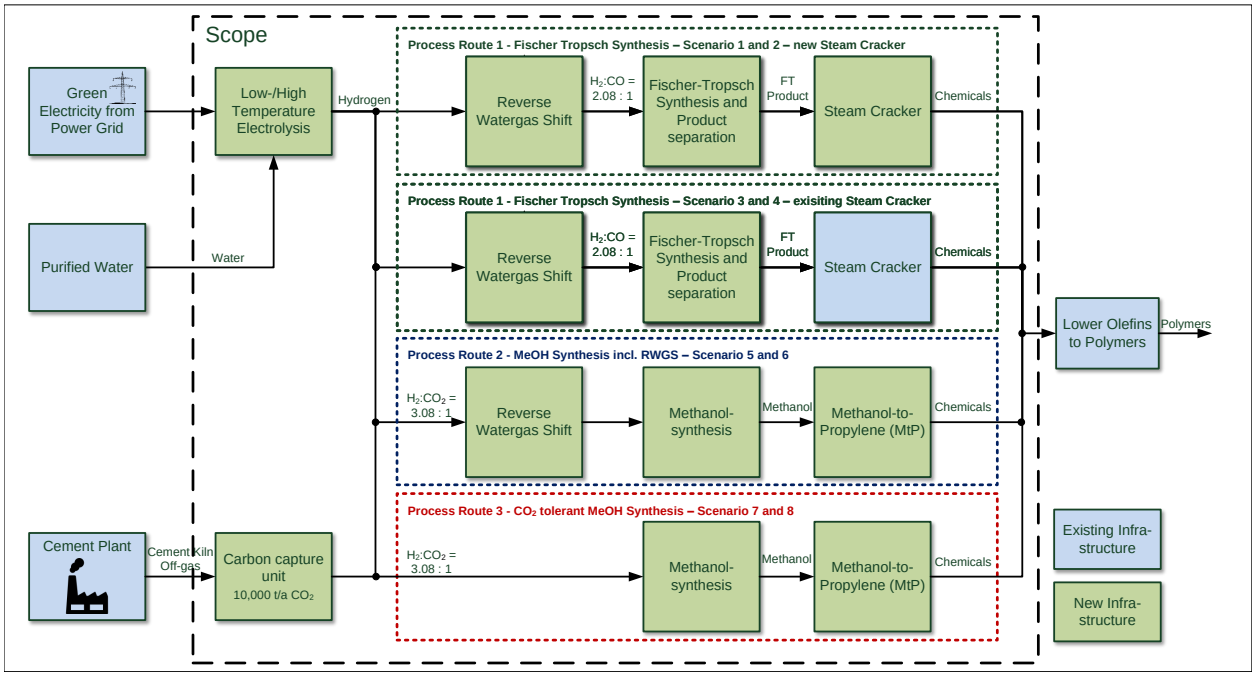

Figure 2.2: Block flow diagram of possible carbon capture and utilization process routes to produce lower olefins as feedstock for the polyolefin production [24]

gas for methanol synthesis. Process route 3 differs in the execution of methanol synthesis. There are suggestions to directly convert CO_2 with hydrogen in the synthesis [17]. This assumption is followed in this process route. The produced methanol is then fed into a methanol-to-propylene (MtP) plant in both process routes to obtain the lower olefin fraction, mainly consisting of propylene.

2.2 Fundamental design of the flow sheet simulation

In the following section, the design of the flow sheet simulation is described. Reference is made to the detailed description of the process simulation in the publications 1, 2 and 3. The simulation was improved with every publication to achieve reasonable comparisons of the various process routes. The most important assumptions regarding operating conditions and process operation that were made are mentioned and explained again in these sections.

For a suitable technical analysis, key performance indicators (KPIs) are defined to obtain meaningful key figures for the process comparison. The power-to-liquid efficiency (η_{PtL} – Equation 2.1), the global efficiency (η_{global} – Equation 2.2), the carbon efficiency (η_{carbon} – Equation 2.3) and the specific energy consumption (SEC – Equation 2.4) are defined as comparable KPIs.

The PtL efficiency (η_{PtL}) is defined in Equation 2.1 as the quotient of the product energy content (multiplication of the mass flow m_i in kg h^{-1} with the lower heating value LHV_i in kWh kg^{-1} of the component i) and the required electrical energy for the electrolysis (P_{el} in kW) and the utilities (Pu in kW, e.g., compressors, pumps).

$$\eta_{\mathrm{PtL}} = \frac{\sum \dot{m}_i * \mathrm{LHV}_i}{P_{el} + P_u} \tag{2.1}$$

The global efficiency (η_{global}) considers also the steam generation ($\dot{Q}_{heat}$ in kW and as negative value) and consumption ($\dot{Q}_{heat}$ in kW and as positive value) beside the electricity demand and is calculated according to Equation 2.2.

$$\eta_{\mathrm{global}} = \frac{\sum \dot{m}_i * \mathrm{LHV}_i}{P_{el} + P_u + \dot{Q}_{heat}} \tag{2.2}$$

The carbon efficiency (η_{carbon}) is given in Equation 2.3 and describes the carbon yield in terms of the ratio of each product carbon atom stream i ($\dot{Q}_{i,product}$ in kmol h^{-1}) to the carbon atoms in the feed stream ($\dot{n}_{feed}$ in kmol h^{-1}).

$$\eta_{\mathrm{carbon}} = \frac{\sum \dot{n}_{i,product}}{\dot{n}_{feed}} \tag{2.3}$$

The specific energy consumption (SEC in kWh kg^{-1}) is calculated by Equation 2.4 and divides the total electrical energy input by the product mass flows.

$$\mathrm{SEC} = \frac{P_{el} + P_u}{\sum \dot{m}_i} \tag{2.4}$$

Heat integration in all described processes is carried out using ASPEN Energy Analyzer V12.1. The process flows are specified in a pinch diagram and the demand for utility flows (e.g. cooling water, heat demand or generation in the form of steam) is calculated. Furthermore, reactor cooling or heating facilities (exothermic or endothermic cooling or heating quantities) are also considered here.

2.2.1 CO_2 separation unit

The exhaust gas of the cement plant consists of 14 vol.-% CO_2, 64 vol.-% N_2, 12 vol.-% H_2O and 10 vol.-% O_2 [7]. There are several options for carbon capture technologies. In this study, an amine scrubber unit is selected. On the one hand, the chemical absorption

process deals well with low CO_2 concentrations in the exhaust gas, which is unsuitable for the application of a physical absorption [26]. On the other hand, the high energy demand for solvent regeneration is a major disadvantage, as it demands additional energy in the range between 3.8 and 5.4 MJ $kg^{-1}_{CO_2}$ for the applied monoethanolamin (MEA) solvent [27]. Nevertheless, the optimal carbon capture technology varies related to the off-gas composition (it is also compulsory to consider impurities, e.g., H_2S, SO_2, NO_x) and needs to be clarified in a separate feasibility study. In general, impurities lead to an advanced degradation of the amine solvent. Therefore, pre-condition units should be implemented to avoid these degradation processes [28], [29]. The selected amine scrubber unit fits for the aforementioned exhaust gas stream and is implemented in this study due to its high technological readiness level (TRL 9) [30].

The principle of the amine scrubber unit is depicted in Figure 2.3. The exhaust gas of the cement plant is supplied at atmospheric pressure and a temperature of about 100 °C. It is compressed slightly higher than atmospheric pressure with a blower, to generate a gas stream flow through the pre-conditioner unit. Herein, the gas stream is cooled to a temperature level of about 40 °C. An aqueous NaOH solution sprinkles from the top of the column in countercurrent flow to the gas to achieve high separation yields of undesired dust particles, achieve the desired temperature decrease and also reduce traces of impurities such as SO_2. Behind the conditioner unit, the gas is contacted with the lean amine solution in the absorber tower. CO_2 dissolves in the solution, whereas the other components exit the column at the top. The loaded amine solution is extracted from the bottom of the absorber column, heated to approx. 100 °C and fed to the stripper or desorber tower. A reboiler provides the required energy in the desorber of about 3.8 MJ $kg^{-1}_{CO_2}$. Because of the increased temperature, CO_2 is endothermically released from the amine solvent and is provided as a highly concentrated gas at the top of the desorber column. The purity of CO_2 in the dry gas stream is 99.9 wt.-% [24].

2.2.2 Water electrolysis unit

In the process routes shown in Figure 2.2, hydrogen is the second reactant beside CO_2. The water electrolysis is the most common route for green hydrogen production nowadays. Green energy sources demand a CO_2 neutral energy mix, whereas the electricity needs to be produced entirely by renewables (e.g., wind turbines, solar parks). The use of hydrogen produced from fossil fuels, e.g. the electricity is generated by coal or gas, or CO_2 releases during steam reforming, would contradict the purpose of a CCU system [31]. In this study, water electrolysis is used for the production of hydrogen and the by-product oxygen. Oxygen is not considered in the process, but further investigations can analyze whether it can be

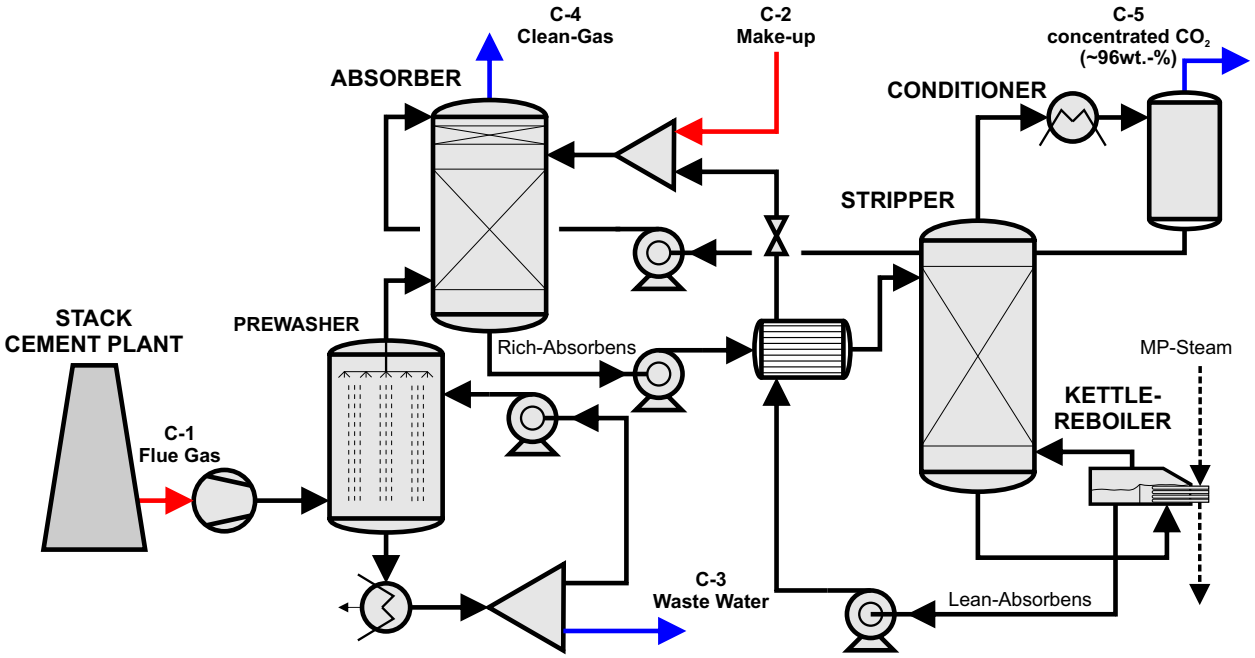

Figure 2.3: Flow sheet of the amine scrubber unit to capture 10,000 tons of CO_2 per year

used for the oxyfuel process in the cement plant. The reaction is strongly endothermic (see Equation 2.5), which leads to a high energy consumption for the production of the hydrogen.

$$H_2O_{(l)} \longrightarrow H_{2(g)} + 0.5\,O_{2(g)} \qquad \Delta H_r^{298K} = 286\,\text{kJ mol}^{-1} \tag{2.5}$$

A distinction of the technology is made into the low (alkali electrolysis - AEL and proton exchange electrolysis - PEM) and the high temperature electrolysis (solid oxide electrolysis - SOEC). The main differences are the feed phase, the specific energy consumption, operating temperature and pressure. Trattner et al. summarized the main properties of each electrolysis as shown in Table 2.1 [32].

Table 2.1: Technical specifications of the alkali electrolysis (AEL), the proton exchange electrolysis (PEM) and solid oxide electrolysis (SOEC) [32]

Electrolysis	**Unit**	**AEL**	**PEM**	**SOEC**
System efficiency	%	< 65	< 65	< 82
Operating temperature	°C	60 - 95	50 - 80	700 - 1,000
Operating pressure	bar	atm. - 32	atm. - 40	1 - 3
System size	MW	< 100	< 100	< 0.15
CAPEX costs	€ kW^{-1}	500 - 1,200	1,000 - 1,800	1,200 - 2,000

For the low temperature technique, the PEM electrolysis is preferred against the AEL, due to the high dynamic operation mode and ultrapure hydrogen quality. The coupling of hydrogen

as energy storage with the unpredictably fluctuating availability of renewable energy sources thus become feasible [32]. The cooling of the PEM electrolysis with 17 % of the electrical energy demand represents a disadvantage and energy loss of this technology [33]. In contrast, SOEC is used in high-temperature technology. Since this technology uses steam as the input stream, it is particularly advantageous for endothermic downstream processes and results in correspondingly lower specific energy consumption. The disadvantage of this technology lies in its operation at very high temperatures of 700 - 1,000 °C, which compromises flexibility and stack lifetime, especially at startup [9], [32]. Trattner et al. also state that the total electrolysis capacity of 0.15 MW is very small, and the investment costs are correspondingly high [32]. However, further development of this technology could potentially drive the cost attractiveness of SOEC [9]. The simulation of the electrolysis is executed as a stoichiometric reactor in ASPEN Plus with operation conditions according to Table 2.1. The water splitting reaction (Equation 2.5) is considered with a conversion rate of H_2O of 95 % [34]. The detailed simulation of the process unit is described in the publications 1, 2 and 3.

2.2.3 Reverse water gas shift reaction

Before addressing synthesis technologies, a closer examination will be conducted on the production of synthesis gas. This section is examined in greater detail, as these theoretical considerations will also be applied in the experimental part of the study (chapter 3).

The reverse water-gas shift (rWGS) reaction is a technology employed to produce synthesis gas from carbon dioxide and hydrogen, as allocated in Equation 2.6.

$$CO_2 + H_2 \longleftrightarrow CO + H_2O \qquad \Delta H_r^{298K} = 41\,\text{kJ mol}^{-1} \tag{2.6}$$

Synthesis gas serves as a feedstock for subsequent syntheses, with a compulsory requirement in Fischer-Tropsch synthesis. The rWGS reaction, as previously mentioned in the introduction, has been sparsely explored, and many simulations have made invalidated assumptions [9], [13], [16], [17]. This study also made initial assumptions, with a focus on considering the thermodynamic equilibrium by minimizing the free Gibbs energy (Gibbs reactor).

In an rWGS reactor, CO_2 and H_2 are ideally converted into CO and H_2O, however all occurring side reactions must be accounted for. The Sabatier (Equation 2.7) and methanation reaction (Equation 2.8) can either convert CO or CO_2 and H_2 into methane (CH_4), which is undesired or may lead to increased operational costs in subsequent processes.

$$CO + 3\,H_2 \longleftrightarrow CH_4 + H_2O \qquad \Delta H_r^{298K} = -206\,kJ\ mol^{-1} \tag{2.7}$$

$$CO_2 + 3\,H_2 \longleftrightarrow CH_4 + 2\,H_2O \qquad \Delta H_r^{298K} = -165\,kJ\ mol^{-1} \tag{2.8}$$

Additionally, the H_2:CO_2 input ratio must be chosen correctly to prevent coke formation in the system, with special consideration for decomposition of methane (Equation 2.9), the Boudouard (Equation 2.10) and Bosch (Equation 2.11) reactions.

$$CH_4 \longleftrightarrow C_{(s)} + 2\,H_2 \qquad \Delta H_r^{298K} = 75\,kJ\ mol^{-1} \tag{2.9}$$

$$2\,CO \longleftrightarrow C_{(s)} + CO_2 \qquad \Delta H_r^{298K} = -172\,kJ\ mol^{-1} \tag{2.10}$$

$$CO_2 + 2\,H_2 \longleftrightarrow C_{(s)} + 2\,H_2O \qquad \Delta H_r^{298K} = -91\,kJ\ mol^{-1} \tag{2.11}$$

Thermodynamic equilibrium is examined in ASPEN Plus over a temperature range of 350 – 1,100 °C and pressures of between 1, 10, and 30 barg. The conventional components CO_2, CO, CH_4, H_2, H_2O and carbon as solid conventional component are considered in the simulation. The thermodynamic equilibrium composition is depicted for the three pressure levels in Figure 2.4. A Gibbs reactor is implemented in the simulation, considering A Gibbs reactor is implemented, which calculates the thermodynamic equilibrium by various species and applying the principle of minimizing the Gibbs free energy. This results in the corresponding product gas composition.

Since downstream processes are often operated with an H_2:CO ratio of 2:1, the rWGS is operated with an input ratio of H_2:CO_2 = 3:1, although the rWGS reaction would require a H_2:CO_2 feed ratio of 1:1 according to Equation 2.6. This offers an additional advantage, particularly, the suppression of coke formation due to the excess of hydrogen. The selectivity is defined in Equation 2.12 for carbon monoxide S(CO) to provide insight into the conversion of CO_2 into CO and the formation of by-products during the reaction (mole flows in kmol h^{-1} of CO and CO_2 into ($\dot{n}_{CO,in}$ and $\dot{n}_{CO_2,in}$), as well as out ($\dot{n}_{CO,out}$ and $\dot{n}_{CO_2,out}$) of the system). The results of the Gibbs reactor represented as the product gas composition with a H_2:CO_2 feed gas ratio of 3:1 is given in Figure 2.4. CO selectivity and its dependence on the temperature and pressure is depicted in Figure 2.5.

$$S(CO) = \frac{\dot{n}_{CO,out} - \dot{n}_{CO,in}}{\dot{n}_{CO_2,in} - \dot{n}_{CO_2,out}} \tag{2.12}$$

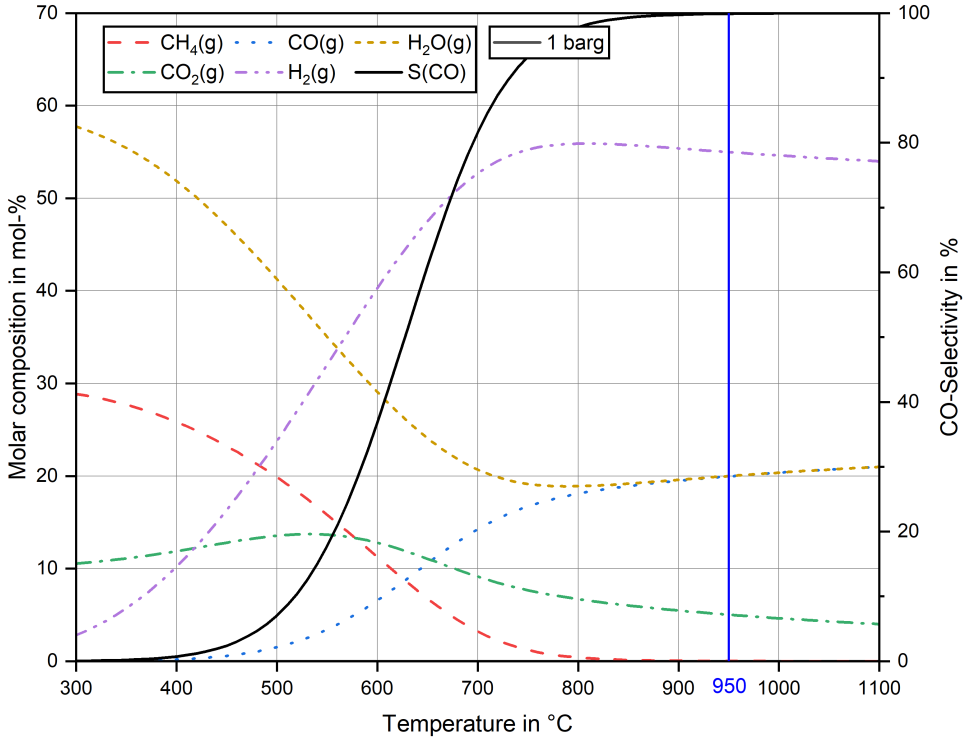

(a)

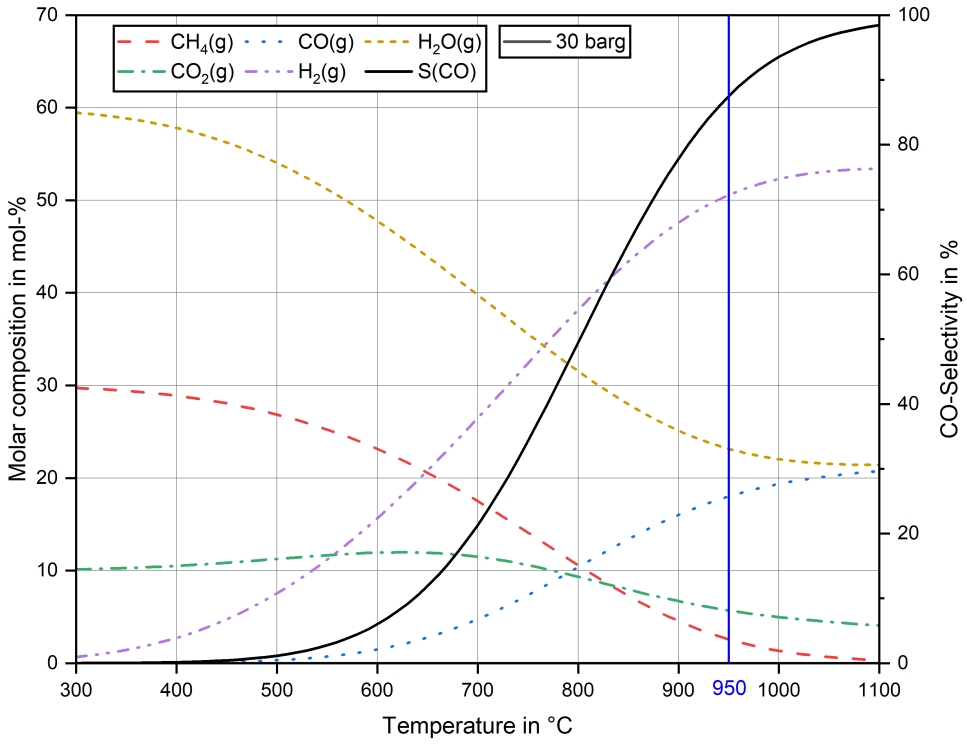

(b)

Figure 2.4: Product gas composition of the reverse water gas shift reaction with a feed gas ratio of H_2:CO_2 = 3:1 for temperatures between 300 and 1,100 °C and pressures of a) 1 and b) 30 barg. Applied operating temperature of 950 °C is marked in both diagrams.

From the analysis of the thermodynamic equilibrium, it becomes evident that methane formation is scarcely noticeable at 1 barg and temperatures exceeding 800 °C. As pressure increases, methane formation also increases. To almost completely obtain 99.9 % CO selectivity and suppress methane formation while approaching the pressure level of the synthesis process, an operating temperature of 950 °C and a pressure level of 10 barg are selected as first assumption for the rWGS Gibbs reactor in the simulations. The CO selectivity with these conditions is 98 % and marked in Figure 2.5 as a cross ("X").

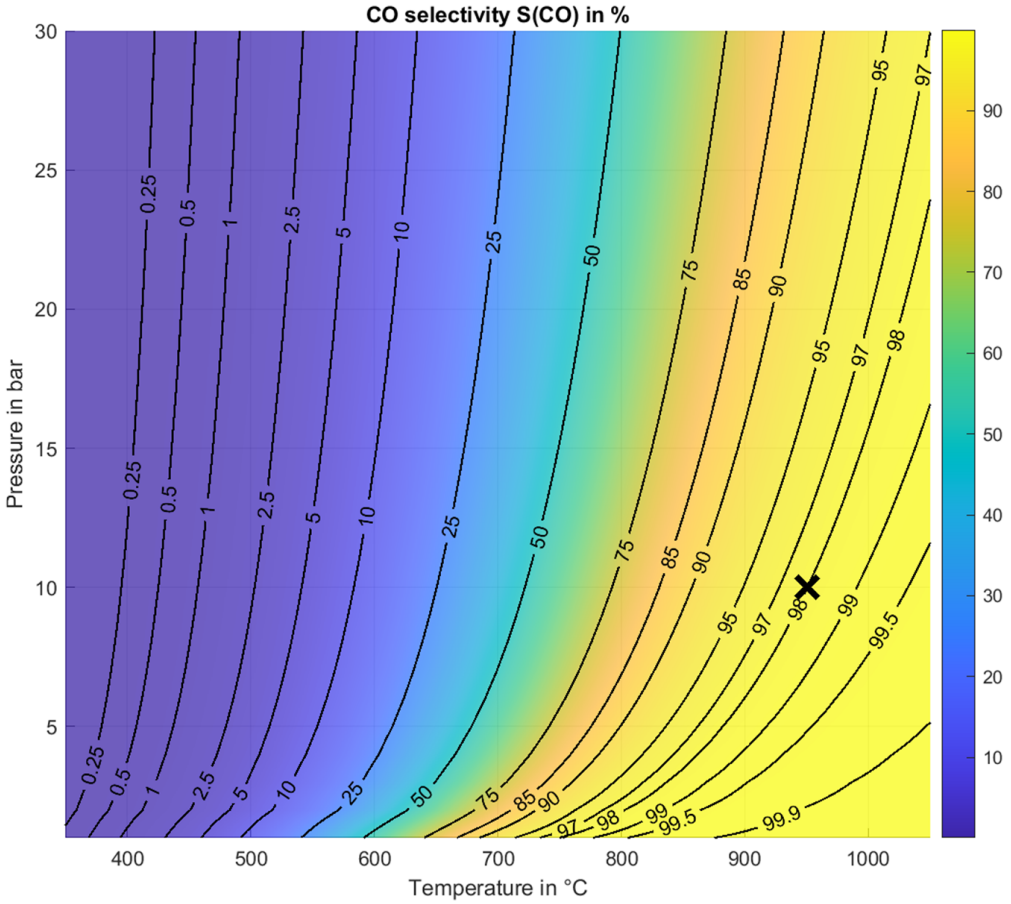

Figure 2.5: Impact of the temperature (350 - 1,050 °C) and the pressure (1 - 30 barg) variation on the CO selectivity for an inlet gas composition of H_2:CO_2 = 3:1. The cross (X) indicates the chosen operation conditions for the simulation with a temperature of 950 °C and pressure of 10 barg

The rWGS reaction can be conducted in a steam methane reformer, where energy is supplied through the combustion of natural gas. A drawback of this approach is the generation of CO_2 emissions due to heat provision, which needs to be addressed with innovative technologies [35]. In Publication 1, two rWGS technologies and their impact on key performance indicators (KPIs, e.g. PtL or global efficiency, defined in section 2.2) are analyzed. The electrified reactor, described by Wismann et al., and the autothermal reactor, described by Chiesa et al., are selected for this comparison [35]–[37].

In the electrified reactor, the required heat is generated using green electricity and resistance heating within the reactor tubes [35]. Conversely, the autothermal reactor achieves energy supply by combusting H_2 and O2 at the reactor inlet, which leads to a basically higher demand of hydrogen production [36]. It is essential to note that this combustion uses green, carbon-neutral hydrogen to count to the CO_2 neutral technology. These two reactor variants are represented in violet (electrified) and blue (autothermal) in the accompanying diagram (Figure 2.6).

Additionally, Publication 1 explores various gas pathways around the rWGS. Typically, the rWGS reactor is simulated as a Gibbs reactor, where CO_2 and H_2 react to thermodynamic equilibrium (Figure 2.5), resulting in some remaining CO_2 in the product gas. As CO_2 can be considered inert in the downstream process (described in 2.2.4 Fischer-Tropsch synthesis), the objective is to maximize CO_2 conversion within the rWGS process. Different recycle streams, as shown in red, are examined to assess potential CO_2 conversions.

In process setup 1, the rWGS reactor is operated as a single pass unit, with the process gas directed to the downstream process. In process setup 2, CO_2 is separated from the product stream through CO_2 absorption and then reintroduced into the feed gas CO_2 stream. Process step 4 involves recycling 34 % of the product gas stream before the rWGS reactor, necessitating an additional compressor. Process setup 3 is similar to setup 4 but utilizes the existing CO_2 compressor for recycling, whereby a pressure loss in the recycled gas flow is accepted.

In Publication 1, the selection of the rWGS technology and recycle streams is investigated while considering a downstream Fischer-Tropsch synthesis to calculate the relevant KPIs. The comparable KPIs (e.g., power-to-liquid, carbon efficiency, global efficiency) are described in detail in Publication 2. The results of the study show that process setup 1, without a recycle stream around the rWGS reactor, is the optimal option with the highest PtL efficiency (44.0 % compared to 43.9 %, 41.5 %, and 43.7 % for setups 2 to 4, respectively). Furthermore, the comparison reveals that the additional hydrogen requirement for the autothermal reactor reduces PtL efficiency from 44.0 % (PEM and process setup 1) and 53.9 % (SOEC and process setup 1) to 41.7 % (PEM, process setup 1) and 53.5 % (SOEC and process Setup 1). This implies that the direct conversion of electrical energy into heat offers a significant advantage of the electrified rWGS reactor over the autothermal reactor.

Based on the findings in Publication 1, the electrified rWGS reactor technology is adopted for all subsequent simulations.

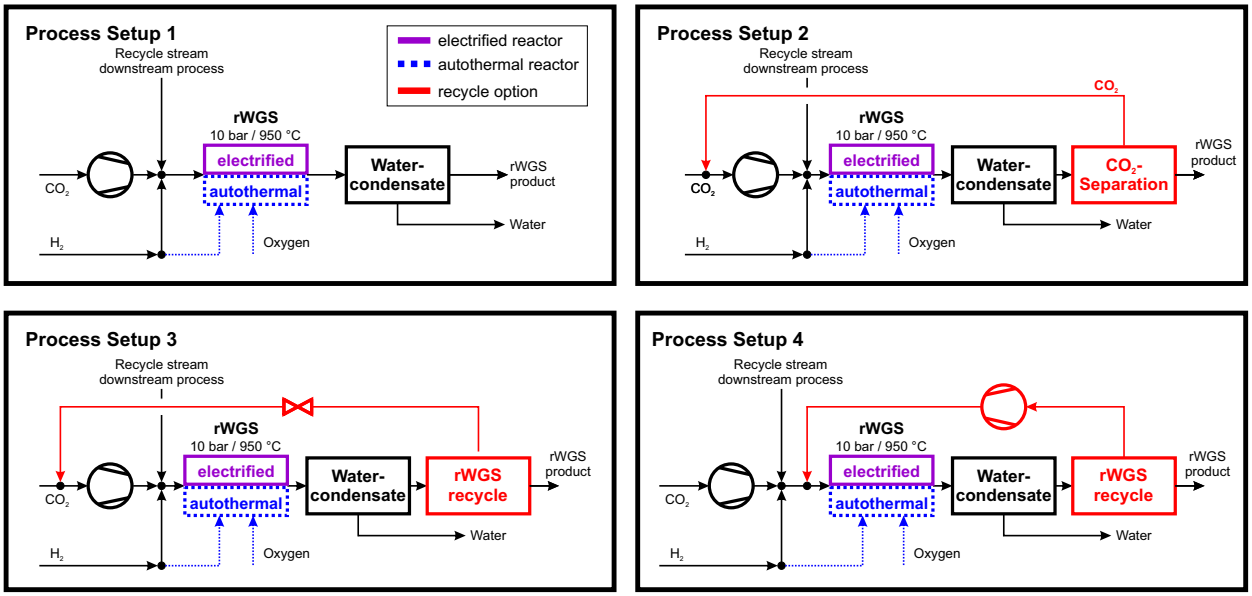

Figure 2.6: Possible process setups for the rWGS reaction in a single stage (process setup 1), with downstream CO_2 separation (process setup 2) or partial product gas recycle (process setup 3 and 4, distinguished to an additional compressor in process setup 4)

2.2.4 Fischer-Tropsch synthesis and steam cracker

In the illustration of the various process routes shown in Figure 2.2, the first process route is the Fischer-Tropsch synthesis with a downstream steam cracker unit. The Fischer-Tropsch synthesis is a highly advanced technology that produces synthetic crude oil from syngas in a strongly exothermic reaction, given in the following Equation 2.13.

$$\mathrm{CO} + 2\,\mathrm{H_2} \longrightarrow -\mathrm{CH_2}- + \mathrm{H_2O} \qquad \Delta \mathrm{H_r^{298K}} = -140\mathrm{to} - 160\ \mathrm{kJ\ mol_{CO}^{-1}} \tag{2.13}$$

Other gases present in the gas stream, such as CO_2, CH_4, or N_2, are considered inert and merely increase the gas volume flow rate. Higher gas volume streams generally have a negative impact on investment cost calculations. The chain growth probability is described by the Anderson-Schulz-Flory distribution, which is also detailed in the publications 2 and 3 [38]. In this study, a fixed-bed reactor is employed as a low-temperature Fischer-Tropsch synthesis with a cobalt catalyst, as it results in paraffins as the predominant component in the product stream [39]. Typical operating conditions include temperatures around 220 °C and a pressure of approximately 25 bar [16]. It is worth noting that the cobalt catalyst exhibits high selectivity for methane, which deteriorates the overall process efficiency, especially the carbon efficiency.

Due to the highly exothermic nature of the reaction, the reactor must be designed with a cooling facility to prevent runaways. This can be achieved through the integration of a boiling water cooling system, which is also used for steam generation. Particularly when coupled with high-temperature electrolysis (SOEC), this heat integration leads to significant energy savings and can substantially enhance the overall process efficiency.

Long-chain hydrocarbons occur in the reactor as a liquid phase, which is directly withdrawn from the reactor. In the product separation of the gas product stream, two flash drums are utilized, containing fractions of middle distillate, naphtha, and a gas phase consisting of short-chain hydrocarbon molecules and unreacted reactants. The fractions of naphtha, middle distillate, and wax are subsequently converted into the main fraction of lower olefins in a downstream steam cracker. These lower olefins serve as the feedstock for polyolefin production. All other fractions are considered byproducts.

In the publication of Markowitsch et al. [21], a detailed analysis of the influence of recycle streams on the Fischer-Tropsch synthesis was conducted. Additionally, the impact of assuming a 40 % CO conversion in the Fischer-Tropsch reactor, as suggested by Adelung et al. and König, is examined, along with the effect of increasing this parameter to 64 % (proposed by Ostadi et al.) [14], [16], [40]. The comparison is based on PtL efficiency, chemical conversion, product quantity, specific energy consumption, and carbon conversion. This investigation also involves varying methane selectivity (from 16 % to 8 %) [16], [40]. The subsequent flow sheet (Figure 2.7) illustrates the CO_2 and H_2 conversion process with two recycle streams, one upstream to the Fischer-Tropsch reactor (recycle stream 1) and the other upstream to the rWGS reactor (recycle stream 2).

The split ratio is defined in Equation 2.14, indicating the volume-based percentage of the gas phase returned to recycle stream 1. A ratio of 2 % from the entire product gas stream is constantly discharged as purge gas to eliminate any gas impurities and prevent the system for impurity-accumulations (e.g., nitrogen). A split ratio of 0.98 indicates that 98 % by volume belongs into recycle stream 1, while 2 % is deducted from the process as a purge gas stream.

$$\text{Split ratio} = \frac{\text{gas flow in recycle stream 1 in m}^3\ \text{h}^{-1}}{\text{total gas flow from the FT synthesis in m}^3\ \text{h}^{-1}} \tag{2.14}$$

The results of the variation in process variables and split ratios are presented in Figure 2.8. The investigation shows that the split ratio in the range of 0 to 0.5 exerts no significant influence on the KPIs. However, a higher split ratio leads to a drastic deterioration of the efficiency parameters. Consequently, the possibility of operating with a complete recycle stream through the Fischer-Tropsch synthesis (split ratio = 0.98) is excluded.

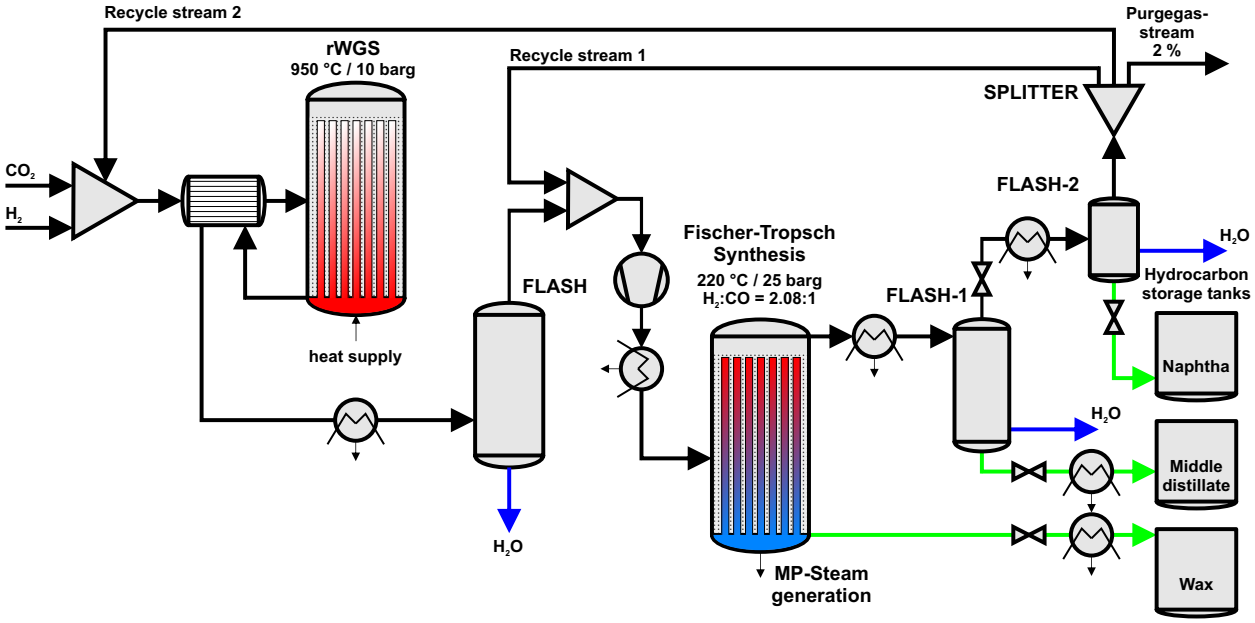

Figure 2.7: Flow sheet of the synthesis with the applied recycle streams 1 (around Fischer-Tropsch reactor) and 2 (upstream the rWGS reactor) and the constant purge gas stream (2 %)

The pivotal factor lies in the accumulation of methane and CO_2 within the recycle gas stream, which is regarded as inert in the Fischer-Tropsch synthesis, contributing solely to gas stream buildup. Given that the purge gas stream is limited to 2 %, the feed gas stream in the Fischer-Tropsch synthesis increases significantly, causing potential carbon or hydrogen species, particularly CH_4 or CO_2, to be directed into the purge gas stream. Recycling these unconverted gases upstream the rWGS reactor results in the conversion of methane and CO_2 into CO and H_2, corresponding to the steam methane reforming (Equation 2.15) and rWGS reaction (Equation 2.6), respectively.

$$CH_4 + H_2O \longleftrightarrow CO + 3\,H_2 \qquad \Delta H_r^{298K} = 206\,\text{kJ mol}^{-1} \tag{2.15}$$

Markowitsch et al. [21] also underscores the advantages of applying catalyst with higher CO conversions ($X_{CO} = 64\,\%$) and lower methane selectivities ($S_{CH_4} = 8\,\%$) for improved PtL efficiencies and reduced specific energy consumptions. In the best-case scenario, a Fischer-Tropsch process with a single recycle stream upstream of the rWGS reactor (recycle stream 2) is implemented, yielding the highest efficiencies, the highest product quantity and the lowest specific energy consumption. These findings are incorporated into all subsequent simulations related to Fischer-Tropsch synthesis (in Publication 1 and 2).

The application of a steam cracker downstream of the Fischer-Tropsch process enables the paraffinic syncrude to be converted into olefins. Usually, only naphtha and middle distillates

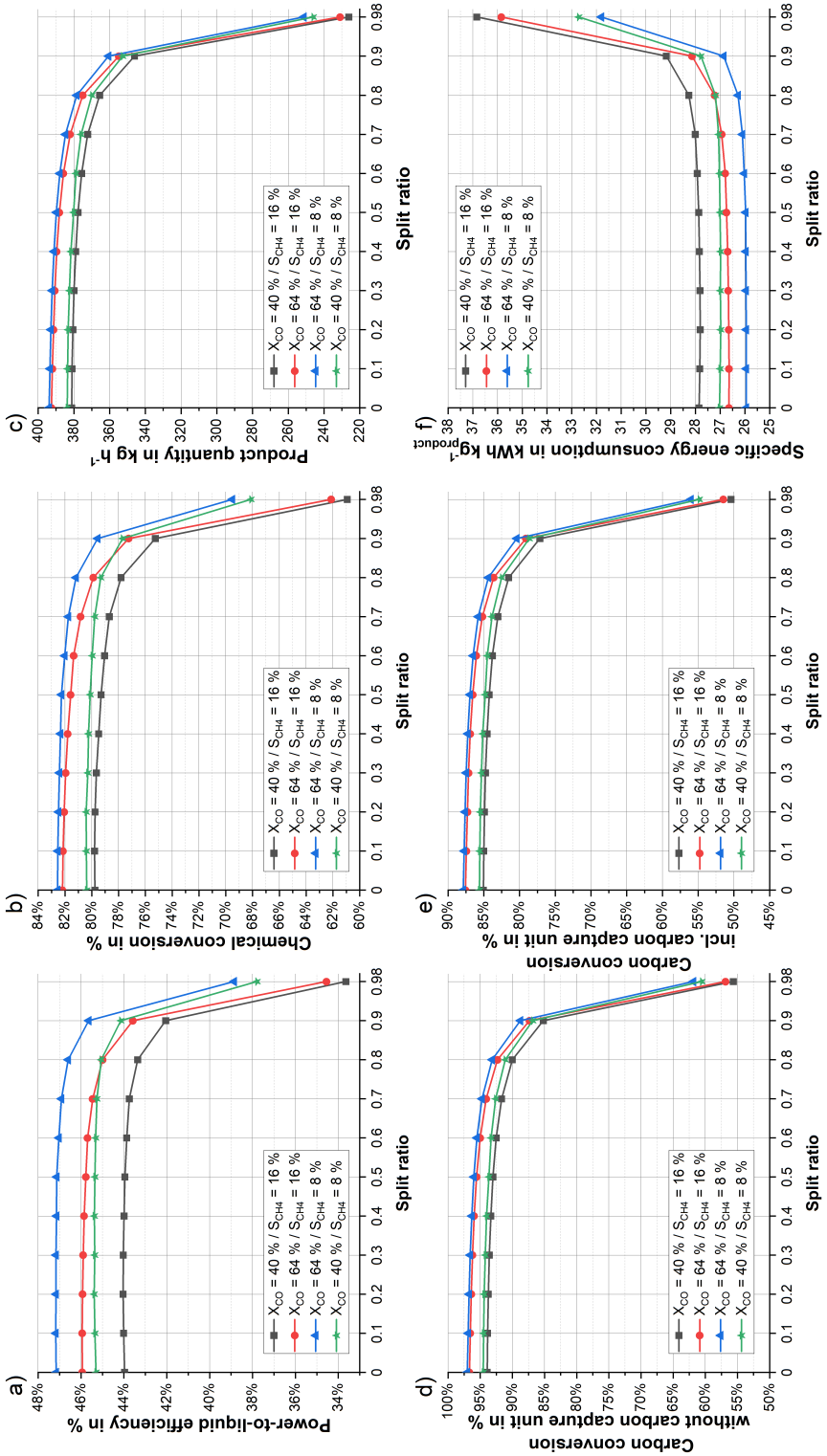

Figure 2.8: Impact of the recycle split ratio, CO conversion and CH_4 selectivity on the a) PtL efficiency, b) the chemical conversion, c) the product quantity, d) the carbon conversion without carbon capture unit (CC), e) the carbon conversion with CC unit and f) the specific energy consumption

are used for the conventional steam cracker technologies. The wax fraction needs to be cracked into lower paraffins in a previous step (hydrocracking), before feeding them to the steam cracker. Karaba et al. investigated the use of the entire Fischer-Tropsch product, which is produced from renewable sources and contained naphtha, middle distillates and waxes [41]. Their unit operates at 850 °C and moderate pressure of 4 barg. Karaba et al. derived yield vectors for the production of the olefins from the input streams, divided into FT lights (C_5 - C_{11}), FT middle distillate (C_{10} - C_{23}) and vacuum residue (C_{18} - C_{43}). Thus, the steam cracker unit is not implemented as a reactor in ASPEN Plus. The product quantities of the Fischer-Tropsch process are utilized in a theoretical calculation with the deployment of yield vectors [41]. The lower olefin fraction contains ethylene, propylene, but-1-ene, i-butene and butadiene. The energy demand to operate the steam cracker is assumed to be provided electrically with a requirement of 15 MJ $kg^{-1}_{\text{FT-Product}}$ [42].

2.2.5 Methanol synthesis and methanol-to-propylene unit

The conventional methanol synthesis is a well-established technology that produces methanol from synthesis gas. In contrast to the Fischer-Tropsch synthesis, the conventional and CO_2 tolerant methanol reactions are given in Equation 2.16 and Equation 2.17, respectively.

$$CO + 2\,H_2 \longleftrightarrow CH_3OH \qquad \Delta H_r^{298K} = -91\,\text{kJ mol}^{-1} \tag{2.16}$$

$$CO_2 + 3\,H_2 \longleftrightarrow CH_3OH + H_2O \qquad \Delta H_r^{298K} = -49\,\text{kJ mol}^{-1} \tag{2.17}$$

To obtain the best operation conditions for the methanol synthesis, the thermodynamic equilibrium is first investigated as shown in Figure 2.9, using a Gibbs reactor in ASPEN Plus. It is important to note that CH_4 must not be considered as a product of the reaction or a side reaction. The catalysts used, such as $Cu/ZnO/Al_2O_3$, are designed to almost completely inhibit CH_4 formation. Minor byproducts like higher alcohols or methyl formate may also be formed, but they constitute a small fraction (approximately 0.06 wt.-%) and are therefore neglected in this study [43]. The analysis covers a temperature range of 120 to 300 °C for pressures of 20, 40, 60, and 80 bar. In Figure 2.9a, the thermodynamic equilibrium for the conventional (Equation 2.16) and in Figure 2.9b for the CO_2 tolerant (Equation 2.17) methanol synthesis are provided. Based on the aforementioned considerations and the existing literature, the reaction conditions of the methanol synthesis are selected with a temperature of 240 °C and pressure of 80 barg, to achieve high CO and CO_2 yields for methanol production.

It is evident that the conversion of CO in conventional methanol synthesis is higher than in the CO_2-tolerant process, and the reaction prefers higher pressure and lower temperatures.

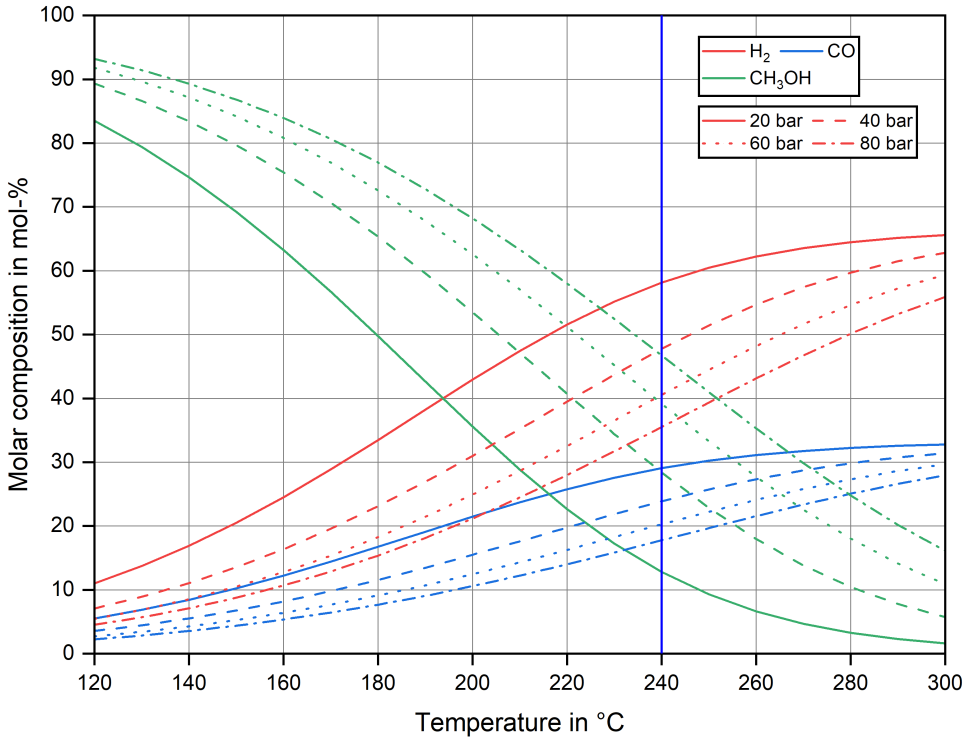

(a)

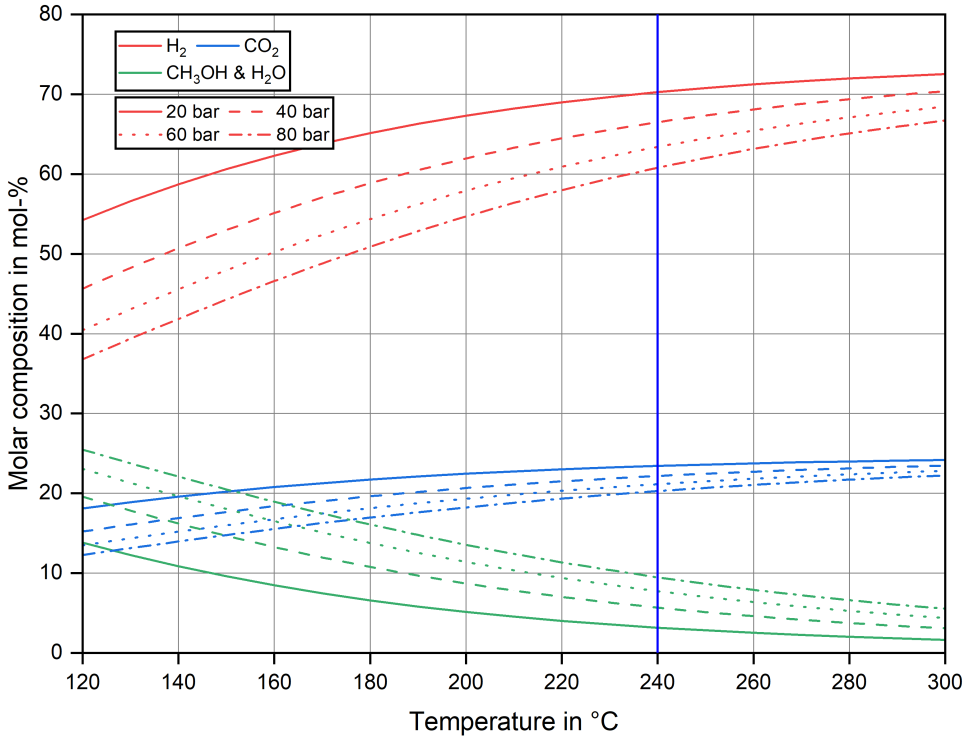

(b)

Figure 2.9: Thermodynamic equilibrium and indicated operating temperature (240 °C) for a) the conventional methanol synthesis and b) the CO_2 tolerant methanol synthesis

In this case, the reaction rate is limited by temperature, leading to kinetic limitations. The kinetics of Bussche et al. are implemented in the next step of the simulation, which is also necessary for an appropriate reactor sizing [44]. They created a kinetic model to calculate the reaction rates for the rWGS (Equation 2.6) and CO_2 based methanol reaction (Equation 2.17). Typically, multitube fixed-bed reactors are used with a temperature of 240 °C, a pressure of 80 barg, tubes measuring 7 m in length, and an inner tube diameter of 0.04 m [43]. Since the reaction is exothermic, suitable steam cooling methods are implemented in the fixed-bed reactors to maintain the catalyst bed temperature in the range of the operating temperature (max. +30 °C temperature peaks).

Process routes 2 and 3 (defined in Figure 2.2) only differ in the process design, not in the reactor design. In process route 2 (Figure 2.10), the rWGS is used for synthesis gas production, followed by methanol synthesis. The rWGS reactor is again implemented as a Gibbs reactor at an operating temperature of 950 °C and a pressure of 10 barg. The advantage is the higher CO conversion in the overall methanol synthesis process. Behind the methanol reactor, the product gas is cooled to remove the condensed methanol-water fraction from the system.

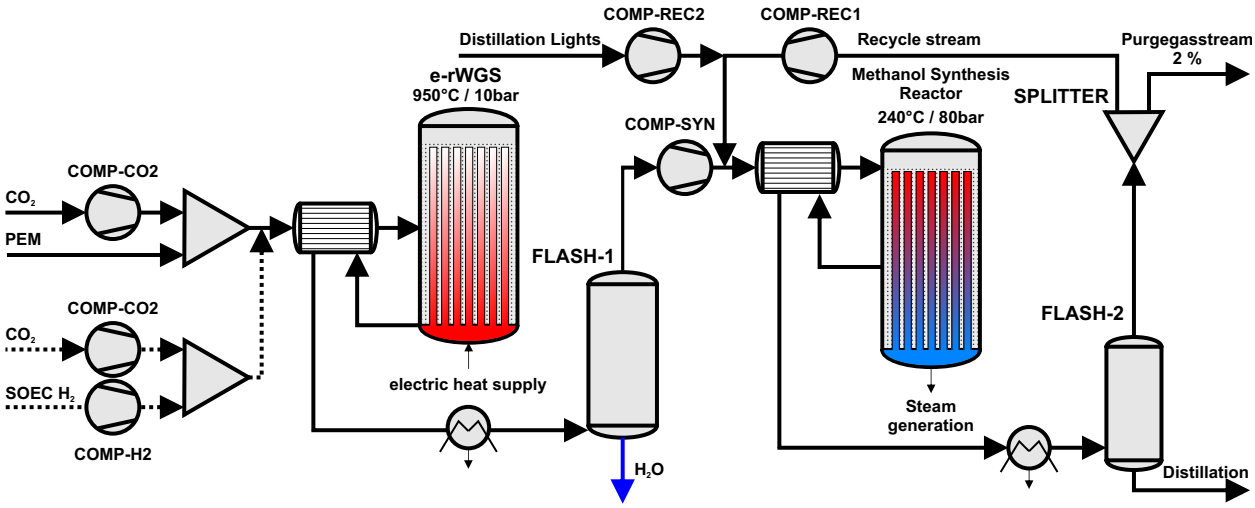

Figure 2.10: Process design of a conventional methanol synthesis with upstream syngas production (rWGS)

Process route 3 (Figure 2.11) consists of three reactors in series, with intermediate cooling and liquid withdrawal [45]. This changes the thermodynamic conditions in the subsequent reactor (only the reactants are present in the feed stream). This three-stage in series process aims to achieve productive methanol production. In both process routes, the unreacted gas, mainly composed of CO_2, CO, and H_2, is recycled to achieve high efficiencies. Similar to the Fischer-Tropsch synthesis, a purge gas stream of 2 % is introduced to prevent potential accumulations (e.g., nitrogen impurities, traces of methane). The collected methanol-water mixture is then separated into the methanol fraction of grade AA (< 0.1 wt.-% H_2O) using a two stage (high and low-pressure) distillation [46], [47].

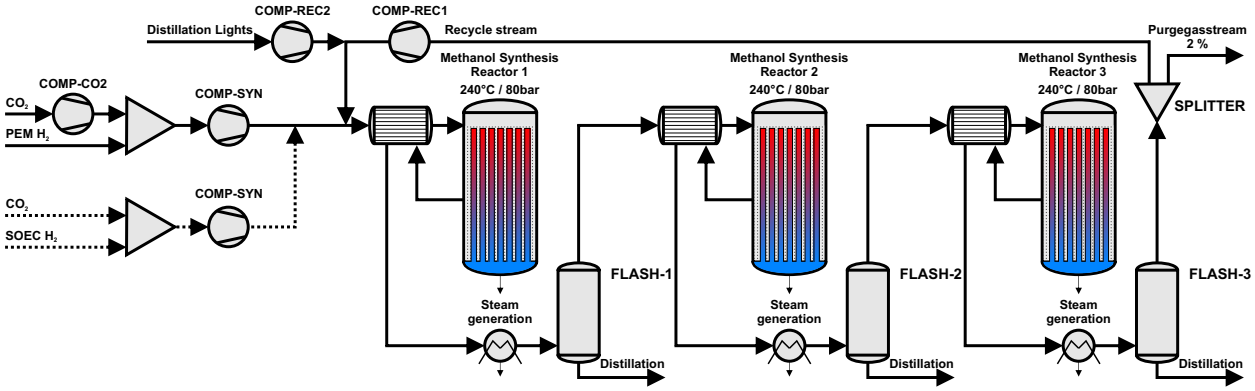

Figure 2.11: Process design of the three-stage CO_2 tolerant methanol synthesis with intermediate cooling units

The methanol-to-propylene (MtP) unit is a commercially available technology and consists of a pre-conversion of methanol to dimethyl ether (DME) with three downstream MtP reactors. Hereby, two are simultaneous in operation and one is in regeneration mode, as coke formation occurs in the conversion reactions ($< 0.5\,\%$ carbon loss). The reaction product is rectified in columns to obtain the main product propylene and the by-products ethylene, liquified petroleum gas (LPG), gasoline and purge or fuel gas. The MtP unit is not simulated in ASPEN Plus and the published yield vectors are incorporated in a theoretical calculation. Due to methanol as feedstock, almost 50 wt.-% of the feed flow reacts to process water [18]. The MtP plant requires energy in the form of steam, which is set at 11 MJ kg^{-1}_{MeOH} electrically supplied energy [42].

2.3 Investment, operating and net production cost calculations

The investment and operating cost calculations allow a more precise comparison of the two process routes (CO_2 conversion via Fischer-Tropsch synthesis with steam cracker and methanol synthesis with MtP unit). These costs are required as a basis for the calculation of the net production costs (NPC) per kg of lower olefins. The comparison therefore takes into account the total equipment costs and plant set-up costs, the utility costs and many other factors that have an influence on the production costs. The estimation of the net production costs is basically described in this chapter. A detailed description of the cost calculation is given in Publication 2.

2.3.1 Investment cost calculation

In this study, the investment cost calculation follows the approach of Peters et al. and is related to the previously described ASPEN Plus flow sheet simulations [48]. The basis for the investment cost calculation is the determination of the equipment costs (EC_{ref}). The main equipment costs (such as for heat exchangers, flash drums, pumps and compressors) are obtained by the software "ASPEN Process Economic Analyzer V12.1 (APEA)". The more specific equipment (e.g., rWGS, methanol or Fischer-Tropsch reactors) require the application of literature-based values. APEA results rely on the most recent published data sources from Q3/2019. It is therefore essential to adapt these values from 2019 to the current situation. This can be done using the so-called "Chemical Engineering Plant Cost Index (CEPCI)", which is published monthly (for the current year) and annually. In this calculation, the equipment costs (EC) for 2022 are adjusted using the following Equation 2.18. The $CEPCI_{ref}$ for 2019 is 607.5 and the current value $CEPCI_{Feb,2022}$ for February 2022 is 801.3 [49].

$$EC = EC_{ref} * \frac{CEPCI_{Feb,2022}}{CEPCI_{ref}} \tag{2.18}$$

The fixed capital investment costs (FCI) are derived from the previously calculated equipment costs (EC), but includes additional factors, which are listed in Table 2.2. The total direct plant costs (D) include additional costs for installation, instrumentation and control, piping and electrical facilities, buildings, yard improvements and service facilities. The indirect plant costs (I) contain the engineering and supervision, construction and legal expenses. The exact cost surcharges of each category are described in detail in Peters et al. [48].

The last section consists of contractor's fees and contingency. In addition, the sum of the FCI and the working capital (WC, which is used for commissioning or startup and usually accounts 10 % of the FCI) gives the total capital investment (TCI).

The annual depreciation (ACC) is calculated for an assumed rate of interest (IR, 7 %) and a specific plant lifetime (PL, 20 years) according to Equation 2.19.

$$ACC = (FCI + WC) * \frac{IR * (1 + IR)^{PL}}{(1 + IR)^{PL} - 1} - \frac{WC}{PL} \tag{2.19}$$

2.3.2 Operating cost calculation

The operating costs are made up of the operating labor costs, including their additional factors in Table 2.3, and the utility costs [48].

Table 2.2: Calculation of the fixed capital costs (FCI) on the basis of the equipment costs (EC) and the additional factor surcharge according to Peters et al. [48]

Fixed Capital Costs (FCI)	**Factor number**	**Basis**	**Typical Value**
Total direct plant costs (D)			
Equipment installation	1	EC	0.47
Instrumentation and control	2	EC	0.36
Piping (installed)	3	EC	0.68
Electrical (installed)	4	EC	0.11
Buildings including services	5	EC	0.24
Yard improvements	6	EC	0.1
Service facilities (installed)	7	EC	0.55
Total indirect plant costs (I)			
Engineering and supervision	8	EC	0.33
Construction expenses	9	EC	0.41
Legal expenses	10	EC	0.04
As a function of total direct and indirect costs (AC)			
Contractor's fee	11	D+I	0.05
Contingency	12	D+I	0.1

The operating labor costs (OL) depend on the plant capacity, the number of process units ($n_{process,steps}$) and the operating time ($h_{plant,operation}$ in h) of the system and are calculated from the product of the labor hours (h_{labor} in h) and the specific labor costs (c_{labor}, 37 € h^{-1}) [10]. The operating time of the cement and CCU plant is estimated to be 7,884 h per year. The calculation of the person labor hours is adopted from Albrecht et al. and given in Equation 2.20 [10].

$$h_{labor} = 2.13 * \text{plant capacity}^{0.242} * n_{process_{steps}} * \frac{h_{plant_{operation}}}{24} \tag{2.20}$$

Additional factors to the operating labor costs include the consideration of operating supervision, maintenance labor, maintenance material, operating supplies, laboratory charges, electrolysis stack replacement, insurance and taxes, plant overhead costs and administrative costs. The listing of these factors is summarized in Table 2.3. The sum of all these positions equals the fixed operation expenditures (FixOPEX).

The utility costs take the electricity costs (200 € MW h^{-1}, [50]), the water costs (1.85 € m^{-3}, [51]) and the steam production costs (26.30 € t^{-1} [10]) into account. In this thesis, the values are considered for Austria in February 2022. The total operating costs (OPEX) are composed of the utility costs and the FixOPEX and are used for the net production cost calculation.

Table 2.3: Additional factors for the calculation of the fixed operating expenditures (FixOPEX) according to Peters et al. [48]

Fixed operating expenditures FixOPEX	**Factor number R_i**	**Basis**	**Typical value**
Direct production costs			
Operating labor [OL]	1	OL	1
Operating supervision	2	OL	0.15
Maintenance labor	3	FCI	0.02
Maintenance material	4	FCI	0.02
Operating supplies	5	MP[1]	0.15
Laboratory charges	6	OL	0.2
Electrolysis stack replacement	7	EC	0.77
Indirect production costs			
Insurance and taxes	8	FCI	0.02
Plant overhead costs [PO]	9	TLC[2]	0.6
General expenses			
Administrative costs	10	PO	0.25

[1]M = Total maintenance costs = R3 + R4
[2]TLC = Total labor costs = R1 + R2 + R3

2.3.3 Net production costs

The net production costs (NPC in € year^{-1}) are referenced to the operating costs (OPEX in € year^{-1}) and annual depreciation (ACC in € year^{-1}). The specific net production costs related to either the product energy content ($\dot{m}_{chemical}$ in kWh h^{-1}) or product mass quantity ($\dot{m}_{quantity}$ in kg h^{-1}) are calculated according to Equation 2.21 and Equation 2.22, respectively.

$$NPC_{ch} = \frac{ACC + OPEX}{\dot{m}_{chemical}} \tag{2.21}$$

$$NPC_{qu} = \frac{ACC + OPEX}{\dot{m}_{quantity}} \tag{2.22}$$

In order to set a basis for the process scenario comparison, these specific net production costs (NPC_{ch} and NPC_{qu}) are calculated for the lower olefin product of each process. It is notable that these specific NPC are calculated for specific assumptions (e.g., fixed electricity price, fixed equipment costs). A sensitivity analysis varies various parameters (e.g., electricity price and equipment costs between -50 % and +100 %) and provides information on which factors have a high or low influence on the NPC. This allows to consider future scenarios and to classify any processes as feasible or not realizable.

2.4 Conclusion of the techno-economic comparison

In this chapter, the results of the simulation and the economic analysis regarding the production of lower olefins out of annually 10,000 tons of CO_2 from a cement plant's exhaust gas are discussed. The process routes consider either a Fischer-Tropsch route or methanol synthesis with their downstream processes steam cracker or methanol-to-propylene unit, respectively. With regard to the process comparison, it is very important that the technical and economic aspects are well compared in every respect.

The technical assessment uses the power-to-liquid (PtL) or global efficiency to provide information on how much electrical energy is required per product energy. High efficiencies mean that the electrical energy requirement is low compared to the product energy content. Furthermore, carbon conversion is essential when comparing these processes. It is crucial that high efficiency is achieved, as any carbon from the point source should end up in the product and not escape the process as purge gas or similar (e.g. coke formation in reactors). Carbon should be converted as completely as possible into a resource for lower olefin production.

On the other hand, the economic analysis assesses the operational capability in terms of investment and operating costs for the production of the lower olefins over a certain process route. The calculated investment and operating costs are related to the product quantity to obtain the specific net production costs (NPC). In terms of economic efficiency, these costs must be minimized in order to achieve a cost-optimized process.

The description of the scenarios and the techno-economic results of the comparison are recorded in detail in Publication 2 and the results of the efficiencies are summarized in Figure 2.12. The summary of the comparison is presented again here. With regard to the technical evaluation, the integration of a Fischer-Tropsch synthesis with high-temperature electrolysis for hydrogen production proves itself. The highest global efficiency is achieved with 38.2 % considering the Fischer-Tropsch process with a downstream steam cracker. The global efficiency not only considers the electricity demand, but also the steam required to operate the process units. The value of the efficiency of the Fischer-Tropsch route is comparatively high compared to the methanol synthesis, where efficiencies between 26.1 and 29.2 % are achieved. This is due to the investigations regarding heat integration, whereby the waste heat from the highly exothermic Fischer-Tropsch reaction is used to provide steam as feed for the high-temperature electrolysis. At 3.6 kWh $Nm^{-3}_{H_2}$, the specific energy demand of the SOEC is approx. 23 % lower compared to the PEM electrolysis with 4.7 kWh $Nm^{-3}_{H_2}$ [32]. The carbon conversion is in the process route with Fischer-Tropsch synthesis with 71.5 % higher than for the methanol synthesis (67.5 – 68.6 %). The carbon conversion must be lower than 100 %, as approx. 10 % of CO_2 is not captured in the amine scrubbing unit and is

released back into the atmosphere within the exhaust gas stream. The rest of the efficiency reduction is due to the downstream process requirements (purge gas) and the conversion into by-products (e.g. higher hydrocarbons). It can therefore be concluded from this comparison that the Fischer-Tropsch synthesis with steam crackers performs significantly better in terms of global and carbon efficiency and is therefore the favorite in the technical evaluation.

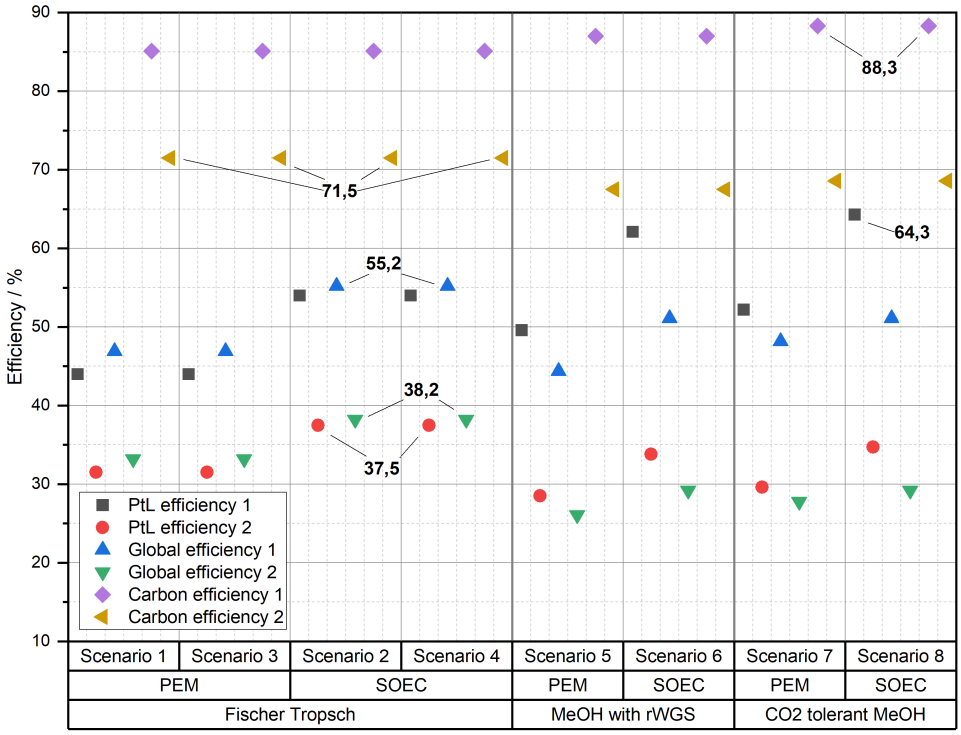

Figure 2.12: Illustration of the PtL, global and carbon efficiency for the Fischer-Tropsch and methanol synthesis, with a distinction of PEM and SOEC (Efficiency 1 neglects the downstream processes (e.g., steam cracker or MtP, whereby they are considered in efficiency 2)

The specific net production costs are used in the economic assessment. In the Fischer-Tropsch synthesis, a distinction is made between the construction of a new steam cracker and the use of an existing unit in a refinery. The lowest NPCs are calculated for the Fischer-Tropsch synthesis with an existing steam cracker at 14.92 € kg^{-1} product and the use of PEM electrolysis. The results of methanol synthesis are in the range of 17.23 - 18.50 € kg^{-1} product. The Fischer-Tropsch process has a clear advantage here with lower production costs of 14.92 - 15.47 € kg^{-1}, which is about 13.4 - 19.4 % lower compared with the methanol process routes. A sensitivity analysis is essential for the process evaluation and the results are depicted in Figure 2.13. The electricity price and equipment costs have a significant influence on the investment and operating costs of the electrolysis. In the future, decreasing equipment costs of the high-temperature electrolysis will prove to be outstanding. A low electricity price will also have a reducing effect on the NPC.

The process comparison for the production of lower olefins from CO_2, with respect to a shorter lifetime of the electrolysis' stacks for the SOEC and the currently lower equipment costs for the PEM, reveals the optimum route with an amine scrubbing unit, a PEM electrolysis, a Fischer-Tropsch synthesis with an upstream rWGS reactor and an existing steam cracker (Scenario 3 in Publication 2).

The process routes with methanol synthesis (scenarios 5 to 8) have no advantage in the production of polyolefins in this study, with an increase in NPC of between 14.4 and 22.9 % compared to the base scenario 1. Decisive for the reduction in production costs is the assumption that the investment costs for electrolysis will decrease in the future, which also reduces the NPC by up to 17.5 % in scenario 4. Figure 2.13 shows, that NPCs of all scenarios are reduced within the range of 82.5 to 88.9 %.

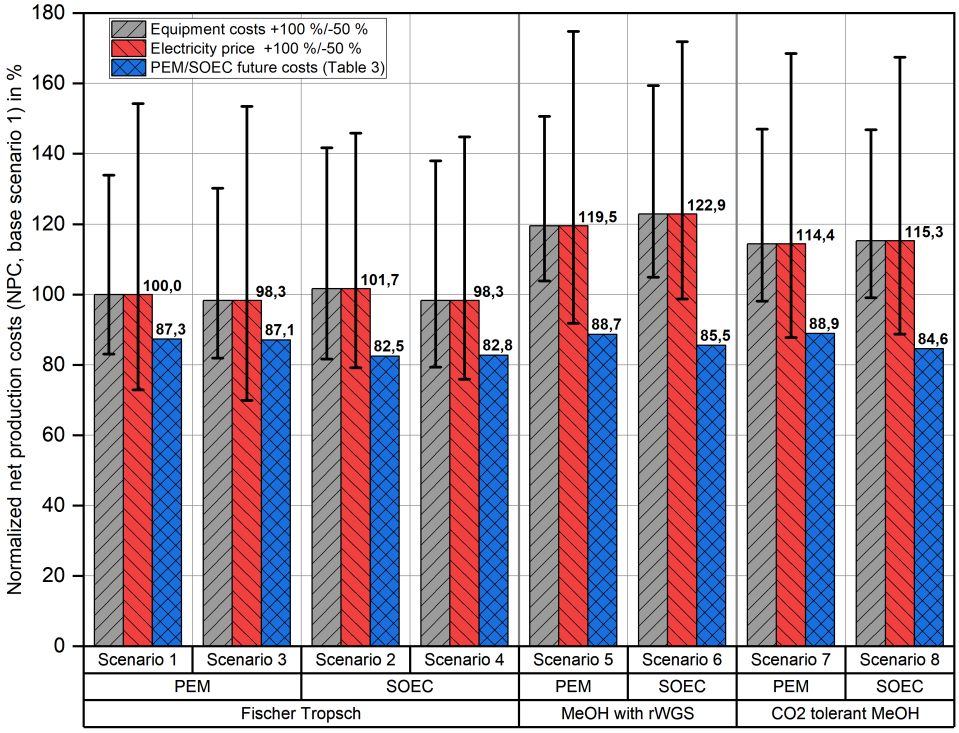

Figure 2.13: Sensitivity analysis and calculation of the normalized NPC (base scenario 1) considering the carbon capture and utilization processes, including a distinction of electrolysis (PEM and SOEC) and synthesis technologies (Fischer-Tropsch and methanol) as well as the variation of the parameters of equipment costs, electricity price and future electrolysis equipment costs

The calculations and simulations in this study assume that the rWGS reaction follows thermodynamic equilibrium and can be integrated as a Gibbs reactor in the PtL processes. In chapter 3, the rWGS reaction is experimentally investigated with a commercially available Ni/Al_2O_3 and self-developed perovskite catalysts in a quartz glass tube reactor to determine the validity of these assumptions for the process simulations.

Chapter 3

Experimental investigation of the reverse water gas shift reaction

Chapter 2 implements the rWGS reaction in the PtL flow sheet simulation as a Gibbs reactor. This reaction is crucial for syngas production, particularly for the Fischer-Tropsch synthesis in the investigated scenarios 1 to 4, and also in the process routes of the methanol synthesis with rWGS as pre-conversion step in scenarios 5 and 6. The technology is still very underdeveloped (technological readiness level – TRL 6 [15]) and is therefore not yet used in industrial applications or large-scale plants. In order to confirm the assumptions of the Gibbs reactor (calculating the thermodynamic equilibrium by minimizing Gibbs free energy) as a rWGS reactor in chapter 2, the rWGS reaction is investigated experimentally in this chapter. A basic explanation of the rWGS reactor setup is provided, followed by the design of experiments in a quartz glass reactor to investigate the reaction on various catalyst materials. These experiments are intended to provide information about the conversion of CO_2 into carbon monoxide and the investigation of other occurring species in the product gas for a Ni/Al_2O_3 (commercial available nickel-based catalyst [52], [53]), two perovskite catalysts and the support material Al_2O_3 to determine the optimum operating conditions. Furthermore, the experimental results will be used to validate the assumption of a Gibbs reactor in the simulations in chapter 2 as a real rWGS reactor or provide proposals how to integrate the rWGS reactor, to obtain realistic product compositions.

3.1 Description of the experimental setup

The fundamentals of the rWGS reaction are already described in detail in subsection 2.2.3. The reaction is endothermic, defined in Equation 2.6 and favors from a thermodynamic point of view high temperatures and low pressures for a high CO selectivity (cf. Figure 2.4 and

Figure 2.5). Figure 3.1 shows the P&ID diagram of the experimental test rig at the Chair of Process Technology and Environmental Protection (Montanuniversität Leoben) to provide a comprehensive study of the real reaction setup. The experimental plant is used to investigate the product gas composition of the reaction of CO_2 and H_2 by varying the temperature in the range from 550 to 950 °C and a pressure higher than ambient pressure, but limited to 8 bara for temperatures up to 650 °C. Higher temperatures are only allowed up to 6 bara, restricted due the properties from the applied quartz glass reactor material.

High-purity CO_2 and H_2 gases are supplied from gas cylinders. These gases are controlled by two mass flow controllers (Bronkhorst Deutschland Nord GmbH, up to 45 NL min^{-1} for each gas) and fed separately into a mixer equipment, where they are mixed and fed into a quartz glass tube reactor. The quartz glass reactor is operated in a tube furnace with a desired temperature level, which is set and constantly controlled over a length of 550 mm. A quartz glass reactor (Figure 3.2) is applied with a total length of 1,700 mm (commissioning and preliminary tests in section 3.2) and 1,500 mm (catalyst comparison in section 3.3). Both tubes have an inner diameter of 15 mm and a wall thickness of 2.5 mm. The stainless steel flanges with a perfluoroelastomeric (FFKM) seal in a squeeze connection are used to connect the gas pipes with the quartz glass reactor. These flanges are located outside of the furnace at ambient temperature and this equipment allows an operation pressure of maximum 8 bara. The product gas contains a considerable amount of water, which means that the gas is cooled down, and the water is condensed out in a downstream condenser. The pressure is regulated by a proportional valve (Buerkert Austria GmbH) downstream of the condenser, which uses the inlet pressure of the reactor (PI-205) for control. The dry product gas is partially probed by a gas analyzer (AO 2020, ABB AG) which measures the corresponding species (CO_2, CO, CH_4 and H_2). It is assumed that higher-value hydrocarbons are consistently with thermodynamic equilibrium not formed. On the one hand, a H_2:CO_2 feed ratio of 3:1 is used to run the rWGS reaction (consumption of 1 mol H_2 for 1 mol CO_2) and to provide a product syngas with a H_2:CO ratio of 2:1 for downstream processes (e.g., Fischer-Tropsch synthesis). On the other hand, the formation of carbon is suppressed as the equilibrium in the occurring carbon related reactions (Equation 2.9 to Equation 2.11) is shifted to gaseous compounds. The remaining gas stream is then burned in a flare with a CH_4 support flame and fed into a ventilation system. Nitrogen and air are also included as gases in the P&ID, as nitrogen is used for purging the flammable gases in emergency shutdown, for a standby position, as dilution gas in the activation procedure or deactivation procedure of the catalytic material in combination with air.

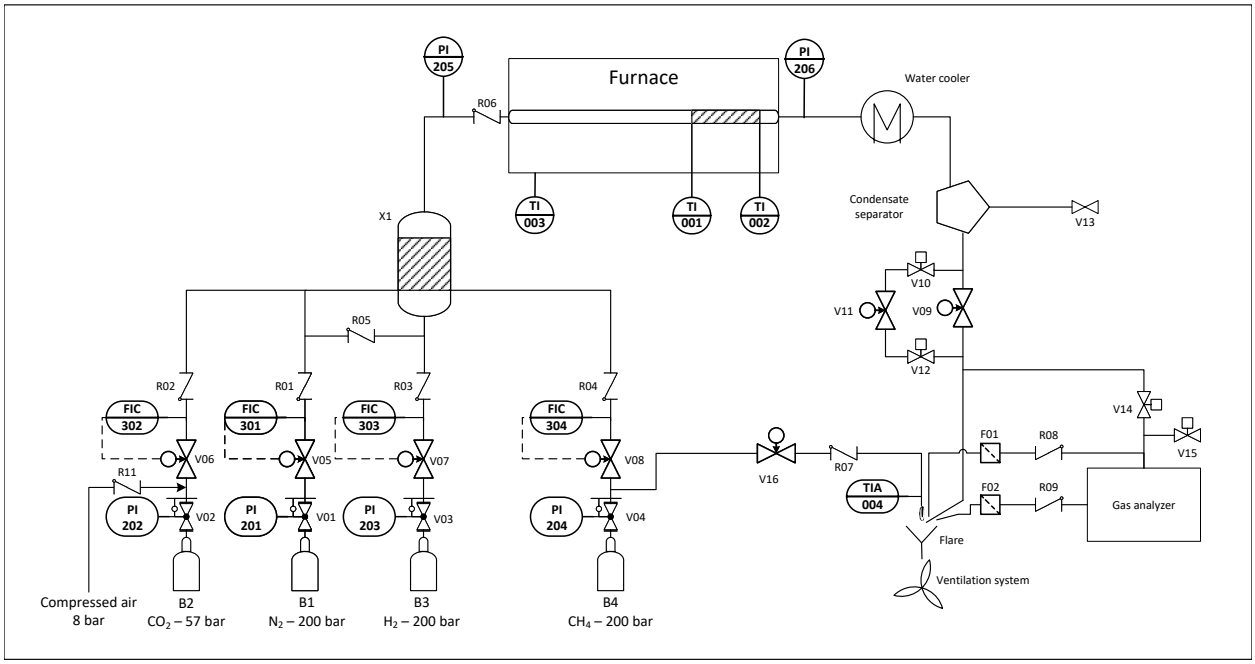

Figure 3.1: P&ID scheme of the rWGS test rig including the gas supply, the quartz glass reactor incl. furnace and product analysis via the ABB gas analysis unit

3.2 Experimental preliminary tests on a Ni/Al_2O_3 catalyst

The first published study describes the first experimental tests of the rWGS reaction and is provided in Publication 3. In this study, the reaction conditions (temperature and pressure changes) are tested on a commercially available nickel-based catalyst [52], [53] for the first time in this experimental setup. The reactor setup is depicted in Figure 3.2 with a catalyst bed length of 75 mm, filled with Ni/Al_2O_3 catalyst particles (shape of cylinders with 3.2x3.2 mm), while six thermocouples before, in and behind the catalyst bed monitor the temperature curve in the inert ball and reactive bed zone. Temperatures are varied between 650 and 950 °C and pressures of 1, 3 and 6 bara are set as operation conditions. The feed gas volume flow is changed to obtain the impact of various gas hourly space velocities (GHSV in h^{-1}) on the product composition, as this factor is not reflected in the thermodynamic examination.

The respective GHSV is calculated in Equation 3.1 by dividing the feed gas volume stream ($\dot{V}_{in}$ in NL h^{-1}) by the catalyst bulk volume (V_{cat} in L) and varies in this study between 6,000 and 40,000 h^{-1}. The entire design of experiments is described in detail in the publication. The gas velocity determines and affects the contact time with the catalyst's surface and the active centers, where the reactions take place. Furthermore, elevated GHSVs require a higher heat demand for feed gas pre-heating and for the supply of the required reaction enthalpy in the catalytic bed.

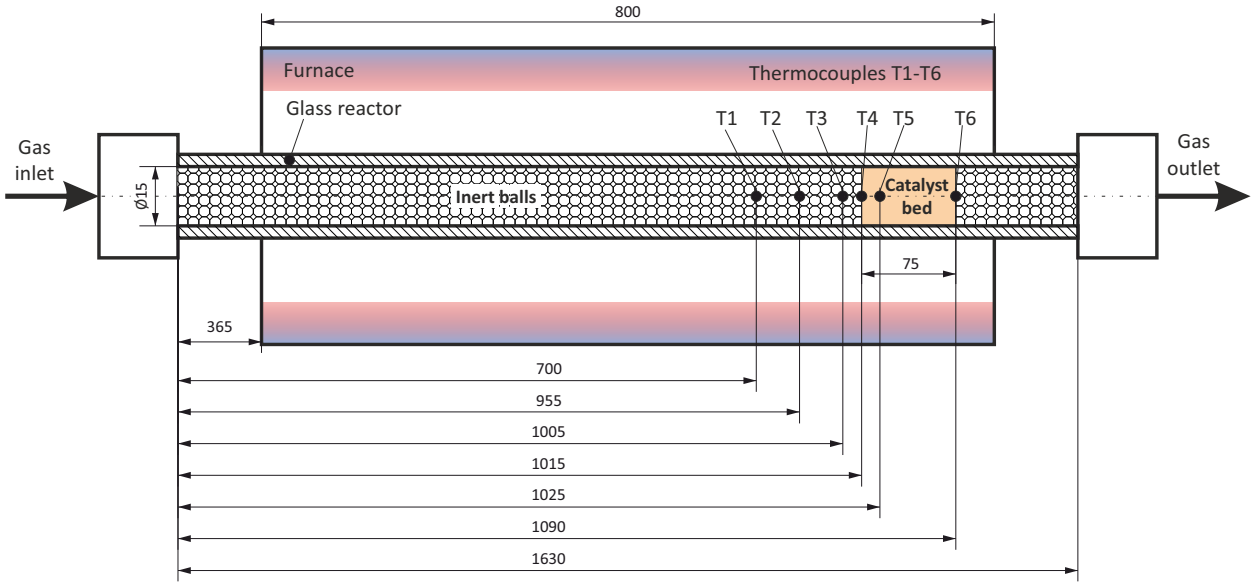

Figure 3.2: Setup of the quartz glass reactor in Publication 3 with the dimensions of the inert ball and catalyst bed as well as the position of the six thermocouples (T1 - T6)

$$\mathrm{GHSV} = \frac{\dot{\mathrm{V}}_{\mathrm{in}}}{\mathrm{V}_{\mathrm{cat}}} \tag{3.1}$$

Under atmospheric, oxygen-rich conditions, the catalyst material is present as oxidized material. Thus, a specific catalyst activation procedure is necessary to reduce the catalyst surface to their active sites and guarantee an optimal conversion of CO_2 and H_2. The procedure of the Ni/Al_2O_3 catalyst activation with H_2 is described in Publication 3.

3.2.1 Results of the Ni/Al_2O_3 catalyst investigation

The product gas composition is plotted in Figure 3.3 for the different experimental settings against the temperature. The thermodynamic equilibrium is also represented in order to show the deviations of the experimental results and from the equilibrium calculation. The detailed experimental evaluation is described in the Publication 3. The test results show that the CO content of the product gas conditionally follows the thermodynamic equilibrium depending on temperature, pressure and GHSV. Furthermore, the results show that there is no methane formation at temperatures higher than 850 °C and at all applied pressures of 1, 3 and 6 bara. As no other species than CO_2, CO, CH_4, H_2O and H_2 are assumed to occur, CO_2 should be completely converted to CO. Higher gas velocities have a negative effect on the CO_2 conversion, decrease the CO formation and increase the CH_4 selectivity.

There is a deviation between the theoretical and experimentally determined CO concentration in Figure 3.3. This can subsequently be caused by three effects:

1. The thermodynamic equilibrium is not reached in the experimental tests.
2. The CO_2 mass flow controller is calibrated for an input pressure range that is too low, the inlet pressure does not match the applied pressure and the recalculation is not carried out properly.
3. There is an error in the calibration of the gas analysis unit.
4. There is a significant temperature change detected by the six thermocouples in the catalyst bed (temperature profile illustrated in Figure 3.4), whereby the comparison of the experimental values with a point temperature can be assumed to be incorrect.

The recorded temperature profile of the quartz glass reactor is depicted in Figure 3.4. To obtain a temperature of 650 or 950 °C at the catalyst bed inlet, a significantly higher tube furnace temperature is required (680 and around 1,000 °C), which is also reflected in a higher temperature in the inert ball zone. The quartz glass reactor is designed for maximum operation temperature of 1,100 °C. Obviously, the temperature is higher than 1,000 °C in the preheating zone. Internal temperature peaks cannot be detected in the reactor range from the beginning of the tube to the location of 700 mm, but the temperature of around 1,000 °C or higher poses a risk for glass breaking under elevated pressures. In the course of further investigation, it becomes known that the tube furnace has an insulation at both outer ends, which hinders the heat transfer between the furnace and the quartz glass tube. This is an indication and explains the decrease of the temperature in the catalyst bed starting at around 900 to 1,100 mm. As expected from the endothermic rWGS reaction, a negative temperature gradient occurs in the catalyst bed and is first detected by the thermocouple number 4. Higher GHSV values cause an overall higher negative temperature gradients.

This first study will provide valuable information for conducting further test series. An exact statement for the implementation of a Gibbs reactor in ASPEN plus is not yet permissible, as the following aspects still have to be addressed:

1. The gas analyzer is calibrated with test gases (e.g., mixture of N_2:CO_2 equal to 70:30 vol.-%/vol.-%) to ensure an accuracy of +/- 1 vol.-% for all occurring species (CO_2, CO, CH_4 and H_2).
2. The mass flow controllers are adapted to the corresponding inlet pressure and the gas mass flows are converted using the conversion factors provided by Bronkhorst AG. For control purposes, the gas input concentration is measured before each experiment and compared with the desired H_2:CO_2 ratio.

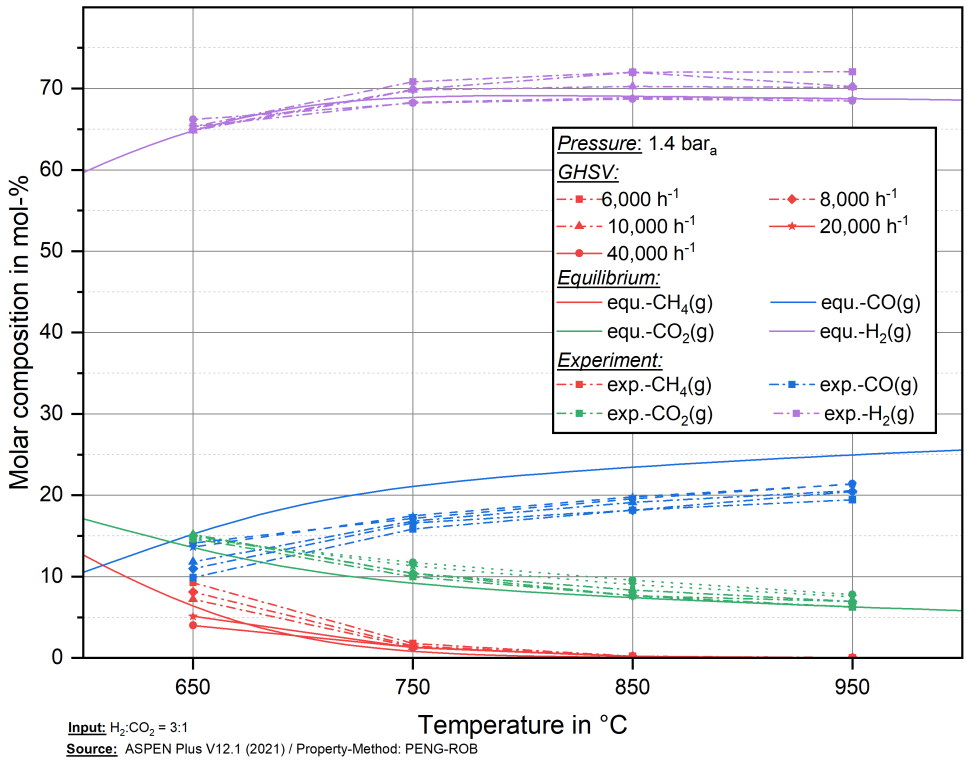

(a)

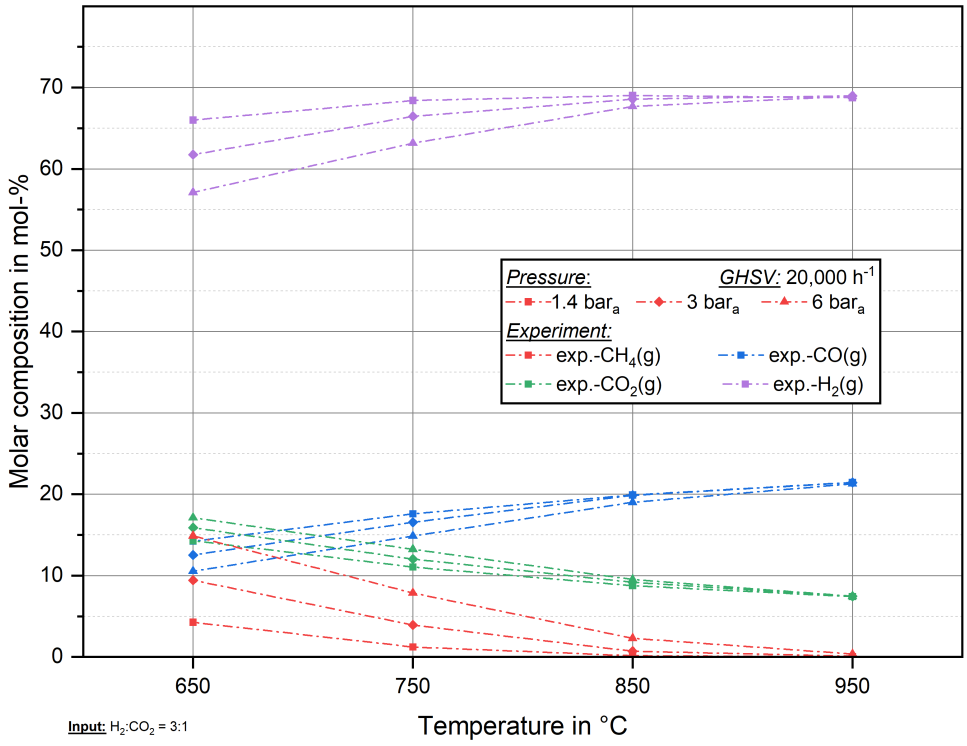

(b)

Figure 3.3: Product gas composition and thermodynamic equilibrium of a feed gas mixture (H_2:CO_2 = 3:1) over a Ni/Al_2O_3 catalyst in a temperature range of 650 - 950 °C, for a variation of a) GHSV (6,000; 8,000; 10,000; 20,000; 40,000 h^{-1}) and of b) pressure (right figure, 1, 3 and 6 bara)

3. The strong fluctuations in the temperature profile and the decrease in temperature at the end of the quartz glass reactor are reduced by improved positioning of the catalyst bed, taking into account the tube furnace insulation.

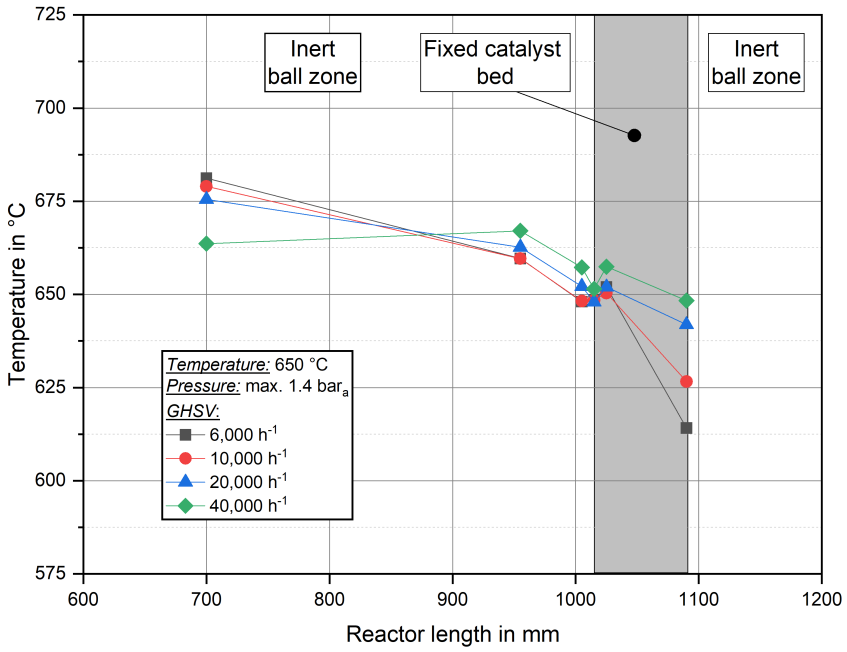

(a)

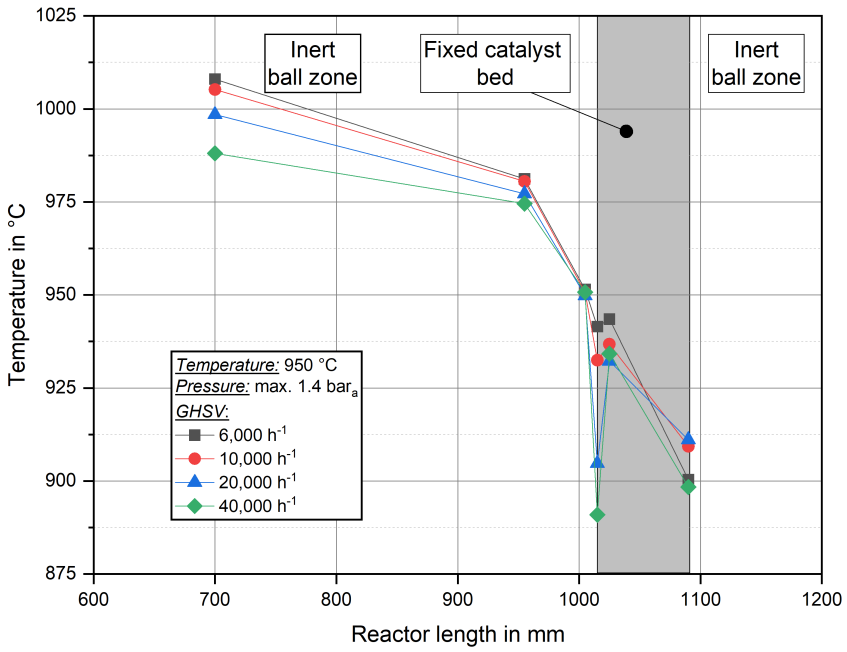

(b)

Figure 3.4: Recorded temperature profile for a) a catalyst inlet temperature of 650 °C and b) an inlet temperature of 950 °C as a function of the position of the six thermocouples in the quartz glass reactor tube with representation of the inert ball and catalyst bed zones.

3.3 Experimental tests with Ni/Al_2O_3, perovskite catalysts and γ-Al_2O_3

In this second part of the experimental tests, a comprehensive investigation of a Ni/Al_2O_3 catalyst, two perovskite materials ($Nd_{0.6}Ca_{0.4}Fe_{0.9}Co_{0.1}O_{3-\delta}$ [54]) and their support material γ-Al_2O_3 is carried out. A detailed description can be found in the Publication 4. The technical process setup of this experiment is the same as described in section 3.1 and the P&ID is depicted in Figure 3.1. The proposed amendments of the previous study are incorporated, and the length and position of the catalyst bed are adapted.

As shown in Figure 3.5, the quartz glass reactor has again an inner diameter of 15 mm, but the total length is reduced to 1,500 mm (compared to 1,700 mm in the experimental setup in section 3.2) to avoid heat loss at the positions outside of the oven (insulation is indicated in Figure 3.5). The reactor contains again a bed of inert balls (SiO_2), the catalyst material (either Ni/Al_2O_3, perovskite or Al_2O_3) and only two thermocouples in this setup that measure the input (T1) and output (T2) temperatures of the gas and catalyst bed. A temperature difference of these two thermocouple temperatures should be avoided (isothermal temperature profile is desired), but a constant temperature curve over the catalyst bed is not measurable due to the absence of intermediate thermocouples.

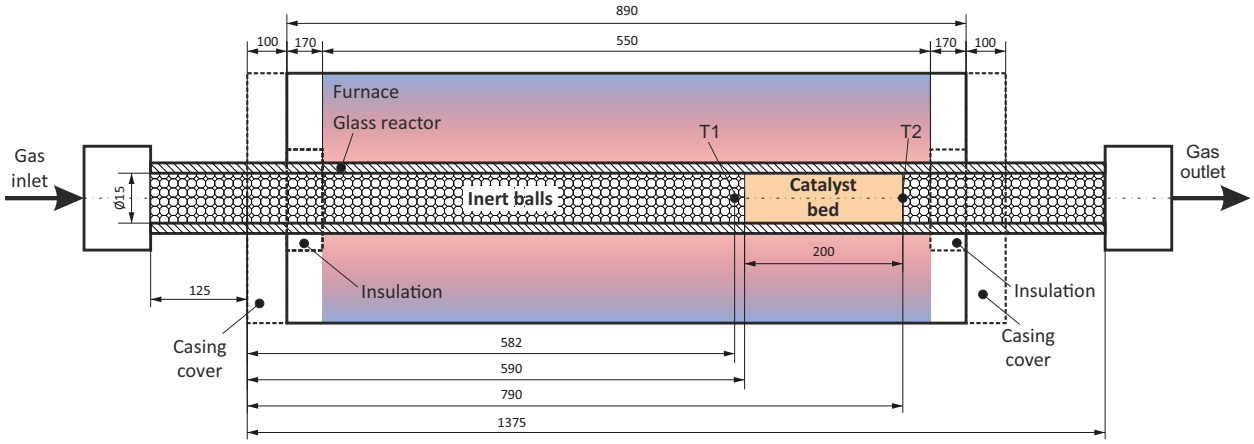

Figure 3.5: Design of the quartz glass reactor used in the experiments in Publication 4 which contains the location of the inert ball section, the catalyst bed and the position of the two thermocouples (T1 and T2). The effective heating zone of the furnace is illustrated.

The catalyst materials implemented in this study are described in Publication 4 and listed in Table 3.1. The Ni/Al_2O_3 catalyst is a commercially available nickel-based catalyst, with high coke resistance and long-term stability [52], [53]. The perovskite catalysts are provided by the Chair of Physical Chemistry at Montanuniversität Leoben (Univ.-Prof. Christoph Rameshan, Dr. Tom Cotter, Lorenz Lindenthal and Hedda Drexler). They have already

investigated these perovskite catalysts on a laboratory scale under atmospheric pressure and published the results in [54]–[56]. The activation procedure is here again required for each catalyst, and the procedure is described in detail in the Publication 4. A main distinction is noted, because the Ni/Al_2O_3 catalyst is activated with a volume flow consisting of 100 vol.-% hydrogen, while the perovskite catalysts are activated with 5 vol.-% H_2 in N_2.

Table 3.1: List of catalyst materials and geometry used in the study

Catalyst number	**Catalyst composition**	**Catalyst geometry**
Catalyst 1	Nickel-catalyst	Cylinders 3.2 mm diameter, 3.2 mm height
Catalyst 2	Perovskite catalyst[1], 20 wt.-% γ-Al_2O_3	Pellets 6.0 mm diameter, 1.4 mm height
Catalyst 3	Perovskite catalyst[1], 50 wt.-% γ-Al_2O_3	Pellets 6.0 mm diameter, 2.2 mm height
Catalyst 4	Aluminum oxide γ-Al_2O_3	Pellets 5.8 mm diameter, 4.2 mm height

[1]Perovskite oxides $Nd_{0.6}Ca_{0.4}Fe_{0.9}Co_{0.1}O_{3-\delta}$

The aim of using perovskite catalysts is to operate them at the lowest possible reaction temperatures (approx. 550 °C) and to reduce methane formation in this low temperature range. Therefore, the experiments are designed to apply the tests in a temperature range between 550 - 950 °C for the Ni/Al_2O_3 catalyst and the Al_2O_3 material, and 550 - 850 °C for the perovskite catalysts. Due to the limited usability of the glass tube under high temperatures and increasing pressures, the reaction is investigated at pressures of 1, 3, 6 and 8 bara at temperatures of 550 and 650 °C, and 1, 3 and 6 bara at temperatures higher than 650 °C. To additionally account for the impact of modified GHSV, this study utilizes gas velocities of 8,000 and 20,000 h^{-1}.

3.3.1 Results of all catalyst investigations

Publication 4 provides detailed information and results of the catalyst tests. It is important to note that an undesired effect was detected during the testing process. The applied heating pipe, which connects the gas mixer to the quartz glass reactor, is catalytically active at 350 °C due to the stainless steel material. However, there are no issues encountered when utilizing the Ni/Al_2O_3 catalyst throughout the duration of the experimental tests, as the nickel catalyst acts as steam methane reforming catalyst and reconverts the previously formed methane into syngas. However, when using the perovskite catalyst, it was found that CH_4 produced in the preheater tubes is not converted by the perovskite catalyst even at higher

temperatures around 850 - 950 °C (although steam reforming should occur, but the catalyst does not appear to be active for this reaction (Equation 2.15) and is passed through the reactor system as an inert gas component.

As a solution of suppressing methane formation in the preheating pipes, the preheating of the feed gas mixture is shifted into the quartz glass region, to prevent the production of methane by the conversion of CO_2 and H_2 due to the catalytic pipe material. This investigation is a valuable finding, as downstream processes may contain or produce methane as by-product, requiring consideration of the use of perovskite catalyst in the entire process gas management. To achieve high carbon efficiencies, an additional steam reforming reactor could be necessary in case of the application of perovskite catalysts to convert the short-chain hydrocarbon by-products (e.g. methane, ethane) into syngas.

The results of the product gas composition for each catalyst are given and discussed in detail in Publication 4. Figure 3.6 shows the experimental results of the dry product gas composition of the four investigated catalysts with a feed gas composition of H_2:CO_2 equal to 3:1. The figure contains the subdivision into the pressures 1, 6 and 8 bara, the respective temperatures between 550 and 850 °C as well as the GHSV of 8,000 and 20,000 h^{-1}. Furthermore, the thermodynamic equilibrium of the individual species (CO_2, CO, CH_4 and H_2) is shown as continuous lines. The dashed lines indicate the thermodynamic equilibrium without consideration of CH_4 formation. Here, only the rWGS reaction is considered as occurring reaction.

The evaluation shows promising results for the implementation of perovskite catalysts regarding lowest or non-measurable CH_4 formation at lower temperatures around 550 - 650 °C. At ***ambient pressure (1 bara)***, no formation of methane is detectable for all investigated temperatures (550 - 850 °C). Due to the fact that no methane is formed with the perovskite catalyst, the comparison of the test results is carried out with the thermodynamic equilibrium without CH_4 formation. The thermodynamic equilibrium is not reached for the temperature of 550 °C, but with increasing temperature from 650°C and higher the CO content approaches the equilibrium very well (17.6 vol.-% of catalyst 3 compared with 19 vol.-% of equilibrium).

Higher gas velocities negatively affect the CO formation of catalysts 2 and 3. When applying a Ni/Al_2O_3 catalyst, increased methane formation occurs specifically at lower temperatures. The effect of higher GHSVs is mirrored in the case of the Ni/Al_2O_3 catalyst. Here, methane formation decreases and CO formation increases with increasing gas velocity. The reason for this is probably a kinetic limitation due to the shorter contact time with the catalyst. Above 650 °C, the Ni/Al_2O_3 catalyst follows the thermodynamic equilibrium with the consideration of CH_4 formation. The support material Al_2O_3 does not form methane at any operating

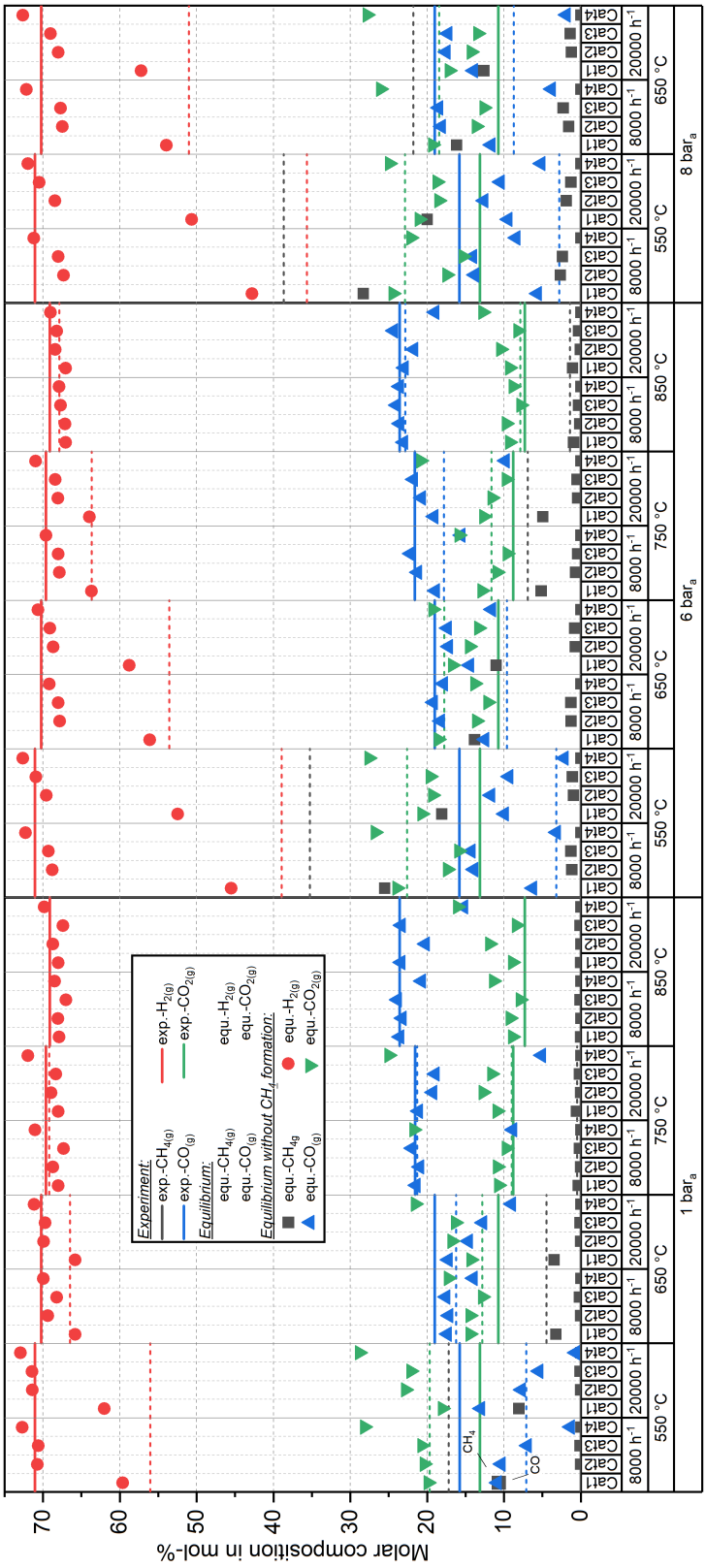

Figure 3.6: Dry gas composition of the product stream with a feed gas composition of H_2:CO_2 equal 3:1 for the four catalysts, pressures of 1, 6 and 8 bara, temperatures between 550 and 950 °C and GHSV of 8,000 and 20,000 h^{-1}

point, and the conversion of CO_2 to CO is hardly noticeable at 550 °C. However, this increases slightly at higher temperatures, but never reaches thermodynamic equilibrium. The reason for this could be the lack of active centers for the conversion of CO_2 to CO.

The methane formation increases thermodynamically at an applied ***pressure of 6 bara***, especially in the low temperature range at 550 to 750 °C. A similar effect can be seen for the catalysts 1 to 3. In the case of the use of the Ni/Al_2O_3 catalyst 1, the produced methane increases to 25.5 vol.-% and the CO concentration decreased from about 10.9 vol.-% at 1 bara to 6.2 vol.-% at 6 bara. However, the thermodynamic equilibrium is not reached, although considering CH_4 formation. With higher GHSV values and higher temperature, methane production decreases again. At the operated pressure level of 6 bara, a low methane content of 1 vol.-% is only reached at temperatures higher than 850 °C. In contrast, the perovskite catalyst produces max. 1.3 vol.-% CH_4 at a temperature of 550 °C and the CO content approaches the thermodynamic equilibrium without CH_4 consideration. A deviation can be observed here due to the low, but detectable CH_4 formation. In this case, a higher gas velocity also leads to a lower CH_4 concentration, but the CO formation also deteriorates. At a temperature level of 650 °C, the CO concentration for catalysts 2 and 3 reaches the thermodynamic equilibrium. There are no significant deviations in the CO concentration, with increasing GHSV values recognizable. The Al_2O_3 material again produces no methane at all operating points. At 550 °C, the CO concentration of 3.8 vol.-% is very low compared with the equilibrium (15.8 vol.-%). The CO concentration never reaches the thermodynamic equilibrium, neither at high temperatures 850 °C and GHSV of 8,000 h^{-1}. The effect of CO reduction with increasing GHSV occurs here too.

The composition of the product gas at a ***pressure level of 8 bara*** and temperatures of 550 and 650 °C is illustrated in Figure 3.6. An additional increase in the methane concentration is observed for the Ni/Al_2O_3 catalyst (catalyst 1), which reaches a maximum of 28.3 vol.-% at 550 °C. This reflects the low CO content of 5.7 vol.-%. Higher GHSVs significantly reduce CH_4 formation for catalyst 1 to 20 vol.-% and increase CO formation to 9.5 vol.-% at a GHSV of 20,000 h^{-1}. In comparison, the perovskite catalysts limit the methane formation to a maximum of 2.7 vol.-% at 550°C. The lower methane formation also results in an increased CO formation of up to 14.1 vol.-% for catalyst 3, followed by 13.8 vol.-% for catalyst 2. The same effect of the increased GHSV values applies to methane formation on catalysts 2 and 3, whereby CO formation also decreases with increasing specific gas velocities. The application of a higher temperature of 650 °C firstly reduces methane production slightly (1.6 and 2.3 vol.-% for both catalysts 2 and 3, respectively) and in this case, the thermodynamic equilibrium (without CH_4 formation) is approached for the carbon monoxide at around 18.5 vol.-%. For the Ni/Al_2O_3 catalyst (catalyst 1), the methane formation also decreases with higher temperatures and GHSVs (16.0 and 12.6 vol.-% for GHSV values of 8,000 and

20,000h^{-1} respectively), which results in a CO content of 11.7 and 14.0 vol.-%, which is due to the normalization of analyzed gaseous compounds in the gas analytic slightly above the thermodynamic equilibrium (CO concentration is 8.7 vol.-%). There is a strong deviation from the equilibrium without CH_4 consideration (CO concentration is 19.0 vol.-%). No methane formation is reported for the support material, Al_2O_3, at any operating point. The CO production increases with rising temperature and decreases with higher GHSVs. A maximum of the CO concentration is detected at 650 °C (8 bara) and 8,000 h^{-1}, but CO production never reaches thermodynamic equilibrium (without CH_4 production).

3.3.2 Calculation of mass and atom balances for data validation

The species CO_2, CO, CH_4 and H_2 present in the product gas stream are analyzed via a gas analyzer (ABB AO 2020). To ensure accuracy, a mass and atom balance can be drawn up. This entails the input mass equating with the output mass, as well as equivalent atom balances. The applied mass flow controllers for CO_2 and H_2 enable carbon, oxygen, and hydrogen atom tracking into the system. The wet product gas flow poses a challenge in terms of calculation, as water condensation data is currently absent. Nevertheless, discrepancies between inlet and outlet can still be detected. To compute the wet product gas composition, Matlab 2020b is employed to create a script which follows the workflow as depicted in Figure 3.7. In an initialization step, the steam content in the product gas phase is assumed to be 10 vol.-%. The steam content is limited within the lower bound (LB) of 0 vol.-% and the upper bound (UL) of 100 vol.-%. Values outside of this range are not representative. The model considers equations to calculate the overall mass balance of inlet and outlet streams and the atom balances of carbon, hydrogen and oxygen. The errors in the balances (C(1) - C(4)) are calculated by balancing the aforementioned equations and linked with the objective function. The objective function calculates a squared error of all balances $\theta(x_{H_2O,out,i})$ utilizing the errors C(1) - C(4) and a weighting factor a_i. The squared error is minimized by the optimizer unit to obtain the most suitable value for the steam content in the product gas phase with minimized weighted errors in all balances. Consequently, CO_2 conversion (Equation 3.2), CO selectivity (Equation 3.3), and CO yield (Equation 3.4) are derived (with mole flows n in kmol h^{-1} and molar fractions x).

$$CO_2 \text{ conversion} = \frac{\dot{n}_{in} * x_{CO_2,in} - \dot{n}_{out} * x_{CO_2,out}}{\dot{n}_{in} * x_{CO_2,in}} \tag{3.2}$$

$$CO \text{ conversion} = \frac{\dot{n}_{in} * x_{CO,in} - \dot{n}_{out} * x_{CO,out}}{\dot{n}_{in} * x_{CO,in}} \tag{3.3}$$

$$\text{CO yield} = \frac{\dot{n}_{out} * x_{CO,out} - \dot{n}_{in} * x_{CO,in}}{\dot{n}_{in} * x_{CO_2,in}} \tag{3.4}$$

Using the atom balance allows objective statements regarding carbon deposition in the reaction system and variations in the feed gas stream (H_2:CO_2 ratio).

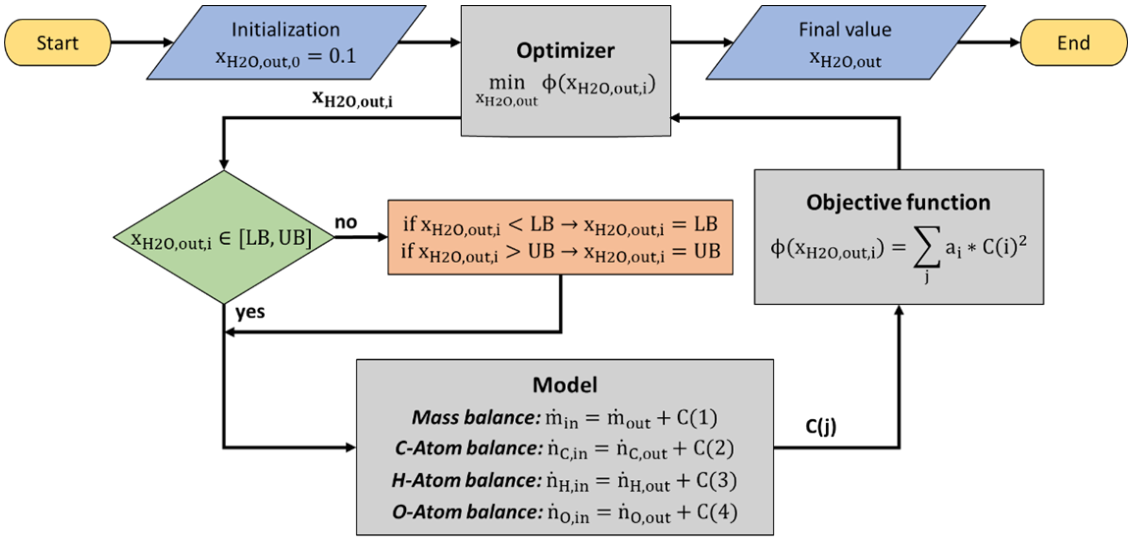

Figure 3.7: Illustration of the optimization process in the Matlab script to determine the water content, as well as the wet product composition of the gas

The following equations indicate the relative deviation of the carbon (Equation 3.5), the oxygen (Equation 3.6) and the hydrogen (Equation 3.7) atoms flowing into and out of the system. The accuracy of the gas analysis (+/- 1 vol.-% for each species) is also considered in the error calculation. To calculate the deviations in Equation 3.5 to Equation 3.7, the input ($\dot{n}_{in}$ in kmol h^{-1}) and output mole flows ($\dot{n}_{out}$ in kmol h^{-1}) of the individual elements (C, H and O) with the respective gas composition ($x_{i,in}$ and $x_{i,out}$ for the component i in vol.-%) are used from the model calculation.

$$\text{Deviation of C Balance in \%} = \left(1 - \frac{\dot{n}_{out} * (x_{CO,out} + x_{CO_2,out} + x_{CH_4,out})}{\dot{n}_{in} * x_{CO_2,in}}\right) * 100 \tag{3.5}$$

$$\text{Deviation of O Balance in \%} = \left(1 - \frac{\dot{n}_{out} * (x_{CO,out} + 2 * x_{CO_2,out} + x_{H_2O,out})}{\dot{n}_{in} * 2 * x_{CO_2,in}}\right) * 100 \tag{3.6}$$

$$\text{Deviation of H Balance in \%} = \left(1 - \frac{\dot{n}_{out} * (x_{H_2,out} + 2 * x_{H_2O,out} + 4 * x_{CH_4,out})}{\dot{n}_{in} * 2 * x_{H_2,in}}\right) * 100 \tag{3.7}$$

In summary, the following diagrams show the relative errors of the carbon (Figure 3.8), oxygen (Figure 3.9), and hydrogen (Figure 3.10) atom balances for all four catalysts at various temperatures (550 - 950 °C) and pressures (1, 3, 6, and 8 bara) for the GHSV value of 8,000 h^{-1}. The detailed description of the results can be found in the supplementary material of Publication 4. The carbon atom balance (Figure 3.8) experiences a relative error ranging between -0.7 and +1.5 % across all catalysts which indicates no carbon formation. These deviations are constant, but also a result of calculation and optimization through minimization. The trend of the relative error in the oxygen atom balance (Figure 3.9), similar to the carbon atom trend, serves as further indication of correctness and is in the range between -2.35 and +1.05 %.

In contrast, the deviation for the hydrogen atom balance (Figure 3.10) is more significant, ranging from -9 to +12.5 %. This difference is attributed to the mass flow controller settings. The maximum flow rate of the mass flow controllers is 45 NL min^{-1}, but only 3.5 NL min^{-1} of hydrogen is used at 8,000 h^{-1}. The controllers have an accuracy of +/- 0.5 % resulting in a deviation for the whole operating range of +/- 0.225 NL min^{-1}. There is the possibility of slight changes of the H_2:CO_2 ratio, which account for the relative error in the atomic balance.

3.4 Conclusion of the experimental rWGS investigation

The experimental tests carried out on the investigated catalysts, comprised of a commercially available Ni/Al_2O_3, two perovskite materials, and the support material Al_2O_3, exhibit encouraging outcomes for the application in a rWGS reactor. The implementation of perovskite catalysts (catalysts 2 and 3) shows promising results of the rWGS reaction in terms of high CO yields and low CH_4 formation in all operating points, when compared with the Ni/Al_2O_3 catalyst (catalyst 1). The nickel catalyst produces significant amounts of methane as an undesired by-product at a temperature of 750 °C and ambient pressure, with methane selectivity measurably increasing with both increasing parameters, higher temperatures and pressure (as early as 850 °C and 6 bara). The support material γ-Al_2O_3 is unsuitable as a catalyst material for the rWGS reaction, since CO_2 conversion to the desired product gas CO substantially deviates from the thermodynamic equilibrium. Perovskite catalysts enable lower temperature usage at approx. 550 °C, converting CO_2 to CO under atmospheric pressure. However, thermodynamic equilibrium without considering CH_4 formation is achieved with increasing pressure (6 bara). At higher pressures, small amounts of methane are measured, which differ significantly from the high value of the Ni/Al_2O_3 catalyst. Higher GHSVs have a positive influence on CO production when using the Ni/Al_2O_3 catalyst. This is related to

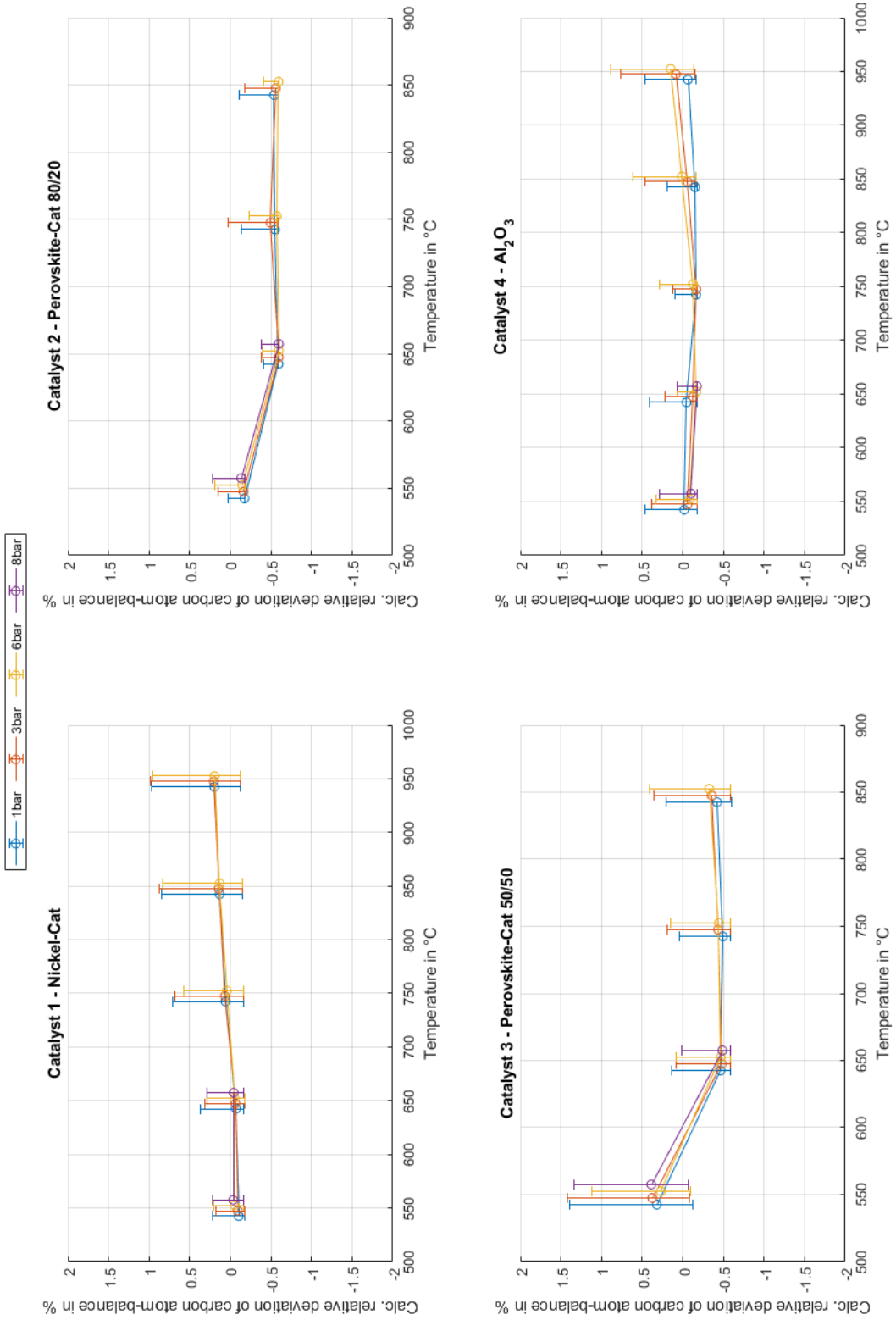

Figure 3.8: Carbon balance of all four catalysts in the temperature range of 550 - 950 °C (catalyst 1 and 4) or 550-850 °C (catalyst 2 and 3) and at pressure levels of 1, 3, 6 and 8 bara

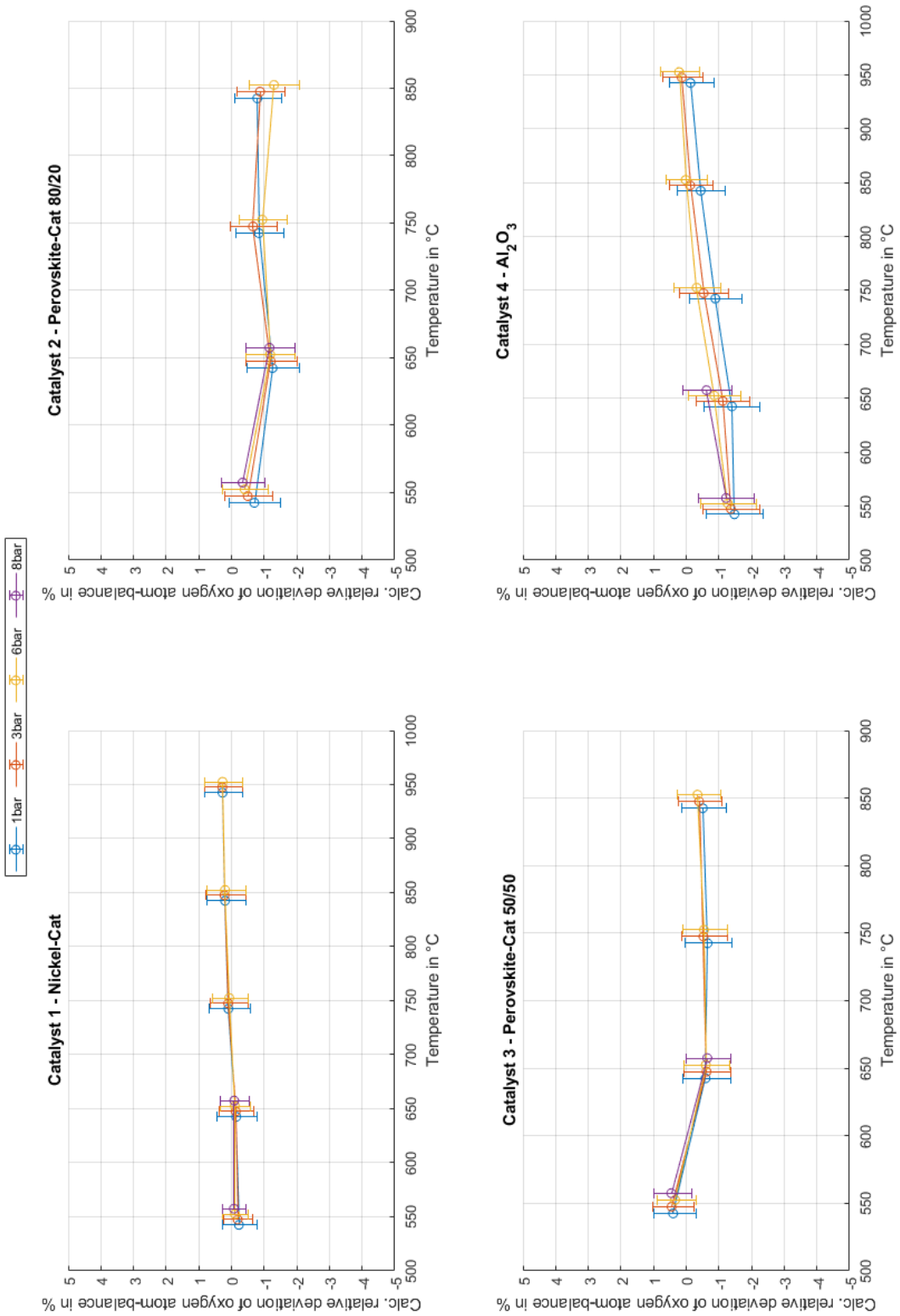

Figure 3.9: Oxygen balance of all four catalysts in the temperature range of 550-950 °C (catalyst 1 and 4) or 550-850 °C (catalyst 2 and 3) and at pressure levels of 1, 3, 6 and 8 bara

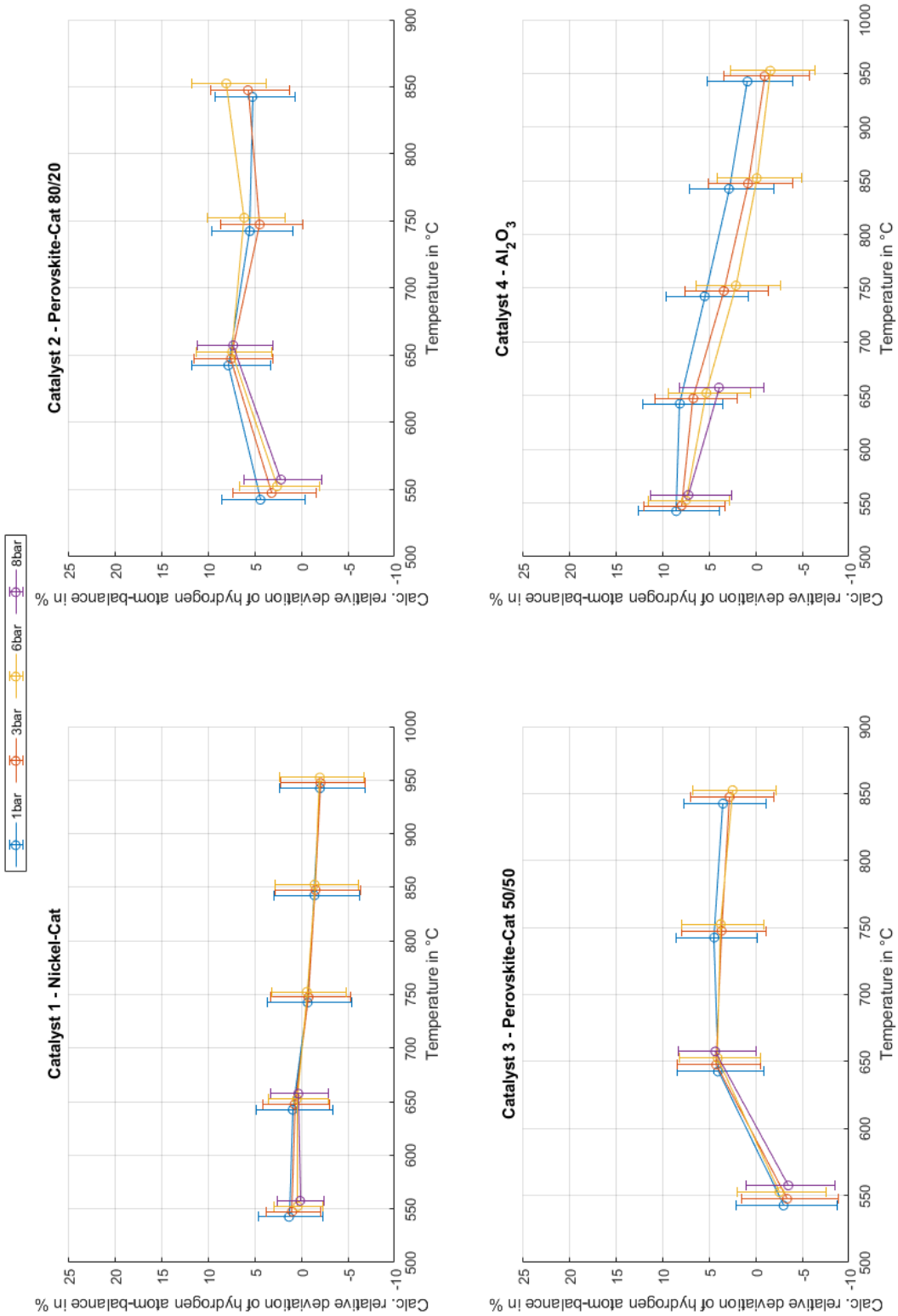

Figure 3.10: Hydrogen balance of all four catalysts in the temperature range of 550 - 950 °C (catalyst 1 and 4) or 550 - 850 °C (catalyst 2 and 3) and at pressure levels of 1, 3, 6 and 8 bara

a slower methane formation reaction resulting from a shorter contact time of the gas with the active catalyst surface. In the case of the perovskite catalysts, in addition to methane formation, CO formation also decreases with increasing GHSV.

It is confirmed that the rWGS reaction can be successfully operated in a high-temperature reactor based on experimental tests. In addition, the perovskite catalysts show high CO yields at low temperatures of 550 °C, and even at higher pressures (8 bara), they significantly suppress methane production. Therefore, selection of suitable catalysts is imperative for efficient PtL processes. Notably, the Ni/Al_2O_3 catalyst generates methane at low temperatures, while the steam reforming reaction occurs at higher temperatures. It is crucial to consider the catalysts utilized in a PtL procedure. Depending on the process design (e.g., recycling streams of downstream processes), for this catalyst it may be necessary to convert methane or other hydrocarbons into CO and hydrogen whereas recent experiments with the perovskite catalysts do not exhibit steam reforming behavior and indicate that it might require an additional process unit for steam reforming in the downstream process.

The implementation of a Gibbs reactor for the Ni/Al_2O_3 catalyst is validated by the previously discussed experiments and is therefore assumed to be viable for further flow sheet simulations. The methane production is for the Ni/Al_2O_3 catalyst slightly overestimated by the Gibbs reactor compared to the experimental results, but the behavior of steam reforming with a CH_4-containing input stream is taken into account. For the flow sheet simulations with perovskite catalysts in the rWGS reactor, the integration of a Gibbs reactor is again allowed. Here, methane and all higher paraffinic and olefinic hydrocarbons need to be considered as inert components, since barely any reaction of CO_2 and H_2 to CH_4 and no steam reforming occurred in the experiments compared to the Ni/Al_2O_3 catalyst. Coke is also considered as inert compound, since there is no indication of coke formation with regard to the atom balance.

Based on the findings, the investigated perovskite catalyst is implemented in PtL process simulations in ASPEN Plus, which is executed in the next chapter 4. The study compares the use of perovskite material as a rWGS catalyst in a Fischer-Tropsch PtL process chain with the initial PtL process route from chapter 2 and assesses additional units, such as a reforming reactor for the catalytic conversion of CH_4 with steam to synthesis gas. Additionally, the process efficiency is investigated by implementing the separation of CO_2 or H_2 downstream of the rWGS reactor. The conclusion drawn in the chapter 4 will determine whether the perovskite catalyst is advantageous as rWGS catalyst in terms of process performance in this PtL process chain compared to the Ni/Al_2O_3 catalyst.

Chapter 4

Power-to-liquid process development with a perovskite catalyst

The rWGS reaction on perovskite catalysts is experimentally investigated in a quartz glass reactor as described in chapter 3. The result of that study is that the methanation reaction is almost suppressed even at temperatures around 650 °C and pressures up to 8 bara, whereby a synthesis gas with a high CO content and appropriate H_2:CO ratio of 2.08:1 can be supplied for a subsequent Fischer-Tropsch process. In chapter 2, the Fischer-Tropsch process route is simulated and the conversion of syngas merely into paraffinic hydrocarbons is considered in this chapter. The rWGS reaction for syngas production is treated as a Gibbs reactor, assuming the conversion rates at thermodynamic equilibrium. The gaseous by-product of the Fischer-Tropsch reactor, consisting of short-chain paraffinic hydrocarbons (mainly CH_4, but also traces of C_2H_6 - C_6H_{14}), is fed back upstream of the rWGS reactor in the PtL process chain simulations. Due to the catalytic activity for steam reforming on a Ni/Al_2O_3 catalyst, it is assumed that the catalyst converts these hydrocarbons to synthesis gas with the steam produced by the rWGS reaction. Based on the findings of the experimental study in chapter 3, which indicate that the perovskite catalyst exhibits no activity for steam reforming, the process chain must be expanded by implementing a reforming reactor. This reactor is responsible for converting CH_4 and other hydrocarbons present into the required syngas. Otherwise, methane and higher hydrocarbons accumulate in the recycle gas stream and the efficiency of the overall process would suffer due to subsequent higher purge gas flow rates.

This chapter examines the use of a perovskite catalyst in a PtL process chain with the focus on process design with different process routes implemented in ASPEN Plus simulations, including for example an intermediate CO_2 or H_2 separation unit. The process setups are described in more detail in the following section 4.1. The study investigates the impact of interconnecting recycle gas streams and adding a steam reforming reactor to convert CH_4, higher hydrocarbons and steam into synthesis gas. Relevant key performance indicators are

the liquid product quantity consisting of naphtha, middle distillate and wax, PtL efficiency (Equation 2.1), carbon deposition in the rWGS or reforming reactor and the carbon efficiency (Equation 2.3) of the entire process. The study also assesses the advantages and disadvantages of using a perovskite catalyst and draws conclusions on necessary additional research tasks.

4.1 Structure of the simulation and the process chain comparison

The process chain described in chapter 2, investigating the Fischer-Tropsch process with a rWGS reactor, is used as the basic process in the following simulations. The assumptions of the operation conditions and product distribution for the Fischer-Tropsch unit as well as the syncrude product separation unit are adopted from subsection 2.2.4. The process chain is simplified and shown as process setup 1 in Figure 2.1. Given that CO_2 capture (carbon capture unit) is a consistent process across all process routes, involving both heat and electrical energy demands, it is not taken into account for the comparison of the different process routes. A pure CO_2 feed gas stream of 1,268 $kg\,h^{-1}$ is taken for this assessment and is used as the reference flow for the following process investigations. A purge gas stream of 2 % is extracted from the recycle gas stream to avoid accumulation of the unconverted gases (e.g. CO, CO_2 or H_2) and gaseous products from the Fischer-Tropsch process (e.g., CH_4, C_2H_6). This recycle gas stream is reintegrated upstream of the rWGS reactor, to reconvert the gaseous hydrocarbons into syngas, with the aim to achieve a high process performance. In process setup 1, the rWGS reactor is operated with a Ni/Al_2O_3 catalyst, which allows the implementation of a Gibbs reactor in ASPEN Plus. This assumption is confirmed by the results of the experimental investigations summarized in chapter 3. The pressure of the rWGS reactor is aligned with the pressure level of the recycled gas flow of the Fischer-Tropsch product separation and is assumed to be 12 bara. The temperature is varied between 650 and 950 °C to obtain the influence of temperature change at constant pressure on the aforementioned liquid product quantity, PtL and carbon efficiency, as well as carbon decomposition. The hydrogen flow is calculated to achieve a H_2:CO ratio of the Fischer-Tropsch feed gas stream of 2.08:1 (adopted from subsection 2.2.4). In all process setups, hydrogen is assumed to be produced in a PEM and SOEC electrolysis with a specific system energy demand of 4.7 and 3.6 $kWh\,Nm^{-3}_{H_2}$, respectively [32].

In process setup 2 (Figure 4.2), the perovskite catalyst is implemented in the simulation as a Gibbs reactor, which treats carbon, methane and higher hydrocarbons from the syncrude separation unit as inert compounds. This assumption is permissible, since the experimental results with perovskite catalysts (described in section 3.3) showed no activity towards steam

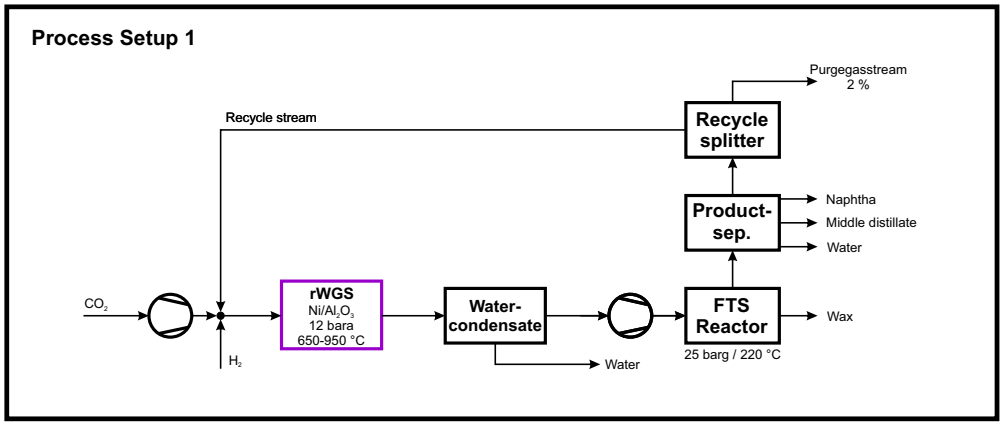

Figure 4.1: Block flow diagram of process setup 1 with an Ni/Al_2O_3 operated rWGS reactor in a temperature range of 650 to 950 °C and 12 bara, a water condenser, a downstream Fischer-Tropsch reactor and a product separation unit

reforming, the methanation reaction or coke formation. Suitable operation conditions with negligible methane formation are identified at a temperature of 650 °C and a pressure up to 8 bara. The product separation unit is adopted from subsection 2.2.4, where the recycle stream is released at a pressure level of 12 bara. Pressure losses in a process chain always result in higher electricity costs, due to the higher compression energy demand. Therefore, it is assumed that the experimentally observed, neglectable methane formation for pressures up to 8 bara can be extended to pressures up to 12 bara. However, this assumption cannot be confirmed with the currently available experimental setup. The recycle gas stream is fed to a reforming reactor to convert methane and higher hydrocarbons into syngas. The occurring endothermic reactions are listed for methane steam reforming in Equation 4.1, for the conversion of higher hydrocarbons with n as number of carbon atoms in Equation 4.2 and for dry reforming in Equation 4.3. Under certain circumstances, the Boudouard reaction (Equation 2.10) occurs at low temperatures, whereby CH_4 decomposition (Equation 2.9) is a further side reaction at high temperature. Both reactions are undesired, lead to carbon formation and must be avoided [57].

$$CH_4 + H_2O \longleftrightarrow CO + 3\,H_2 \qquad \Delta H_r^{298K} = 206\,\text{kJ mol}^{-1} \tag{4.1}$$

$$C_nH_{2n+2} + nH_2O \longleftrightarrow nCO + (2n+1)\,H_2 \qquad \Delta H_r^{298K} > 0 \tag{4.2}$$

$$CH_4 + CO_2 \longleftrightarrow 2\,CO + 2\,H_2 \qquad \Delta H_r^{298K} = 247\,\text{kJ mol}^{-1} \tag{4.3}$$

Within a sensitivity analysis, the temperature of the reactor is varied between 600 and 950 °C (increment of 50 K) at a constant pressure of 12 bara. Additionally, the steam to carbon ratio (S:C ratio) is defined in Equation 4.4 as the molar flow of steam ($\dot{n}_{steam}$ in kmol h^{-1}) divided

by the molar flow of hydrocarbons ($\dot{n}_{C_nH_{2n+2}}$ in kmol h^{-1} for CH_4 - C_6H_{14}) and is varied from 1 to 4 to obtain information regarding the coking regime and determine the operating conditions with the highest efficiencies and product quantities of the whole process chain.

$$S : C = \frac{\dot{n}_{steam}}{\sum \dot{n}_{C_nH_{2n+2}}} \tag{4.4}$$

The carbon deposition is defined as the produced carbon in the rWGS and steam reforming process units based on the carbon feed, which diminishes the entire carbon efficiency significantly. Those operation conditions must be avoided, because coke formation goes along with catalyst deactivation, which reduces the active sites of the catalyst surface and suppresses the conversion of hydrocarbons with steam to syngas. Since hydrogen is also a product of the reforming reaction, the H_2:CO ratio of the Fischer-Tropsch feed gas needs to be adjusted by separating a specific amount of hydrogen (modelled as a partial flow separation of H_2 via an e.g., pressure swing adsorption), which is compressed in an additional compressor and recycled in the H_2 feed upstream of the rWGS reactor. The ratio of recycled H_2 and feed H_2 is indicated by the H_{2rec}:H_{2feed} ratio. A ratio of 0 % means no separation of H_2 is required to achieve the H_2:CO feed ratio of 2.08:1 for the Fischer-Tropsch synthesis, whereas in contrast, a ratio of higher than 100 % means that more H_2 is recycled than fed into the process to either fulfill the H_2:CO Fischer-Tropsch feed ratio or the H_2:CO_2 ratio of 3:1 for the rWGS gas feed.

The block flow diagram of process setup 3 is given in Figure 4.3 and represents an extension of process setup 2 by a CO_2 separation unit downstream of the water condenser to provide syngas with low concentration of CO_2 for the Fischer-Tropsch reactor. The efficiency of the CO_2 separation unit is assumed to be 95 % (e.g., membrane separation) [58]. The separated CO_2 is compressed in an additional compressor and recycled upstream the rWGS reactor.

Process setup 4 (Figure 4.4) differs only slightly from process setup 3. Here, the feed point of the recycling stream is switched upstream of the CO_2 capture unit.

4.2 Simulation results and calculation of efficiencies

The results of the liquid product quantity, the PtL (for PEM and SOEC technology) and the carbon efficiency, as well as carbon formation and the H_{2rec}:H_{2feed} ratio are given for each process setup in Table 4.1 to Table 4.4.

Process setup 1 consists of the rWGS reactor with a Ni/Al_2O_3 catalyst (implementation as usual by a Gibbs reactor in ASPEN Plus) and is operated at a constant pressure of 12 bara, while the temperature is varied between 650 and 950 °C. This is the simplified basic

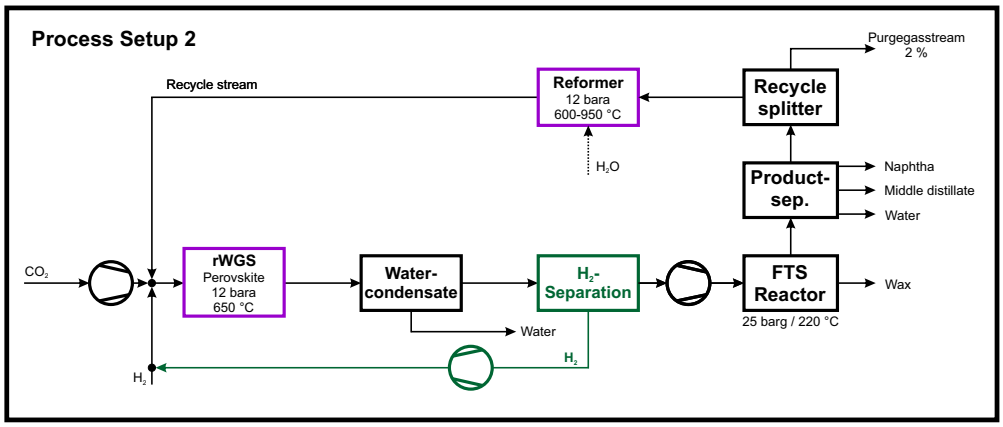

Figure 4.2: Block flow diagram of process setup 2 with the implementation of the perovskite catalyst in the rWGS reactor, a water condenser, a H_2 separation unit, a Fischer-Tropsch reactor with product separation and a reformer

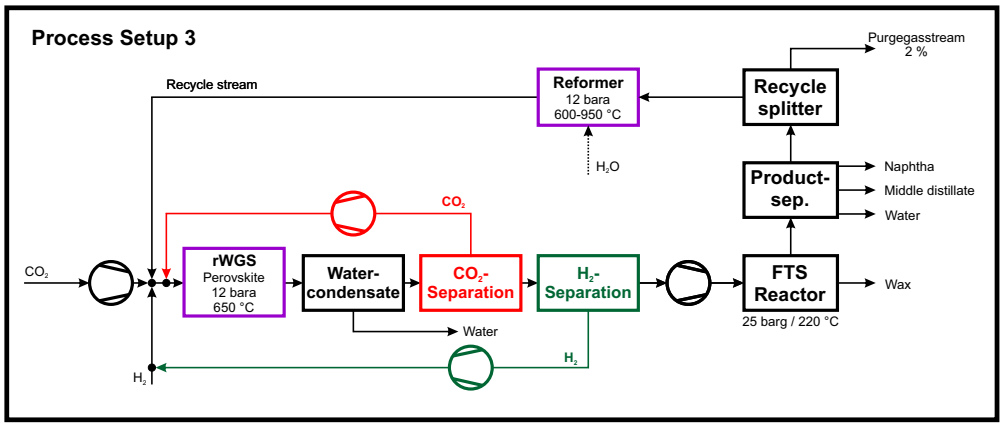

Figure 4.3: Block flow diagram of process setup 3 with the perovskite catalyst rWGS reactor, a water condenser, downstream CO_2 and H_2 separation unit, a Fischer-Tropsch reactor with product separation unit and a reforming unit for the recycle gas

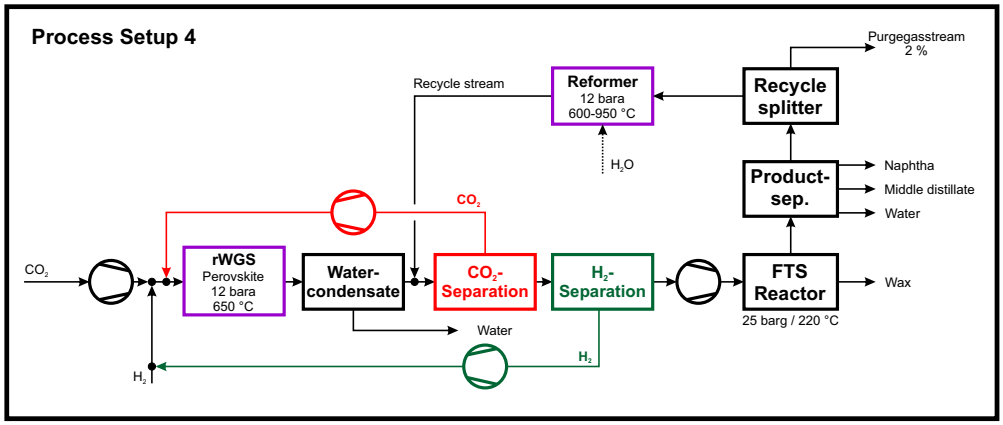

Figure 4.4: Block flow diagram of process setup 4 (similar to process setup 3) with a change of the recycle gas feed from the rWGS reactor upstream of the CO_2 separation unit

process from chapter 2, including the rWGS reaction, Fischer-Tropsch synthesis and product separation. The results of the investigation of process setup 1 are summarized in Table 4.1. Low temperatures lead to low product quantities, low PtL and carbon efficiencies (e.g., considering an operation temperature of 650 °C in the rWGS reactor, a product quantity of 32.6 kg h^{-1} with a PtL efficiency of 4.2 % (PEM) and 5.4 % (SOEC) is achieved). The carbon efficiency of the entire process route is in this worst case 7.9 %, which corresponds to a loss of carbon molecules of more than 90 %. In the temperature range between 650 and 850 °C, coke deposition also occurs in the rWGS reactor with a selectivity between 85.9 and 7.3 %. It can therefore be concluded that this temperature regime (650 - 850 °C) must be avoided due to carbon deposition. With an rWGS reactor operating temperatures above 900 °C, a high product quantity of 382.6 kg h^{-1} is achieved with high PtL efficiencies of 43.0 and 56.1 % for PEM and SOEC, respectively. This first investigation concludes that high temperatures in the rWGS reactor have a positive effect on all key figures and product quantity. For reason of comparison with the upcoming process setups, the best case is used with an operating temperature of 950 °C, resulting in a production volume of 382.6 kg h^{-1}, PtL efficiencies of 43.0 % for PEM and 56.1 % for SOEC, and a carbon efficiency of 94.1 % for the whole process chain.

Table 4.1: Results of the process simulation for process setup 1 by varying the rWGS reactor temperature between 650 and 950 °C and influence on the product quantity, the PtL efficiency for PEM and SOEC, coke deposition in the rWGS reactor and entire carbon efficiency

rWGS Temp. in °C	**Product quantity in kg h^{-1}**	**PtL efficiency (PEM) in %**	**PtL efficiency (SOEC) in %**	**Coke deposition in %**	**Carbon efficiency in %**
650	32.6	4.2	5.4	85.9	7.9
700	64.9	8.5	11.1	78.3	16.0
750	116.5	15.0	19.6	65.6	28.7
800	187.8	23.2	30.3	48.0	46.2
850	270.1	31.5	41.1	27.5	66.4
900	350.6	38.6	50.4	7.3	86.3
950	382.6	43.0	56.1	0.0	94.1

The results from the simulation of process setup 2 are given in Table 4.2. Here, the rWGS reactor is operated with the perovskite catalyst (Gibbs reactor with carbon, CH_4 and higher hydrocarbons treated as inert gases in ASPEN Plus) and a reformer is implemented in the recycle gas stream, to convert methane and higher hydrocarbons into syngas. As shown in the result table, a low reformer temperature of 600 °C leads due to carbon formation to a low

product quantity (142.9 kg h^{-1}), compared to the base scenario in Table 4.1. Higher steam to carbon ratios (S:C ratio > 1) upstream of the reformer have a positive influence on the product quantity for the temperature range up to 950 °C. The highest product quantity is achieved for a reformer temperature of 950 °C and an S:C ratio equal 2 and 3 with 381.8 kg h^{-1} (cf. 382.6 kg h^{-1} in the base process route 1). High PtL efficiencies are also achieved at a reformer temperature of 950 °C and S:C ratios between 2 and 4 with the maximum of 46.2 and 60.3 % for PEM and SOEC, respectively. The results furthermore show that higher S:C ratios and increasing temperatures suppress the formation of carbon in the reformer. No carbon formation is at least detected for all S:C ratios higher than 1 and temperatures higher than 850 °C in case of an S:C ratio equal to 1. Elevated temperatures are also reflected in the highest carbon efficiency of 93.9 %, which is not remarkably lower than the basic process (process setup 1 with 94.1 %). There is an excess of hydrogen (H_2:CO > 2.08:1) in the feed gas stream of the Fischer-Tropsch synthesis, whereby hydrogen needs to be partially separated. This results in a H_{2rec}:H_{2feed} ratio of 149.8 % at a reforming operating temperature of 600 °C (S:C ratio is 4). The H_{2rec}:H_{2feed} ratio decreases with elevated temperatures but never achieves 0 %, due to the over-stoichiometric operation mode of H_2:CO_2 of 3:1 in the rWGS feed gas stream. The theoretical investigation of process setup 2 reveals, that the implementation of the rWGS with a perovskite catalyst has no positive added value for the overall system due to the lower product quantity and carbon efficiency compared to the base scenario in process setup 1 with a Ni/Al_2O_3 catalyst applied in the rWGS reactor. To increase the product quantity and carbon efficiency, the influence of a CO_2 separation unit downstream of the rWGS reactor and water condenser is therefore considered in the next process setup 3.

The results of the performance indicators of process setup 3 are summarized in Table 4.3. Same as for the process 2, higher temperatures in the reforming reactor lead to higher product quantities and improved KPIs. A higher S:C ratio has a coke reducing effect in the range of low temperatures, however coke formation occurs for an S:C ratio of 1 and all investigated reforming temperatures between 600 and 950 °C (coke deposition between 3.4 and 39.2 %). In the reforming reactor, there is no carbon formation observed at an S:C ratio higher than 1. In this investigation, H_{2rec}:H_{2feed} ratios of up to 156.1 % occur for low reforming temperatures (at 600 °C and S:C ratio equal 4), which are decreasing with elevated temperatures to 93 % (at 950 °C and an S:C ratio of 4). The product quantity has its maximum at a reforming operating temperature of 950 °C and an S:C ratio equal 4 with 386.6 kg h^{-1}. Based on the same CO_2 feed gas flow in all setups, the yield in liquid products as well as the PtL efficiency with 46.2 % (base scenario: 43.0 %) for PEM and 60.3 % (base scenario: 56.1 %) and the carbon efficiency of 95.1 % (base scenario: 94.1 %) are remarkably higher compared to the base scenario in process setup 1 and also to process setup 2, without the CO_2 separation unit.

Table 4.2: Simulation results of process setup 2 with product quantity, H_{2rec}:H_{2feed} ratio, PtL efficiency for PEM and SOEC, coke deposition in the reforming reactor and entire carbon efficiency

Reformer Temp. in °C	**Product quantity in kg h^{-1}** S:C ratio				**H_{2rec}:H_{2feed} in %** S:C ratio			
	4	3	2	1	4	3	2	1
600	349.6	344.6	336.4	142.9	149.8	145.7	138.9	78.5
650	358.9	355.5	349.8	153.9	140.0	135.5	129.8	78.2
700	366.1	364.1	360.5	175.2	126.0	121.3	114.4	77.6
750	372.0	370.7	368.5	210.9	109.1	104.6	98.5	76.0
800	375.9	375.3	374.2	265.0	94.2	87.6	83.3	72.4
850	378.8	378.6	378.0	336.9	81.7	78.0	72.7	66.6
900	380.6	380.6	380.4	379.5	74.1	70.3	65.6	59.9
950	381.6	381.8	381.8	381.4	68.3	65.0	61.0	56.2

Reformer Temp. in °C	**PtL efficiency (PEM) in %** S:C ratio				**PtL efficiency (SOEC) in %** S:C ratio			
	4	3	2	1	4	3	2	1
600	42.2	41.5	40.3	22.7	55.1	54.1	52.6	29.6
650	43.5	43.0	42.1	24.3	56.8	56.1	55.0	31.8
700	44.4	44.1	43.5	27.2	58.0	57.6	56.8	35.5
750	45.1	44.9	44.5	31.6	58.8	58.6	58.1	41.3
800	45.5	44.8	45.2	37.2	59.4	58.5	59.0	48.6
850	45.9	45.7	45.7	42.8	59.9	59.7	59.6	55.9
900	46.0	46.0	45.9	45.8	60.1	60.1	60.0	59.8
950	46.2	46.1	46.1	46.0	60.3	60.2	60.2	60.1

Reformer Temp. in °C	**Coke deposition in %** S:C ratio				**Carbon efficiency in %** S:C ratio			
	4	3	2	1	4	3	2	1
600	0.0	0.0	0.0	59.0	86.1	84.8	82.8	35.2
650	0.0	0.0	0.0	57.0	88.4	87.5	86.1	37.9
700	0.0	0.0	0.0	51.9	90.2	89.6	88.7	43.1
750	0.0	0.0	0.0	42.8	91.5	91.2	90.7	51.9
800	0.0	0.0	0.0	29.0	92.6	92.4	92.1	65.2
850	0.0	0.0	0.0	10.6	93.2	93.2	93.0	82.9
900	0.0	0.0	0.0	0.0	93.7	93.7	93.6	93.4
950	0.0	0.0	0.0	0.0	93.9	93.9	93.9	93.8

Table 4.3: Simulation results of process setup 3 with product quantity, H_{2rec}:H_{2feed} ratio, PtL efficiency for PEM and SOEC, coke deposition in the reforming reactor and entire carbon efficiency

Reformer Temp. in °C	**Product quantity in kg h^{-1}** S:C ratio				**H_{2rec}:H_{2feed} in %** S:C ratio			
	4	3	2	1	4	3	2	1
600	361.7	356.5	347.7	255.3	156.1	152.4	147.2	117.6
650	369.6	365.7	359.3	224.4	151.0	147.4	141.8	104.7
700	375.3	372.6	368.1	223.1	141.2	137.4	131.6	98.4
750	379.6	377.7	374.8	238.4	129.2	125.0	119.4	95.1
800	382.5	381.3	379.2	265.2	116.6	112.2	106.7	92.0
850	384.5	383.8	382.5	301.6	105.2	101.7	96.8	88.3
900	385.8	385.4	384.4	339.7	97.8	93.9	90.0	84.4
950	386.6	386.2	385.8	371.5	93.0	89.0	85.2	80.7

Reformer Temp. in °C	**PtL efficiency (PEM) in %** S:C ratio				**PtL efficiency (SOEC) in %** S:C ratio			
	4	3	2	1	4	3	2	1
600	42.4	41.7	40.4	32.9	55.4	54.4	52.8	43.0
650	43.8	43.2	42.3	31.3	57.1	56.4	55.2	40.8
700	44.5	44.1	43.5	31.8	58.1	57.6	56.9	41.5
750	45.1	44.9	44.4	33.8	58.9	58.6	58.0	44.1
800	45.6	45.4	45.1	36.9	59.5	59.2	58.9	48.1
850	45.8	45.8	45.6	40.0	59.8	59.7	59.5	52.2
900	46.0	46.0	45.9	42.9	60.1	60.0	59.9	55.9
950	46.2	46.1	46.0	45.0	60.3	60.2	60.1	58.8

Reformer Temp. in °C	**Coke deposition in %** S:C ratio				**Carbon efficiency in %** S:C ratio			
	4	3	2	1	4	3	2	1
600	0.0	0.0	0.0	24.3	88.9	87.6	85.5	62.7
650	0.0	0.0	0.0	36.9	90.9	89.9	88.3	55.2
700	0.0	0.0	0.0	39.2	92.3	91.6	90.5	54.8
750	0.0	0.0	0.0	36.2	93.3	92.9	92.1	58.6
800	0.0	0.0	0.0	29.9	94.0	93.7	93.3	65.2
850	0.0	0.0	0.0	20.8	94.5	94.4	94.0	74.1
900	0.0	0.0	0.0	11.3	94.9	94.7	94.5	83.5
950	0.0	0.0	0.0	3.4	95.1	95.0	94.8	91.3

In process setup 4, a modification is made to process route 3, wherein the recycle stream from the reforming reactor is introduced directly upstream of the CO_2 separation unit. This reduces, on the one hand, the volume flow in the feed gas stream of the rWGS reactor since merely the separated CO_2 of the recycle stream is returned to the rWGS reactor and, on the other hand, the design size and investment costs of the reactor itself (this evaluation is not considered in this study). The results of the performance indicators of this simulation are shown in Table 4.4.

Despite yielding similar product quantities as in process setup 3, it is immediately apparent that the H_2 recycle streams are notably higher, reaching H_{2rec}:H_{2feed} ratios up to 321.1 %. This indicates, that more H_2 is recycled in the case of an operating temperature of 600 °C and an S:C ratio of 4, than fed from the electrolysis. In process setups 2 and 3, the hydrogen produced from the reforming reactor is used for the rWGS reaction by feeding the recycle gas of the reforming reactor upstream of the rWGS reactor. In contrast, in process setup 4 the reformer product gas is recycled upstream the CO_2 separation, and the separated H_2 is recirculated upstream the rWGS reactor. The high H_{2rec}:H_{2feed} ratio is a result of the calculation of the H_2:CO ratio in the simulation for the Fischer-Tropsch synthesis feed gas stream using corresponding design specifications. The hydrogen flow present in the reforming reactor consists on the one hand of recycled H_2, and is on the other hand a product of the reforming reactions (Equation 4.1 to Equation 4.3), which increase the H_2:CO ratio excessively. It is therefore mandatory to separate the H_2 partly from the Fischer-Tropsch feed stream. High H_2 recycle flows mean higher investment costs for the H_2 separation unit, especially the compressors, which is also reflected in high electrical energy consumption and results in higher operating costs. The higher electrical energy demand is also considered in the PtL efficiency, where the highest values are achieved with 46.1 % for the PEM and 60.2 % for the SOEC at the highest operating temperature of 950 °C and the highest S:C ratio of 4 applied in the reforming reactor.

Process setup 4 has a significant advantage in terms of the basic scenario, but no better key performance indicators compared to process setup 3, as the indicators are highest at a reforming reactor temperature of 950 °C and a S:C ratio of 4 with a product quantity of max. 386.6 $kg\,h^{-1}$, PtL efficiencies with 46.1 % for PEM and 60.2 % for SOEC and a carbon efficiency of 95.0 %, which are the same or below compared to the performance indicators of process setup 3.

Table 4.4: Simulation results of process setup 4 with product quantity, H_{2rec}:H_{2feed} ratio, PtL efficiency for PEM and SOEC, coke deposition in the reforming reactor and entire carbon efficiency

Reformer Temp. in °C	**Product quantity in kg h^{-1}** S:C ratio				**H_{2rec}:H_{2feed} in %** S:C ratio			
	4	3	2	1	4	3	2	1
600	360.7	355.4	347.0	244.8	321.1	309.6	290.6	206.6
650	368.5	364.8	358.6	220.0	291.5	282.8	265.4	171.2
700	374.8	372.0	367.4	221.3	255.4	244.3	226.9	150.7
750	379.1	377.3	374.3	238.0	212.7	200.1	182.0	134.3
800	382.2	381.2	379.2	265.5	171.1	158.6	142.8	117.1
850	384.4	383.7	382.4	301.3	137.7	126.8	112.9	98.7
900	385.6	385.3	384.3	339.1	115.1	104.2	94.3	82.4
950	386.6	386.1	385.7	371.0	99.6	89.2	79.8	69.7

Reformer Temp. in °C	**PtL efficiency (PEM) in %** S:C ratio				**PtL efficiency (SOEC) in %** S:C ratio			
	4	3	2	1	4	3	2	1
600	42.3	41.5	40.3	32.1	55.2	54.2	52.6	41.9
650	43.2	43.1	42.2	30.8	56.5	56.2	55.1	40.3
700	44.4	44.0	43.7	31.6	58.0	57.5	57.1	41.2
750	45.0	44.8	44.4	33.8	58.8	58.5	57.9	44.1
800	45.5	45.4	45.1	36.9	59.4	59.2	58.9	48.1
850	45.8	45.7	45.5	40.0	59.8	59.7	59.4	52.2
900	46.1	45.9	46.2	42.8	60.1	60.0	60.3	55.9
950	46.1	45.9	46.0	45.0	60.2	59.9	60.1	58.8

Reformer Temp. in °C	**Coke deposition in %** S:C ratio				**Carbon efficiency in %** S:C ratio			
	4	3	2	1	4	3	2	1
600	0.0	0.0	0.0	27.6	88.7	87.4	85.3	60.1
650	0.0	0.0	0.0	38.3	90.7	89.7	88.2	54.1
700	0.0	0.0	0.0	39.7	92.2	91.5	90.4	54.4
750	0.0	0.0	0.0	36.3	93.2	92.8	92.1	58.5
800	0.0	0.0	0.0	29.8	94.0	93.7	93.2	65.3
850	0.0	0.0	0.0	20.9	94.5	94.3	94.0	74.1
900	0.0	0.0	0.0	11.5	94.8	94.7	94.5	83.4
950	0.0	0.0	0.0	3.5	95.0	95.0	94.8	91.2

4.3 Conclusion of the process simulations with a perovskite catalyst

In this chapter, the integration of a perovskite catalyst in the PtL process chain is examined and the performance indicators such as product quantity, PtL efficiencies for PEM and SOEC, carbon deposition, H_2 recycle ratio and the overall carbon efficiency of the process are calculated. The four process routes are defined, which differ mainly in the design of the recycling streams, catalyst material, and additional CO_2 and H_2 separation units.

The process flow sheet simulation shows that the perovskite catalyst has a positive impact in the production of syngas and its integration into PtL process chains with regard to increasing efficiency. The comparison of the process routes clearly indicates that the use of the perovskite material (process setup 2 to 4) as an rWGS catalyst is particularly useful in process setup 3. A recycle stream of the gaseous Fischer-Tropsch products via a reformer upstream of the rWGS reactor, with integrated CO_2 capture downstream of the rWGS reactor, demonstrates the best efficiencies. Decisive for high efficiencies is the reforming temperature and the steam to carbon ratio (S:C ratio) in the reforming reactor. High temperatures and low S:C ratios show an improvement in product quantity and efficiencies, resulting in operating conditions for the reforming reactor with a temperature of 950 °C and an S:C ratio of 4 as optimum. The comparison with the base scenario (Ni/Al_2O_3 catalyst in process setup 1) shows that in process setup 3 the product quantity is increased from max. $382.6\,kg\,h^{-1}$ in setup 1 to $386.6\,kg\,h^{-1}$, which is also reflected in increased PtL efficiencies of 46.2 % for PEM (cf. 43.0 % in setup 1) and 60.3 % for the SOEC (cf. 56.1 % in setup 1). It is worth noting that, despite the use of an additional reforming reactor and a CO_2 separation unit, process setup 3 with a perovskite catalyst exhibits overall better efficiencies than process setup 1 with a Ni/Al_2O_3 catalyst.

In process setup 2, CO_2 is not separated behind the rWGS reactor and the water condenser. As a result, CO_2 is passed through the Fischer-Tropsch reactor as an inert gas, which increases the volume flow in the reactor. Additionally, due to the 2 % purge gas flow, the loss of carbon is slightly increased. This leads to a decrease in both the product quantity (maximum of $381.6\,kg\,h^{-1}$) and carbon efficiency (93.9 %) compared to process setup 3 (maximum of $386.6\,kg\,h^{-1}$ and 95.1 %).

The routing of the recycle stream from the reforming reactor upstream of the CO_2 separation unit in process setup 4 is problematic, since hydrogen produced in the reformer cannot be directly used in contrast when it is recycled back upstream the rWGS reactor. To achieve a H_2:CO_2 ratio of 3:1 in the rWGS feed gas stream, a higher hydrogen stream must be separated, compressed, and fed back upstream of the rWGS reactor to avoid operation

conditions in the coking regime. For a reforming temperature of 600 °C and a S:C ratio of 4, the H_{2rec}:H_{2feed} ratio is in process setup 4 with up to 321.1 % comparably much higher than 156.1 % in process setup 3. However, both process routes are similar in case of high reforming operating temperatures and S:C ratio of 4 (93.0 % in process setup 3 compared to 99.6 % in process setup 4).

In summary, this investigation demonstrates that integrating a perovskite catalyst in PtL process chains has a positive effect on key performance indicators, which allows and forces further research in this topic. On a theoretical basis, the process simulation could be extended with heat integration systems (calculation of global efficiency in Equation 2.2) and the economic assessment (calculation of investment, operating and net production costs as described in chapter 2). Furthermore, a focus should be on the experimental work to execute further experiments with the aim to investigate the effect of the additional recycle gas stream from the steam reformer regarding coke formation in the rWGS reactor. Beside of coke formation, it is necessary to observe the long-term stability of the catalyst (e.g., more than 100 hours of continuous operation) and, if necessary, execute an improvement in stability through further development of the catalytic material (e.g., geometry and shape of the catalyst particles).

Chapter 5

Summary and conclusion

The present study focuses on the development of power-to-liquid processes from a theoretical and experimental point of view. The goal is to use carbon-rich exhaust gas streams from the cement industry as a resource for producing valuable products like polyolefins or e-fuels. The production of polyolefins is advantageous, as carbon remains bound in the product for several decades when used as, for example, high-voltage cable sheathing. However, this is not the case with e-fuels, as the carbon is released into the atmosphere once it is burned in an internal combustion engine (for instance, as gasoline in cars or kerosene in airplanes).

The objective of the first part of the study is to investigate various process routes to capture CO_2 from the cement plant exhaust gas employing carbon capture technologies (in this study particularly amine scrubber unit) and convert the concentrated CO_2 in a catalytically, multi-stage reactor setup into polyolefins by the use of green hydrogen. The Fischer-Tropsch and methanol synthesis are considered as main conversion processes, but the rWGS reaction needs to be occasionally considered as pre-reaction, when applying a conversion technology which requires syngas as feedstock like the Fischer-Tropsch synthesis. The CO_2-tolerant methanol synthesis, in which the CO_2 and H_2 gas mixture is directly converted to methanol, is an innovative technology which is included in the process comparison.

An assessment of these process routes based on the degree of technical maturity, process design, product production costs, and economic cost calculation is performed, to obtain the optimal PtL process chain from a techno-economic perspective. ASPEN Plus simulations are the fundamentals for the technical analysis, where an amine-based carbon capture unit for the separation of 10,000 tons of CO_2 per year is assumed with a downstream rWGS and Fischer-Tropsch synthesis. The carbon capture unit provides a highly concentrated dry CO_2 gas stream with a CO_2 purity of 99.9 wt.-%. The production of hydrogen is incorporated into the simulation by means of water electrolysis. CO_2 and H_2 are fed into the rWGS reactor, which is conceived as a Gibbs reactor and is operated at 950 °C and 10 barg to attain a high

CO selectivity and almost completely suppress methane formation. The synthesis gas is fed to a low-temperature Fischer-Tropsch synthesis, which is optimized by varying operating parameters such as methane selectivity and CO conversion, as well as investigating recycle streams around the Fischer-Tropsch reactor itself and upstream of the rWGS reactor. The recycle stream directly around the Fischer-Tropsch synthesis leads to an accumulation of unreacted gases (syngas, but also CH_4 or higher gaseous hydrocarbons), which results in low product quantity, PtL and carbon efficiency (Figure 2.8, 226 – 251 kg h^{-1}, 33.6 – 38.9 %, 50.4 – 56.0 % for a purge gas split ratio of 0.98 compared to 381 – 393 kg h^{-1}, 44.0 – 47.2 % and 85.1 – 87.9 % for a split ratio of 0, respectively for product quantity, PtL and carbon conversion). One recycle stream behind the Fischer-Tropsch product separation unit upstream of the rWGS reactor and the serial arrangement of rWGS and Fischer-Tropsch reactor without any intermediate recycle streams proves to be the most sufficient process, with which the highest efficiencies and product yields are also achieved. These key figures are also heightened if high CO conversions and low CH_4 selectivities are realized by selecting suitable catalysts in the Fischer-Tropsch reactor itself.

The setup of the investigated Fischer-Tropsch process is adopted in the techno-economic study, where eight scenarios with individual electrolysis (PEM and SOEC) and synthesis technologies (Fischer-Tropsch and methanol) are examined. Scenarios 1 to 4 consist of the Fischer-Tropsch synthesis with rWGS reactor and product separation, with the distinction in the downstream process. Here, a newly constructed (scenarios 1 and 2) and an existing (scenarios 3 and 4) steam cracker for the Fischer-Tropsch route is compared with a methanol synthesis in combination with an rWGS reactor (scenarios 5 and 6) and a three-stage CO_2-tolerant methanol synthesis with intermediate product separation (scenarios 7 and 8). The assessment reveals that the PtL process, consisting of a PEM electrolysis, a Fischer-Tropsch reactor together with a preceding rWGS reaction, and a subsequent existing steam cracker is the most cost-effective solution with NPC for lower olefins of 14.92 € kg^{-1}. Nevertheless, the production costs are strongly dependent on the electricity costs required for hydrogen production and the electrolysis cell manufacturing costs. These effects are identified in the sensitivity analysis of NPC comparisons. The NPCs for the SOEC are the most economical one, if the future investment costs for high-temperature electrolysis and current electricity prices are considered in the assessment.

The techno-economic analysis in chapter 2 favors a process chain in which the rWGS reaction pre-converts CO_2 and H_2 into syngas. Given the low TRL of this reaction (TRL 6), experimental tests are conducted to verify the feasibility of an rWGS reactor. The hypothesis of handling the rWGS reaction in the simulation as a Gibbs reactor must be validated by executing appropriate experiments. The experimental setup comprises solely the analysis of a feed gas mixture of H_2 and CO_2 in a 3:1 ratio, as the feed composition for the downstream

Fischer-Tropsch synthesis approaches H_2:CO equal to 2.08:1. These experiments exclude the admixture of the recycle stream compounds produced in the PtL process for the first tests. The catalyst materials utilized are composed of a commercially available Ni/Al_2O_3 catalyst, two perovskite catalysts (perovskite oxides $Nd_{0.6}Ca_{0.4}Fe_{0.9}Co_{0.1}O_{3-\delta}$, developed by the Chair of Physical Chemistry at Montanuniversität Leoben), and the support material γ-Al_2O_3.

The Ni/Al_2O_3 catalyst follows almost the Gibbs reaction utilized in the ASPEN Plus flow sheet simulation, as CO_2 methanation occurs at low temperatures (550 to 750 °C and atmospheric pressure). With increasing pressure, methane formation experimentally increases and is detectable at 6 bara and up to 850 °C. Nevertheless, the production of methane is measured marginally less than predicted by the thermodynamic equilibrium. Higher GHSV values significantly impact the product composition with lower methane formation and higher CO proportion by applying the Ni/Al_2O_3 catalyst. This clearly indicated that CO formation is kinetically favored against methane formation. In addition to catalyzing the rWGS reaction in the higher temperature range of 750 - 950 °C, the Ni/Al_2O_3 catalyst also acts as a steam reforming catalyst in the experimental tests. This results in the conversion of methane in the feed gas stream into synthesis gas. The ability of the nickel catalyst to convert CH_4 is significant for the process design of a PtL plant, since recycle flows of downstream conversion (for example Fischer-Tropsch) may contain CH_4 which is reacted back to syngas in the rWGS. Consequently, the implementation of the Gibbs reactor anticipates the least efficient methane production scenario for the nickel-based catalyst in the PtL process. In contrast to the Ni/Al_2O_3 catalyst, the perovskite catalysts are active only for the rWGS reaction and suppress methane formation at atmospheric pressure and temperatures starting at 550 °C. Equilibrium is almost reached from 650 °C onward. With increasing pressure (higher than 3 bara), CO formation approaches equilibrium at 650 °C, with a low concentration of methane measurable in the product gas stream (< 2 vol.-% for 8 bara). However, the perovskite catalyst exhibits a negative effect on CO production when the GHSV increases. Within the experimental tests, the inactivity of the perovskite catalysts regarding steam reforming was identified. Consequently, additional process units with appropriate catalysts active for steam reforming are required to achieve a high process performance. Finally, the integration of a Gibbs reactor is for all catalysts permissible, with the distinction of no carbon and methane formation for the perovskite catalyst (treatment of carbon, CH_4 and any higher hydrocarbons as inert gases in the Gibbs reactor).

The results of the experimental investigation with the perovskite catalysts (section 3.3) are adopted in ASPEN Plus flow sheet simulations to investigate numerous performance indicators (product quantity, H_{2rec}:H_{2feed} ratio, carbon decomposition, PtL and carbon efficiency) of the entire PtL process chain. The objective is to get an indication, whether a Ni/Al_2O_3 or

perovskite catalyst is favorable in this PtL processes. The process setup consists of a rWGS reactor, a Fischer-Tropsch synthesis and the product separation. Since the perovskite catalyst suppresses methane formation in the experimental investigation even at low temperatures around 550 °C and increased pressure of around 8 bara, it is simulated as a Gibbs reactor, in which carbon and hydrocarbons (CH_4 and higher) are regarded as inert and are not converted or produced in the rWGS reactor. A detailed sensitivity analysis in chapter 4 shows that the utilization of the perovskite catalyst in the rWGS reactor in PtL process chain with Fischer-Tropsch synthesis result in higher efficiencies compared with the basic scenario, which uses a nickel-based catalyst. In the case of applying perovskite catalysts in the rWGS reactor, an additional steam reformer is mandatory to reconvert gaseous hydrocarbons produced in the Fischer-Tropsch synthesis to syngas. Furthermore, a CO_2 separation unit behind the rWGS reactor is required to supply purified syngas for the downstream Fischer-Tropsch reactor and there is also a necessity of an additional hydrogen separation unit downstream of the rWGS reactor to adjust the H_2:CO ratio in the Fischer-Tropsch feed gas. Both separated gases (CO_2 and H_2) are compressed and recycled upstream of the rWGS reactor.

In conclusion, the use of perovskite catalysts offers theoretical advantages. When comparing the Ni/Al_2O_3 and perovskite process routes 1 and 3 in case of an operating temperature of 950 °C and an S:C ratio of 4 in the reforming reactor, the PtL efficiency increased from 43.0 to 46.2 % for the PEM, and from 56.1 to 60.3 % for the SOEC technology. From the experimental assessment, the results demonstrate that the perovskite catalyst enables the rWGS reaction to occur at low temperatures (observed at 550 °C) and moderate pressures (studied up to 8 bara) without excessive methane production (< 2 vol.-%). This provides a significant benefit over commercially available Ni/Al_2O_3 catalysts, as lower reactor temperatures positively impact the engineering and design properties of the reactor equipment. Lower temperatures allow a higher opportunity of material selection, making it a decisive advantage. Reduced temperatures also result in lowered heat losses in the reactor system, consequently decreasing operating expenses and net production costs.

Finally, the research study is concluded by answering the research questions stated in the introduction.

1. *How should a PtL process for the production of polyolefins from cement plant off-gas be designed in order to obtain an optimal, efficient and cost-effective plant from a techno-economic point of view?*

   The techno-economic study in chapter 2 has shown that the process route consisting of an amine scrubbing for CO_2 separation, the production of hydrogen with a PEM electrolysis, a Fischer-Tropsch synthesis including product separation with an upstream rWGS reactor and the embedding of an existing steam cracker is the cost-optimized solution for polyolefin production and thus advantageous compared to the methanol synthesis with methanol-to-propylene unit.

2. *The hypothesis of implementing a Gibbs reactor in the flow sheet simulations must be confirmed by experimental tests. Is this assumption validated by the experimental investigation of nickel- and perovskite-based materials?*

   The use of a Gibbs reactor in the Aspen Plus flow sheet simulations is permissible and was confirmed by the experimental results. When using a nickel-based catalyst, the product gas composition is described very well by the Gibbs reactor. In the case of methane formation in the lower temperature range ($< 750\,°C$), the experimental results are marginally overestimated by the Gibbs reactor. The use of this reactor type therefore considers the worst-case scenario, namely that thermodynamic equilibrium is reached. In contrast to the nickel-based catalyst, methane formation is largely overestimated by the Gibbs reactor when applying the perovskite catalysts. At temperatures around 650 °C and a pressure of 8 bara, a methane content of less than 2 vol.% is determined in the experimental tests. A valuable finding was the inactivity of the perovskite catalyst with regard to steam reforming reactions during the experiments. Therefore, the implementation of the Gibbs reactor is permissible here, but with the restriction of carbon and methane formation and conversion (carbon, methane and higher hydrocarbons must be treated as inert components).

3. *Which influence has the perovskite catalyst compared to the nickel-based catalyst on the KPIs, in particular on the efficiencies in the overall process, and is it worthwhile to conduct further research in the field of perovskite catalyst materials?*

   The implementation of the behavior of a perovskite catalyst as a Gibbs reactor with restrictions in methane formation and conversion has shown that an additional process unit (steam reformer) needs to be incorporated into the process chain. This is caused by the limited activity with regard to steam reforming. Despite this additional unit, the efficiencies (PtL and carbon efficiency) and also the product quantity are higher compared to nickel-based catalyst. The employment of the perovskite catalyst favors the process performance, which shows PtL efficiency increases of up to 4.2 percentage-points and carbon efficiencies up to 1 percentage-points. Due to the lower operating temperature in the rWGS reactor, further development of these catalyst materials and the scale-up of the reactor design could cause far more efficient PtL process chains.

Chapter 6

Outlook on further investigations

The comparison of various PtL process chains with a Fischer-Tropsch synthesis reveals, that the implementation of a perovskite catalyst shows promising results for industrial and large-scale applications. The initial tests of the perovskite catalyst yielded in suppression of the methanation reaction at low temperatures and pressures up to 8 bara, limited to less than 2 vol.-% CH_4 (at 650 °C and 8 bara) in the product gas. In the operating scenario with perovskite catalysts, the reintegration of the recycled gas stream from the steam reformer and the behaviour of carbon formation in the rWGS reactor should be part of future investigation. A method needs to be developed to quantify carbon formation after each experiment to obtain a more accurate mass balance of the experiments.

Efforts to enhance the catalyst's properties, primarily its specific surface area, could handle the occurring problem with a decreasing CO formation with elevated GHSVs. Further research on augmenting the specific surface could be executed by the Chair of Physical Chemistry at Montanuniversität Leoben to achieve the highest possible CO concentration and thermodynamic equilibrium for all operation points and increased GHSVs. The research could on the one hand be extended by adding experimental tests with gas mixtures, adopted by the combination of feed and recycle gas compositions. On the other hand, there could be an increase of the reaction pressure up to 20 bara to obtain the product composition for these operating conditions and expand the range of applications. The influence of higher pressure on further side-reactions (e.g., formation of higher hydrocarbons such as C_2H_6, C_2H_4, C_3H_8, or C_3H_6) is still unclear in the experimental setup and requires further research.

Within the first experimental tests, methanation was detected as an undesired reaction when the feed gas mixture (CO_2 and H_2) was preheated using a heating pipe, where the material was catalytically active for the methanation reaction. To address this issue, an optimization of the experimental setup needs to be implemented to guarantee a separate heating zone and non-catalytic mixing of the gases prior to feeding them into the reactor. The change

of gas supply in separate lines and mixing shortly before entering the quartz glass reactor aims to enable improved preheating without pre-reactions and facilitates higher GHSV values in the system. Further adjustments in reactor design are necessary, if operating pressures of 20 bara should be reachable at elevated temperatures up to 650 °C for perovskite and up to 750 or 850 °C for nickel-based catalysts. At higher pressures, the reactor needs to be modified, as the quartz glass tube cannot handle a pressure difference (outer-inner tube side) of 20 bara anymore. Commercial stainless steel consisting of nickel-based materials, promotes methane formation and increases the methane content in the reactor. Catalysts such as the investigated perovskite material require unreactive reactor materials, otherwise, undesired side-reactions (e.g. methanation) could occur and distort the actual results. Thus, the focus should be on designing a reactor tube with a non-catalytic material or wall coating to suppress those side-reactions.

Considering the mentioned modifications in the experimental system and the continued advancement of the perovskite catalyst, the operating range could be expanded to 20 bara with the benefit of supplementary experiments. These findings can be reintegrated into ASPEN Plus simulations, with valuable knowledge for further process developments and comparisons. Higher operating pressures in the rWGS reactor could eliminate the need for intermediate compression between the rWGS and Fischer-Tropsch units, reducing the need for compressors to only compensate for pressure losses. The reduction of pressure levels could result in lower investment and operating costs, particularly in electricity costs. After conducting the technical evaluation with the newly developed process chain in ASPEN Plus, the net production costs could be recalculated using the investment and operating cost calculation. These results may reveal further performance improvements and raise more research questions, as well as offering initial decision-making options for scaling up to a pilot plant.

Chapter 7

Publications and dissemination

7.1 List of publications relevant for this thesis

Table 7.1: List of conference papers and the peer-reviewed manuscripts referred to in this study

Publication number	Title	Journal or conference	Citation
Publication 1	Evaluation of process structures and reactor technologies of an integrated power-to-liquid plant at a cement factory	*Peer-reviewed journal* Published in Journal of CO_2 Utilization	[23]
Publication 2	Comparison and techno-economic evaluation of process routes for lower olefin production via Fischer–Tropsch and methanol synthesis	*Peer-reviewed journal* Published in International Journal of Greenhouse Gas Control	[24]
Publication 3	Impact of the Operation Conditions on the Reverse-Water-Gas Shift Reaction	*Conference paper* EURECA Pro 2022	[25]
Publication 4	Process intensification of the rWGS reaction by perovskite-based catalyst	Submitted for review	

7.2 List of further publications

Table 7.2: List of further manuscripts published at conferences or in preparation for submission in a journal

Publication type	Title	Journal or conference	Citation
Article 1	C2PAT - Carbon to Product Austria	*Conference paper* 17. Symposium Energieinnovation 2022	[21]
Article 2	Evaluation and Comparison of the Conventional and Renewable-based Polyolefin Production based on Greenhouse Gas Reduction	*Conference paper* 17$^{\text{th}}$ Minisymposium Verfahrenstechnik, BOKU Wien, Vienna (2023)	[59]
Article 3	Kinetic model of the Guerbet coupling reaction	In progress	

7.3 Conference attendances and presentations

- 26.01.2022 – Energieforschungsgespräche Disentis 2022, Disentis, Swiss
- 16.02.2022 – 17. Symposium Energieinnovation, Graz, Austria
- 31.03.2022 – Fachgruppentreffen Energieverfahrenstechnik, Bamberg, Germany
- 20.04.2022 – 22. Österreichischer Klimatag, Poster presentation, Vienna, Austria
- 22.08.2022 – ACHEMA 2022, Frankfurt/Main, Germany
- 19.09.2022 – Chemietage 2022, TU Wien, Austria
- 11.04.2022 – 23. Österreichischer Klimatag, Poster presentation, Vienna, Austria
- 13.04.2023 – 17. Minisymposium und 8. Partikelforum, BOKU Wien, Austria
- 30.05.2023 – 15th Mediterranean Congress of Chemical Engineering, Barcelona, Spain

7.4 Co-supervised bachelor and master theses

- David Laimer. Simulation and evaluation of different methanol synthesis routes. Master thesis. Montanuniversität Leoben, 2021.
- Alexander Pichler. Entwicklungen und Einsatz der Hochtemperatur-Fischer-Tropsch-Synthese zur direkten Hydrierung von CO_2. Bachelor thesis. Montanuniversität Leoben, 2023.
- Willy Duan. Literature review of the sustainable alcohol-to-jet fuel process. Bachelor thesis. Montanuniversität Leoben, 2023.
- Marie Christin Böhm. Kinetik der Reverse-Water-Gas-Shift Reaktion. Bachelor thesis. Montanuniversität Leoben, 2023.
- Stefan Hinterberger. Direct-Air-Capture-Verfahren - Ist-Erhebung zum Stand der Technik und Techno-Economic-Analyse. Bachelor thesis. Montanuniversität Leoben,(2024).
- Dominik Schrotter. Experimentelle Untersuchung der reversen Wasser-Gas Shift Reaktion im Labormaßstab. Master thesis. Montanuniversität Leoben, in progress (2024).
- Stefan Eigenschink. Experimentelle Untersuchung von Perovskite Katalysatoren für den Einsatz in der reversen Wasser-Gas Shift Reaktion im Labormaßstab. Master thesis. Montanuniversität Leoben, in progress (2024).

References

[1] A. B. Smith. "U.S. Billion-dollar Weather and Climate Disasters, 1980 - present (NCEI Accession 0209268)." (2020).

[2] P. Friedlingstein, M. O'Sullivan, M. W. Jones, et al., "Global Carbon Budget 2022," *Earth System Science Data*, vol. 14, no. 11, pp. 4811–4900, 2022. DOI: 10.5194/essd-14-4811-2022.

[3] UNFCCC United Nations Framework Convention. "United Nations - Climate Change - Annual Report 2022." UNFCCC United Nations Framework Convention, Ed. (2023), [Online]. Available: https://unfccc.int/process-and-meetings/the-paris-agreement.

[4] Climate Action. "Übereinkommen von Paris." (2.02.2022), [Online]. Available: https://ec.europa.eu/clima/eu-action/international-action-climate-change/climate-negotiations/paris-agreement_de.

[5] Umweltbundesamt Environment Agency Austria, "Austria's National Inventory Report 2022," 2022. [Online]. Available: https://www.umweltbundesamt.at/fileadmin/site/publikationen/rep0811.pdf.

[6] VoestAlpine AG. "Greentec steel." VoestAlpine AG, Ed. (2023), [Online]. Available: https://www.voestalpine.com/greentecsteel/en/.

[7] G. Mauschitz. "Emissionen aus Anlagen der österreichischen Zementindustrie - Berichtsjahr 2021." (2022).

[8] S. Spaun, C. Bauer, C. Dankl, R. Friedle, and F. Papsch. "Roadmap zur CO_2-Neutralität der österreichischen Zementindustrie bis 2050." Vereinigung der Österreichischen Zementindustrie, Ed. (2022), [Online]. Available: https://www.zement.at/downloads/downloads_2022/Roadmap_VOEZ_bis_2050.pdf.

[9] G. Herz, C. Rix, E. Jacobasch, N. Müller, E. Reichelt, M. Jahn, and A. Michaelis, "Economic assessment of power-to-liquid processes – influence of electrolysis technology and operating conditions," *Applied Energy*, vol. 292, p. 116 655, 2021. DOI: 10.1016/j.apenergy.2021.116655.

[10] F. G. Albrecht, D. H. König, N. Baucks, and R.-U. Dietrich, "A standardized methodology for the techno-economic evaluation of alternative fuels – A case study," *Fuel*, vol. 194, pp. 511–526, 2017. DOI: 10.1016/j.fuel.2016.12.003.

[11] S. Schemme, J. L. Breuer, M. Köller, S. Meschede, F. Walman, R. C. Samsun, R. Peters, and D. Stolten, "H_2-based synthetic fuels: A techno-economic comparison of alcohol, ether and hydrocarbon production," *International Journal of Hydrogen Energy*, vol. 45, no. 8, pp. 5395–5414, 2020. DOI: 10.1016/j.ijhydene.2019.05.028.

[12] G. Zang, P. Sun, A. A. Elgowainy, A. Bafana, and M. Wang, "Performance and cost analysis of liquid fuel production from H_2 and CO_2 based on the Fischer-Tropsch process," *Journal of CO_2 Utilization*, vol. 46, p. 101 459, 2021. DOI: 10.1016/j.jcou.2021.101459.

[13] D. H. König, "Techno-ökonoonlinehe Prozessbewertung der Herstellung synthetischen Flugturbinentreibstoffes aus CO_2 und H_2," Dissertation, Universitätsbibliothek der Universität Stuttgart, Stuttgart, 2016. DOI: 10.18419/opus-9043.

[14] D. H. König, N. Baucks, R.-U. Dietrich, and A. Wörner, "Simulation and evaluation of a process concept for the generation of synthetic fuel from CO_2 and H_2," *Energy*, vol. 91, pp. 833–841, 2015. DOI: 10.1016/j.energy.2015.08.099.

[15] S. Adelung and R.-U. Dietrich, "Impact of the reverse water-gas shift operating conditions on the Power-to-Liquid fuel production cost," *Fuel*, vol. 317, p. 123 440, 2022. DOI: 10.1016/j.fuel.2022.123440.

[16] S. Adelung, S. Maier, and R.-U. Dietrich, "Impact of the reverse water-gas shift operating conditions on the Power-to-Liquid process efficiency," *Sustainable Energy Technologies and Assessments*, vol. 43, p. 100 897, 2021. DOI: 10.1016/j.seta.2020.100897.

[17] B. Anicic, P. Trop, and D. Goricanec, "Comparison between two methods of methanol production from carbon dioxide," *Energy*, vol. 77, pp. 279–289, 2014. DOI: 10.1016/j.energy.2014.09.069.

[18] M. Rothaemel, M. Gorny, and S. Haag. "Methanol-to-Propylene (MTP®): A proven technology for on-purpose propylene production." (2016).

[19] S. Ghosh, V. Uday, A. Giri, and S. Srinivas, "Biogas to methanol: A comparison of conversion processes involving direct carbon dioxide hydrogenation and via reverse water gas shift reaction," *Journal of Cleaner Production*, vol. 217, pp. 615–626, 2019. DOI: 10.1016/j.jclepro.2019.01.171.

[20] O.-S. Joo, K.-D. Jung, I. Moon, A. Y. Rozovskii, G. I. Lin, S.-H. Han, and S.-J. Uhm, "Carbon Dioxide Hydrogenation To Form Methanol via a Reverse-Water-Gas-Shift Reaction (the CAMERE Process)," *Industrial & Engineering Chemistry Research*, vol. 38, no. 5, pp. 1808–1812, 1999. DOI: 10.1021/ie9806848.

[21] C. Markowitsch, M. Lehner, J. Kitzweger, W. Haider, S. Ivanovici, M. Unfried, and M. Maly. "[Conference EnInnov 2022 TU Graz] C2PAT - Carbon to Product Austria." 17. Symposium Energieinnovation - EnInnov 2022, Ed. (2022), [Online]. Available: https://www.tugraz.at/fileadmin/user_upload/tugrazExternal/738639ca-39a0-4129-b0f0-38b384c12b57/files/lf/Session_D6/464_LF_Markowitsch.pdf.

[22] Aspen Technology Inc. "ASPEN Plus V12.1." (2023), [Online]. Available: https://www.aspentech.com/en/.

[23] C. Markowitsch, M. Lehner, and M. Maly, "Evaluation of process structures and reactor technologies of an integrated power-to-liquid plant at a cement factory," *Journal of CO_2 Utilization*, vol. 70, p. 102 449, 2023. DOI: 10.1016/j.jcou.2023.102449.

[24] C. Markowitsch, M. Lehner, and M. Maly, "Comparison and techno-economic evaluation of process routes for lower olefin production via Fischer–Tropsch and methanol synthesis," *International Journal of Greenhouse Gas Control*, vol. 129, p. 103 985, 2023. DOI: 10.1016/j.ijggc.2023.103985.

[25] C. Markowitsch and M. Lehner, "Impact of the Operation Conditions on the Reverse-Water-Gas Shift Reaction," in *Global Challenges for a Sustainable Society*, ser. Springer Proceedings in Earth and Environmental Sciences, J. A. Benítez-Andrades, P. García-Llamas, Á. Taboada, L. Estévez-Mauriz, and R. Baelo, Eds., Cham: Springer International Publishing and Imprint Springer, 2023, pp. 66–76, ISBN: 978-3-031-25839-8.

[26] A. Dubey and A. Arora, "Advancements in carbon capture technologies: A review," *Journal of Cleaner Production*, vol. 373, p. 133 932, 2022. DOI: 10.1016/j.jclepro.2022.133932.

[27] R. Sakwattanapong, A. Aroonwilas, and A. Veawab, "Behavior of Reboiler Heat Duty for CO_2 Capture Plants Using Regenerable Single and Blended Alkanolamines," *Industrial & Engineering Chemistry Research*, vol. 44, no. 12, pp. 4465–4473, 2005. DOI: 10.1021/ie050063w.

[28] S. Zhou, S. Wang, C. Sun, and C. Chen, "SO_2 effect on degradation of MEA and some other amines," *Energy Procedia*, vol. 37, pp. 896–904, 2013. DOI: 10.1016/j.egypro.2013.05.184.

[29] G. T. Rochelle, "Thermal degradation of amines for CO_2 capture," *Current Opinion in Chemical Engineering*, vol. 1, no. 2, pp. 183–190, 2012. DOI: 10.1016/j.coche.2012.02.004.

[30] S. Vaz, Rodrigues de Souza, Ana Paula, and B. E. Lobo Baeta, "Technologies for carbon dioxide capture: A review applied to energy sectors," *Cleaner Engineering and Technology*, vol. 8, p. 100 456, 2022. DOI: 10.1016/j.clet.2022.100456.

[31] M. Katebah, M. Al-Rawashdeh, and P. Linke, "Analysis of hydrogen production costs in Steam-Methane Reforming considering integration with electrolysis and CO2 capture," *Cleaner Engineering and Technology*, vol. 10, p. 100 552, 2022. DOI: 10.1016/j.clet.2022.100552.

[32] A. Trattner, M. Höglinger, M.-.-G. Macherhammer, and M. Sartory, "Renewable Hydrogen: Modular Concepts from Production over Storage to the Consumer," *Chemie Ingenieur Technik*, vol. 93, no. 4, pp. 706–716, 2021. DOI: 10.1002/cite.202000197.

[33] W. J. Tiktak, "Heat Management of PEM Electrolysis," Master thesis, Delft University of Technology, Amsterdam, Netherlands, 2019. [Online]. Available: https://www.dynamictidalpower.eu/resources/Documenten/ThesisRepository-PEM-TUdelft.pdf.

[34] J. Allen, S. Panquet, and A. Bastiani, "Electrochemical Ammonia: Power to Ammonia Ratio and Balance of Plant Requirements for Two Different Electrolysis Approaches," *Frontiers in Chemical Engineering*, vol. 3, p. 67, 2021. DOI: 10.3389/fceng.2021.765457.

[35] S. T. Wismann, J. S. Engbæk, S. B. Vendelbo, F. B. Bendixen, W. L. Eriksen, K. Aasberg-Petersen, C. Frandsen, I. Chorkendorff, and P. M. Mortensen, "Electrified methane reforming: A compact approach to greener industrial hydrogen production," *Science (New York, N.Y.)*, vol. 364, no. 6442, pp. 756–759, 2019. DOI: 10.1126/science.aaw8775.

[36] P. Chiesa, "15 - Advanced technologies for syngas and hydrogen (H_2) production from fossil-fuel feedstocks in power plants," in *Advanced power plant materials, design and technology*, ser. Woodhead Publishing series in energy, D. Roddy, Ed., Boca Raton, Fla. and Oxford: CRC Press and Woodhead Publ, 2010, pp. 383–411, ISBN: 978-1-84569-515-6. DOI: 10.1533/9781845699468.3.383.

[37] Haldor Topsoe. "eRWGS™: New technology essential for electrofuels production." (2022), [Online]. Available: https://www.topsoe.com/products/equipment/e-rwgs.

[38] D. Förtsch, K. Pabst, and E. Groß-Hardt, "The product distribution in Fischer–Tropsch synthesis: An extension of the ASF model to describe common deviations," *Chemical Engineering Science*, vol. 138, pp. 333–346, 2015. DOI: 10.1016/j.ces.2015.07.005.

[39] A. de Klerk, *Fischer–Tropsch Refining*, 1. ed. Hoboken, NJ and Weinheim: Wiley, 2011, ISBN: 9783527635603. DOI: 10.1002/9783527635603.

[40] M. Ostadi, E. Rytter, and M. Hillestad, "Evaluation of kinetic models for Fischer–Tropsch cobalt catalysts in a plug flow reactor," *Chemical Engineering Research and Design*, vol. 114, pp. 236–246, 2016. DOI: 10.1016/j.cherd.2016.08.026.

[41] A. Karaba, J. Rozhon, J. Patera, J. Hájek, and P. Zámostný, "Fischer–Tropsch Wax from Renewable Resources as an Excellent Feedstock for the Steam–Cracking Process," *Chemical Engineering & Technology*, vol. 44, no. 2, pp. 329–338, 2021. DOI: 10.1002/ceat.202000400.

[42] International Energy Agency. "Simplified levelised cost of petrochemicals for selected feedstocks and regions, 2017." (2022).

[43] F. Bisotti, M. Fedeli, K. Prifti, A. Galeazzi, A. Dell'Angelo, M. Barbieri, C. Pirola, G. Bozzano, and F. Manenti, "Century of Technology Trends in Methanol Synthesis: Any Need for Kinetics Refitting?" *Industrial & Engineering Chemistry Research*, vol. 60, no. 44, pp. 16 032–16 053, 2021. DOI: 10.1021/acs.iecr.1c02877.

[44] K. Bussche and G. F. Froment, "A Steady-State Kinetic Model for Methanol Synthesis and the Water Gas Shift Reaction on a Commercial $Cu/ZnO/Al_2O_3$ Catalyst," *Journal of Catalysis*, vol. 161, no. 1, pp. 1–10, 1996. DOI: 10.1006/jcat.1996.0156.

[45] T. Oelmann, T. Schuhmann, C. Drosdzol, S. Haag, and F. Castillo-Welter, "A New Reactor Concept for Conversion of CO_2 to Methanol (AirLiquide)," 2020. [Online]. Available: https://www.i3upgrade.eu/files/2022/01/dgmk-2020-a-new-reactor-concept-for-conversion-of-co2-to-methanol.pdf.

[46] T. A. Adams II, T. Thatho, M. C. Le Feuvre, and C. L. E. Swartz, "The Optimal Design of a Distillation System for the Flexible Polygeneration of Dimethyl Ether and Methanol Under Uncertainty," *Frontiers in Energy Research*, vol. 6, p. 41, 2018. DOI: 10.3389/fenrg.2018.00041.

[47] International Methanol Producers & Consumers Association. "IMPCA Methanol Reference Specifications." (8.12.2015), [Online]. Available: https://www.methanol.org/wp-content/uploads/2016/07/IMPCA-Ref-Spec-08-December-2015.pdf.

[48] M. S. Peters, K. D. Timmerhaus, and R. E. West, *Plant design and economics for chemical engineers* (McGraw-Hill chemical engineering series), 5. ed, international ed. 2004. Boston: McGraw-Hill, 2004, ISBN: 0071240446.

[49] Towering Skills LLC, Ed. "Cost Indices – Towering Skills." (2022), [Online]. Available: https://www.toweringskills.com/financial-analysis/cost-indices/#cepci-2001-to-present.

[50] Energie-Control Austria für die Regulierung der Elektrizitäts- und Erdgaswirtschaft. "Aktueller Marktpreis gemäß § 41 Ökostromgesetz." (13.10.2022), [Online]. Available: https://www.e-control.at/industrie/oeko-energie/oekostrommarkt/marktpreise-gem-paragraph-20.

[51] Hof am Leithaberge. "Hof am Leithaberge - Wasserbezugsgebühr." (13.01.2022), [Online]. Available: http://www.hof-leithaberge.gv.at/Wasserbezugsgebuehr.

[52] J. LinSean and M. Kelly, "High aspect ratio catalytic reactor and catalyst inserts therefor," US9938146B2, 2015. [Online]. Available: https://patents.google.com/patent/US9938146B2/en.

[53] S. M. Chun, D. H. Shin, S. H. Ma, G. W. Yang, and Y. C. Hong, "CO_2 Microwave Plasma—Catalytic Reactor for Efficient Reforming of Methane to Syngas.," *Catalysts*, vol. 9, no. 6, p. 543, 2019. DOI: 10.3390/catal9060543.

[54] L. Lindenthal, J. Popovic, R. Rameshan, J. Huber, F. Schrenk, T. Ruh, A. Nenning, S. Löffler, A. K. Opitz, and C. Rameshan, "Novel perovskite catalysts for CO_2 utilization - Exsolution enhanced reverse water-gas shift activity," *Applied Catalysis B: Environmental*, vol. 292, p. 120 183, 2021. DOI: 10.1016/j.apcatb.2021.120183.

[55] L. Lindenthal, T. Ruh, R. Rameshan, H. Summerer, A. Nenning, C. Herzig, S. Löffler, A. Limbeck, A. K. Opitz, P. Blaha, and C. Rameshan, "Ca-doped rare earth perovskite materials for tailored exsolution of metal nanoparticles," *Acta Crystallographica Section B: Structural Science, Crystal Engineering and Materials*, vol. 76, no. Pt 6, pp. 1055–1070, 2020. DOI: 10.1107/S2052520620013475.

[56] J. Popovic, L. Lindenthal, R. Rameshan, T. Ruh, A. Nenning, S. Löffler, A. K. Opitz, and C. Rameshan, "High Temperature Water Gas Shift Reactivity of Novel Perovskite Catalysts," *Catalysts*, vol. 10, no. 5, p. 582, 2020. DOI: 10.3390/catal10050582.

[57] L. García, "4 - Hydrogen production by steam reforming of natural gas and other nonrenewable feedstocks," in *Compendium of Hydrogen Energy : Woodhead Publishing Series in Energy*, V. Subramani, A. Basile, and T. N. Veziroğlu, Eds., Oxford: Woodhead Publishing, 2015, pp. 83–107, ISBN: 978-1-78242-361-4. DOI: 10.1016/B978-1-78242-361-4.00004-2.

[58] X. Xu, J. Wang, A. Zhou, S. Dong, K. Shi, B. Li, J. Han, and D. O'Hare, "High-efficiency CO_2 separation using hybrid LDH-polymer membranes," *Nature Communications*, vol. 12, no. 1, p. 3069, 2021. DOI: 10.1038/s41467-021-23121-z.

[59] C. Markowitsch, M. Lehner, J. Kitzweger, W. Haider, S. Ivanovici, M. Unfried, and M. Maly. "Evaluation and Comparison of the Conventional and Renewable-based Polyolefin Production based on Greenhouse Gas Reduction." BOKU Wien, Ed. (2023).

Publication I

Evaluation of process structures and reactor technologies of an integrated power-to-liquid plant at a cement factory

Christoph Markowitsch, Markus Lehner, Markus Maly

Journal of CO_2 Utilization (2023)
Volume 70, P. 102449
DOI: 10.1016/j.jcou.2023.102449

Conception and planning	Simulation	Analysis and interpretation	Manuscript preparation
90%	100%	90%	100%

Journal of CO2 Utilization 70 (2023) 102449

Contents lists available at ScienceDirect

Journal of CO2 Utilization

journal homepage: www.elsevier.com/locate/jcou

Evaluation of process structures and reactor technologies of an integrated power-to-liquid plant at a cement factory

Christoph Markowitsch [a,*], Markus Lehner [a], Markus Maly [b]

[a] Chair of Process Technology and Environmental Protection, Montanuniversitaet Leoben, Franz-Josef-Str. 18, A-8700 Leoben, Austria
[b] OMV Downstream GmbH, Trabrennstrasse 6-8, A-1020 Vienna, Austria

ARTICLE INFO

Keywords:
Power-to-Liquid (PtL)
Reverse water-gas shift (rWGS)
PEM & SOEC
Fischer-Tropsch synthesis
Techno-economic evaluation

ABSTRACT

A novel carbon capture and utilization (CCU) process is described in which process-related carbon dioxide is captured from cement plant exhaust gas (10,000 tons/year) and converted with green hydrogen in a Fischer Tropsch synthesis to liquid, mainly paraffinic hydrocarbons (syncrude, approx. 3000 tons/year) which is finally processed to polyolefins. This CCU process chain is simulated with the software package ASPEN Plus V12.1®. In a first step, the influence of hydrogen production technology, such as PEM and SOEC, and reverse water-gas shift reactor (rWGS) technology (electrified and autothermal design) on plant specific efficiencies (Power-to-Liquid PtL, carbon conversion), product volumes, and investment, operating and net production costs (NPC) is investigated. Furthermore, process routes reducing the CO_2 content in the Fischer Tropsch feed gas are elaborated, implementing a CO_2 separation unit, or recycle streams back to the rWGS reactor. Unexpectedly, CO_2 capture and recycle streams back to the rWGS show no significant impact on the performance of each process scenario, particularly in terms of the product quantity. However, lower PtL efficiencies and higher NPC are noticeable for these cases. The techno-economic assessment reveals that the use of a SOEC and an electrified rWGS reactor offers the technologically best and economically most optimized process chain with NPC of 8.40 EUR/$kg_{syncrude}$, a PtL efficiency of 54% and a carbon conversion of 85%.

1. Introduction

1.1. Motivation

Triggered by the Paris Agreement, a step-by-step plan must be fulfilled in the European Union in order not to exceed the maximum prescribed increase in global warming of 1.5 °C. In the case of Austria, tightened climate targets envisage a reduction in greenhouse gas emissions of 40% by 2030 compared to the reference year 1990. Austria should reach climate-neutrality by 2040 [1]. The Austrian cement industry emitted about 9% of the country's ETS-certified carbon dioxide emissions and almost 3.3% of total national greenhouse gas emissions in 2019. Total CO_2 emissions from Austria's cement plants reached nearly 3 million tons of CO_2 in 2020. Potential savings in CO_2 emissions from cement production can be achieved by further optimizing processes in clinker production, covering fuel demand with low carbon sources, using green electricity in the entire production process and switching to carbon-neutral transportation routes [2]. However, about two-thirds of the carbon dioxide emitted originates from the calcination of calcium carbonate, and only one-third from fuel combustion [3]. The increase in

Abbreviations: APEA, Aspen Process Economic Analyzer V12; CAPEX, Capital Expenditures [EUR]; CCU, Carbon Capture and Utilization; e-RWGS, electrified reveres Water-Gas Shift; ETS, European Trading System; EUR, Euro; FTS, Fischer-Tropsch Synthesis; IC, Intermediate Costs; ISBL, Inside Battery Limit; KPI, Key Performance Indicator; LHV, Lower Heating Value [kWh/kg]; LTFT, Low temperature Fischer-Tropsch Synthesis; MEA, Monoethanolamin; MEUR, Million Euro; NPC, Net production costs [EUR/$kg_{syncrude}$]; NPC_{ch}, Net production costs [EUR/kg_{ch}]; OPEX, Operational Expenditures [EUR/year]; OSBL, Outside Battery Limit; PE, Polyethylene; PEM, Proton Exchange Membrane Electrolysis; PP, Polypropylene; PtL, Power to Liquid; R, Chilton Factor; ROI, Return On Investment; rWGS, reverse Water-Gas Shift; S, Selectivity [-]; SEC, Specific Energy Consumption [kWh/kg]; SMR, Steam Methane Reformer; SOEC, Solid Oxide Electrolysis; TIC, Total Investment Costs [EUR]; X, Conversion [-]; ηPtL, Power-to-Liquid Efficiency [-]; η_{Carbon}, Carbon Conversion [-]; $\dot{m}_{i/total}$, Mass flow of component I / total [kg/h]; $\dot{m}_{syncrude}$, Mass flow of syncrude [kg/h]; $\dot{n}_{i/total}$, Molar flow of component I / total [kmol/h]; P_{el}, Electric Power of Electrolysis [kW]; P_{ut}, Electric Power of Utilities [kW].

* Corresponding author.
E-mail address: christoph.markowitsch@unileoben.ac.at (C. Markowitsch).

https://doi.org/10.1016/j.jcou.2023.102449
Received 1 December 2022; Received in revised form 9 February 2023; Accepted 27 February 2023
Available online 1 March 2023

CO_2 prices (ramped up from 26 EUR/t_{CO2} at the beginning of 2020–80 EUR/t_{CO2} by start of 2022) and the recent decision to introduce a CO_2 tax (30 EUR/t_{CO2} in 2022, as envisaged in Austrian law "ÖkoStRefG 2022 Teil I") have raised the economic pressure further [4]. The use of carbon capture and utilization plants in cement production could reduce 1771 kt of clinker production-related CO_2 emissions [5]. One possible utilization option is the conversion of the emitted CO_2 into plastics. Globally, plastic consumption increased from 1.5 billion tons in 1950–359 billion tons in 2018 [6], of which polypropylene (PP) comprised 17 wt.-%, and polyethylene (PE) 28 wt.-%. These polyolefins are mainly used in the packaging and bottle-production industries [7]. Currently, fossil feedstock such as crude oil are partially converted into naphtha and further processed into PP and PE. The use of carbon dioxide as a renewable based feedstock for polyolefins production is unique in combination with a cement plant and is addressed in detail in this study. A pilot plant for syncrude production should be planned for a cement plant in order to obtain practical experience with the process of producing renewable plastics from CO_2. Since the synergies of an existing refinery are to be utilized, the polyolefin production via FTS is considered in this study, since the post-processing of the syncrude can be performed in the existing steam crackers. The potential process route to methanol and further to olefins is not feasible in this case, since a methanol-to-olefin plant is not available and is also not appropriate in pilot plant size.

Many studies deal with the simulation and economical assessment of a PtL plant producing electrified fuels (e-fuels) from CO_2 and hydrogen [8–12]. All these studies include a reverse water-gas shift reactor (rWGS), producing in a first step synthesis gas (a mixture of H_2 and CO), which is downstream converted in a Fischer Tropsch synthesis to syncrude and upgraded to jet fuel or diesel. Adelung et al. simplifies the carbon capture process by implementing a pseudo amine-based carbon capture unit with a thermal energy demand of 3.8 MJ/kg CO_2 and an electrical energy demand of 0.14 MJ_{el}/kg CO_2. Hydrogen production is based on one technology, namely the low temperature PEM electrolysis with an efficiency variation from 60% to 70%, as well as only one rWGS reactor technology (combustion of recycle gas) is simulated in their study [11]. Albrecht et al. considers different CO_2 sources from biomass and fossil origin, but also included only the low temperature PEM electrolysis for hydrogen production in the simulation and economic evaluation [10]. In a preliminary study by Markowitsch et al. [13], the recycle streams of the Fischer-Tropsch synthesis (FTS) purge gas and factors affecting catalyst selection were investigated systematically. It was shown that the variation of the gas recycle streams, one back to the rWGS-, and the second back to the FTS reactor, has an impact on process efficiencies. The best performance is achieved with a complete gas recycle stream back to the rWGS reactor. In addition, CO conversion and CH_4 selectivity play important roles in achieving high efficiencies.

Beyond these previous studies, in this work the impact of different process configurations which vary the CO_2 content in the feed gas to the Fischer Tropsch synthesis, as well as various technological options for the rWGS reactor and the electrolysis are systematically investigated for the first time. A reference Process Setup is defined in chapter 2 and therefrom, four fully heat integrated PtL process chains are defined as independent simulation cases to capture 10,000 tons of CO_2 annually. In each of these four PtL process chains, two different types of electrolysis (low- and high-temperature, with an electrical demand of 10.7 and 7.0 MW, respectively) and two different rWGS reactor technologies (electrified and autothermal design), respectively, are integrated, and the effect on the overall performance is examined. For this purpose, key performance indicators (KPIs, defined in chapter 3), such as the PtL efficiency and carbon conversion, the specific energy consumption as well as the total product quantity and investment, operation and net production costs are calculated. Finally, a comparison of the different Process Setups and reactor/electrolysis technologies is done, and an optimum PtL process chain is determined based on technological and economical considerations.

In conclusion, this study aims to compare the investigated process routes to form the basis for a decision on the overall process design and proper selection of operation conditions as well as available technological options.

2. Detailed process description

A basic process concept for a pilot plant is created with the aim of providing an experimental platform for further research on a complete PtL process chain. The data obtained and general experience shall be used for the preparation of the basic engineering for a full-scale, industrial plant. Fig. 1 shows a block-flow diagram of the PtL process. Captured carbon dioxide from cement plant flue gases is used as feedstock for a multi-step catalytic conversion to renewable polyolefins.

In a first step, CO_2 is separated from the cement plant exhaust gas with an amine scrubber unit. In order to catalytically convert CO_2, green hydrogen is produced as reaction partner in an electrolysis unit powered by renewable electricity from the grid. The green hydrogen and CO_2 are converted in a reverse water-gas shift reactor to synthesis gas (syngas). Syngas is used as feedstock in the subsequent Fischer-Tropsch synthesis. In a low temperature FTS reactor, the syngas usually reacts to predominantly long chain paraffinic hydrocarbons. The FTS product, also called syncrude, is separated downstream into three fractions: naphtha, middle distillate, and wax. These products are transported separately to a nearby refinery, where these fractions are further treated in appropriate steam crackers, and the produced ethylene and propylene are integrated into the existing polyolefin production process.

The simulation starts with the separation of CO_2 from cement exhaust gas and ends with the synthesis product separation downstream of the Fischer-Tropsch reactor, since the downstream process units steam cracker and polymerization are already existing installations in the refinery. In this chapter, the main equipment used for the comparison is described and the simulation assumptions are explained. In general, four different structures of such a PtL plant are used for comparison purposes (Fig. 2). The basic process consists of an amine scrubber, an electrolysis for hydrogen production, a Fischer-Tropsch synthesis with upstream reverse water-gas shift reactor, and the product separation unit (Process Setup 1). According to the findings of Markowitsch et al., the gas stream from the product separation unit is recycled upstream of the rWGS reactor. There is no recycle stream around the Fischer-Tropsch reactor [13]. The basic process (Process Setup 1) is shown in Fig. 2 and Fig. 4. Due to the fact that CO_2 is treated as inert gas in the FTS, the influence of CO_2 separation downstream of the rWGS reactor is investigated in Process Setup 2. A generic carbon capture unit is implemented behind the water condensation flash drum with an assumed capture efficiency of 95%. In the third Process Setup an internal recycle stream for part of the rWGS product gas (34 mol-%) back to the CO_2 feed gas stream is realized, as first proposed by Elsernagawy et al. [14]. For saving an additional compressor, the rWGS recycle gas is expanded, mixed with the concentrated CO_2 from the carbon capture unit and compressed again to operating pressure by the existing CO_2-compressor. (Process Setup 3). Finally, the fourth option is an internal recycle stream (34 mol-%) around the rWGS reactor, whereby an additional compressor compensates the pressure difference (Process Setup 4) [14].

In addition to the modification of the process structure in the four scenarios as shown in Fig. 2, the second part of the study investigates the impact of different rWGS reactor and electrolysis technologies. The heat demand of the rWGS reactor can be covered by electricity (electrified rWGS, colored violet) or by the combustion of hydrogen (autothermal rWGS reactor, colored blue in Fig. 2) [15,16]. The autothermal reactor is designed as an in-situ combustion to supply heat for the rWGS reaction. The burner is fed with additional hydrogen and oxygen, which is fired in a combustion chamber and the reaction takes place in the catalyst section. The reaction gas is fed into the reactor via a side inlet and reacts in the catalyst bed to synthesis gas [17]. Wismann et al. describe an

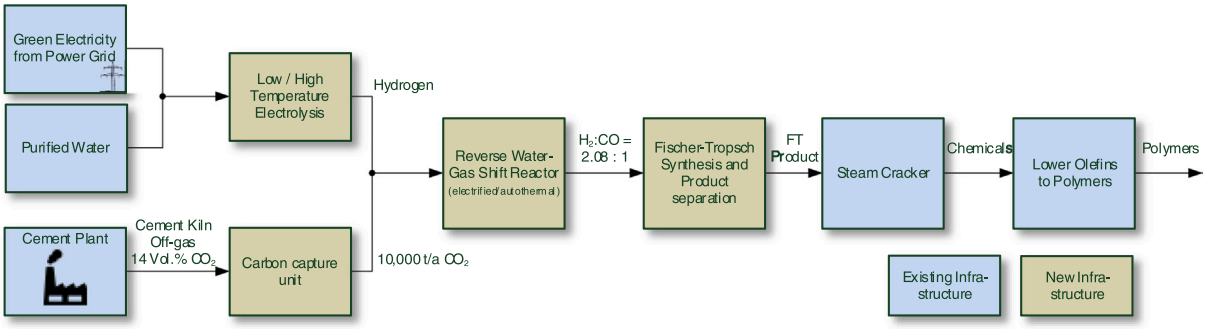

Fig. 1. Block-flow diagram to produce polypropylene and polyethylene from a cement plant off-gas.

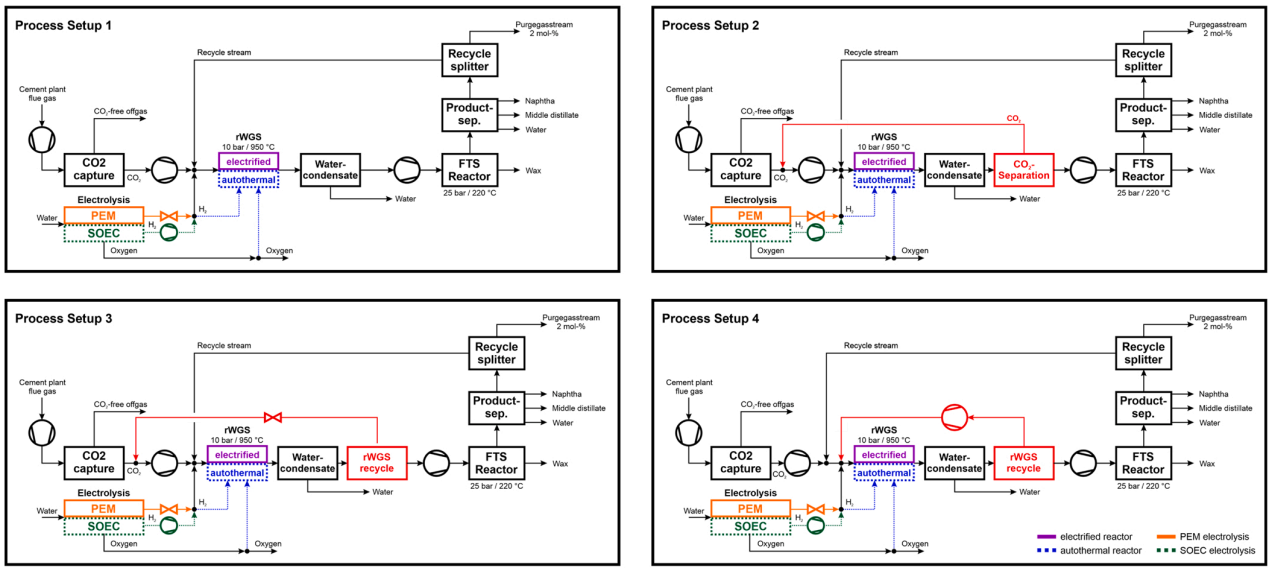

Fig. 2. Process Setup 1: Basic structure of the PtL process; Process Setup 2: Implementation of a CO_2-separation unit downstream of the rWGS reactor; Process Setup 3: Recycle stream around the rWGS reactor with pressure reduction; Process Setup 4: compressed recycle around the rWGS reactor.

electrically heated steam methane reforming reactor. It is assumed that this technology can also be applied to the rWGS reactor [15]. Chiesa et al. reported on the other option the use of an autothermal reactor in which additionally generated green hydrogen is fired to cover the heat demand [16]. In terms of hydrogen production by electrolysis, an additional technology comparison is carried out between a low temperature electrolysis (PEM, colored orange) and high temperature electrolysis (SOEC, colored green in Fig. 2) [18]. All combinations of process chains and equipment options result in 16 individual cases, which are compared in this study.

2.1. Amine scrubber unit

The exhaust gas from the cement plant has a composition of 14 vol.-% CO_2, 64 vol.-% N_2, 12 vol.-% H_2O and 10 vol.-% O_2 and a total volume flow of 1.41 Nm^3 /s. Impurities such as SO_x, NO_x, Hg can also be present in small concentrations due to the cement production process, depending on the raw material and fuel used, as well as the operating conditions [3]. A pre-treatment unit has to be installed to reduce the concentrations of these components in order to protect the amine solvent from degradation. However, the pretreatment unit is not integrated into the simulation as it does not influence the product yields of this study. Taking the equipment costs of bed guards of Albrecht et al. into consideration, these units have no significant impact on the total investment costs [10]. The hot exhaust gas is extracted from the stack at atmospheric pressure and compressed by a blower. The gas outlet temperature is close to 110 °C, and in the pre-wash system, cooling and dust removal takes place. Only water is used in the prewasher tower due to the assumption of pretreated and SO_x free off gas. The carbon capture unit is simulated as an amine scrubber, using a 30 wt.-% monoethanolamin (MEA) solution as solvent. The entrance to the packed absorber tower is at the bottom, where the gas stream enters at a temperature of 40 °C and pressure of 0.4 barg. The solvent is injected at the top and trickles down countercurrently to the gas stream. The CO_2 dissolves in the solvent and the lean gas leaves the absorber tower at the top. At the bottom, the rich solvent is removed, heated, and fed to the desorber tower. In the desorber tower, a reboiler is installed to balance the required heat for CO_2 release of about 3.8 MJ/kg_{CO2} (e.g., using steam from the cooling system of the Fischer-Tropsch reactor) [19]. By rising the temperature, CO_2 and water (steam) desorb from the loaded MEA solvent. The steam is condensed to achieve a purity of more than 95 wt.-% CO_2 in the product stream. To maintain a closed loop, the lean absorbent is fed back into the absorber tower. Possible degradation of the amine solvent is not considered in the simulation. Degradation would lead to additional amine consumption and subsequently to higher operational costs. The complete range of contaminants in cement plant off-gas are unknown. However, previous cleaning units protect the sorbent from sulfur (CuO and NiO guard beds) and guarantee a long life

time [20,21]. Therefore, this simplification is justified.

2.2. Hydrogen production

Green hydrogen is used as reaction partner to produce synthesis gas and the associated activation of CO_2. Green hydrogen production technology can be divided in two main categories – low- and high-temperature electrolysis. Both types require very pure water as feed. However, a water treatment plant is not included in the simulation because it would be the same for both technologies. In an electrolysis, the fed water is split into its main components, hydrogen and oxygen, by a strongly endothermic reaction (Eq. 1).

$$H_2O_{(aq)} \rightarrow H_{2,(g)} + \frac{1}{2}O_{2,(g)} \quad \Delta H_r^{298K} = +286\,kJ \Big/ mol \tag{1}$$

A major advantage of high temperature electrolysis, which operates at temperatures between 700 and 1000 °C and atmospheric pressure, is that part of the reaction enthalpy required is covered by the heat supply (in the form of steam). Consequently, the electrical energy demand is lower, while the PtL efficiency is significantly improved [18]. To increase the pressure of the hydrogen stream to the operating conditions of the rWGS reactor (10 bar (g)), an additional compressor must be applied downstream the SOEC unit, in contrast to PEM electrolysis. However, PEM electrolysis requires cooling facilities, which is unfavorable in terms of energy efficiency, as these may require up to 17% of total electrical energy demand [22]. In the simulation, the specific energy demand for the production of green hydrogen is assumed to 4.7 kWh/Nm^3 H_2 for PEM electrolysis, and 3.6 kWh/Nm^3 H_2 for SOEC [18,23]. Green hydrogen forces the use of renewable energy by definition. The simulation of the electrolysis is performed as a stoichiometric reactor with an assumed total conversion efficiency of 95% of the water feed [24]. Water is pre-heated to 75 °C in case of PEM and steam is produced in case of SOEC (according to the feed specifications of technology provider "Sunfire" [23]). It is assumed that the SOEC has an internal heat integration for high temperature heat, and only the electrical system energy consumption (3.6 kWh/Nm^3 H_2) needs to be provided externally. The output flows of the SOEC (H_2 and O_2-air mixture) are estimated at a temperature of 160 °C (same as input temperature).

2.3. Syngas production

As mentioned earlier, some authors have discussed the simulation and operation conditions of the rWGS reaction. Whereas Adelung et al. and König aimed to design a PtL process with high efficiencies and product yields in kerosene production, the operation conditions of Markowitsch et al. have been chosen in order to maximize syncrude product quantity [8,11,13]. The rWGS reaction (Eq. 2) is due to the high operating temperatures not kinetically, but thermodynamically limited [25,26].

$$CO_2 + H_2 \leftrightarrow CO + H_2O \quad \Delta H_r^{298K} = +41\,kJ/mol \tag{2}$$

Therefore, it is a reasonable assumption to treat the rWGS reaction in the simulation as Gibbs reactor, whereas CO, CO_2, CH_4, H_2, H_2O, $C_{(S)}$ and higher hydrocarbons ($C_2 - C_{30}$) are defined as occurring species. The Gibbs reactor calculates the product composition by minimizing the level of Gibbs-free energy for an H_2:CO_2 ratio of 3:1 (Fig. 3) [27]. This thermodynamic analysis was carried out without taking into account possible recycle streams (e.g. FT recycle). When considering the thermodynamic equilibrium of the rWGS reaction (Eq. 2), steam reforming (Eq. 3), dry reforming (Eq. 4), the Bosch reaction (Eq. 5) and Boudouard equilibrium (Eq. 6) are potential side reactions within the rWGS reactor. The operating conditions of the rWGS reactor are optimized to reach high CO selectivity (Eq. 7) and high CO_2 conversion (Eq. 8).

$$CH_4 + H_2O \leftrightarrow CO + 3H_2 \quad \Delta H_r^{298K} = +206\,kJ/mol \tag{3}$$

$$CH_4 + CO_2 \leftrightarrow 2CO + 2H_2 \quad \Delta H_r^{298K} = +247\,kJ/mol \tag{4}$$

$$CO_2 + 2H_2 \leftrightarrow C_{(s)} + 2H_2O \quad \Delta H_r^{298K} = -91\,kJ/mol \tag{5}$$

$$2CO \leftrightarrow CO_2 + C_{(s)} \quad \Delta H_r^{298K} = -172\,kJ/mol \tag{6}$$

The selectivity is defined in Eq. 7 as the ratio of carbon monoxide produced ($\dot{n}_{CO}$ in kmol/h) to converted carbon dioxide ($\dot{n}_{CO_2}$ in kmol/h).

$$S(CO) = \frac{\dot{n}_{CO,out} - \dot{n}_{CO,in}}{\dot{n}_{CO_2,in} - \dot{n}_{CO_2,out}} \tag{7}$$

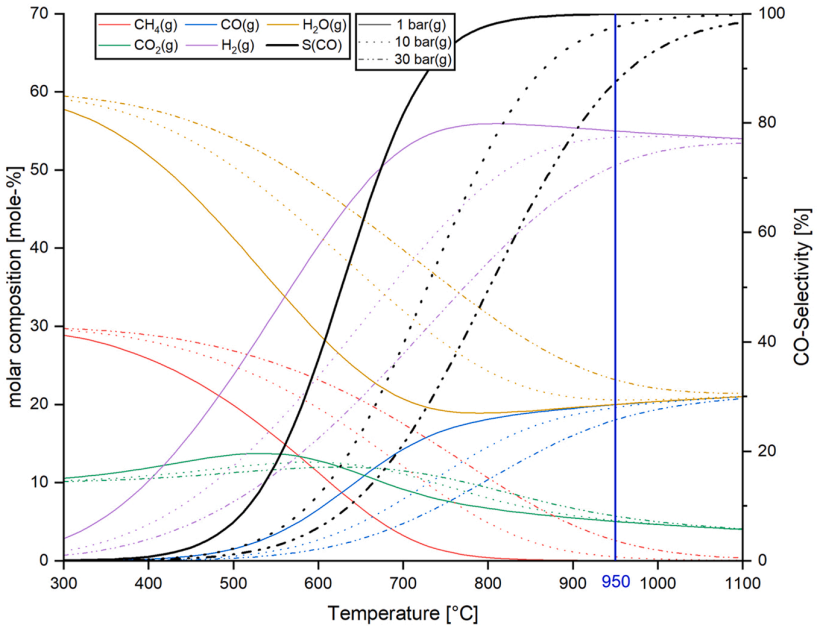

Fig. 3. Thermodynamic equilibrium and CO selectivity of the rWGS reaction for an inlet ratio of H_2:CO_2 = 3:1 as a function of temperature (300–1100 °C) and pressure (1, 10 and 30 barg).

CO_2 conversion is defined in Eq. 8 as the ratio of converted CO_2 ($\dot{n}_{CO_2,in}$-$\dot{n}_{CO_2,out}$ in kmol/h) to the inlet CO_2 mole stream ($\dot{n}_{CO_2,in}$ in kmol/h).

$$X(CO_2) = \frac{\dot{n}_{CO_2,in} - \dot{n}_{CO_2,out}}{\dot{n}_{CO_2,in}} \quad (8)$$

The chosen operating temperature is 950 °C, and the pressure is set as low as possible at 10 barg to achieve high CO selectivity and CO_2 conversion. These conditions suppress also undesired side reactions such as methanation, the Bosch reaction and Boudouard equilibrium (Eq. 3 to Eq. 6) [13,28]. Since coke formation leads to catalyst deactivation, the rWGS reactor is operated with an over-stochiometric H_2:CO_2 input ratio. Furthermore, the hydrogen flow is adjusted to achieve the desired output ratio of H_2:CO = 2.08 (specification of FT feed gas composition explained in chapter 2.4). The over-stochiometric feed gas composition suppresses these deactivation reactions [13].

The gaseous components emerging from the product separation unit downstream of the FTS consist of methane and higher order hydrocarbons, and are therefore recycled back to the rWGS reactor. Feeding methane into the rWGS reactor results in a higher heat demand compared to the rWGS reaction (Eq. 2) alone, due to the high reaction enthalpy of reforming reactions (Eq. 3 and Eq. 4). However, methane and higher hydrocarbons are converted back to syngas in the rWGS reactor, which is operated under conditions favorable for reforming, and thus the overall process efficiency is influenced positively.

2.4. Fischer-Tropsch synthesis

Low-temperature Fischer-Tropsch (LTFT) synthesis is used in the simulation, which enables changes in the final products depending on market demand. The production of normal paraffinic hydrocarbons is assumed, which can be further processed into a wide spectrum, e.g., chemicals, fuels and plastics, such as polypropylene or polyethylene, and other products. The main reaction (Eq. 10) is highly exothermic. Side reactions converting syngas into oxygenates, aromatics and naphthene are ignored in the simulation. This assumption is acceptable because syncrude mainly consists of paraffins. The product separation does not contain a distillation unit, but the Fischer-Tropsch product is only separated with flash drums [13,29]. Exact boiling cuts of each fraction are not necessary, since further processing of the produced fractions in the steam cracker of the refinery is considered [29]. The impact of various CO conversions (40% and 60%) and CH_4 selectivities (8% and 16%) have been already investigated in a preliminary study [13]. The FTS is considered to be a conversion reactor in which the CO conversion is set to X_{CO} = 40% [9,11,13]. Product formation follows the Anderson-Schulz-Flory (ASF) distribution model. In the standardized ASF distribution, the formation of CH_4 is underestimated, and the formation of C_2H_6 is overestimated [30]. For an approach to real hydrocarbon distributions with higher methane selectivity, the methanation reaction (Eq. 9) also proceeds in the FTS with an CH_4 selectivity of S_{CH4} = 16% [9,11,13]. The overestimation of C_2H_6 formation is neglected in the FTS (same strategy as Adelung et al. and König et al.) [9,11]. The product distribution strongly depends on temperature, pressure, H_2:CO ratio, and catalyst properties. The chain growth probability α needs to reach a high value between 0.9 and 0.95 to achieve high conversion rates and good efficiencies [31].

$$CO_2 + 4H_2 \leftrightarrow CH_4 + 2H_2O \quad \Delta H_r^{298K} = -165 kJ/mol \quad (9)$$

$$CO + 2H_2 \rightarrow - CH_2 - + H_2O \quad \Delta H_r^{298K} = -140 to - 160 kJ/mol_{CO} \quad (10)$$

For a chain growth probability of 0.92, according to Ostadi et al., a feed-gas ratio of H_2:CO = 2.08:1 is necessary [32]. A temperature of 220 °C and pressure of 25 barg are selected as operating conditions [11,32]. The product separation into three fractions (naphtha, middle distillate, and wax) is achieved by extracting the wax (>C_{22}) directly from the Fischer-Tropsch reactor as a liquid due to its high boiling point (>220 °C). In the downstream two-stage flash unit, the gaseous stream is cooled to 100 °C at the same pressure level. At this stage, the middle distillate (C_{11}-C_{22}) and water liquifies partially and are separated. The remaining gas stream is depressurized to 11 barg and further cooled to 20 °C to obtain the naphtha (C_5-C_{10}) and water fractions. The water is removed from the products in a three-phase separator. The remaining gaseous stream contains unconverted gases (CO, H_2), hydrocarbons (C_1-C_4) and inert gases such as nitrogen or CO_2. Therefore, a purge gas stream (2 mol-%) is introduced which avoids the accumulation of unreactive gases. The remainder is recycled upstream of the rWGS reactor. This recycle design delivered the best simulation results and KPIs in a previous study [13].

3. Simulation procedure

The PtL plant is simulated in ASPEN Plus V12.1® to capture 10.000 tons CO_2 annually (stream C-5 in Fig. 4). The flow sheet consists of two main sections: the carbon capture unit which is simulated with the ELECNRTL property method, taking into consideration the amine and CO_2 absorption and desorption reactions [33]. The second part, including the electrolysis and synthesis, is implemented using the PENG-ROB method. Fig. 4 shows the basic flow sheet (for Process Setup 1) of the process chain.

Since the simulations consist of different equipment and process structures, the main settings are summarized in Table 1. The mass and energy balances, as well as the following key performance indicators, Power-to-Liquid efficiency (Eq. 11), carbon efficiency (Eq. 12), specific energy consumption (Eq. 13), product fraction and total product quantity, are calculated as results of the performed simulations. The energy balance of each scenario is performed using the software ASPEN Energy Analyzer V12. This allows a comparison of the heat integration for each scenario with a pinch analysis (standard temperature difference of 10 °C), and reveals whether energy is used or generated (e.g. steam) in the different process setups. For this purpose, the supplied and dissipated heat flows at the corresponding temperatures are plotted in an H-T diagram (enthalpy over temperature). The carbon capture unit, electrolysis and FTS inclusive product separation unit are included. The final products (naphtha, middle distillate and wax) are cooled to 40 °C, but the oxygen stream from the electrolysis does not require cooling, as it can be used directly in the cement plant. The energy balance is strongly influenced by the different technology options (i.e. high temperature electrolysis (SOEC) versus PEM electrolysis).

The PtL efficiency η_{PtL} is calculated as the quotient of the heating value of the individual product fraction i (LHV_i in kWh/kg) multiplied by the associated product quantity ($\dot{m}_i$ in kg/h) to the electrical energy used by the electrolysis (P_{el} in kW) and the utilities (P_u in kW).

$$\eta_{PtL} = \frac{\sum(\dot{m}_i * LHV_i)}{P_{el} + P_u} \quad (11)$$

The carbon efficiency η_{carbon} is the ratio of carbon atoms present in the liquid product fractions ($\sum \dot{n}_{c,prod,i}$) to carbon atoms fed to the PtL plant including the carbon capture unit ($\dot{n}_{c,feed}$).

$$\eta_{carbon} = \frac{\sum \dot{n}_{c,prod,i}}{\dot{n}_{c,feed}} \quad (12)$$

The specific energy consumption (SEC, Eq. 13) is defined as the ratio of required total energy to the total Fischer-Tropsch product quantity.

$$SEC = \frac{P_{el} + P_u}{\dot{m}_{total}} \quad (13)$$

4. Investment and operating cost calculations

Economic considerations also play an important role in the determination of the optimum process for syncrude production, in addition to

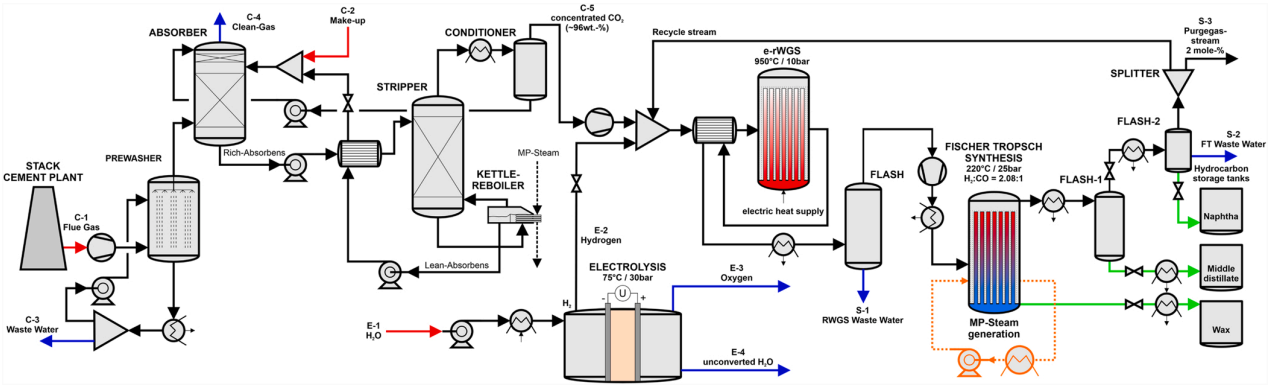

Fig. 4. Simplified flow sheet of the ASPEN Plus simulation consisting of the carbon capture unit, the PEM electrolysis and the synthesis with product separation.

Table 1
Compilation of the different PtL scenarios with variations in main equipment and process structure.

SCENARIO	1	2	3	4	5	6	7	8	9	10	11	12	13	14	15	16
PEM	X	X	X	X	X	X	X	X								
SOEC									X	X	X	X	X	X	X	X
e-rWGS	X	X	X	X					X	X	X	X				
Autothermal reactor					X	X	X	X					X	X	X	X
CO_2 separation		X				X				X				X		
rWGS recycle			X				X				X				X	
rWGS rec. incl. compression				X				X				X				X

technical issues. For a valid comparison, it is necessary to calculate investment and operating costs for each process configuration considered, which are in line with Table 1. The use of different equipment and process setups in the PtL value chain results in significant changes in cost structures.

Investment cost calculations are executed with additional software by AspenTech, namely Aspen Process Economic Analyzer V12® (APEA), which has implemented an investment cost database from Q1/2019. This PtL plant is in the design stage, therefore an investment cost deviation of − 50/+ 100% of the total inside battery limit (ISBL) cost must be considered [34]. ISBL costs include the main pieces of equipment such as heat exchangers, compressors, heaters and coolers. The outside battery limit (OSBL) costs (contributed of auxiliary facilities such as cooling towers, substations for electricity grids, etc.) are not exactly known due to uncertainties in local infrastructure. They are considered in the investment calculation as surcharge factors (factors R_6 and R_7 in Table 2). The simulation built up in Aspen Plus is imported into APEA and the investment cost of the simulated equipment is calculated. For the Fischer-Tropsch reactor, a tube bundle heat exchanger is used according to Markowitsch et al. [13], for which purchase costs of 180,000 EUR are considered in all Process Setups since the gas volume flow through the Fischer-Tropsch reactor is nearly the same for all scenarios. The investment costs for the two electrolysis technologies are taken from Trattner et al. with an average of 1400 EUR/kW for PEM technology. Since the plant size of the manufactured SOEC is according to Trattner et al. still very low (<0.15 MW), the investment costs of 1900 EUR/kW are assumed from the upper cost range for this technology [18].

The technology readiness level (TRL) for a rWGS reactor is relatively low with TRL 6 compared to the Fischer-Tropsch synthesis (TRL 9) [35]. Therefore, the investment costs cannot be derived from projects using this type of reactor. A simplification can be made by using figures from the literature for reactors operated with the same or more advanced requirements, e.g., the steam methane reforming (SMR) reactor. The investment costs for a small-scale SMR reactor (0.15–15 MW) are reported in the range of 3000–5000 USD/kW [36]. The exchange rate between EUR and USD is not decisive for this comparison. As two types of rWGS reactors, the electrified and autothermal versions, are

Table 2
Definition of used Chilton factors for total investment calculation [37].

Factor	Markup category	Factor range	Factors used for carbon capture & FTS	Factors used for electrolysis
EC	Equipment costs			
R_1	Equipment installation		1.15	0.00
$R_{2,1}$	Process piping – Process Setup 1	liquid (30–60%)	0.35	0.15
$R_{2,2}$	Process piping – Process Setup 2	liquid (30–60%)	0.40	0.15
$R_{2,3}$	Process piping – Process Setup 3	liquid (30–60%)	0.40	0.15
$R_{2,4}$	Process piping – Process Setup 4	liquid (30–60%)	0.40	0.15
$R_{3,1}$	Electrified rWGS reactor	addition to pipeline factor	0.00	0.00
$R_{3,2}$	Autothermal rWGS reactor	addition to pipeline factor	0.05	0.05
R_4	Instrumentation and automatic control	largely (12–20%)	0.15	0.00
R_5	Building and construction	outdoor (10–30%)	0.20	0.20
R_6	Auxiliary systems	strong addition (5–25%)	0.15	0.10
R_7	Outside lines	medium (5–15%)	0.15	0.00
IT	Intermediate Total			
R_8	Engineering and construction	difficult (35–60%)	0.40	0.00
R_9	Risk and unforeseen	possible adjustments (20–30%)	0.20	0.00
R_{10}	Size factor	pilot plant	0.50	0.00
TIC	Total investment costs			

considered, a differentiation must be made. According to Wismann et al., the implementation of an electrified rWGS reactor (e-RWGS) leads to lower sizing due to improved thermal management [15]. Therefore, the literature assumption for the specific costs of a SMR reactor can be reduced by one third to 2000 EUR/kW [36]. In comparison, an autothermal reactor with H_2 combustion is assumed to have the same investment costs as an SMR reactor with 3000 EUR/kW [36].

In Process Setup 2, the investment costs for the additional CO_2 separation unit downstream of the rWGS reactor is calculated with the same specific investment costs of 530 EUR/(t_{CO2}/year) as for the carbon capture unit at the cement plant. The specific costs are derived from the investment costs calculated of 5.3 MEUR (Table 10) of the amine scrubber unit capturing 10,000 tons of CO_2 per year (100,000 tons of CO_2 for 10 years).

The total investment costs of each scenario are determined by using the Chilton factor method, whereas i indicates the scenario number [37]. First, the intermediate total (IT_i, Eq. 14) is calculated using the equipment costs (EC_i) calculated by APEA and additional factors (R) listed for each category as markup costs in Table 2. By applying the supplement factors, it is distinguished between carbon capture, FTS and electrolysis unit, because electrolysis is a modular design, and thus some factors do not apply. Index j indicates the considered Process Setup 1–4 and is applied in factor R_2 (e.g., j = 1 – $R_{2,1}$ – Process Piping for Process Setup 1). Index k describes the implemented rWGS reactor technology in factor R_3 (k = 1 – $R_{3,1}$ – electrified, k = 2 – $R_{3,2}$ – autothermal reactor design).

$$IT_i = EC_i{*}R_1{*}(1 + R_{2,j} + R_{3,k} + R_4 + R_5 + R_6 + R_7) \quad (14)$$

The total investment costs (TIC_i, Eq. 15) consider the engineering and construction (R_8), the risks and unforeseen events (R_9) as well as the size (R_{10}) of the designed plant.

$$TIC_i = IT_i{*}(1 + R_8 + R_9 + R_{10}) \quad (15)$$

Beside the investment costs, also the operation needs to be considered. The operation time of the PtL plant is assumed to match the typical annual operation hours of a cement plant of 7880 h/a. The main driver in the category of operating costs is the electricity price covering the demand of electrical energy for hydrogen production in the electrolysis. Electricity prices are rising nowadays and are at an average value of 200 EUR/MWh (rounded average value of Q4/2021 and Q1/2022) [38]. Water prices are assumed to be at 1.85 EUR/m^3 [39]. Furthermore, operation and maintenance (O&M) costs, as well as personnel costs, are considered in the form of additional costs amounting to 4% (average of 3% for electrolysis and 5% for reformer unit, adopted from Keipi et al. [40]) and 1.5% of total capital investment costs, respectively [13]. In order to amortize the investment costs in 10 years, the depreciation rate (DR) corresponds to 10%. An interest rate (ROI) of 8% should also be included. The tax introduced in Austria in line with "ÖkoStRefG 2022 Teil I" (30 EUR/t_{CO2}) and additional carbon dioxide emission costs (80 EUR/t_{CO2}) have a positive impact on the product price calculation, but not on net production costs. Therefore, these costs are not included in this study [41]. The net production costs of syncrude are related, on the one hand, to the product quantity (NPC in EUR/$kg_{syncrude}$ in Eq. 16), and on the other hand to the product (chemical) energy content expressed by the Lower Heating Value (LHV, 44 MJ/kg) calculated by ASPEN Plus (NPC_{ch} in EUR/kg_{ch} in Eq. 17).

$$NPC = \frac{OPEX\ incl.ROI}{\dot{m}_{syncrude}} \quad (16)$$

$$NPC_{ch} = \frac{OPEX\ incl.ROI}{LHV{*}\dot{m}_{syncrude}} \quad (17)$$

Recent turbulence in market prices of electricity, water and rising investment and personnel costs require the creation of a sensitivity study for operational and net production cost calculations exemplarily for scenario 1 and 9, including the effect of electrolysis technology on these expenditures. Therefore, the prices used and ratios for the main categories (electricity, water, O&M, personnel and also investment costs) are differentiated using an optimistic (−50%) and a pessimistic (+100%) case for base prices or factors. The considered sensitivity cases are given in Table 3.

5. Results and discussion

For each of the aforementioned 16 scenarios the product flows, as well as heat and energy balances are simulated, and financial figures, i.e., investment costs and operating costs, are calculated. The most important technical key performance indicators are the power-to-liquid efficiency and the product quantity, while the investment, operating and net production costs involved have a major influence on the economic assessment and decision on the optimum process chain [8].

5.1. Mass and energy balance, efficiency calculation

The mass balance is divided into two sections, namely the carbon capture unit and the synthesis including the electrolysis unit. The carbon capture section is balanced only once, as the capture quantity of 10,000 tons of CO_2 annually is the same for each scenario.

The mass balance for the carbon capture unit is given in Table 4. The separation efficiency of the amine scrubber unit is calculated with 90%. High amounts of water escape in the clean gas of the absorber tower, whereas also MEA is released into the atmosphere. To obtain constant liquid volume flows, an amine make-up is necessary, which balances the water and amine losses. The purity of concentrated CO_2 equals to 96 wt.-% wet or 99.9 wt.-% dry.

Table 5 and Table 6 quantify the inlet and the outlet streams of the water electrolysis and the downstream Fischer-Tropsch synthesis unit, respectively. The locations of the balanced media in the process are indicated in the flow sheet (Fig. 4). The water demand for the electrolysis feed varies for each scenario, depending on the applied rWGS reactor and hydrogen production technologies. Comparing the Process Setups in terms of the implementation of previously defined process facilities (CO_2 separation and recycle stream around rWGS reactor), the mass balance shows that an additional recycle stream with and without compression (Process Setup 3 and 4) has no impact on the total product quantity compared with the standard process route (Process Setup 1). In all scenarios, about 60 wt.-% contributes wax, 29 wt.-% middle distillate and 11 wt.-% naphtha. Only the inclusion of an additional CO_2 capture unit downstream of the rWGS reactor produces a small amount of 2 kg/h additional product, as the CO_2 capture from the rWGS product gas stream and recycle upstream of the rWGS reactor increases the CO_2 concentration of the gas fed into the rWGS reactor. A capture efficiency of 95% was selected for this calculation. In order to maintain the H_2:CO ratio, more H_2 must be supplied correspondingly in Process Setup 2. In these simulation results, this leads to an additional hydrogen demand of 1 kg/h. The four scenarios 2, 6, 10 and 14 with additional CO_2 separation (Process Setup 2) differ from the mass balances of Process Setups 1, 3 and 4 and are therefore shown individually in Table 5 and Table 6. It can be concluded that a capture of the CO_2 downstream of the rWGS reactor has no significant impact on the product yield, and CO_2 behaves like an inert gas in the Fischer-Tropsch synthesis. Whether CO_2 is

Table 3
Assumptions for sensitivity analysis on net production costs.

Utility or ratio	Optimistic case (- 50%)	Base case (+/- 0%)	Pessimistic case (+ 100%)
Electricity price	100 EUR/MWh	200 EUR/MWh	400 EUR/MWh
Water price	0.93 EUR/m^3	1.85 EUR/m^3	3.90 EUR/m^3
O&M	2%	4%	8%
Personnel	0.75%	1.5%	3%
Investment costs	50%	100%	200%

Table 4
Mass balance of the carbon capture unit for all scenarios.

Mass balance		Inlet		Outlet		
Carbon capture unit		C-1 Flue gas	C-2 Makeup water	C-3 Prewasher waste water	C-4 Clean gas	C-5 Concentrated CO_2
Total	kg/h	6686	785.03	243	5926	1302
H_2O	*kg/h*	*504*	*785*	*243*	*1006*	*41*
CO_2	*kg/h*	*1391*			*130*	*1260*
N_2	*kg/h*	*4049*			*4048*	*1*
O_2	*kg/h*	*742*			*742*	
MEA	*kg/h*		*0.03*		*0.03*	

Table 5
Mass balance of all scenarios for the electrolysis unit.

Mass balance - Electrolysis			Scenario number			
			1, 3, 4 and 9, 11, 12	5, 7, 8 and 13, 15, 16	2 and 10	6 and 14
Inlet						
E-1 Water	H_2O	kg/h	1652	1915	1661	1925
Outlet						
E-2 Hydrogen	H_2	kg/h	176	204	177	205
E-3 Oxygen	O_2	kg/h	1394	1615	1401	1624
E-4 Unconverted water	H_2O	kg/h	83	96	83	96

recycled in front of or behind the FTS has no significant impact on the product yield, as stated before. This is also confirmed by the fact that unreacted gases behind the FTS (including CO_2) are anyway recycled back upstream of the rWGS reactor. It even leads to the disadvantage that due to the recycling flow via the rWGS reactor larger volume flows are available and the reactor size has to be scaled up accordingly.

The comparison between the two rWGS reactor technologies leads to the conclusion that the technology selection creates a significant difference in the mass balance, specifically in the amount of hydrogen required and, as a result, in hydrogen production itself. The autothermal reactor design (scenarios 5–8 and 13–16) is based on combustion of hydrogen for the supply of the high temperature heat required for the endothermic rWGS reaction. Therefore, an additional hydrogen demand of approximately 16% is required compared to the electrified reactor. Additionally, water is produced which must be separated and treated in the condenser downstream [17]. This additional hydrogen is not required in the electrified technology (scenarios 1–4 and 9–12) since the energy is supplied into the system electrically. However, the two technologies differ only in the method of providing high temperature heat for the rWGS reactor, because the total product quantity (syncrude) remains unchanged.

The energy balance is divided into electrical (Table 7) and thermal energy demand (Table 8). The amount of consumed electrical energy is crucial for the PtL efficiency calculation and is composed of electrolysis, e-rWGS and utilities. A combination of the individual scenarios is no longer possible because the electrical energy requirement, in particular, mainly depends on the level of hydrogen demand and electrolysis technology. The use of PEM electrolysis, which has a higher specific electricity demand, leads to higher energy consumption in scenarios 1–8, compared with the high temperature electrolysis used in scenarios 9–16. The higher hydrogen demand in scenarios 5–8 and 13–16, deriving from the autothermal rWGS reactor technology, also leads to higher electrical energy consumption compared with the scenarios in which the e-rWGS technology is integrated (scenarios 1–4 and 9–13).

Table 6
Mass balance of all scenarios for the synthesis unit.

Mass balance - Synthesis			Scenario number			
			1, 3, 4 and 9, 11, 12	5, 7, 8 and 13, 15, 16	2 and 10	6 and 14
Inlet						
C-5 concentrated CO_2	Total	kg/h	1302			
	H_2O	*kg/h*	*41*			
	CO_2	*kg/h*	*1260*			
	N_2	*kg/h*	*1*			
E-2 Hydrogen	H_2	kg/h	176	204	177	205
Outlet						
S-1 rWGS waste water	H_2O	kg/h	376	626	378	629
S-2 FT waste water	H_2O	kg/h	670	1615	673	1615
S-3 FT purge gas	Total	kg/h	48		42	
	CO	*kg/h*	*31*		*31*	
	H_2	*kg/h*	*4*		*4*	
	CO_2	*kg/h*	*6*		*0*	
	N_2	*kg/h*	*1*		*1*	
	CH_4	*kg/h*	*5*		*5*	
	$>C_1$	*kg/h*	*1*		*1*	
S-4 FT product	Total	kg/h	383		385	
	H_2O	*kg/h*	2		2	
	Naphtha	*kg/h*	41		41	
	Middle Distillate	*kg/h*	110		112	
	Wax	*kg/h*	230		230	
	Total C_5-C_{22+}	kg/h	381		383	

Table 7
Electricity demand and product energy content for each scenario.

Electricity		Scenario number															
		1	2	3	4	5	6	7	8	9	10	11	12	13	14	15	16
Power-electrolysis	[MW]	9.18	9.22	9.20	9.20	10.63	10.69	10.65	10.65	7.03	7.06	7.05	7.05	8.10	8.14	8.12	8.12
Power-e-rWGS	[MW]	0.89	0.89	0.92	0.91	0.01	0.01	0.02	0.02	0.89	0.89	0.92	0.91	0.01	0.01	0.02	0.02
Power consumption Electrolysis + e-rWGS	[MW]	10.07	10.12	10.11	10.11	10.64	10.70	10.68	10.68	7.92	7.96	7.96	7.96	8.11	8.15	8.14	8.14
Power-utilities (compressor, pump)	[MW]	0.55	0.57	1.11	0.57	0.55	0.57	1.11	0.57	0.74	0.76	1.30	0.76	0.77	0.79	1.18	0.79
Total electric power demand	[MW]	10.62	10.69	11.23	10.68	11.19	11.27	11.79	11.25	8.66	8.72	9.27	8.72	8.88	8.94	9.33	8.93
Product energy content	[MW]	4.66	4.69	4.66	4.66	4.66	4.69	4.66	4.66	4.66	4.69	4.66	4.66	4.66	4.69	4.66	4.66

Table 8
Heat and cooling demand/steam generation of all scenarios.

Heat and cooling demand		Scenario number															
		1	2	3	4	5	6	7	8	9	10	11	12	13	14	15	16
Total heat demand	[MW]	0.89	0.89	0.92	0.91	0.01	0.01	0.02	0.02	0.89	0.89	0.92	0.91	0.01	0.01	0.02	0.02
Total cooling demand	[MW]	4.12	4.16	4.73	4.16	4.66	4.70	5.26	4.69	1.44	1.47	2.05	1.48	1.53	1.56	1.67	1.56
Steam generation	[MW]	0.64	0.66	0.64	0.64	0.92	0.94	0.92	0.91	0.18	0.23	0.20	0.11	0.38	0.43	0.40	0.29
Cooling water demand	[MW]	3.48	3.50	3.66	3.52	3.73	3.76	3.91	3.78	1.26	1.24	1.38	1.37	1.15	1.13	1.27	1.27

However, the total amount of energy input has to be considered in the comparison of the rWGS reactor technologies. In the scenarios with electrified rWGS reactor, the total energy required (hydrogen production and electrical energy for the rWGS reactor) is lower than for the autothermal reactor in which only hydrogen production energy and neglectable thermal energy for rWGS reactor preheating is required. The power demand for scenarios 1–4 is 10.07–10.12 MW, while the implementation of the autothermal reactor results in a power demand of 10.64–10.70 MW for scenarios 5–8. The difference between e-rWGS and autothermal reactor is substantial with about 0.6 MW. This is a result of the implementation of a SOEC, where the power demand with e-rWGS is between 7.92 and 7.96 MW for scenarios 9–12, and between 8.11 and 8.15 MW for scenarios 13–16 with an autothermal reactor. The difference which results from the choice of the rWGS reactor technology is only 0.2 MW. This reduction is solely caused by H_2 production, which is determined by the technology-defined system efficiencies. Therefore, the process variants with integrated SOEC are more efficient.

The higher energy demands of Process Setup 3 in scenarios 3, 7, 11, 15 are due to the pressure drops of the rWGS recycle stream relaxation and its recompression from low pressure levels (approx. 1 barg, as it is released from the carbon capture unit). In contrast to Process Setup 2, in which only CO_2 is recycled back upstream the rWGS reactor, in Process Setup 3 a partial recycle of all the components is implemented. Accordingly, electricity demand is higher for the recycle gas compressor.

The thermal energy balance was prepared using ASPEN Energy Analyzer V12 software and allows the calculation of the required and generated heat for each scenario. ASPEN Energy Analyzer performs a pinch analysis (standard temperature difference of 10 °C) with supplied and dissipated heat flows, with which the heat integration of the process is optimized. The necessary input and output energy demand is delivered for each scenario. In the pinch analysis in Fig. 5, the heat and cooling requirements for scenarios 1 and 9 are shown as examples to provide an overview of the influence of an SOEC on heat integration. The gaps indicate the heat (Q_{in} on the right side) and cooling demand (Q_{out} on the left side) for scenarios 1 and 9. Scenarios 1–8 with the implementation of a low temperature electrolysis require more cooling duty, for example, scenario 1 has a cooling requirement of 3.48 MW. On the other hand, if low temperature heat is integrated properly, steam for the SOEC feed is generated by waste heat, as shown in scenarios 9–16. In the scenarios 1–4 and 9–12 with an installed e-rWGS, the required high temperature heat (Q_{in}) needs to be supplied with an overall duty between 0.89 and 0.92 MW. In the cases of the application of an autothermal reactor (scenarios 5–8 and 13–16), hydrogen firing is already considered as an additional heat source in the simulation and therefore

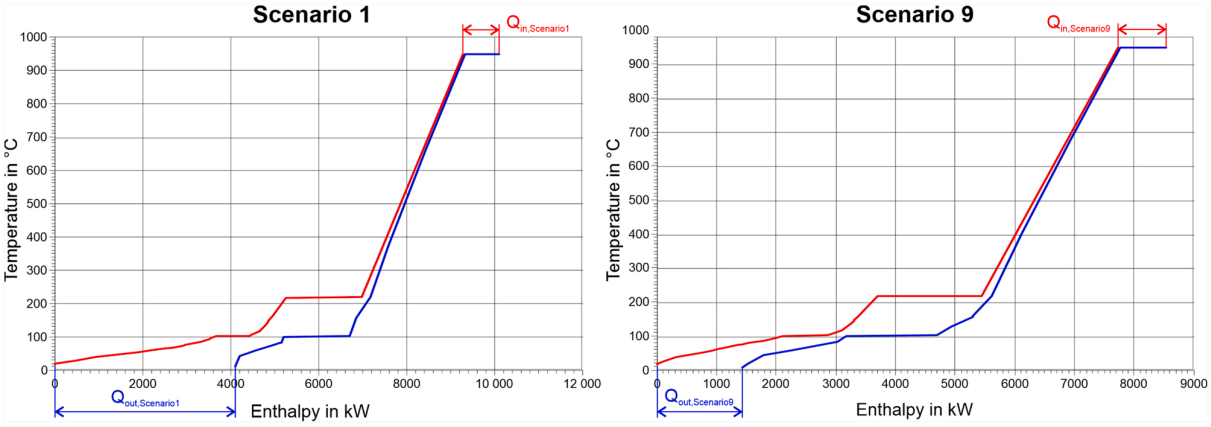

Fig. 5. Pinch analysis of Scenario 1 and 9 performed with ASPEN Energy Analyzer V12.

also integrated in the pinch analysis. As a result, for the operation of the autothermal reactor no additional heat is required, except for a small electrical heating unit to preheat the feed gas to rWGS reactor operation temperature (heat demand is between 0.01 and 0.02 MW).

The results in Table 8 show that excess heat in the form of steam is generated in each scenario. The use of PEM electrolysis is accompanied by an increased cooling demand, because low temperature heat (approx. 70 °C) has to be removed. However, more steam is produced compared to the scenarios with a SOEC. This is due to the fact that excess steam can be used as an input stream for the SOEC in scenarios 9–16. Furthermore, the high-temperature heat behind the SOEC can be used optimally for heat integration, as high temperature heat flows (> 700 °C) are more efficient in energy exchange than low temperature heat. Low temperature heat has to be dissipated with cooling water, which contributes to a reduction in efficiency. The cooling requirements drop by almost half when high temperature electrolysis is implemented. The effects of additional CO_2 capture and a recycle with an additional compressor are not significant, as the steam and cooling demand remains almost unchanged. The deviations stem from the different operation units included into the system (CO_2 separation, additional compressors and relief of pressure). For the scenarios 5–8 and 13–16 with an implemented autothermal reactor, more steam is produced due to a higher gas volume flow in the condenser behind the rWGS reactor. High temperature heat is used for rWGS reactor operation and is provided electrically, which is also considered in Table 7 as e-rWGS.

Table 9 lists the PtL efficiency, carbon conversion and specific energy consumption (per kg syncrude) for all scenarios. Obviously, variations in reactor and electrolysis technology does not change the carbon conversion level, as can be seen for scenarios 1, 5, 9, 13, or 2, 6, 10, 14 and so on, which all have different equipment combinations. In regard to PtL efficiency, the main difference lies in the implementation of the electrolysis technology. Whereas in scenario 1–8, the PtL efficiency ranges between 39.5% and 44.0% with a share of electrolysis power consumption of about 86%, the PtL efficiency ranges between 50.0% and 53.9% for scenarios 9–16 with a share of about 81% of the total electricity demand for the SOEC. The higher efficiency of the SOEC results in almost 10% points higher PtL efficiency and lower specific energy consumption for scenarios 9–16. The scenarios with the implementation of an autothermal reactor (5−8, 13−16) also have lower efficiencies, because electrical energy is needed for additional hydrogen production. This deviation is not as relevant as the electrolysis technology used, as it results only in slightly lower efficiencies. (−3.3% comparing scenario 1 and 5, and −1.3% for scenario 9 and 13). In a preliminary conclusion, scenario 9 and scenario 10 show the best key performance indicators with a product quantity of 381 kg/h, a PtL efficiency of almost 54% and a specific energy consumption of 22.7 kWh/$kg_{Syncrude}$. The implementation of a recycle stream around the rWGS reactor without a compressor leads to low PtL efficiencies due to energy losses caused by pressure reduction. This is also evident in the operating cost calculation, see chapter 5.3. The second parameter for the assessment of the PtL process is the overall carbon conversion (Eq. 12), which is 85% in scenario 9% and 86% in scenario 10, thus higher than the 73.7% reported by König et al., but slightly lower than the 88% in Adelung et al. [8,11].

5.2. Total investment cost comparison

The calculation of investment costs also has to be taken into account for the determination of the most suitable PtL process design and equipment selection. In Table 10, the total calculated investment costs are reported for each scenario. Scenario 1 is used as base case against all other scenarios are normalized. For scenario 1, the contributions of the individual process units (amine scrubber, synthesis, electrolysis, additional CO_2 capture) to total investment costs are given. Scenarios 2–16 refer to the calculated costs of scenario 1, and their deviations to this baseline scenario are calculated. Table 10 also summarizes the costs for the process units for all scenarios. Scenario 1 has the lowest investment volume with 46.4 $MEUR_{2019}$ (price basis year 2019), the investment costs for scenarios 2–16 differ from the base case from + 4.4 up to + 30.3%. Since the same amount of CO_2 is captured in each scenario, the amine scrubbing costs remain unchanged. A significant deviation can be recognized in the synthesis section, where the impact of piping and the size and type of rWGS reactor plays an important role. The autothermal reactor has about 15% higher investment costs (scenario 5) than the e-rWGS reactor in the base scenario 1, which is due to higher specific investment costs (3000 EUR/kW) and additional hydrogen and oxygen piping for heat supplies. In addition, the higher investment costs of the SOEC electrolysis with 1900 EUR/kW compared to 1400 EUR/kW for PEM electrolysis are responsible for the increased investment costs of scenarios 9–16 compared to the electrolysis costs in scenarios 1–8 [18,23].

The calculation of the specific investment costs based on Herz et al. [42] results in 15.9 and 6.5 MEUR/(kt/a) for PEM and SOEC, respectively. The calculation of this study yields 15.5 MEUR/(kt/a) for PEM electrolysis in scenario 1 and 16.4 MEUR/(kt/a) for SOEC in scenario 9. The difference of the specific investment costs with the PEM technology and calculations of Herz et al. is almost negligible. For SOEC, however, Herz et al. assumed the specific SOEC investment costs to be about 12% cheaper than the PEM costs. In this study, the opposite is the case, our SOEC costs are about 36% higher than those of PEM, which justifies the difference in specific investment costs for scenario 9 with SOEC technology.

5.3. Operating and net production cost calculation

Finally, annual operating costs are calculated with a PtL plant operating time of 7884 h/a (see chapter 4), which corresponds to the usual operating time of a cement plant. Table 11 shows the results of the operating cost calculations for each scenario divided into the main categories electricity costs, water costs, operation and maintenance (O&M) costs, personnel costs and ROI. In this comparison, scenario 1 is again the baseline scenario, and all other scenarios are normalized to scenario 1. The main driver of operating costs is electricity with a share of 60.4% (16.7 MEUR/year) in scenario 1. The lower energy demand of the SOEC with 3.6 kWh/Nm^3 H_2 compared to the PEM electrolysis with 4.7 kWh/Nm^3 H_2 is responsible for the significant difference between scenarios 1–8 and 9–16 [18,23]. As higher electricity prices are predicted for the future, the gap between SOEC and PEM electrolysis will widen further. In general, the overall operating costs will continuously increase for both technologies. Furthermore, 16.8% (4.6 MEUR/year) of the costs are related to depreciation, 13.4% (3.7 MEUR/year) to ROI,

Table 9
PtL efficiency, carbon conversion and specific energy consumption for all scenarios.

Key performance indicators (KPIs)		Scenario number															
		1	2	3	4	5	6	7	8	9	10	11	12	13	14	15	16
PtL efficiency	[%]	44.0	43.9	41.5	43.7	41.7	41.6	39.5	41.5	53.9	53.8	50.3	53.5	52.6	52.5	50.0	52.2
Carbon conversion	[%]	85.1	85.5	85.0	85.0	85.1	85.5	85.0	85.0	85.1	85.5	85.0	85.0	85.1	85.5	85.0	85.0
Specific energy consumption (SEC)	[kWh/kg]	27.9	27.9	29.5	28.0	29.4	29.4	31.0	29.5	22.7	22.7	24.3	22.9	23.3	23.3	24.5	23.5

Table 10
Compilation of the total investment costs of all scenarios.

Cost calculation - CAPEX		Scenario number															
		1	2	3	4	5	6	7	8	9	10	11	12	13	14	15	16
Amine scrubber unit	[MEUR]	5.3	5.3	5.3	5.3	5.3	5.3	5.3	5.3	5.3	5.3	5.3	5.3	5.3	5.3	5.3	5.3
Synthesis	[MEUR]	22.4	23.1	25.3	26.3	26.3	27.0	29.1	30.5	21.8	22.5	24.8	26.1	25.9	26.7	28.7	30.0
Electrolysis	[MEUR]	18.6	18.7	18.7	18.7	21.6	21.7	21.6	21.6	22.0	22.1	22.1	22.1	25.0	25.1	25.1	25.1
Additional CO_2-separation (Process Setup 2)	[MEUR]	0.0	1.3	0.0	0.0	0.0	1.3	0.0	0.0	0.0	1.3	0.0	0.0	0.0	1.3	0.0	0.0
Total investment costs (TIC)	[MEUR]	46.4	48.5	49.3	50.3	53.2	55.3	56.0	57.4	49.1	51.2	52.2	53.5	56.2	58.5	59.1	60.4
Share/Deviation of TIC																	
Amine scrubber unit	[%]	11.5	+/− 0	+/− 0	+/− 0	+/− 0	+/− 0	+/− 0	+/− 0	+/− 0	+/− 0	+/− 0	+/− 0	+/− 0	+/− 0	+/− 0	+/− 0
Synthesis	[%]	48.4	+ 1.4	+ 6.2	+ 8.4	+ 8.2	+ 9.9	+ 14.3	+ 17.3	-1.4	+ 0.2	+ 5.1	+ 7.8	+ 7.5	+ 9.2	+ 13.5	+ 16.4
Electrolysis	[%]	40.2	+ 0.2	+ 0.1	+ 0.1	+ 6.4	+ 6.6	+ 6.5	+ 6.5	+ 7.3	+ 7.5	+ 7.4	+ 7.4	+ 13.8	+ 14.0	+ 13.9	+ 13.9
Additional CO_2-separation (Process Setup 2)	[%]	0.0	+ 2.8	+/− 0	+/− 0	+/− 0	+ 2.8	+/− 0	+/− 0	+/− 0	+ 2.8	+/− 0	+/− 0	+/− 0	+ 2.8	+/− 0	+/− 0
Total investment costs (TIC)	[%]	100.0	+ 4.4	+ 6.3	+ 8.5	+ 14.6	+ 19.3	+ 20.7	+ 23.7	+ 5.9	+ 10.5	+ 12.5	+ 15.3	+ 21.2	+ 26.0	+ 27.4	+ 30.3

Table 11
Operating and net production cost calculation for all scenarios.

Cost calculation - OPEX		Scenario number															
		1	2	3	4	5	6	7	8	9	10	11	12	13	14	15	16
Electricity costs	[MEUR/year]	16.7	16.8	17.7	16.8	17.6	17.8	18.6	17.7	13.7	13.7	14.6	13.7	14.0	14.1	14.7	14.1
Water cost	[MEUR/year]	0.1	0.1	0.1	0.1	0.1	0.1	0.1	0.1	0.1	0.1	0.1	0.1	0.1	0.1	0.1	0.1
Operation and maintenance costs O&M	[MEUR/year]	1.9	1.9	2.0	2.0	2.1	2.2	2.2	2.3	2.0	2.0	2.1	2.1	2.2	2.3	2.4	2.4
Personnel costs	[MEUR/year]	0.7	0.7	0.7	0.8	0.8	0.8	0.8	0.8	0.9	0.7	0.8	0.8	0.8	0.8	0.9	0.9
ROI - Return on investment (8%)	[MEUR/year]	3.7	3.9	3.9	4.0	4.3	4.4	4.5	4.6	3.9	4.1	4.2	4.3	4.5	4.7	4.7	4.8
Depreciation (10%)	[MEUR/year]	4.6	4.8	4.9	5.0	5.3	5.5	5.6	5.7	4.9	5.1	5.2	5.3	5.6	5.8	5.9	6.0
Total OPEX incl. ROI	[MEUR/year]	27.7	28.3	29.3	28.7	30.2	30.8	31.8	31.3	25.2	25.8	26.9	26.4	27.3	27.9	28.6	28.3
Net production costs (NPC)	[EUR/$kg_{Syncrude}$]	9.22	9.36	9.77	9.57	10.05	10.21	10.60	10.42	8.40	8.55	8.97	8.79	9.07	9.23	9.54	9.45
Net production costs (NPC_{ch})	[EUR/kWh_{ch}]	0.75	0.76	0.80	0.78	0.82	0.83	0.87	0.85	0.69	0.70	0.73	0.72	0.74	0.75	0.78	0.77
Share/Deviation of costs																	
Electricity costs	[%]	60.4	+ 0.4	+ 3.5	+ 0.3	+ 3.3	+ 3.7	+ 6.7	+ 3.6	-11.1	-10.8	-7.7	-10.8	-9.9	-9.5	-7.4	-9.6
Water cost	[%]	0.2	+ 0.0	+ 0.0	+ 0.0	+ 0.0	+ 0.0	+ 0.0	+ 0.0	+ 0.0	+ 0.0	+ 0.0	+ 0.0	+ 0.0	+ 0.0	+ 0.0	+ 0.0
Operation and maintenance costs O&M	[%]	6.7	+ 0.3	+ 0.4	+ 0.6	+ 1.0	+ 1.3	+ 1.4	+ 1.6	+ 0.4	+ 0.7	+ 0.8	+ 1.0	+ 1.4	+ 1.7	+ 1.8	+ 2.0
Personnel costs	[%]	2.5	+ 0.1	+ 0.2	+ 0.2	+ 0.4	+ 0.5	+ 0.5	+ 0.6	+ 0.1	+ 0.3	+ 0.3	+ 0.4	+ 0.5	+ 0.7	+ 0.7	+ 0.8
ROI - Return on investment (8%)	[%]	13.4	+ 0.6	+ 0.8	+ 1.1	+ 2.0	+ 2.6	+ 2.8	+ 3.2	+ 0.8	+ 1.4	+ 1.7	+ 2.0	+ 2.8	+ 3.5	+ 3.7	+ 4.1
Depreciation (10%)	[%]	16.8	+ 0.7	+ 1.1	+ 1.4	+ 2.5	+ 3.2	+ 3.5	+ 4.0	+ 1.0	+ 1.8	+ 2.1	+ 2.6	+ 3.6	+ 4.4	+ 4.6	+ 5.1
Total OPEX incl. ROI	[%]	100.0	+ 2.1	+ 5.9	+ 3.7	+ 9.1	+ 11.3	+ 14.9	+ 12.9	-8.8	-6.7	-2.8	-4.8	-1.5	+ 0.7	+ 3.4	+ 2.4
Net production costs (NPC)	[%]	100.0	+ 1.6	+ 6.0	+ 3.8	+ 9.0	+ 10.7	+ 15.0	+ 13.1	-8.8	-7.2	-2.7	-4.7	-1.6	+ 0.2	+ 3.5	+ 2.5

6.7% (1.9 MEUR/year) to O&M costs and 2.5% (0.7 MEUR/year) to personnel costs in scenario 1, which sums up to almost one quarter of the total operating costs. The higher hydrogen demand in scenarios 5–8 and 13–16 with an autothermal rWGS reactor is also reflected in higher electricity costs (owed to higher hydrogen production). The use of the additional equipment in Process Setups 2–4 (CO_2 separation unit, recycle stream with and without compression behind and around the rWGS reactor) has also a negative impact on operating costs, as the electricity, O&M, personnel costs, depreciation and ROI all increase with these additional facilities. Higher operating costs lead to higher net production costs, for constant product flows. The net production costs are calculated for scenario 1 with 9.22 EUR/$kg_{syncrude}$. However, NPC vary from 8.40 EUR/$kg_{syncrude}$ (−8.8%) for scenario 9 to maximum costs of 10.60 EUR/$kg_{syncrude}$ (+15.0%) for scenario 7. In terms of calculated operating costs inclusive ROI and net production costs, scenario 9 proves to be the best case with a deviation of − 8.8% compared to the base scenario 1.

In this study, the lowest NPC are achieved in scenario 9 and are high (8.40 EUR/$kg_{syncrude}$ or 0.69 EUR/kWh_{ch}) at a first glance compared to other works. Herz et al. [42] calculated the NPC_{ch} for a PtL process, using a PEM and Co-SOEC with a downstream Fischer Tropsch synthesis, which results in chemical NPC_{ch} of 0.434 and 0.460 EUR/kWh_{ch}, respectively. The lower operating costs is the main reason for the difference to our calculation, as an electricity price of 76.8 EUR/MWh_{el} was assumed. Recalculating the NPC of this study for the aforementioned electricity price results in 0.47 and 0.46 EUR/kWh_{ch} for PEM and SOEC, respectively, which underlines the importance of the electricity costs for NPC.

The comparison of the NPC with results published by other authors requires some caution, as the process setups, desired products and calculation bases are defined differently (e.g., main product varies between syncrude, gasoline, kerosene, etc.). König [8] simulates a PtL plant to produce kerosene out of CO_2 and hydrogen, whereas a rWGS reactor, a PEM electrolysis and a Fischer Tropsch synthesis with a hydrocracker unit (to increase the yield of low chain hydrocarbons) is considered. König assumed an electricity price with 117 EUR/MWh_{el} which results in calculated NPC with 0.46 EUR/kWh_{ch}. A recalculation in our study with the electricity price of König et al. results in NPC of 0.56 EUR/kWh_{ch}. The deviation can be explained, as the costs of the carbon capture unit were not taken into account in its calculation.

Adelung et al. [12] also calculated NPC for kerosene production (C_{5+}) via a rWGS and Fischer Tropsch reactor with a variation of hydrogen production costs between 2.3 and 7.6 EUR/kg_{H2}. Recalculation is difficult to implement because these figures were assumed from forecasts for the year 2030 and past year 2012, respectively, without precise electricity price information. An average hydrogen production cost of 4.1 EUR/kg_{H2} was used in their study, assumed by Bertuccioli et al. with an electricity price of 51 EUR/MWh [43]. Therefrom, NPC were calculated within the range between 1.81 and 5.47 EUR/kg_{C5+}, respectively [12]. Recalculating the NPC for our study with the electricity price of 51 EUR/MWh, the NPC results in 5.07 EUR/$kg_{syncrude}$ for scenario 1. Scenario 1 utilizes a PEM electrolysis like in the study of Adelung et al., and the NPC calculation yields costs in a comparable range.

The comparison of the three studies shows that the range of the calculated NPC depends mainly on the assumed electricity prices. In case of a recalculation with the electricity prices used in literature, the NPC of this study are in a comparable range with other literature results which supports the validity of the own calculations. The influence of the electricity price in the NPC is examined in more detail in the sensitivity analysis (chapter 5.4).

5.4. Sensitivity analysis of net production costs

In the previous chapter, the net production costs were calculated with fixed utility costs, O&M personnel costs and investment volume. A sensitivity analysis has been performed to investigate the impact of each cost factor. The results are shown in Fig. 6, based on the net production costs for scenario 1 and 9.

As mentioned above, electricity costs are the main driver of operating costs. Therefore, a decrease to 100 EUR/MWh or an increase to 400 EUR/MWh has the largest impact on the net production costs with a range of − 30 to + 60% for scenario 1 and − 33 to + 40% for scenario 9. As expected, the high temperature electrolysis achieves better net production costs even at higher electricity prices due to the greater efficiency of the SOEC compared to PEM electrolysis. The second most

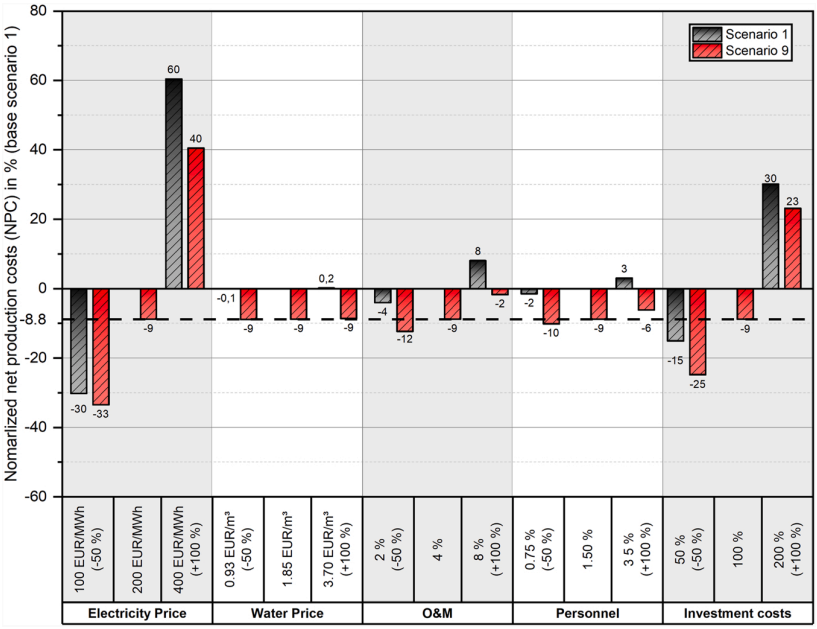

Fig. 6. Results of the sensitivity study on net production costs for an optimistic (−50%) and pessimistic (+100%) case for scenario 1 and scenario 9 (related to base scenario 1).

important factor is investment costs, which vary in the analysis between − 15 and + 30% for scenario 1 and − 25 to + 23% for scenario 9. Future learning curves (especially for electrolysis) can reduce the NPC accordingly, whereas e.g. increasing material prices can also significantly increase the NPC. Changes in the water price, O&M, personnel factors and investment costs result in a maximum variation of − 4 to + 8% for scenario 1 and − 12 to − 2% for scenario 9. Therefore, all these operating and investment costs have a much lower impact on net production costs than electricity prices and investment costs. The decision for the most appropriate process setup and process scenario is strongly influenced by the electricity demand of the different options. Thus, scenario 9, which uses SOEC electrolysis and an e-rWGS reactor, represents the best possible configuration of the PtL plant in this study.

6. Conclusion and outlook

In order to compare the different process scenarios of a PtL pilot plant, an assessment of KPIs and product yield, as well as investment and operating costs has been performed. Unexpectedly, the process structure, i.e. the separation of CO_2, or an additional recycling stream via the rWGS with and without compression, has no significant influence in the product yield. Process Setups 1, 3 and 4 achieve a product quantity of 381 kg/h, whereby the choice of rWGS reactor technology or electrolysis technology shows no influence on the product quantity in all process routes. Process Setup 2, with CO_2 separation behind the rWGS reactor, reaches 383 kg/h and is not significantly better than the others, with a deviation of + 0.5% only. The main differences for the process routes with additional equipment are higher investment and operating costs compared to Process Setup 1, as well as a higher power demand for Process Setup 3, using a recycle stream without compression. However, the PtL efficiency increases by 10% points by using a SOEC unit instead of PEM electrolysis for hydrogen production. It must be mentioned here that this increase can only be achieved by interconnecting the systems and integrating heat coupling (e.g. steam generation from exothermic FT reaction to provide steam for SOEC). However, the SOEC negatively influence NPC due to its higher investment costs compared to PEM electrolysis. However, the PtL efficiency increase (of 10%) has a positively influence the NPC calculation, as electricity costs are reduced, which has a more significant impact on the NPC compared to the investment costs. The carbon efficiency remains almost constant (85% and 86%) for both electrolysis technologies.

The investment costs mainly depend on the technology readiness level (TRL) of the individual equipment (PEM and SOEC electrolysis, rWGS and FT reactor). The use of PEM electrolysis in scenarios 1–8 has the advantage of a high TRL level, which would simplify the construction and operation of the electrolysis with approximately 10 MW power. The investment costs for such equipment are still high due to the low TRL for the rWGS reactor concepts, as well as the SOEC, and their missing integration in industrial scale plants. Moreover, there is no validation for conversion factors in the rWGS reaction, neither at laboratory scale nor under real industrial boundary conditions. So, further investigations on this catalytic conversion, particularly regarding catalysts, reactor design and operating conditions, need to be carried out. However, it has become evident in this study that the integration of an electrified rWGS instead of an autothermal rWGS results in lower overall costs. Additional hydrogen demand leads to higher electricity and investment costs. As long as the produced hydrogen is dependent on the local electricity price, the electrified reactor design can be evaluated as the more efficient technology. This also applies to the SOEC, where the stack size of 0.15 MW is still very small and the whole hydrogen production system, including heat integration, can be further developed through installation in larger plants [18]. Further development of SOEC technology also brings the advantage of decreasing equipment costs, which could simply improve the business case [44].

The lower PtL efficiency originates from a higher specific energy consumption in PEM electrolysis compared to SOEC (4.7 compared to 3.6 kWh/Nm^3 H_2) [18]. These increased energy demands impact the costs to be borne for electricity significantly, as shown in the operating cost calculation in Table 11. For the PEM electrolysis, these costs demand 60.4% (16.7 MEUR/year) of the total operating costs for scenario 1, whereas for the SOEC technology used in scenario 9, the share of electricity costs is only 54.1% (13.7 MEUR/year). The sensitivity analysis also reveals that the electricity price has the largest impact on operating costs. Rising electricity prices could increase operating costs by approximately 60%. This influences the final net production costs considerably. However, other operating costs such as for water, O&M and personnel, as well as the investment costs must be taken into account in the comparison but are not that decisive compared with the calculated electricity costs.

When comparing all the investigated scenarios and considering efficiencies, product quantity and cost profitability, scenario 9 emerges as the best option for a PtL plant, in which hydrogen, produced by the SOEC, and CO_2 are fed into an electrified rWGS reactor for syngas production and further processed using a Fischer-Tropsch synthesis to highly paraffinic syncrude. In scenario 9, the PtL efficiency is 54%, the carbon conversion is 85%, and the specific energy consumption is 22.7 $kWh/kg_{Syncrude}$. From an economic perspective, the total investment is 5.9% (49.1 $MEUR_{2019}$) higher than calculated for the base scenario 1 (46.4 $MEUR_{2019}$), with 8.8% lower net production costs resulting in 8.40 $EUR/kg_{syncrude}$ for scenario 9. Given the low technical maturity of the rWGS and SOEC, the 10,000 tons per year CO_2 capture and utilization project needs to be turned into reality so that process unit integration, heat integration, as well as operating conditions and dynamic modes, can be investigated and further developed. Such a pilot plant would verify the simulated results, which would allow a scale up of the process to apply it for different CO_2 point sources. A scale up is permissible, since all assumptions are not based on absolute but on relative mass. The mass flows in the reactors as well as the flashes result from scaling up with the same input-output ratio. It also leads to a reduction of the investment costs of the implemented equipment in the long-term due to learning effects and thus to a reduction of the NPC.

CRediT authorship contribution statement

C. Markowitsch: Conceptualization, Project administration, Methodology, Software, Evaluation, Validation, Roles/Writing – original draft; Writing – review & editing, **M. Lehner:** Conceptualization, Methodology, Evaluation, Validation, Writing – review & editing, **M. Maly:** Conceptualization, Validation, Supervision– review & editing.

Declaration of Competing Interest

The authors declare that they have no known competing financial interests or personal relationships that could have appeared to influence the work reported in this paper.

Data availability

Data will be made available on request.

Acknowledgements

This research was developed as a part of the “C2PAT – Carbon to product Austria” project. The financial support by Holcim Technology Ltd., Verbund Energy4Business GmbH, OMV AG and Borealis Polyolefine GmbH is gratefully acknowledged.

Appendix A. Supporting information

Supplementary data associated with this article can be found in the online version at doi:10.1016/j.jcou.2023.102449.

References

[1] Bundesministerium für Klimaschutz, Umwelt, Energie, Mobilität, Innovation und Technologie. Das Übereinkommen von Paris. [February 02, 2022]; Available from: https://www.oesterreich.gv.at/themen/bauen_wohnen_und_umwelt/klimaschutz/1/Seite.1000325.html.

[2] Spaun S., Bauer C., Dankl C., Friedle R., Papsch F. Roadmap zur CO2-Neutralität der österreichischen Zementindustrie bis 2050. Wien; 2022.

[3] Mauschitz G. Emissionen aus Anlagen der österreichischen Zementindustrie - Berichtsjahr 2020. Wien; 2021.

[4] Parlament Österreich. 158/ME (XXVII. GP) - Ökosoziales Steuerreformgesetz 2022 Teil I | Parlament Österreich. [January 15, 2022]; Available from: https://www.parlament.gv.at/PAKT/VHG/XXVII/ME/ME_00158/#.

[5] Umweltbundesamt Environment Agency Austria. Austria's National Inventory Report 2021 2021.

[6] Europäisches Parlament. Plastikmüll und Recycling in der EU: Zahlen und Fakten. [January 18, 2022]; Available from: https://www.europarl.europa.eu/news/de/headlines/society/20181212STO21610/plastikmull-und-recycling-in-der-eu-zahlen-und-fakten.

[7] GLOBAL 2000. Plastikatlas 2019: Daten und Fakten über eine Welt voller Kunststoffe. [January 18, 2022]; Available from: https://www.global2000.at/sites/global/files/2019-Plastikatlas-Oesterreich.pdf.

[8] König D.H. Techno-ökonomische Prozessbewertung der Herstellung synthetischen Flugturbinentreibstoffes aus CO2 und H2. Dissertation. Stuttgart; 2016.

[9] D.H. König, N. Baucks, R.-U. Dietrich, A. Wörner, Simulation and evaluation of a process concept for the generation of synthetic fuel from CO_2 and H2, Energy 91 (2015) 833–841.

[10] F.G. Albrecht, D.H. König, N. Baucks, R.-U. Dietrich, A standardized methodology for the techno-economic evaluation of alternative fuels – A case study, Fuel 194 (2017) 511–526.

[11] S. Adelung, S. Maier, R.-U. Dietrich, Impact of the reverse water-gas shift operating conditions on the Power-to-Liquid process efficiency, Sustain. Energy Technol. Assess. 43 (2021), 100897.

[12] S. Adelung, R.-U. Dietrich, Impact of the reverse water-gas shift operating conditions on the Power-to-Liquid fuel production cost, Fuel 317 (2022), 123440.

[13] Markowitsch C., Lehner M., Kitzweger J., Haider W., Ivanovici S., Unfried M. et al. [Conference EnInnov 2022 TU Graz] C2PAT - Carbon to Product Austria. [February 18, 2022]; Available from: https://www.tugraz.at/fileadmin/user_upload/tugrazExternal/738639ca-39a0–4129-b0f0–38b384c12b57/files/lf/Session_D6/464_LF_Markowitsch.pdf.

[14] O.Y. Elsernagawy, A. Hoadley, J. Patel, T. Bhatelia, S. Lim, N. Haque, et al., Thermo-economic analysis of reverse water-gas shift process with different temperatures for green methanol production as a hydrogen carrier, J. CO_2 Util. 41 (2020), 101280.

[15] S.T. Wismann, J.S. Engbæk, S.B. Vendelbo, F.B. Bendixen, W.L. Eriksen, K. Aasberg-Petersen, et al., Electrified methane reforming: A compact approach to greener industrial hydrogen production, Science 364 (6442) (2019) 756–759.

[16] Roddy D. (ed.). Advanced power plant materials, design and technology. Boca Raton, Fla, Oxford: Woodhead Pub. Ltd; 2010.

[17] Murzin D. Chemical Reaction Technology. 2nd ed. Berlin: De Gruyter; 2022.

[18] A. Trattner, M. Höglinger, M.-G. Macherhammer, M. Sartory, Renewable hydrogen: modular concepts from production over storage to the consumer, Chem. Ing. Tech. 93 (4) (2021) 706–716.

[19] R. Sakwattanapong, A. Aroonwilas, A. Veawab, Behavior of reboiler heat duty for CO_2 capture plants using regenerable single and blended alkanolamines, Ind. Eng. Chem. Res. 44 (12) (2005) 4465–4473.

[20] G.T. Rochelle, Thermal degradation of amines for CO_2 capture, Curr. Opin. Chem. Eng. 1 (2) (2012) 183–190.

[21] S. Zhou, S. Wang, C. Sun, C. Chen, SO2 effect on degradation of MEA and some other amines, Energy Procedia 37 (2013) 896–904.

[22] Tiktak W.J. Heat Management of PEM Electrolysis. Master thesis. Amsterdam, Netherlands; 2019.

[23] Sunfire GmbH. Sunfire Factsheet HyLink SOEC. [February 05, 2022]; Available from: https://www.sunfire.de/files/sunfire/images/content/Sunfire.de%20(neu)/Sunfire-Factsheet-HyLink-SOEC-20210303.pdf.

[24] J. Allen, S. Panquet, A. Bastiani, Electrochemical ammonia: power to ammonia ratio and balance of plant requirements for two different electrolysis approaches, Front. Chem. Eng. 3 (2021) 67.

[25] Unde R.B. Kinetics and Reaction Engineering Aspects of Syngas Production by the Heterogeneously Catalysed Reverse Water Gas Shift Reaction. Dissertation. Bayreuth; 2012.

[26] F. Vidal Vázquez, P. Pfeifer, J. Lehtonen, P. Piermartini, P. Simell, V. Alopaeus, Catalyst screening and kinetic modeling for CO production by high pressure and temperature reverse water gas shift for fischer–tropsch applications, Ind. Eng. Chem. Res. 56 (45) (2017) 13262–13272.

[27] H. Kirsch, U. Sommer, P. Pfeifer, R. Dittmeyer, Power-to-fuel conversion based on reverse water-gas-shift, Fischer-Tropsch Synthesis and Hydrocracking: Mathematical modeling and simulation in Matlab/Simulink, Chem. Eng. Sci. 227 (2020), 115930.

[28] L. Barelli, G. Bidini, G. Cinti, Steam vs. dry reformer: experimental study on a solid oxide fuel cell short stack, Catalysts 8 (12) (2018) 599.

[29] Klerk A. de Fischer-Tropsch Refining. 1st ed. Hoboken, NJ, Weinheim: Wiley; 2011.

[30] D. Förtsch, K. Pabst, E. Groß-Hardt, The product distribution in Fischer–Tropsch synthesis: an extension of the ASF model to describe common deviations, Chem. Eng. Sci. 138 (2015) 333–346.

[31] D. Vervloet, F. Kapteijn, J. Nijenhuis, J.R. van Ommen, Fischer–Tropsch reaction–diffusion in a cobalt catalyst particle: aspects of activity and selectivity for a variable chain growth probability, Catal. Sci. Technol 2 (6) (2012) 1221.

[32] M. Ostadi, E. Rytter, M. Hillestad, Evaluation of kinetic models for Fischer–Tropsch cobalt catalysts in a plug flow reactor, Chem. Eng. Res. Des. 114 (2016) 236–246.

[33] Shi F. Reactor and process design in sustainable energy technology. Amsterdam, Netherlands: Elsevier; 2014.

[34] AACE International Recommended Practices. Cost Estimate Classification System: AACE International Recommended Practice No. 18R-97; 2020.

[35] Wirtschaftskammer Österreich. Readiness Levels: Technologie - Innovation - Markt. [January 26, 2022]; Available from: https://www.wko.at/service/innovation-technologie-digitalisierung/readiness-levels-technologie-innovation-markt.html.

[36] IEA. Technology Roadmap Hydrogen and Fuel Cells. [December 22, 2021]; Available from: https://www.iea.org/reports/technology-roadmap-hydrogen-and-fuel-cells.

[37] C.H. Chilton, Cost data correlated, Chem. Eng. 56 (1949) 97–106.

[38] Energie-Control Austria für die Regulierung der Elektrizitäts- und Erdgaswirtschaft. Aktueller Marktpreis gemäß § 41 Ökostromgesetz. [October 13, 2022]; Available from: https://www.e-control.at/industrie/oeko-energie/oekostrommarkt/marktpreise-gem-paragraph-20.

[39] Hof am Leithaberge. Hof am Leithaberge - Wasserbezugsgebühr. [January 15, 2022]; Available from: http://www.hof-leithaberge.gv.at/Wasserbezugsgebuehr.

[40] T. Keipi, H. Tolvanen, J. Konttinen, Economic analysis of hydrogen production by methane thermal decomposition: Comparison to competing technologies, Energy Convers. Manag. 159 (2018) 264–273.

[41] Trading Economics. EU- Carbon Permits (EUR). [January 15, 2022]; Available from: https://tradingeconomics.com/commodity/carbon%20(13.01.2022).

[42] G. Herz, C. Rix, E. Jacobasch, N. Müller, E. Reichelt, M. Jahn, et al., Economic assessment of Power-to-Liquid processes – Influence of electrolysis technology and operating conditions, Appl. Energy 292 (2021), 116655.

[43] Luca Bertuccioli, Alvin Chan, David Hart, Franz Lehner, Ben Madden, Eleanor Standen (eds.). Development of Water Electrolysis in the European Union: Hydrogen Knowledge Centre; 2014.

[44] H. Böhm, M. Lehner, T. Kienberger, Techno-economic assessment of thermally integrated co-electrolysis and methanation for industrial closed carbon cycles, Front. Sustain 2 (2021) 77.

Evaluation of Process Structures and Reactor Technologies of an integrated Power-to-Liquid Plant at a Cement Factory

Christoph Markowitsch, Markus Lehner, Markus Maly

Supplementary Material

This supplementary material includes detailed ASPEN flow sheets, the heat integration (inclusive pinch analysis) and the detailed cost calculation of scenarios 1 and 9. Since 10,000 tons of CO_2 are processed in all scenarios, one carbon capture flow sheet inclusive mass balance for the carbon capture plant can be created for all scenarios.

1. Carbon Capture Unit

The carbon capture unit is simulated in ASPEN Plus V12.1® for an annual CO_2 capture of 10,000 tons. The operation conditions of the carbon capture unit are given in the manuscript in section "2.1 Amine scrubber unit". The flow sheet is given in Figure 1 with the associated mass balance in Table 1.

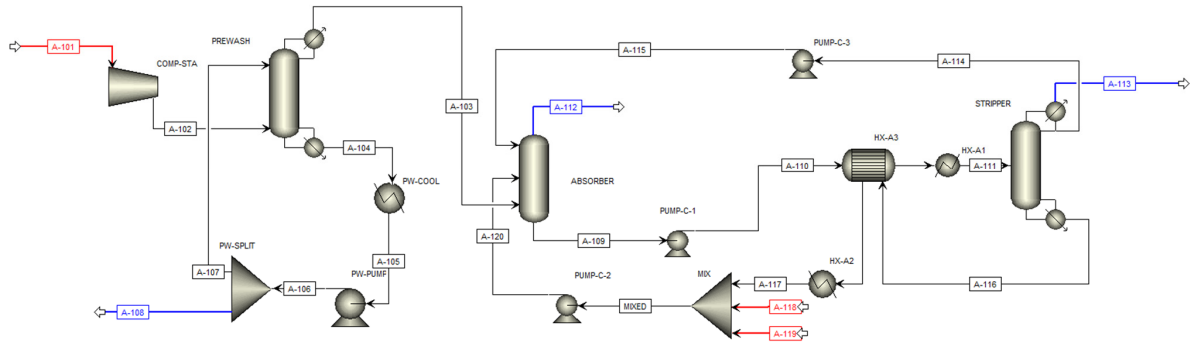

Figure 1: Flow sheet of the amine scrubber unit to capture 10,000 tons CO_2 per year

Table 1: Mass balance of the amine scrubber unit

Stream number	Units	A-101	A-102	A-103	A-104	A-105	A-106	A-107	A-108	A-109	A-110	A-111	A-112	A-113	A-114	A-115	A-116	A-117	A-118	A-119	A-120
Manuscript Stream		C-1							C-3				C-4	C-5					C-2		
Temperature	°C	110,0	169,0	40,0	60,3	20,0	20,0	20,0	20,0	46,1	45,4	85,0	64,6	40,0	40,0	40,3	104,3	40,0	20,0	20,0	39,2
Pressure	bar	1,0	1,5	1,1	1,1	1,1	1,5	1,5	1,5	1,1	1,1	1,1	1,0	1,0	1,0	1,1	1,1	1,1	1,1	1,1	1,1
Mole Flows	kmol/hr	227,3	227,3	213,9	501,8	501,8	501,8	488,3	13,5	853,0	852,9	854,7	226,5	31,0	10,6	10,6	839,9	839,9	43,6	0,0	883,5
Mass Flows	kg/hr	6686,0	6686,0	6443,4	9040,9	9040,9	9040,9	8798,3	242,6	22098,2	22098,2	22098,2	5926,0	1302,2	192,0	192,0	20604,0	20604,0	784,7	0,0	21388,7
CO	kg/hr	0,0	0,0	0,0	0,0	0,0	0,0	0,0	0,0	0,0	0,0	0,0	0,0	0,0	0,0	0,0	0,0	0,0	0,0	0,0	0,0
H2	kg/hr	0,0	0,0	0,0	0,0	0,0	0,0	0,0	0,0	0,0	0,0	0,0	0,0	0,0	0,0	0,0	0,0	0,0	0,0	0,0	0,0
H2O	kg/hr	504,1	504,1	262,5	9039,9	9039,9	9039,9	8797,3	242,5	13416,9	13353,9	13320,3	1005,7	41,6	191,5	191,4	13238,1	13261,3	784,7	0,0	14045,3
CO2	kg/hr	1390,5	1390,5	1389,7	0,9	0,9	0,9	0,9	0,0	2,2	0,7	77,2	130,3	1259,4	0,2	0,0	0,0	0,0	0,0	0,0	0,0
N2	kg/hr	4049,3	4049,3	4049,2	0,1	0,1	0,1	0,1	0,0	0,9	0,9	0,9	4048,3	0,9	0,0	0,0	0,0	0,0	0,0	0,0	0,0
O2	kg/hr	742,1	742,1	742,0	0,0	0,0	0,0	0,0	0,0	0,3	0,3	0,3	741,7	0,3	0,0	0,0	0,0	0,0	0,0	0,0	0,0
MEA	kg/hr	0,0	0,0	0,0	0,0	0,0	0,0	0,0	0,0	225,7	385,9	760,0	0,0	0,0	0,3	0,1	3551,0	3455,8	0,0	0,0	3456,7
MEA+	kg/hr	0,0	0,0	0,0	0,0	0,0	0,0	0,0	0,0	3257,0	3309,4	3152,6	0,0	0,0	0,0	0,3	1463,1	1479,9	0,0	0,0	1481,4
MEACOO-	kg/hr	0,0	0,0	0,0	0,0	0,0	0,0	0,0	0,0	4890,9	4529,9	4155,4	0,0	0,0	0,0	0,0	2231,2	2365,1	0,0	0,0	2361,2
HCO3-	kg/hr	0,0	0,0	0,0	0,0	0,0	0,0	0,0	0,0	276,0	440,2	601,9	0,0	0,0	0,0	0,2	111,8	16,7	0,0	0,0	17,6
CO3-2	kg/hr	0,0	0,0	0,0	0,0	0,0	0,0	0,0	0,0	28,3	76,9	29,6	0,0	0,0	0,0	0,0	8,7	25,0	0,0	0,0	26,5

2. Scenario 1

In this section, the flow sheet (Figure 2) includes the PEM electrolysis, the rWGS reactor and the Fischer Tropsch synthesis for scenario 1.
The feed (water) for the PEM electrolysis (modelled as stoichiometric reactor) is preheated by a heat exchanger (3-HX-1) and an electric heater (E-HEAT-1) to 75 °C (for a detailed description refer to manuscript chapter 2.2).
The rWGS reactor is modeled as a GIBBS reactor (950 °C, 10 barg). Waste heat of the rWGS reactor is used in the heat exchanger (1-HX-1) for feed-gas preheating (for a detailed description refer to manuscript chapter 2.3).
The Fischer Tropsch reactor is modelled as a stoichiometric reactor. The product follows the Anderson-Schulz-Flory (ASF) distribution with a chain growth probability of 0.92. CH_4 is excluded; here a selectivity of 16 % is assumed (for a detailed description refer to manuscript chapter 2.4).
The main reactions in the Fischer Tropsch synthesis are the methanation (equation 9 in manuscript) and Fischer-Tropsch reaction (equation 10 in manuscript) with an overall CO conversion of 40 %.
The input data of the ASPEN model is given for the methanation reaction and FT reaction in Table 2.

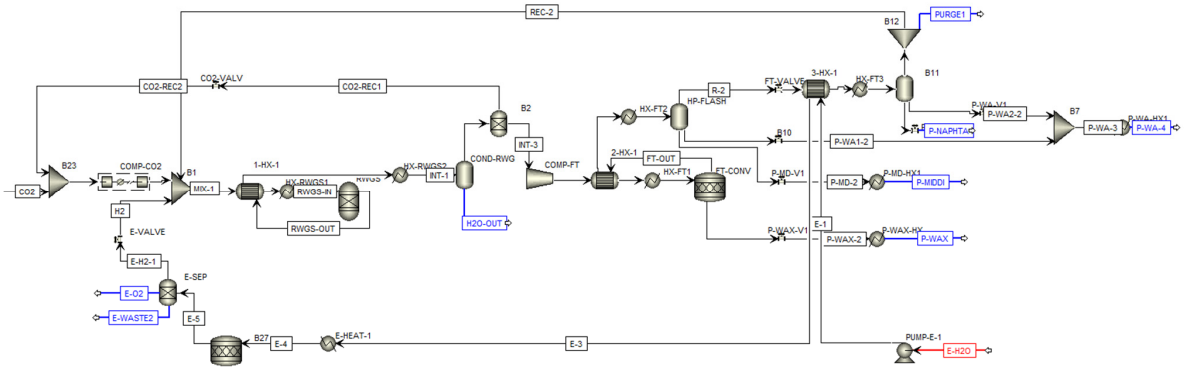

Figure 2: Flow sheet of scenario 1 (includes PEM electrolysis, rWGS reactor, Fischer Tropsch synthesis)

Table 2: Input data for the FTS in ASPEN Plus (methanation and FTS reaction)

Fischer Tropsch reaction (Equation 10 in manuscript)					
Component	Coefficient	Component	Coefficient	Component	Coefficient
CO	-1	H2O	1	C16H34	0,0018
H2	-2,08	CH4	0,0064	C17H36	0,0017
		C2H6	0,0059	C18H38	0,0016
		C3H8	0,0054	C19H40	0,0014
		C4H10	0,0050	C20H42	0,0013
		C5H12	0,0046	C21H44	0,0012
		C6H14	0,0042	C22H46	0,0011
		C7H16	0,0039	C23H48	0,0010
		C8H18	0,0036	C24H50	0,0009
		C9H20	0,0033	C25H52	0,0009
		C10H22	0,0030	C26H54	0,0008
		C11H24	0,0028	C27H56	0,0007
		C12H26	0,0026	C28H58	0,0007
		C13H28	0,0024	C29H60	0,0006
		C14H30	0,0022	C30H62	0,0006
		C15H32	0,0020	C30+	0,0066
Fractional conversion of 0.338 of component CO					

Methanation reaction (Equation 9 in manuscript)			
Component	Coefficient	Component	Coefficient
CO	-1	CH4	1
H2	-3	H2O	1
Fractional conversion of 0.062 of component CO			

The mass balance for flow sheet 2 is given in Table 3.

Table 3: Mass balance of Scenario 1 (excl. carbon capture unit)

Stream number		1	2	3	4	5	6	7	8	9	10	11	12	13	14	15
Mass balance	Units	CO2	E-1	E-4	E-5	E-H2-1	E-H2O	E-O2	E-WASTE2	FT-FEED	FT-OUT	H2	H2O-OUT	INT-1	INT-3	MIX-1
Temperature	°C	40,0	10,1	75,0	75,0	75,0	10,0	75,0	75,0	220,0	220,0	70,0	30,0	30,0	30,0	83,9
Pressure	bar	1,0	33,0	33,0	33,0	33,0	1,0	33,0	33,0	26,0	26,0	11,0	10,0	10,0	10,0	11,0
Mole Flows	kmol/hr	31,0	96,8	96,8	140,4	87,1	193,6	43,6	9,7	303,7	229,2	87,1	20,4	324,1	303,7	304,9
Mass Flows	kg/hr	1302,2	1744,1	1744,1	1744,1	175,7	3488,3	1394,1	174,4	3503,1	3272,2	175,7	367,1	3870,2	3503,1	3870,2
CO	kg/hr	0,0	0,0	0,0	0,0	0,0	0,0	0,0	0,0	2587,5	1552,3	0,0	0,0	2587,5	2587,5	1520,9
H2	kg/hr	0,0	0,0	0,0	175,7	175,7	0,0	0,0	0,0	387,3	221,8	175,7	0,0	387,4	387,4	393,0
H2O	kg/hr	41,6	1744,1	1744,1	174,4	0,0	3488,3	0,0	174,4	20,1	684,8	0,0	367,0	387,1	20,1	47,2
CO2	kg/hr	1259,4	0,0	0,0	0,0	0,0	0,0	0,0	0,0	313,3	313,2	0,0	0,0	313,3	313,3	1565,9
N2	kg/hr	0,9	0,0	0,0	0,0	0,0	0,0	0,0	0,0	45,8	45,8	0,0	0,0	45,8	45,8	45,8
O2	kg/hr	0,3	0,0	0,0	1394,1	0,0	0,0	1394,1	0,0	0,0	0,0	0,0	0,0	0,0	0,0	0,3
CH4	kg/hr	0,0	0,0	0,0	0,0	0,0	0,0	0,0	0,0	149,1	244,1	0,0	0,0	149,1	149,1	239,1
C2H6	kg/hr	0,0	0,0	0,0	0,0	0,0	0,0	0,0	0,0	0,0	5,5	0,0	0,0	0,0	0,0	5,4
C3H8	kg/hr	0,0	0,0	0,0	0,0	0,0	0,0	0,0	0,0	0,0	7,5	0,0	0,0	0,0	0,0	7,3
C4H10	kg/hr	0,0	0,0	0,0	0,0	0,0	0,0	0,0	0,0	0,0	9,0	0,0	0,0	0,0	0,0	8,7
C5H12	kg/hr	0,0	0,0	0,0	0,0	0,0	0,0	0,0	0,0	0,0	10,3	0,0	0,0	0,0	0,0	9,7
C6H14	kg/hr	0,0	0,0	0,0	0,0	0,0	0,0	0,0	0,0	0,0	11,3	0,0	0,0	0,0	0,0	9,8
C7H16	kg/hr	0,0	0,0	0,0	0,0	0,0	0,0	0,0	0,0	0,0	12,1	0,0	0,0	0,0	0,0	8,4
C8H18	kg/hr	0,0	0,0	0,0	0,0	0,0	0,0	0,0	0,0	0,0	12,6	0,0	0,0	0,0	0,0	5,3
C9H20	kg/hr	0,0	0,0	0,0	0,0	0,0	0,0	0,0	0,0	0,0	13,0	0,0	0,0	0,0	0,0	2,3
C10H22	kg/hr	0,0	0,0	0,0	0,0	0,0	0,0	0,0	0,0	0,0	13,1	0,0	0,0	0,0	0,0	0,7
C11H24	kg/hr	0,0	0,0	0,0	0,0	0,0	0,0	0,0	0,0	0,0	13,1	0,0	0,0	0,0	0,0	0,2
C12H26	kg/hr	0,0	0,0	0,0	0,0	0,0	0,0	0,0	0,0	0,0	13,0	0,0	0,0	0,0	0,0	0,0
C13H28	kg/hr	0,0	0,0	0,0	0,0	0,0	0,0	0,0	0,0	0,0	12,6	0,0	0,0	0,0	0,0	0,0
C14H30	kg/hr	0,0	0,0	0,0	0,0	0,0	0,0	0,0	0,0	0,0	12,0	0,0	0,0	0,0	0,0	0,0
C15H32	kg/hr	0,0	0,0	0,0	0,0	0,0	0,0	0,0	0,0	0,0	11,3	0,0	0,0	0,0	0,0	0,0
C16H34	kg/hr	0,0	0,0	0,0	0,0	0,0	0,0	0,0	0,0	0,0	10,3	0,0	0,0	0,0	0,0	0,0
C17H36	kg/hr	0,0	0,0	0,0	0,0	0,0	0,0	0,0	0,0	0,0	9,1	0,0	0,0	0,0	0,0	0,0
C18H38	kg/hr	0,0	0,0	0,0	0,0	0,0	0,0	0,0	0,0	0,0	7,9	0,0	0,0	0,0	0,0	0,0
C19H40	kg/hr	0,0	0,0	0,0	0,0	0,0	0,0	0,0	0,0	0,0	6,6	0,0	0,0	0,0	0,0	0,0
C20H42	kg/hr	0,0	0,0	0,0	0,0	0,0	0,0	0,0	0,0	0,0	5,3	0,0	0,0	0,0	0,0	0,0
C21H44	kg/hr	0,0	0,0	0,0	0,0	0,0	0,0	0,0	0,0	0,0	4,1	0,0	0,0	0,0	0,0	0,0
C22H46	kg/hr	0,0	0,0	0,0	0,0	0,0	0,0	0,0	0,0	0,0	3,2	0,0	0,0	0,0	0,0	0,0
C23H48	kg/hr	0,0	0,0	0,0	0,0	0,0	0,0	0,0	0,0	0,0	2,3	0,0	0,0	0,0	0,0	0,0
C24H50	kg/hr	0,0	0,0	0,0	0,0	0,0	0,0	0,0	0,0	0,0	1,6	0,0	0,0	0,0	0,0	0,0
C25H52	kg/hr	0,0	0,0	0,0	0,0	0,0	0,0	0,0	0,0	0,0	1,2	0,0	0,0	0,0	0,0	0,0
C26H54	kg/hr	0,0	0,0	0,0	0,0	0,0	0,0	0,0	0,0	0,0	0,8	0,0	0,0	0,0	0,0	0,0
C27H56	kg/hr	0,0	0,0	0,0	0,0	0,0	0,0	0,0	0,0	0,0	0,5	0,0	0,0	0,0	0,0	0,0
C28H58	kg/hr	0,0	0,0	0,0	0,0	0,0	0,0	0,0	0,0	0,0	0,4	0,0	0,0	0,0	0,0	0,0
C29H60	kg/hr	0,0	0,0	0,0	0,0	0,0	0,0	0,0	0,0	0,0	0,3	0,0	0,0	0,0	0,0	0,0
C30H62	kg/hr	0,0	0,0	0,0	0,0	0,0	0,0	0,0	0,0	0,0	0,2	0,0	0,0	0,0	0,0	0,0
C30+	kg/hr	0,0	0,0	0,0	0,0	0,0	0,0	0,0	0,0	0,0	0,1	0,0	0,0	0,0	0,0	0,0

Stream number		16	17	18	19	20	21	22	23	24	25	26	27	28	29	30
Mass balance	Units	P-MIDDI	P-NAPHTA	P-WA1-2	P-WA2-2	P-WA-4	P-WAX	PURGE1	R-1	R-2	R-3	R-4	R-5	REC-1	RWGS-IN	RWGS-OUT
Temperature	°C	40,0	20,3	100,4	20,1	60,0	40,0	20,0	100,0	100,0	99,1	20,0	20,0	20,0	950,0	950,0
Pressure	bar	5,0	5,0	5,0	5,0	5,0	1,0	12,0	26,0	26,0	12,0	12,0	12,0	12,0	11,0	11,0
Mole Flows	kmol/hr	0,6	0,3	30,2	7,4	37,7	0,6	3,8	229,2	198,3	198,3	198,3	190,6	186,8	304,9	324,1
Mass Flows	kg/hr	112,0	40,5	544,6	134,0	678,6	230,8	48,8	3272,2	2615,6	2615,6	2615,6	2441,1	2392,3	3870,2	3870,2
CO	kg/hr	0,2	0,1	0,0	0,0	0,0	0,2	31,0	1552,3	1552,0	1552,0	1552,0	1552,0	1520,9	1520,9	2587,5
H2	kg/hr	0,0	0,0	0,0	0,0	0,0	0,0	4,4	221,8	221,8	221,8	221,8	221,7	217,3	393,0	387,4
H2O	kg/hr	0,5	0,0	544,6	133,9	678,5	0,9	0,1	684,8	139,7	139,7	139,7	5,7	5,6	47,2	387,1
CO2	kg/hr	0,2	0,1	0,0	0,0	0,0	0,1	6,3	313,2	312,9	312,9	312,9	312,8	306,5	1565,9	313,3
N2	kg/hr	0,0	0,0	0,0	0,0	0,0	0,0	0,9	45,8	45,8	45,8	45,8	45,8	44,9	45,8	45,8
O2	kg/hr	0,0	0,0	0,0	0,0	0,0	0,0	0,0	0,0	0,0	0,0	0,0	0,0	0,0	0,3	0,0
CH4	kg/hr	0,1	0,0	0,0	0,0	0,0	0,1	4,9	244,1	244,0	244,0	244,0	244,0	239,1	239,1	149,1
C2H6	kg/hr	0,0	0,0	0,0	0,0	0,0	0,0	0,1	5,5	5,5	5,5	5,5	5,5	5,4	5,4	0,0
C3H8	kg/hr	0,0	0,0	0,0	0,0	0,0	0,0	0,1	7,5	7,4	7,4	7,4	7,4	7,3	7,3	0,0
C4H10	kg/hr	0,0	0,1	0,0	0,0	0,0	0,0	0,2	9,0	9,0	9,0	9,0	8,9	8,7	8,7	0,0
C5H12	kg/hr	0,1	0,3	0,0	0,0	0,0	0,0	0,2	10,3	10,2	10,2	10,2	9,9	9,7	9,7	0,0
C6H14	kg/hr	0,3	1,0	0,0	0,0	0,0	0,0	0,2	11,3	11,0	11,0	11,0	10,0	9,8	9,8	0,0
C7H16	kg/hr	0,7	2,8	0,0	0,0	0,0	0,1	0,2	12,1	11,4	11,4	11,4	8,6	8,4	8,4	0,0
C8H18	kg/hr	1,4	5,8	0,0	0,0	0,0	0,1	0,1	12,6	11,2	11,2	11,2	5,4	5,3	5,3	0,0
C9H20	kg/hr	2,7	7,9	0,0	0,0	0,0	0,2	0,0	13,0	10,3	10,3	10,3	2,4	2,3	2,3	0,0
C10H22	kg/hr	4,6	7,8	0,0	0,0	0,0	0,3	0,0	13,1	8,5	8,5	8,5	0,8	0,7	0,7	0,0
C11H24	kg/hr	6,7	6,2	0,0	0,0	0,0	0,4	0,0	13,1	6,4	6,4	6,4	0,2	0,2	0,2	0,0
C12H26	kg/hr	8,8	4,1	0,0	0,0	0,0	0,6	0,0	13,0	4,1	4,1	4,1	0,1	0,0	0,0	0,0
C13H28	kg/hr	10,5	2,1	0,0	0,0	0,0	1,0	0,0	12,6	2,1	2,1	2,1	0,0	0,0	0,0	0,0
C14H30	kg/hr	10,9	1,1	0,0	0,0	0,0	1,4	0,0	12,0	1,1	1,1	1,1	0,0	0,0	0,0	0,0
C15H32	kg/hr	10,7	0,6	0,0	0,0	0,0	1,9	0,0	11,3	0,6	0,6	0,6	0,0	0,0	0,0	0,0
C16H34	kg/hr	10,0	0,3	0,0	0,0	0,0	2,6	0,0	10,3	0,3	0,3	0,3	0,0	0,0	0,0	0,0
C17H36	kg/hr	9,0	0,1	0,0	0,0	0,0	3,5	0,0	9,1	0,1	0,1	0,1	0,0	0,0	0,0	0,0
C18H38	kg/hr	7,9	0,1	0,0	0,0	0,0	4,4	0,0	7,9	0,1	0,1	0,1	0,0	0,0	0,0	0,0
C19H40	kg/hr	6,6	0,0	0,0	0,0	0,0	5,4	0,0	6,6	0,0	0,0	0,0	0,0	0,0	0,0	0,0
C20H42	kg/hr	5,2	0,0	0,0	0,0	0,0	6,3	0,0	5,3	0,0	0,0	0,0	0,0	0,0	0,0	0,0
C21H44	kg/hr	4,1	0,0	0,0	0,0	0,0	7,1	0,0	4,1	0,0	0,0	0,0	0,0	0,0	0,0	0,0
C22H46	kg/hr	3,2	0,0	0,0	0,0	0,0	7,6	0,0	3,2	0,0	0,0	0,0	0,0	0,0	0,0	0,0
C23H48	kg/hr	2,3	0,0	0,0	0,0	0,0	8,1	0,0	2,3	0,0	0,0	0,0	0,0	0,0	0,0	0,0
C24H50	kg/hr	1,6	0,0	0,0	0,0	0,0	8,3	0,0	1,6	0,0	0,0	0,0	0,0	0,0	0,0	0,0
C25H52	kg/hr	1,2	0,0	0,0	0,0	0,0	8,4	0,0	1,2	0,0	0,0	0,0	0,0	0,0	0,0	0,0
C26H54	kg/hr	0,8	0,0	0,0	0,0	0,0	8,3	0,0	0,8	0,0	0,0	0,0	0,0	0,0	0,0	0,0
C27H56	kg/hr	0,5	0,0	0,0	0,0	0,0	8,2	0,0	0,5	0,0	0,0	0,0	0,0	0,0	0,0	0,0
C28H58	kg/hr	0,4	0,0	0,0	0,0	0,0	7,9	0,0	0,4	0,0	0,0	0,0	0,0	0,0	0,0	0,0
C29H60	kg/hr	0,3	0,0	0,0	0,0	0,0	7,6	0,0	0,3	0,0	0,0	0,0	0,0	0,0	0,0	0,0
C30H62	kg/hr	0,2	0,0	0,0	0,0	0,0	7,3	0,0	0,2	0,0	0,0	0,0	0,0	0,0	0,0	0,0
C30+	kg/hr	0,1	0,0	0,0	0,0	0,0	122,4	0,0	0,1	0,0	0,0	0,0	0,0	0,0	0,0	0,0

The cold and hot streams (includes carbon capture unit, PEM electrolysis, rWGS and FTS) are summarized in Table 4. Negative enthalpy defines cooling demand, positive enthalpy needs energy supply.

Table 4: Compilation of cold and hot streams of scenario 1

Input stream	Output stream	Inlet Temperature	Outlet Temperature	Enthalpy
		[°C]	[°C]	[kW]
FT-OUT	R-1	220,0	100,0	-150,5
R-3	R-4	100,0	20,0	-731,7
A-116	A-117	104,3	40,0	-1311,2
INT-5	FT-FEED	160,4	220,0	150,5
RWGS-OUT	INT-1	950,0	30,0	-2904,0
MIX-1	RWGS-IN	95,6	950,0	2524,0
A-110	A-111	45,4	85,0	860,7
P-MD-2	P-MIDDI	100,0	40,0	-4,1
A-104	A-105	60,3	20,0	-423,6
E-1	E-4	11,7	75,0	139,7
P-WA-3	P-WA-4	20,1	60,0	33,6
P-WAX-2	P-WAX	220,4	40,0	-27,2
Reboiler Stripper	heat	102,6	104,3	1500,0
Condenser Stripp	cooling	87,2	40,0	-435,7
Flash	cooling	20,0	19,5	-9,2
RWGS	heat	950,0	950,5	777,5
FT-CONV	cooling	220,0	219,5	-1738,0
Electrolysis	cooling	75,0	74,9	-1560,0

The pinch analysis is performed for heat integration. For scenario 1, additional heat in form of steam can be produced according to Figure 3 (balanced composite curves), the remainder must be cooled by cooling water.

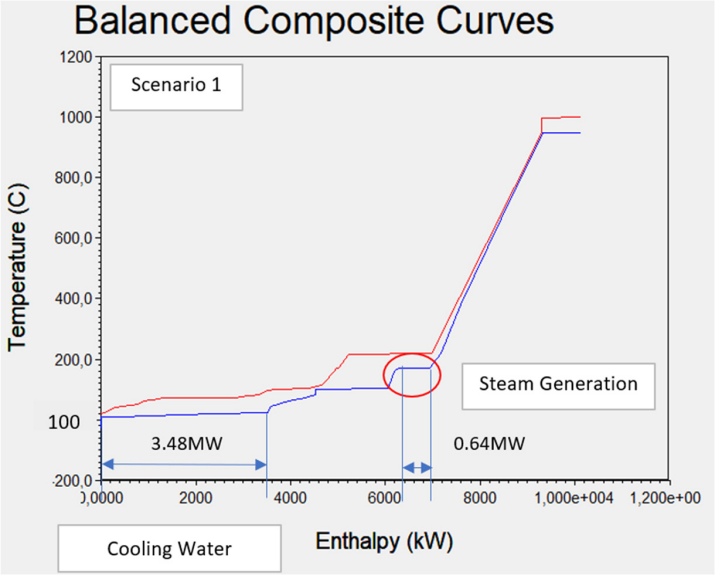

Figure 3: Balanced composite curves of scenario 1 with differentiation between cooling water and steam generation

The calculated equipment costs (EC), as well as the calculation of the intermediate costs (IT) and total investment costs (TIC) are given for scenario 1 in Table 5. Furthermore, a comparison with the Lang Factor for liquids (TIC = ECx4.84) is applied.

Table 5: Cost calculation and listing of EC, IT and TIC for scenario 1

CARBON CAPTURE UNIT Equipment Simulation	Equipment Description	EC Equipment Cost [EUR]	R1 Equipment installation [EUR]	R2+R3 Process Piping [EUR]	R4 Instrument-ation [EUR]	R5 Builing and construction [EUR]	R6 Auxiliary systems [EUR]	R7 Outside lines [EUR]	IT [EUR]	R8 Engineering [EUR]	R9 Risk and unforseen [EUR]	R10 Size factor [EUR]	TIC [EUR]
			1,15	0,35	0,15	0,2	0,15	0,15		0,4	0,2	0,5	
HX-A1	Heat Exchanger	51 600	59 340	20 769	8 901	11 868	8 901	8 901	118 680	47 472	23 736	59 340	249 228
HX-A2	Heat Exchanger	21 800	25 070	8 775	3 761	5 014	3 761	3 761	50 140	20 056	10 028	25 070	105 294
HX-A3	Heat Exchanger	83 900	96 485	33 770	14 473	19 297	14 473	14 473	192 970	77 188	38 594	96 485	405 237
PREWASH-tower	Column	60 500	69 575	24 351	10 436	13 915	10 436	10 436	139 150	55 660	27 830	69 575	292 215
PUMP-C-1	Pump	7 400	8 510	2 979	1 277	1 702	1 277	1 277	17 020	6 808	3 404	8 510	35 742
PUMP-C-2	Pump	8 400	9 660	3 381	1 449	1 932	1 449	1 449	19 320	7 728	3 864	9 660	40 572
PUMP-C-3	Pump	5 700	6 555	2 294	983	1 311	983	983	13 110	5 244	2 622	6 555	27 531
PW-COOL	Heat Exchanger	18 400	21 160	7 406	3 174	4 232	3 174	3 174	42 320	16 928	8 464	21 160	88 872
PW-PUMP	Pump	6 600	7 590	2 657	1 139	1 518	1 139	1 139	15 180	6 072	3 036	7 590	31 878
STRIPPER-cond	Heat Exchanger	12 900	14 835	5 192	2 225	2 967	2 225	2 225	29 670	11 868	5 934	14 835	62 307
STRIPPER-cond acc	Drum	21 200	24 380	8 533	3 657	4 876	3 657	3 657	48 760	19 504	9 752	24 380	102 396
STRIPPER-reb	Reboiler	20 500	23 575	8 251	3 536	4 715	3 536	3 536	47 150	18 860	9 430	23 575	99 015
STRIPPER-reflux pump	Pump	5 700	6 555	2 294	983	1 311	983	983	13 110	5 244	2 622	6 555	27 531
STRIPPER-tower	Tower	199 200	229 080	80 178	34 362	45 816	34 362	34 362	458 160	183 264	91 632	229 080	962 136
ABSORBER-tower	Tower	423 900	487 485	170 620	73 123	97 497	73 123	73 123	974 970	389 988	194 994	487 485	2 047 437
COMP-STA	Blower	155 100	178 365	62 428	26 755	35 673	26 755	26 755	356 730	142 692	71 346	178 365	749 133
Total Carbon Capture Unit		**1 102 800**							**2 536 440**				**5 326 524**
												Calculation with Lang Factor (ECx4.84):	**5 337 552**

SYNTHESIS UNIT Equipment Simulation	Equipment Description	EC Equipment Cost [EUR]	R1 Equipment installation [EUR]	R2+R3 Process Piping [EUR]	R4 Instrument-ation [EUR]	R5 Builing and construction [EUR]	R6 Auxiliary systems [EUR]	R7 Outside lines [EUR]	IT [EUR]	R8 Engineering [EUR]	R9 Risk and unforseen [EUR]	R10 Size factor [EUR]	TIC [EUR]
			1,15	0,35	0,15	0,2	0,15	0,15		0,4	0,2	0,5	
1-HX-1	Heat Exchanger	97 900	112 585	39 405	16 888	22 517	16 888	16 888	225 170	90 068	45 034	112 585	472 857
1-HX-2	Heat Exchanger	23 800	27 370	9 580	4 106	5 474	4 106	4 106	54 740	21 896	10 948	27 370	114 954
1-HX-3	Heat Exchanger	18 300	21 045	7 366	3 157	4 209	3 157	3 157	42 090	16 836	8 418	21 045	88 389
2-HX-1	Heat Exchanger	18 700	21 505	7 527	3 226	4 301	3 226	3 226	43 010	17 204	8 602	21 505	90 321
2-HX-3	Heat Exchanger	9 700	11 155	3 904	1 673	2 231	1 673	1 673	22 310	8 924	4 462	11 155	46 851
2-HX-2	Heat Exchanger	12 400	14 260	4 991	2 139	2 852	2 139	2 139	28 520	11 408	5 704	14 260	59 892
3-HX-1	Heat Exchanger	13 800	15 870	5 555	2 381	3 174	2 381	2 381	31 740	12 696	6 348	15 870	66 654
3-HX-2	Heat Exchanger	10 700	12 305	4 307	1 846	2 461	1 846	1 846	24 610	9 844	4 922	12 305	51 681
3-HX-3	Heat Exchanger	14 900	17 135	5 997	2 570	3 427	2 570	2 570	34 270	13 708	6 854	17 135	71 967
COMP-FT	Compressor	1 361 500	1 565 725	548 004	234 859	313 145	234 859	234 859	3 131 450	1 252 580	626 290	1 565 725	6 576 045
COND-RWG-flash vessel	Drum	21 900	25 185	8 815	3 778	5 037	3 778	3 778	50 370	20 148	10 074	25 185	105 777
HP-FLASH-flash vessel	Drum	27 000	31 050	10 868	4 658	6 210	4 658	4 658	62 100	24 840	12 420	31 050	130 410
P-WAX-HX	Heat Exchanger	9 600	11 040	3 864	1 656	2 208	1 656	1 656	22 080	8 832	4 416	11 040	46 368
PUMP-E-1	Pump	96 300	110 745	38 761	16 612	22 149	16 612	16 612	221 490	88 596	44 298	110 745	465 129
B11-flash vessel	Drum	21 900	25 185	8 815	3 778	5 037	3 778	3 778	50 370	20 148	10 074	25 185	105 777
COMP-CO2	Compressor	1 090 600	1 254 190	438 967	188 129	250 838	188 129	188 129	2 508 380	1 003 352	501 676	1 254 190	5 267 598
Fischer-Tropsch-Reactor	Reactor	180 000	207 000	72 450	31 050	41 400	31 050	31 050	414 000	165 600	82 800	207 000	869 400
rWGS-Reactor	Reactor	1 616 898	1 859 433	650 801	278 915	371 887	278 915	278 915	3 718 865	1 487 546	743 773	1 859 433	7 809 617
Total Synthesis Unit		**4 645 898**							**10 685 565**				**22 439 687**
												Calculation with Lang Factor (ECx4.84):	**22 486 146**

ELECTROLYSER UNIT Equipment Simulation	Power demand [kW]	Specific Costs [EUR/kW]	R1 Equipment installation [EUR]	R2+R3 Process Piping [EUR]	R4 Instrumentat ion [EUR]	R5 Builing and construction [EUR]	R6 Auxiliary systems [EUR]	R7 Outside lines [EUR]	IT [EUR]	R8 Engineering [EUR]	R9 Risk and unforseen [EUR]	R10 Size factor [EUR]	TIC [EUR]
				0,15	0,00	0,20	0,10	0,00		0,00	0,00	0,00	
Electrolysis	9177	1 400	12 847 800	1 927 170	-	2 569 560	1 284 780	-	18 629 310	-	-	-	18 629 310
Total Electrolysis Unit									**18 629 310**				**18 629 310**

Total Investment Costs	[EUR]
Carbon capture unit	5 326 524
Synthesis unit	22 439 687
Electrolysis unit	18 629 310
Total	**46 395 521**

3. Scenario 9

In this section, the flow sheet (Figure 4) for scenario 9 includes the SOEC electrolysis, the rWGS reactor and the Fischer Tropsch synthesis.

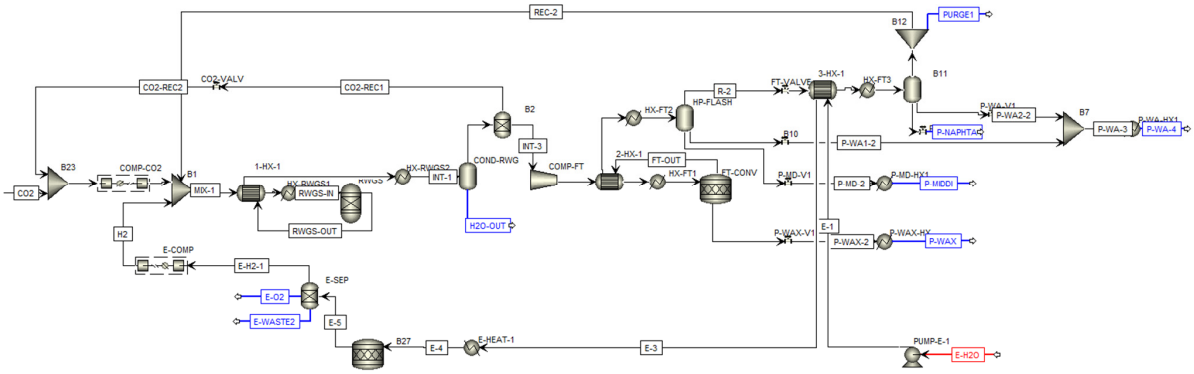

Figure 4: Flow sheet of scenario 9 (includes SOEC, rWGS reactor, Fischer Tropsch synthesis)

The mass balance for scenario 9 is given in Table 9. The carbon capture unit has the same mass balance as stated in Table 1.

Table 6: Mass balance of scenario 9 (excl. carbon capture unit)

Stream number		1	2	3	4	5	6	7	8	9	10	11	12	13	14	15
Mass Balance	Units	CO2	E-2	E-4	E-5	E-H2-2	E-H2O	E-O2	E-WASTE2	FT-FEED	FT-OUT	H2	H2O-OUT	INT-1	INT-3	MIX-1
Temperature	C	40,0	10,1	159,8	160,0	241,6	10,0	160,0	160,0	220,0	220,0	241,6	30,0	30,0	30,0	129,6
Pressure	bar	1,0	2,5	6,0	2,0	11,0	1,0	2,0	2,0	26,0	26,0	11,0	10,0	10,0	10,0	11,0
Mole Flows	kmol/hr	31,0	96,7	96,7	140,2	87,0	193,3	43,5	9,7	302,8	228,3	87,0	20,4	323,1	302,7	303,9
Mass Flows	kg/hr	1302,2	1741,4	1741,4	1741,4	175,4	3482,8	1391,9	174,1	3501,3	3270,4	175,4	367,0	3868,3	3501,3	3868,3
CO	kg/hr	0,0	0,0	0,0	0,0	0,0	0,0	0,0	0,0	2587,3	1552,1	0,0	0,0	2587,3	2587,3	1520,8
H2	kg/hr	0,0	0,0	0,0	175,4	175,4	0,0	0,0	0,0	385,6	220,1	175,4	0,0	385,5	385,5	391,0
H2O	kg/hr	41,6	1741,4	1741,4	174,1	0,0	3482,8	0,0	174,1	20,0	684,7	0,0	367,0	387,0	20,0	47,2
CO2	kg/hr	1259,4	0,0	0,0	0,0	0,0	0,0	0,0	0,0	314,6	314,5	0,0	0,0	314,7	314,7	1567,2
N2	kg/hr	0,9	0,0	0,0	0,0	0,0	0,0	0,0	0,0	45,9	45,9	0,0	0,0	45,9	45,9	45,9
O2	kg/hr	0,3	0,0	0,0	1391,9	0,0	0,0	1391,9	0,0	0,0	0,0	0,0	0,0	0,0	0,0	0,3
CH4	kg/hr	0,0	0,0	0,0	0,0	0,0	0,0	0,0	0,0	147,9	243,0	0,0	0,0	147,9	147,9	238,0
C2H6	kg/hr	0,0	0,0	0,0	0,0	0,0	0,0	0,0	0,0	0,0	5,5	0,0	0,0	0,0	0,0	5,4
C3H8	kg/hr	0,0	0,0	0,0	0,0	0,0	0,0	0,0	0,0	0,0	7,5	0,0	0,0	0,0	0,0	7,3
C4H10	kg/hr	0,0	0,0	0,0	0,0	0,0	0,0	0,0	0,0	0,0	9,0	0,0	0,0	0,0	0,0	8,7
C5H12	kg/hr	0,0	0,0	0,0	0,0	0,0	0,0	0,0	0,0	0,0	10,3	0,0	0,0	0,0	0,0	9,7
C6H14	kg/hr	0,0	0,0	0,0	0,0	0,0	0,0	0,0	0,0	0,0	11,3	0,0	0,0	0,0	0,0	9,8
C7H16	kg/hr	0,0	0,0	0,0	0,0	0,0	0,0	0,0	0,0	0,0	12,1	0,0	0,0	0,0	0,0	8,4
C8H18	kg/hr	0,0	0,0	0,0	0,0	0,0	0,0	0,0	0,0	0,0	12,6	0,0	0,0	0,0	0,0	5,3
C9H20	kg/hr	0,0	0,0	0,0	0,0	0,0	0,0	0,0	0,0	0,0	13,0	0,0	0,0	0,0	0,0	2,3
C10H22	kg/hr	0,0	0,0	0,0	0,0	0,0	0,0	0,0	0,0	0,0	13,1	0,0	0,0	0,0	0,0	0,7
C11H24	kg/hr	0,0	0,0	0,0	0,0	0,0	0,0	0,0	0,0	0,0	13,1	0,0	0,0	0,0	0,0	0,2
C12H26	kg/hr	0,0	0,0	0,0	0,0	0,0	0,0	0,0	0,0	0,0	13,0	0,0	0,0	0,0	0,0	0,0
C13H28	kg/hr	0,0	0,0	0,0	0,0	0,0	0,0	0,0	0,0	0,0	12,6	0,0	0,0	0,0	0,0	0,0
C14H30	kg/hr	0,0	0,0	0,0	0,0	0,0	0,0	0,0	0,0	0,0	12,0	0,0	0,0	0,0	0,0	0,0
C15H32	kg/hr	0,0	0,0	0,0	0,0	0,0	0,0	0,0	0,0	0,0	11,3	0,0	0,0	0,0	0,0	0,0
C16H34	kg/hr	0,0	0,0	0,0	0,0	0,0	0,0	0,0	0,0	0,0	10,3	0,0	0,0	0,0	0,0	0,0
C17H36	kg/hr	0,0	0,0	0,0	0,0	0,0	0,0	0,0	0,0	0,0	9,1	0,0	0,0	0,0	0,0	0,0
C18H38	kg/hr	0,0	0,0	0,0	0,0	0,0	0,0	0,0	0,0	0,0	7,9	0,0	0,0	0,0	0,0	0,0
C19H40	kg/hr	0,0	0,0	0,0	0,0	0,0	0,0	0,0	0,0	0,0	6,6	0,0	0,0	0,0	0,0	0,0
C20H42	kg/hr	0,0	0,0	0,0	0,0	0,0	0,0	0,0	0,0	0,0	5,2	0,0	0,0	0,0	0,0	0,0
C21H44	kg/hr	0,0	0,0	0,0	0,0	0,0	0,0	0,0	0,0	0,0	4,1	0,0	0,0	0,0	0,0	0,0
C22H46	kg/hr	0,0	0,0	0,0	0,0	0,0	0,0	0,0	0,0	0,0	3,2	0,0	0,0	0,0	0,0	0,0
C23H48	kg/hr	0,0	0,0	0,0	0,0	0,0	0,0	0,0	0,0	0,0	2,3	0,0	0,0	0,0	0,0	0,0
C24H50	kg/hr	0,0	0,0	0,0	0,0	0,0	0,0	0,0	0,0	0,0	1,6	0,0	0,0	0,0	0,0	0,0
C25H52	kg/hr	0,0	0,0	0,0	0,0	0,0	0,0	0,0	0,0	0,0	1,2	0,0	0,0	0,0	0,0	0,0
C26H54	kg/hr	0,0	0,0	0,0	0,0	0,0	0,0	0,0	0,0	0,0	0,8	0,0	0,0	0,0	0,0	0,0
C27H56	kg/hr	0,0	0,0	0,0	0,0	0,0	0,0	0,0	0,0	0,0	0,5	0,0	0,0	0,0	0,0	0,0
C28H58	kg/hr	0,0	0,0	0,0	0,0	0,0	0,0	0,0	0,0	0,0	0,4	0,0	0,0	0,0	0,0	0,0
C29H60	kg/hr	0,0	0,0	0,0	0,0	0,0	0,0	0,0	0,0	0,0	0,3	0,0	0,0	0,0	0,0	0,0
C30H62	kg/hr	0,0	0,0	0,0	0,0	0,0	0,0	0,0	0,0	0,0	0,2	0,0	0,0	0,0	0,0	0,0
C30+	kg/hr	0,0	0,0	0,0	0,0	0,0	0,0	0,0	0,0	0,0	0,1	0,0	0,0	0,0	0,0	0,0

Stream number		16	17	18	19	20	21	22	23	24	25	26	27	28	29	30
Mass Balance	Units	P-MIDDI	P-NAPHTA	P-WA1-2	P-WA2-2	P-WA-4	P-WAX	PURGE1	R-1	R-2	R-3	R-4	R-5	REC-2	RWGS-IN	RWGS-OUT
Temperature	C	40,0	20,3	100,4	20,1	60,0	40,0	20,0	100,0	100,0	99,1	20,0	20,0	20,0	950,0	950,0
Pressure	bar	5,0	5,0	5,0	5,0	5,0	1,0	12,0	26,0	26,0	12,0	12,0	12,0	12,0	11,0	11,0
Mole Flows	kmol/hr	0,6	0,3	30,3	7,4	37,7	0,6	3,8	228,3	197,4	197,4	197,4	189,7	185,9	303,9	323,1
Mass Flows	kg/hr	111,9	40,5	545,2	133,3	678,5	230,9	48,8	3270,4	2613,3	2613,3	2613,3	2439,5	2390,7	3868,3	3868,3
CO	kg/hr	0,2	0,1	0,0	0,0	0,0	0,2	31,0	1552,1	1551,9	1551,9	1551,9	1551,8	1520,8	1520,8	2587,3
H2	kg/hr	0,0	0,0	0,0	0,0	0,0	0,0	4,4	220,1	220,1	220,1	220,1	220,0	215,6	391,0	385,5
H2O	kg/hr	0,5	0,0	545,1	133,3	678,5	0,9	0,1	684,7	139,1	139,1	139,1	5,7	5,6	47,2	387,0
CO2	kg/hr	0,2	0,1	0,0	0,0	0,0	0,1	6,3	314,5	314,2	314,2	314,2	314,1	307,8	1567,2	314,7
N2	kg/hr	0,0	0,0	0,0	0,0	0,0	0,0	0,9	45,9	45,8	45,8	45,8	45,8	44,9	45,9	45,9
O2	kg/hr	0,0	0,0	0,0	0,0	0,0	0,0	0,0	0,0	0,0	0,0	0,0	0,0	0,0	0,3	0,0
CH4	kg/hr	0,1	0,0	0,0	0,0	0,0	0,1	4,9	243,0	242,9	242,9	242,9	242,8	238,0	238,0	147,9
C2H6	kg/hr	0,0	0,0	0,0	0,0	0,0	0,0	0,1	5,5	5,5	5,5	5,5	5,5	5,4	5,4	0,0
C3H8	kg/hr	0,0	0,0	0,0	0,0	0,0	0,0	0,1	7,5	7,4	7,4	7,4	7,4	7,3	7,3	0,0
C4H10	kg/hr	0,0	0,1	0,0	0,0	0,0	0,0	0,2	9,0	9,0	9,0	9,0	8,9	8,7	8,7	0,0
C5H12	kg/hr	0,1	0,3	0,0	0,0	0,0	0,0	0,2	10,3	10,2	10,2	10,2	9,9	9,7	9,7	0,0
C6H14	kg/hr	0,3	1,0	0,0	0,0	0,0	0,0	0,2	11,3	11,0	11,0	11,0	10,0	9,8	9,8	0,0
C7H16	kg/hr	0,7	2,8	0,0	0,0	0,0	0,1	0,2	12,1	11,4	11,4	11,4	8,6	8,4	8,4	0,0
C8H18	kg/hr	1,4	5,8	0,0	0,0	0,0	0,1	0,1	12,6	11,2	11,2	11,2	5,4	5,3	5,3	0,0
C9H20	kg/hr	2,7	7,9	0,0	0,0	0,0	0,2	0,0	13,0	10,3	10,3	10,3	2,4	2,3	2,3	0,0
C10H22	kg/hr	4,6	7,7	0,0	0,0	0,0	0,3	0,0	13,1	8,5	8,5	8,5	0,8	0,7	0,7	0,0
C11H24	kg/hr	6,7	6,2	0,0	0,0	0,0	0,4	0,0	13,1	6,4	6,4	6,4	0,2	0,2	0,2	0,0
C12H26	kg/hr	8,8	4,1	0,0	0,0	0,0	0,6	0,0	13,0	4,1	4,1	4,1	0,1	0,0	0,0	0,0
C13H28	kg/hr	10,5	2,1	0,0	0,0	0,0	1,0	0,0	12,6	2,1	2,1	2,1	0,0	0,0	0,0	0,0
C14H30	kg/hr	10,9	1,1	0,0	0,0	0,0	1,4	0,0	12,0	1,1	1,1	1,1	0,0	0,0	0,0	0,0
C15H32	kg/hr	10,7	0,6	0,0	0,0	0,0	2,0	0,0	11,3	0,6	0,6	0,6	0,0	0,0	0,0	0,0
C16H34	kg/hr	10,0	0,3	0,0	0,0	0,0	2,6	0,0	10,3	0,3	0,3	0,3	0,0	0,0	0,0	0,0
C17H36	kg/hr	9,0	0,1	0,0	0,0	0,0	3,5	0,0	9,1	0,1	0,1	0,1	0,0	0,0	0,0	0,0
C18H38	kg/hr	7,8	0,1	0,0	0,0	0,0	4,4	0,0	7,9	0,1	0,1	0,1	0,0	0,0	0,0	0,0
C19H40	kg/hr	6,6	0,0	0,0	0,0	0,0	5,4	0,0	6,6	0,0	0,0	0,0	0,0	0,0	0,0	0,0
C20H42	kg/hr	5,2	0,0	0,0	0,0	0,0	6,3	0,0	5,2	0,0	0,0	0,0	0,0	0,0	0,0	0,0
C21H44	kg/hr	4,1	0,0	0,0	0,0	0,0	7,1	0,0	4,1	0,0	0,0	0,0	0,0	0,0	0,0	0,0
C22H46	kg/hr	3,2	0,0	0,0	0,0	0,0	7,6	0,0	3,2	0,0	0,0	0,0	0,0	0,0	0,0	0,0
C23H48	kg/hr	2,3	0,0	0,0	0,0	0,0	8,1	0,0	2,3	0,0	0,0	0,0	0,0	0,0	0,0	0,0
C24H50	kg/hr	1,6	0,0	0,0	0,0	0,0	8,3	0,0	1,6	0,0	0,0	0,0	0,0	0,0	0,0	0,0
C25H52	kg/hr	1,2	0,0	0,0	0,0	0,0	8,4	0,0	1,2	0,0	0,0	0,0	0,0	0,0	0,0	0,0
C26H54	kg/hr	0,8	0,0	0,0	0,0	0,0	8,3	0,0	0,8	0,0	0,0	0,0	0,0	0,0	0,0	0,0
C27H56	kg/hr	0,5	0,0	0,0	0,0	0,0	8,2	0,0	0,5	0,0	0,0	0,0	0,0	0,0	0,0	0,0
C28H58	kg/hr	0,4	0,0	0,0	0,0	0,0	7,9	0,0	0,4	0,0	0,0	0,0	0,0	0,0	0,0	0,0
C29H60	kg/hr	0,3	0,0	0,0	0,0	0,0	7,6	0,0	0,3	0,0	0,0	0,0	0,0	0,0	0,0	0,0
C30H62	kg/hr	0,2	0,0	0,0	0,0	0,0	7,3	0,0	0,2	0,0	0,0	0,0	0,0	0,0	0,0	0,0
C30+	kg/hr	0,1	0,0	0,0	0,0	0,0	122,3	0,0	0,1	0,0	0,0	0,0	0,0	0,0	0,0	0,0

The cold and hot streams (includes carbon capture unit, SOEC electrolysis, rWGS and FTS) are summarized in Table 7. Negative enthalpy defines cooling demand, positive enthalpy needs energy supply. A main difference to scenario 1 is the omission of the entry “Electrolysis cooling”. Furthermore, the heat demand for electrolysis’ feed pre-heating is significantly increased (steam @ 5 barg, 160 °C).

Table 7: Compilation of cold and hot streams of scenario 9

Input stream	Output stream	Inlet Temperature	Outlet Temperature	Enthalpy
		[°C]	[°C]	[kW]
A-116	A-117	104,3	40,0	-1311,2
P-WAX-2	P-WAX	220,4	40,0	-27,2
RWGS-OUT	INT-1	950,0	30,0	-2903,9
P-MD-2	P-MIDDI	100,0	40,0	-4,1
MIX-1	RWGS-IN	130,3	950,0	2402,8
FT-OUT	R-1	220,0	100,0	-154,8
R-3	R-4	100,0	20,0	-732,0
A-110	A-111	45,4	85,0	860,7
INT-5	FT-FEED	159,2	220,0	153,8
A-104	A-105	60,3	20,0	-423,6
E-1	E-4	10,3	159,8	1380,4
P-WA-3	P-WA-4	20,1	60,0	33,6
Reboiler Stripper	heat	102,6	104,3	1500,0
Condenser Stripper	cooling	87,2	40,0	-435,7
B11	heat	20,0	19,5	-9,2
RWGS	heat	950,0	950,5	777,9
FT-CONV	cooling	220,0	219,5	-1738,9

The Balance Composite Curves of the pinch analysis (Figure 5) shows exactly, where steam generation is possible, as well as, where cooling water is reqired in scenario 9. The pinch analysis includes the carbon capture unit, electrolysis, rWGS and Fischer Tropsch synthesis inclusive product separation.

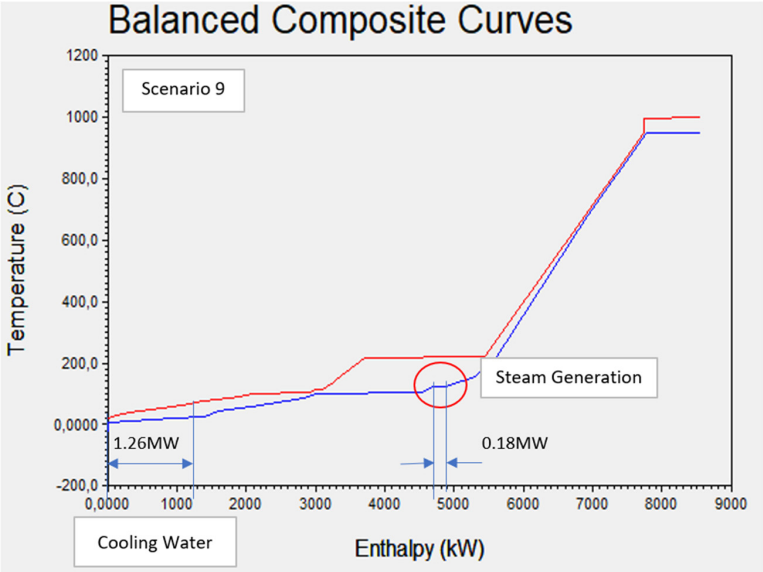

Figure 5: Balanced composite curves of scenario 9 with differentiation between cooling water and steam generation

The calculated equipment costs (EC), as well as the calculation of the intermediate costs (IT) and total investment costs (TIC) are given in Table 8 for scenario 9. Once again, a comparison with the Lang Factor for Liquids (TIC = ECx4.84) is applied.

Table 8: Cost calculation and listing of EC, IT and TIC for scenario 9

CARBON CAPTURE UNIT Equipment Simulation	Equipment Description	EC Equipment Cost [EUR]	R1 Equipment installation [EUR]	R2+R3 Process Piping [EUR]	R4 Instrument-ation [EUR]	R5 Builing and construction [EUR]	R6 Auxiliary systems [EUR]	R7 Outside lines [EUR]	IT [EUR]	R8 Engineering [EUR]	R9 Risk and unforseen [EUR]	R10 Size factor [EUR]	TIC [EUR]
			1,15	0,35	0,15	0,2	0,15	0,15		0,4	0,2	0,5	
HX-A1	Heat Exchanger	51 600	59 340	20 769	8 901	11 868	8 901	8 901	118 680	47 472	23 736	59 340	249 228
HX-A2	Heat Exchanger	21 800	25 070	8 775	3 761	5 014	3 761	3 761	50 140	20 056	10 028	25 070	105 294
HX-A3	Heat Exchanger	83 900	96 485	33 770	14 473	19 297	14 473	14 473	192 970	77 188	38 594	96 485	405 237
PREWASH-tower	Column	60 500	69 575	24 351	10 436	13 915	10 436	10 436	139 150	55 660	27 830	69 575	292 215
PUMP-C-1	Pump	7 400	8 510	2 979	1 277	1 702	1 277	1 277	17 020	6 808	3 404	8 510	35 742
PUMP-C-2	Pump	8 400	9 660	3 381	1 449	1 932	1 449	1 449	19 320	7 728	3 864	9 660	40 572
PUMP-C-3	Pump	5 700	6 555	2 294	983	1 311	983	983	13 110	5 244	2 622	6 555	27 531
PW-COOL	Heat Exchanger	18 400	21 160	7 406	3 174	4 232	3 174	3 174	42 320	16 928	8 464	21 160	88 872
PW-PUMP	Pump	6 600	7 590	2 657	1 139	1 518	1 139	1 139	15 180	6 072	3 036	7 590	31 878
STRIPPER-cond	Heat Exchanger	12 900	14 835	5 192	2 225	2 967	2 225	2 225	29 670	11 868	5 934	14 835	62 307
STRIPPER-cond acc	Drum	21 200	24 380	8 533	3 657	4 876	3 657	3 657	48 760	19 504	9 752	24 380	102 396
STRIPPER-reb	Reboiler	20 500	23 575	8 251	3 536	4 715	3 536	3 536	47 150	18 860	9 430	23 575	99 015
STRIPPER-reflux pump	Pump	5 700	6 555	2 294	983	1 311	983	983	13 110	5 244	2 622	6 555	27 531
STRIPPER-tower	Tower	199 200	229 080	80 178	34 362	45 816	34 362	34 362	458 160	183 264	91 632	229 080	962 136
ABSORBER-tower	Tower	423 900	487 485	170 620	73 123	97 497	73 123	73 123	974 970	389 988	194 994	487 485	2 047 437
COMP-STA	Blower	155 100	178 365	62 428	26 755	35 673	26 755	26 755	356 730	142 692	71 346	178 365	749 133
Total Carbon Capture Unit		**1 102 800**							**2 536 440**				**5 326 524**
												Calculation with Lang Factor (ECx4.84):	**5 337 552**

Continuation of Table 8: Cost calculation and listing of EC, IT and TIC for scenario 9

SYNTHESIS UNIT Equipment Simulation	Equipment Description	EC Equipment Cost [EUR]	R1 Equipment installation [EUR]	R2+R3 Process Piping [EUR]	R4 Instrument-ation [EUR]	R5 Builing and construction [EUR]	R6 Auxiliary systems [EUR]	R7 Outside lines [EUR]	IT [EUR]	R8 Engineering [EUR]	R9 Risk and unforseen [EUR]	R10 Size factor [EUR]	TIC [EUR]
			1,15	0,35	0,15	0,2	0,15	0,15		0,4	0,2	0,5	
1-HX-1	Heat Exchanger	83 900	96 485	33 770	14 473	19 297	14 473	14 473	192 970	77 188	38 594	96 485	405 237
1-HX-2	Heat Exchanger	22 800	26 220	9 177	3 933	5 244	3 933	3 933	52 440	20 976	10 488	26 220	110 124
1-HX-3	Heat Exchanger	15 300	17 595	6 158	2 639	3 519	2 639	2 639	35 190	14 076	7 038	17 595	73 899
2-HX-1	Heat Exchanger	18 200	20 930	7 326	3 140	4 186	3 140	3 140	41 860	16 744	8 372	20 930	87 906
2-HX-3	Heat Exchanger	12 300	14 145	4 951	2 122	2 829	2 122	2 122	28 290	11 316	5 658	14 145	59 409
2-HX-2	Heat Exchanger	9 700	11 155	3 904	1 673	2 231	1 673	1 673	22 310	8 924	4 462	11 155	46 851
3-HX-1	Heat Exchanger	12 700	14 605	5 112	2 191	2 921	2 191	2 191	29 210	11 684	5 842	14 605	61 341
3-HX-2	Heat Exchanger	14 500	16 675	5 836	2 501	3 335	2 501	2 501	33 350	13 340	6 670	16 675	70 035
3-HX-3	Heat Exchanger	16 300	18 745	6 561	2 812	3 749	2 812	2 812	37 490	14 996	7 498	18 745	78 729
COMP-FT	Compressor	1 324 600	1 523 290	533 152	228 494	304 658	228 494	228 494	3 046 580	1 218 632	609 316	1 523 290	6 397 818
COND-RWG-flash vessel	Drum	21 900	25 185	8 815	3 778	5 037	3 778	3 778	50 370	20 148	10 074	25 185	105 777
HP-FLASH-flash vessel	Drum	27 000	31 050	10 868	4 658	6 210	4 658	4 658	62 100	24 840	12 420	31 050	130 410
P-WAX-HX	Heat Exchanger	9 600	11 040	3 864	1 656	2 208	1 656	1 656	22 080	8 832	4 416	11 040	46 368
PUMP-E-1	Pump	14 000	16 100	5 635	2 415	3 220	2 415	2 415	32 200	12 880	6 440	16 100	67 620
B11-flash vessel	Drum	21 900	25 185	8 815	3 778	5 037	3 778	3 778	50 370	20 148	10 074	25 185	105 777
COMP-CO2	Compressor	1 090 600	1 254 190	438 967	188 129	250 838	188 129	188 129	2 508 380	1 003 352	501 676	1 254 190	5 267 598
Fischer-Tropsch-Reactor	Reactor	180 000	207 000	72 450	31 050	41 400	31 050	31 050	414 000	165 600	82 800	207 000	869 400
rWGS-Reactor	Reactor	1 617 240	1 859 826	650 939	278 974	371 965	278 974	278 974	3 719 652	1 487 861	743 930	1 859 826	7 811 269
Total Synthesis Unit		**4 512 540**							**10 378 842**				**21 795 568**
												Calculation with Lang Factor (ECx4.84):	**21 840 694**

ELECTROLYSER UNIT Equipment Simulation	Power demand [kW]	Specific Costs [EUR/kW]	R1 Equipment installation [EUR]	R2+R3 Process Piping [EUR]	R4 Instrumentat ion [EUR]	R5 Builing and construction [EUR]	R6 Auxiliary systems [EUR]	R7 Outside lines [EUR]	IT [EUR]	R8 Engineering [EUR]	R9 Risk and unforseen [EUR]	R10 Size factor [EUR]	TIC [EUR]
				0,15	0,00	0,20	0,10	0,00		0,00	0,00	0,00	
Electrolysis	7030	1 900	13 357 000	2 003 550	-	2 671 400	1 335 700	-	19 367 650	-	-	-	19 367 650
E-COMP (Hydrogen compressor)			1 823 300	273 495	-	364 660	182 330	-	2 643 785	-	-	-	2 643 785
Total Electrolysis Unit									**22 011 435**				**22 011 435**

Total Investment Costs	[EUR]
Carbon capture unit	5 326 524
Synthesis unit	21 795 568
Electrolysis unit	22 011 435
Total	**49 133 527**

Publication II

Comparison and techno-economic evaluation of process routes for lower olefin production via Fischer–Tropsch and methanol synthesis

Christoph Markowitsch, Markus Lehner, Markus Maly

International Journal of Greenhouse Gas Control (2023)
Volume 129, P. 103985
DOI: 10.1016/j.ijggc.2023.103985

Conception and planning	Simulation	Analysis and interpretation	Manuscript preparation
90%	100%	90%	100%

International Journal of Greenhouse Gas Control 129 (2023) 103985

Contents lists available at ScienceDirect

International Journal of Greenhouse Gas Control

journal homepage: www.elsevier.com/locate/ijggc

Comparison and techno-economic evaluation of process routes for lower olefin production via Fischer–Tropsch and methanol synthesis

Christoph Markowitsch [a,*], Markus Lehner [b], Markus Maly [c]

[a] Montanuniversitaet Leoben, Chair of Process Technology and Environmental Protection, Austria
[b] Chair of Process Technology and Environmental Protection, Montanuniversitaet Leoben, Austria
[c] Head of RN-N New Technologies & Innovation, OMV Downstream GmbH, Austria

ARTICLE INFO

Keywords:
Carbon capture and utilization
Reverse water gas shift (rWGS)
Methanol synthesis
Fischer–Tropsch synthesis
Power-to-lower olefins

ABSTRACT

This paper describes the simulation and techno-economic evaluation of a carbon dioxide capture and utilization unit integrated in a cement plant with a capacity of 10,000 tons of CO_2 per year. The aim is to utilize CO_2 along with hydrogen to produce lower olefins (C_2–C_4), the feedstock for polyolefin production. In a first step, three process routes, namely a Fischer–Tropsch synthesis with steam cracker, a methanol synthesis with rWGS syngas production and a methanol synthesis with direct hydrogenation of CO_2, latter two followed by a methanol-to-propylene unit, are simulated in ASPEN Plus V12.1®. Furthermore, the effect of a high- and a low-temperature electrolysis on key performance indicators are also considered in the evaluation. Additionally, an estimation of investment, operating and specific net production costs (NPC_{PR}) of the different process routes is made. The evaluation is based on the comparison of calculated global efficiencies, specific energy consumption (SEC), NPC_{Pr} and yields of the lower olefine products (C_2–C_4). The power-to-lower olefin plant, consisting of an amine scrubber unit, a PEM electrolysis and a Fischer–Tropsch synthesis with downstream steam cracker proves to be the most efficient process route for polyolefin production, resulting in a global efficiency of 38.2 %, an SEC of 34.4 kWh/kg and an NPC_{Pr} of 14.92 EUR/kg of lower olefine product.

1. Introduction

1.1. Motivation

A maximum temperature increase of 2 °C was agreed in the Paris Agreement in 2015, with an ambition to achieve a lower level of 1.5 °C compared to pre-industrial levels. The European Commission has set a step-by-step plan to decarbonize CO_2-emitting sectors to achieve climate neutrality by 2050. In Austria, a more stringent plan has been developed to reduce 55 % of emissions by 2030 compared to the reference year 1990 and to achieve climate neutrality by 2040 (Bundesministerium Austria, 2022). The cement industry emitted 9.0 % of EU ETS (European Emission Trading System) certified carbon dioxide emissions and was responsible for 3.3 % of total national greenhouse gas emissions in Austria in 2019, resulting in about 2.9 million tons of emitted CO_2 in 2020 (Mauschitz, 2021). Two thirds of the released CO_2 are accounted for process-related CO_2 from limestone calcination (calcium carbonate) which is hardly to reduce, and therefore counts as unavoidable carbon emissions. The other third is generated by the provision of energy through the combustion of conventional fuels such as coal, waste oil or substitute fuels (Mauschitz, 2021). In a report of the 'VÖZ-Verein österreichischer Zementwerke (Austrian Cement Works Association)' a roadmap for CO_2 neutral cement production is published. To decarbonize the cement production sector, 44 % of CO_2 emitted today must be reduced through carbon capture and utilization or storage (CCUS) (Spaun et al., 2022). The increase in the cost of ETS allowances from 26 EUR/t CO_2 at the beginning of 2020 to more than 90 EUR/t_{CO2} at the beginning of 2022 and the newly introduced tax (30 EUR/t_{CO2} in 2022, Austrian environmental law 'ÖkoStRefG 2022 Teil I') on emitted CO_2 in Austria represent a major challenge for companies to manage their business plans (Economics, 2022; Parlament Österreich, 2022). Carbon capture and storage (CCS) is currently still prohibited in Austria (Austrian law – 'BGBl. I Nr. 144/2011'). Nevertheless, the industries must reduce their CO_2 emissions. On the one hand, CO_2 can be transported over many kilometers to CO_2 storage facilities (e.g. Norway). On the other hand, the prohibition of CCS is another incentive to implement carbon capture and utilization (CCU) plants regionally. CCU allows on the one hand the possibility of CO_2 reduction, on the other hand it can be used as a resource to produce new products like chemicals, electrified

* Corresponding author at: 36TUU36T, Franz-Josef-Strasse 18, 8700 Leoben, Austria.
E-mail address: christoph.markowitsch@unileoben.ac.at (C. Markowitsch).

https://doi.org/10.1016/j.ijggc.2023.103985
Received 7 January 2023; Received in revised form 20 July 2023; Accepted 13 September 2023
Available online 22 September 2023

Abbreviations and nomenclature

AC	additional costs [EUR]
ACC	annualized capital costs [EUR]
APEA	ASPEN process economic analyzer V12.1
ARC	annual replacement costs of electrolysis stack [EUR/year]
CAPEX	capital expenditures
CCU	carbon capture and utilization
CCS	carbon capture and storage
CCUS	carbon capture utilization and storage
CEPCI	chemical engineering plant cost index [-]
c_{labor}	labor costs [EUR/h]
D	direct plant costs [EUR]
DME	dimethyl ether
EC	equipment costs [EUR]
EC_{ref}	reference equipment costs [EUR]
ETS	EU emissions trading system
FCI	fixed capital costs [EUR]
FixOPEX	fixed operational expenditures [EUR/year]
FTS	Fischer–Tropsch synthesis
GHSV	gas houly space velocity [1/h]
h_{labor}	labor hours [h/year]
$h_{plant,operation}$	operation hours [h/year]
HTFT	high temperature Fischer–Tropsch synthesis
I	indirect plant costs [EUR]
ISBL	inside battery limit
IR	rate of interest [%]
LHV	lower heating value [kWh/kg]
LTFT	low temperature Fischer–Tropsch synthesis
$\dot{m}_i$	mass flow of product fraction i [kg/h]
$\dot{m}_{product}$	mass flow of total product [kg/h]
MeOH	methanol synthesis
MtP	methanol to propylene
$\dot{n}_{c,feed}$	carbon atoms in feedstock [atoms]
$\dot{n}_{c,prod,\ i}$	carbon atoms in product i [atoms]
$\dot{n}_{CO_2}$	mole flow CO_2 [kmol/h]
$\dot{n}_{CO}$	mole flow CO [kmol/h]
NPC	net production costs [EUR/kg, EUR/kWh]
$n_{process,step}$	number of units [-]
OPEX	operational expenditures
OL	operating labor costs [EUR/year]
OSBL	outside battery limit
P_{el}	electricity demand of electrolysis [kW]
P_u	electricity demand of utilities [kW]
PE	polyethylene
PEM	proton exchange membrane electrolysis
PET	polyethylene terephthalate
PL	plant lifetime [a]
PP	polypropylene
PtL	power to Liquid
PVC	polyvinyl chloride
$\dot{Q}_{heat}$	excess steam generation [kW]
R	ratio factor [-]
rWGS	reverse water-gas shift
S	simulated mole flow [kmol/s]
SEC	specific energy consumption
SOEC	solid oxide electrolysis
SR	electrolysis stack replacement cycles [-]
S_{ref}	reference mole flow [kmol/s]
TCI	total capital investment [EUR]
WC	working capital [EUR]
η_{carbon}	carbon efficiency [-]
η_{global}	global efficiency [-]
η_{PtL}	power-to-liquid efficiency [-]

fuels (e-fuels) or plastics. The latter one has the advantage to use carbon dioxide for long life applications and CO_2 is bound in the product, which contributes to a long-term CO_2 reduction (e.g., as coating in high voltage cables).

The plastics production has increased from 1.5 billion tons in 1950 to 359 billion tons in 2018 (Europäisches Parlament, 2022). This amount is allocated to the main plastic categories polyethylene (PE, 28 wt.- %), polypropylene (PP, 17 wt.- %), polyvinyl chloride (PVC, 13 wt.- %), and polyethylene terephthalate (PET, 6 wt.- %) (GLOBAL 2000, 2022). Today, European plastics production is based on fossil sources, as dominantly crude oil is distilled, and the naphtha fraction is used in steam crackers for the conversion into ethylene and propylene. These chemicals are further processed in a downstream polymerization step to produce the desired polyolefins, mainly polypropylene and polyethylene.

In several studies, CO_2 is utilized via the implementation of a Fischer–Tropsch synthesis (FTS) and synthesized to e-fuels. In those studies simulations and techno-economic comparisons are performed. Also pilot projects are planned for power-to-liquid (PtL) plants, using CO_2 and H_2 as feedstock for the catalytic conversion to the main product kerosene (Adelung et al., 2021; König, 2016; Boudier, 2021; SAF+ Consortium, 2022; Adelung et al., 2021). König et al. and Adelung et al. built up on the same process structure, using a PEM electrolysis, an externally fired reverse water gas shift (rWGS) reactor for syngas production and an FTS with hydrocracker. Carbon capture (CC) was only included as generic process without any simulation (Adelung et al., 2021; König et al., 2015). König et al. did also not include CC in the economic considerations (König, 2016). Herz et al. performed a techno-economic analysis of an FTS and summarized studies for C_{5+} production (Herz et al., 2021). Pratschner et al. investigated a PtL route to produce the fractions naphtha, middle distallate and waxes via Fischer Tropsch synthesis and Co-SOEC (Pratschner et al., 2023). However, studies for utilizing CO_2 to fuels are mostly elaborated. The process route to achieve lower olefins as main product is not yet considered in any study.

As an alternative to FTS, CO_2 and H_2 can be converted to methanol, with a methanol-to-propylene (MtP) unit downstream to produce mainly propylene. A distinction and evaluation between a direct and a two-step methanol synthesis is done by Anicic et al., who only considers pure methanol production (Anicic et al., 2014). Ghosh et al. also studied the difference of methanol production between direct hydrogenation of CO_2 and pre-conversion via an rWGS reactor (Ghosh et al., 2019). Both authors do not consider the post-conversion to the end-product lower olefins and do not compare economics of the processes.

During this research, no literature was found, where process-related CO_2 from a cement plant is used as a resource for lower olefins production, especially for further use as feedstock for renewable based polyolefins. Therefore, the process analysis and techno-economic evaluation performed during this work is novel.

Regarding a future climate neutral polyolefin production and the associated change from fossil to renewable raw materials, this work compares available technologies of Power-to-Lower olefin routes. The comparison includes the different synthesis units (Fischer Tropsch and methanol) with the downstream upgrade processes to lower olefins (steam cracker or methanol to propylene (MtP) unit). Since the polymerization step is the same for both technology pathways, and these are existing technologies, this step is not considered further in the simulation, i.e. the comparison ends with the lower chain olefins. In a first step,

available and existing process routes of CO_2 conversion via methanol synthesis and FTS for the intermediate production (syncrude or methanol) are simulated in ASPEN Plus® to obtain mass and energy balances. This includes the carbon capture unit, the electrolysis for hydrogen production and the synthesis part. As the steam cracker and MtP units are commercially available, the mass and energy balance data and conversion yields are taken from literature for these process steps. For a more detailed comparison, the calculation of key performance indicators (KPIs), such as the PtL global efficiency and carbon conversion, the total product yield for lower olefins (C_2–C_4) and the consideration of side products is carried out in a second step. Furthermore, the impact of an existing steam cracker in a nearby located refinery is also considered in the process analysis. In order to design a cost-efficient and process optimized PtL plant, the advantages and disadvantages of the individual process routes and technologies are discussed with regard to the calculated key figures, cost aspects and the implementation of the existing infrastructure. Finally, a recommendation for the process design to convert CO_2 and H_2 into lower olefins is made. The results deliver the basis for a potential large-scale implementation. The chosen process should utilize 10,000 tons of CO_2 annually. It is determined which process route performs best in case of lower olefin production and how the process should be realized in terms of the interconnection of the necessary units (CC, electrolysis, synthesis, …).

2. Detailed process description

The general process route for a power-to-lower olefin plant consists of the catalytic conversion of CO_2 with green hydrogen into hydrocarbons (low chain olefins) and, in a downstream polymerization step, into polypropylene and polyethylene. The main process steps are structured into categories, namely CO_2 capture, electrolysis, synthesis, downstream processing, and polymerization as depicted in Fig. 1.

In the first step, carbon dioxide is captured from the exhaust gas of the cement plant using a solvent-based scrubber unit. Chemical absorption technologies range from conventionally available and proven amine-based solvents to advanced solvents, and hot potassium carbonate as absorbent. In this study, an amine scrubbing unit is used as carbon capture step due to its generally higher technical maturity (Kearns et al., 2021).

Two different feedstocks, methanol and syncrude, are considered for lower olefine production. Therefore, two main conversion technologies, the methanol synthesis and the FTS, are analyzed for comparison. The feedstock for both technologies is captured CO_2, which is catalytically converted with green hydrogen to intermediate products methanol or syncrude. In the simulation, the main hydrogen production technologies are implemented with heat-integrated low and high temperature electrolysis in both process chains.

On the one hand, methanol is used with a post-processing MtP unit achieving high conversion rates to propylene. On the other hand, syncrude is further processed in a steam cracker, yielding mainly ethylene and propylene. Finally, these intermediates should be polymerized to polypropylene and polyethylene in a last step, but this polymerization step is out of this scope. A block flow diagram of the investigated process chains is shown in Fig. 1.

In this paper, an FTS for syncrude production (process route 1), a pre-conversion via an rWGS reactor with downstream methanol synthesis (process route 2) and a direct hydrogenation of CO_2 to methanol (process route 3) are compared, in which either a low or a high temperature electrolysis is used for green hydrogen production, and post-processing units, such as a steam cracker and MtP unit, respectively.

2.1. Carbon capture unit – amine scrubber unit

The composition of the exhaust gas from the cement plant is 14 vol.-% CO_2, 64 vol.- % N_2, 12 vol.- % H_2O and 10 vol.- % O_2 (Mauschitz, 2021). In this work, an annual carbon dioxide capture capacity of 10,000 tons should be achieved by an amine scrubber unit. Impurities contained in the exhaust gas (e.g., sulfur oxides, nitrogen oxides or mercury) are not considered in this work, thus pre-cleaning systems are not included in the simulation. The gas stream exits from the cement plant's stack at atmospheric pressure and a temperature of about 100 °C. It is withdrawn, compressed to 0.5 bar(g) and fed to a pre-washer tower

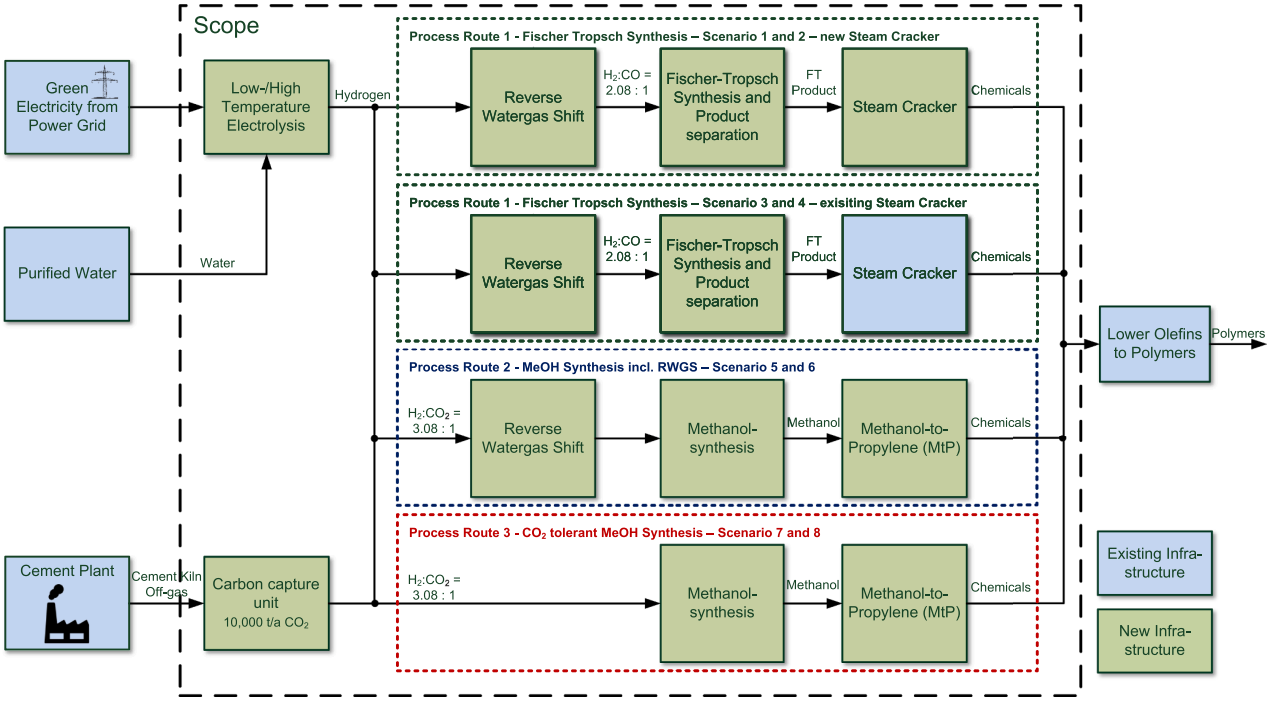

Fig. 1. Block flow diagram for the production of polypropylene and polyethylene from a cement plant off-gas.

where it is cooled to an absorber inlet temperature of 40 °C. In the pre-washer tower, NaOH solution is used for dedusting, cooling and reducing SO_x traces that would lead to amine degradation (Zhou et al., 2013). The cleaned and cooled gas is further fed to the lower part of the absorber tower. The amine solution consists of 30 wt.- % monoethanolamin (MEA) and water. The solvent flows into the tower from the top in counter-current flow to the gas, and the CO_2 dissolves in the amine solution. The carbon capture efficiency is assumed to be 90 %. The CO_2 reduced waste gas exits the absorber tower at the top and is discharged to the environment. The CO_2 rich amine solvent is preheated in a heat exchanger and fed to the desorber tower, which operates at atmospheric pressure. Due to the high feed temperature and the additional heat input from a reboiler of approximately 3.8 MJ/kg_{CO2}, CO_2 releases and water is evaporated from the amine solvent (Sakwattanapong et al., 2005). The gaseous product is withdrawn at the column head and cooled downstream to 50 °C. The water condenses in a flash and is recycled to the desorber tower. The gas fraction, which consists of >95 wt.- % CO_2 (99 wt.- % dry), is processed for further use. The lean amine solution is collected at the bottom of the column and is returned to the absorber tower, which maintains an amine solvent cycle. Amine degradation is not considered in the simulation (Zhou et al., 2013; Rochelle, 2012).

2.2. Electrolysis

The technologies for hydrogen production from water can be categorized in low- and high-temperature electrolysis. The main differences, apart from the system design, are the feed phase, specific energy consumption, operating temperature, and operating pressure of the respective technology. Both electrolysis technologies must be fed with ultrapure water, which requires a water treatment plant, which is not in the scope of this simulation. Hydrogen production follows the overall reaction Eq. (1). The reaction is highly endothermic, and energy must be supplied in the form of electrical energy and heat.

$$2H_2O \rightarrow 2H_{2,(g)} + O_{2,(g)} \qquad \Delta H_r^{298K} = +286\ kJ/mol \tag{1}$$

Proton exchange membrane (PEM) electrolysis belongs to the low-temperature electrolysis technologies. The operating temperature is typically between 50 and 80 °C with an operating pressure of up to 40 bar(a) and a specific system energy consumption of 4.7 kWh/Nm^3_{H2} (Trattner et al., 2021). In the simulation, feed water is heated to 75 °C and the electrolysis is operated at the same temperature. A disadvantage of the PEM electrolysis, resulting in lower energy efficiency, is the need for cooling water, which accounts for about 17 % of total electrical energy supplied (Tiktak, 2019). In contrast to PEM electrolysis, the solid oxide electrolysis (SOEC) belongs to the high temperature electrolysis processes. Typical operating temperatures range from 700 to 1000 °C and outlet pressures from 1 to 3 bar(a) (Trattner et al., 2021). This technology is fed with low pressure (LP) steam, which introduces heat into the system, and lowers the electrical power demand according to the Gibbs free enthalpy (Sunfire GmbH, 2022). This advantage results in a specific electricity system energy consumption of 3.6 kWh/Nm^3_{H2} (Trattner et al., 2021; Sunfire GmbH, 2022). Heat integration of the whole process is included in the simulation by using waste heat (e.g., heat release from the exothermic Fischer–Tropsch reaction) instead of electrical preheating. For green hydrogen production, it is inevitable to run the electrolysis with renewable energy. Both electrolysers are implemented as stoichiometric reactor in ASPEN Plus®, considering a total water conversion of 95 % (Allen et al., 2021).

2.3. Synthesis gas production

The implementation of an FTS and methanol synthesis in the process chain usually requires the supply of synthesis gas. Newly explored technologies also allow direct hydrogenation of CO_2 for methanol synthesis, but this is still in the laboratory phase for FTS (Brübach et al., 2022; Schemme et al., 2020). The performance of the rWGS reaction has been investigated on nickel catalysts by different authors (Unde, Adelung et al., König et al. and Markowitsch et al.), leading to different operation conditions (Adelung et al., 2021; König, 2016; Markowitsch et al., 2022; Unde, 2012; Markowitsch and Lehner, 2023). Adelung et al. and König et al. simulated a PtL plant with kerosene as main product, and the optimization process and operation conditions were completely different from syncrude or methanol production (Adelung et al., 2021; König, 2016). Markowitsch et al. implemented an electrified rWGS reactor and considered main and side reactions, optimizing for high selectivity of carbon monoxide in the product gas and high operating pressure (Markowitsch et al., 2022). The endothermic main reaction is given in Eq. (2).

$$CO_2 + H_2 \leftrightarrow CO + H_2O \qquad \Delta H_r^{298K} = +41\ kJ/mol \tag{2}$$

For suitable operation conditions, the thermodynamic consideration must consider all occurring side reactions, as some are mentioned in Eq. (3) to Eq. (6). In the Fischer–Tropsch process, the tail-gas stream from the product separation unit is recycled upstream of the rWGS reactor. Methane and higher gaseous components are reconverted to syngas in the rWGS reactor according to the endothermic steam and dry reforming reactions (Eq. (3) and Eq. (4)).

$$CH_4 + H_2O \leftrightarrow CO + 3H_2 \quad \Delta H_r^{298K} = +206\ kJ/mol \tag{3}$$

$$CH_4 + CO_2 \leftrightarrow 2CO + 2H_2 \qquad \Delta H_r^{298K} = +247\ kJ/mol \tag{4}$$

$$CO_2 + 2H_2 \leftrightarrow C_{(s)} + 2H_2O \qquad \Delta H_r^{298K} = -91\ kJ/mol \tag{5}$$

$$2CO \leftrightarrow CO_2 + C_{(s)} \qquad \Delta H_r^{298K} = -172\ kJ/mol \tag{6}$$

In order to reach high conversion rates and high carbon monoxide selectivity, appropriate operation temperature and pressure must be chosen. Selectivity is defined in Eq. (7) as the number of CO_2 molecules ($\dot{n}_{CO_2}$ in kmol/h) converted to carbon monoxide molecules ($\dot{n}_{CO}$ in kmol/h).

$$S(CO) = \frac{\dot{n}_{CO,out} - \dot{n}_{CO,in}}{\dot{n}_{CO_2,in} - \dot{n}_{CO_2,out}} \tag{7}$$

Fig. 2 illustrates the thermodynamic equilibrium calculated with the software HSC 7 (Outotech). CO selectivities yield in 99.9, 98 and 88 % for investigated pressures of 1, 10 and 30 bar(g), respectively, and a temperature of 950 °C. Conversion to carbon monoxide favors high temperatures and low pressures, whereby the rWGS reactor is introduced as a Gibbs reactor in ASPEN Plus® with operation conditions set at 950 °C and 10 bar(g) (Markowitsch et al., 2022; Markowitsch et al., 2023). These operating conditions and the over-stoichiometric use of hydrogen (H_2:CO_2 at 3.1:1) suppress the carbon formation via Bosch reaction (Eq. (5)) or Boudouard equilibrium (Eq. (6)) to prevent catalyst deactivation. The assumed operating temperatures and pressures were previously determined and validated experimentally in a test rig on a nickel based catalyst (Markowitsch and Lehner, 2023).

2.4. Fischer–Tropsch synthesis – process route 1

A low temperature FTS (LTFT) is assumed for this simulation and the flow sheet for process route 1 is depicted in Fig. 3. Normal paraffinic hydrocarbons constitute the main component of the product. A remarkable advantage is the change of operating conditions (temperature and/or pressure), to achieve the best yields of the desired product (syncrude, kerosene, diesel, …) and the adaptability to market demand. This is possible, as the product composition follows the extended Anderson-Schulz-Flory distribution with a chain growth probability α (Markowitsch et al., 2022). A cobalt-based catalyst is applied in the LTFT and the operating conditions are set to a temperature of 220 °C and

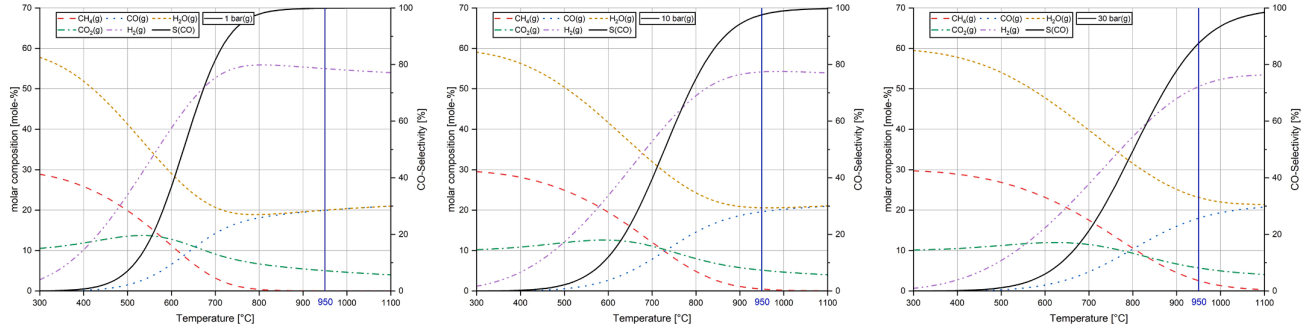

Fig. 2. Thermodynamic equilibrium of the rWGS reaction and CO selectivity in a temperature range of 300–1100 °C and at pressures of 1, 10 and 30 bar(g).

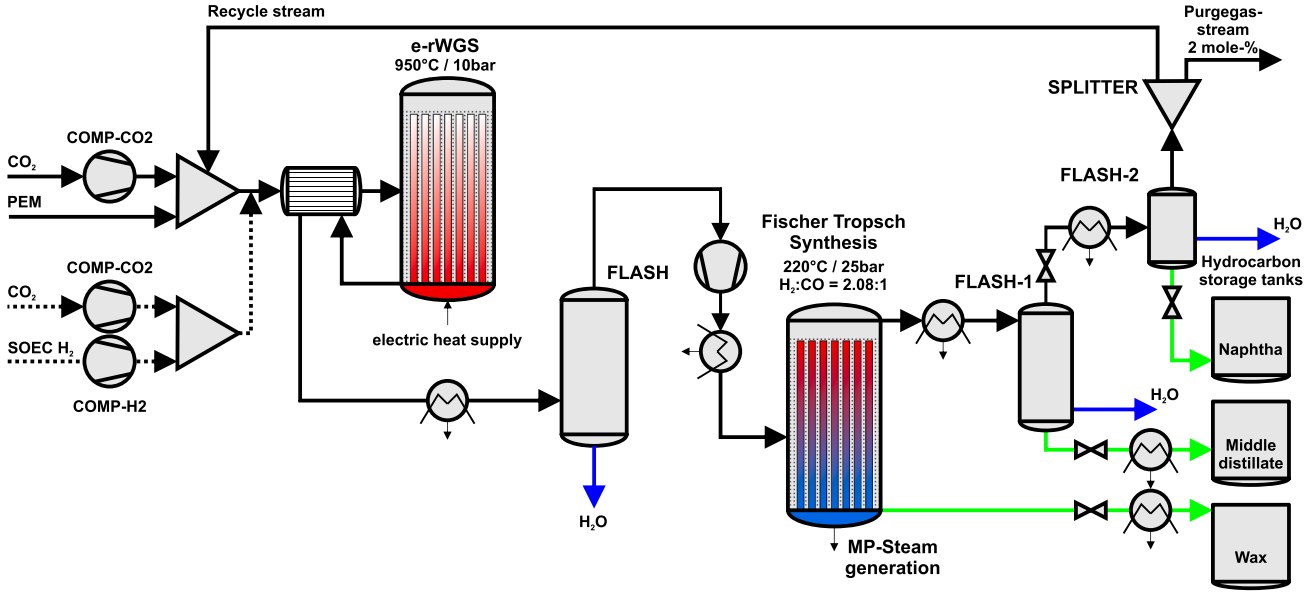

Fig. 3. Flow sheet of the implemented FTS with rWGS, two-stage flash product separation and PEM/SOEC hydrogen production.

a pressure of 25 bar (g) (Adelung et al., 2021; Markowitsch et al., 2023). In addition, the input ratio of H_2:CO should be constant at 2.08 to achieve an α-value of 0.92, which favors the production of higher normal paraffinic hydrocarbons (high wax content). Consequently, the syncrude can be fed into the existing refinery infrastructure and directly replace fossil crude oil for plastics production (Klerk, 2011). The single pass CO conversion is set at 40 % and the selectivity of methane is set to 16.1 % (Adelung et al., 2021). The main reaction (Eq. (8)) of the conversion of syngas to paraffins is highly exothermic. Therefore, the Fischer–Tropsch reactor is simulated as stoichiometric reactor in ASPEN Plus® and designed as a multitube reactor with boiling water as a coolant. Since by-products (olefins, oxygenates, aromatics and naphthene) account only for approximately 10 wt.- % of the total product mixture, the simulation is simplified, and it is assumed that only n-paraffins are produced from the feed gas. (Adelung et al., 2021; Markowitsch et al., 2023; Klerk, 2011). In the FTS itself, methane, CO_2 and nitrogen are treated as inert gasses (Klerk, 2011).

$$\begin{aligned} &CO + 2H_2 \rightarrow -CH_2- + H_2O \\ &\Delta H_r^{298K} = -140 \text{ to } -160 \text{ kJ/mol}_{CO} \end{aligned} \quad (8)$$

The liquid reaction product phase consists of waxes and is directly taken from the reactor. A sharp cut is not necessary as the product is fed to the steam cracker, covering the complete syncrude product (Karaba et al., 2021). The gaseous compounds are separated in a two-stage flash separation unit. In the first stage, the pressure remains unchanged and the temperature is reduced to 100 °C to obtain the middle distillate fraction and water. In the second stage, the pressure is reduced to 11 bar (g) and the gas is cooled to 20 °C to remove the naphtha and water fraction in liquid form. Most of the unconverted gasses and methane are contained in the product processing unit outlet stream and are recycled upstream of the rWGS reactor. To avoid accumulation of inert gasses, 2 mol- % of the recycled gas is purged (Markowitsch et al., 2022). The assumed operating conditions of the model fall within the ranges of 196.85–256.85 °C, 12–36 bar and a H_2:CO ratio of 1–3 validated by Vervloet et al. (Vervloet et al., 2012).

2.5. Methanol synthesis – process route 2 and 3

Methanol synthesis is a commercially available technology that usually uses syngas as a feed gas stream to convert CO and H_2 in an exothermic catalytic reaction to methanol (Eq. (9)).

$$\begin{aligned} &CO + 2H_2 \leftrightarrow CH_3OH \\ &\Delta H_r^{298K} = -91 \text{ kJ/mol} \end{aligned} \quad (9)$$

The reactors for direct hydrogenation of CO_2 and syngas conversion to methanol are similar. Boiling water cooled multitube reactors with a gas hourly space velocity (GHSV) of 10,000 $hP^{-1}P$ are used in this simulation (Oelmann et al., 2020). Due to principle of Le Chatelier, the

reaction is pressure dependent and favors higher pressure and lower temperature. Fig. 4 shows the thermodynamic analysis of the methanol reaction and depicts the conversion rates for temperatures between 120 and 300 °C and pressures of 20, 40, 60 and 80 bar.

In this paper, the methanol synthesis is implemented as a plug flow reactor with a $Cu/ZnO/Al_2O_3$ catalyst, which operates at a temperature of 240 °C and pressure of 80 bar (g). The tubes of the plug flow reactor are assumed with an inner diameter of 0.04 m and a length of 7 m (Bisotti et al., 2022). The methanol reaction (Eq. (9)) is thermodynamically limited, but for a proper design and cost estimation of the methanol reactor, kinetics need to be considered. The kinetic data is taken from Bussche et al. (Bussche and Froment, 1996). Possible side products, consisting of higher alcohols or methyl formate, account for about 0.06 wt.- % and are not considered in the kinetic model (Bisotti et al., 2022). A validation of the model assumptions (190–255 °C, 50–150 bar) with commercial methanol technologies is performed by Bisotti et al. (Bisotti et al., 2022). The product stream must be cooled to liquify and separate the products. The unconverted gas is split into a recycle gas stream and a purge gas stream (2 mol- %), again avoiding the accumulation of inert gasses such as nitrogen or methane (Bisotti et al., 2022). Behind the synthesis, the gas stream is cooled to 30 °C to obtain the liquid phases water and methanol. The product consists of a methanol-water mixture, the ratio depends on the process variant used. The product separation step consists of two distillation columns, the first one operates at a higher pressure of 10 bar(g). Dissolved gaseous compounds such as CO_2 are released from the liquid and exit the distillation at the top. The gas stream is compressed to the operating pressure of the methanol synthesis and fed upwards the methanol unit. Methanol and water are separated in the second distillation column at atmospheric pressure to achieve methanol specification grade AA (<0.1 wt.- % H_2O) (Adams et al., 2018; International Methanol Producers & Consumers Association, 2015).

In process route 2 (flow sheet in Fig. 5), the input streams CO_2 and H_2 are not directly fed to the methanol reactor, as they are first converted to syngas in an rWGS reactor, again treated as Gibbs reactor at 950 °C and 10 bar(g). Downstream of the rWGS reactor, the process water is condensed and extracted, and only CO, H_2, unconverted CO_2 and byproducts of the rWGS reaction such as methane are fed to the methanol reactor. This pre-conversion unit allows higher yield in single pass when syngas is used for methanol synthesis, as shown in Fig. 3.

The direct hydrogenation of CO_2 to methanol (Eq. (10)) combines the methanol reaction (Eq. (9)) and the rWGS reaction (Eq. (1)) (Bussche and Froment, 1996).

$$CO_2 + 3H_2 \leftrightarrow CH_3OH + H_2O \qquad \Delta H_r^{298K} = -49\ \mathrm{kJ/mol} \tag{10}$$

In process route 3, the methanol synthesis is carried out under the same operating conditions and under assumption of the same kinetic model as before. For methanol production, carbon dioxide and hydrogen are used in a ratio of 1:3.08. The aim is to achieve high conversion rates in three single pass reactors in series. This concept follows the design of Air Liquide and is shown in Fig. 6 (Oelmann et al., 2020). In this case, additional reaction water is generated as steam, resulting in higher volume flow through the reactor. This affects the total size and number of reactor tubes. As discussed earlier and shown in Fig. 4, Eq. (10) is also favored by high pressure and low temperature for high conversion rates to methanol. Behind the methanol reactor, the liquid product is again separated in a two stage distillation, whereas a high- and low pressure unit are implemented to achieve the specification of methanol grade AA (International Methanol Producers & Consumers Association, 2015). A recycle stream with a 2 mol- % purge gas stream is implemented to avoid inert gas accumulation.

2.6. Methanol-to-propylene unit

The methanol-to-propylene (MtP) technology is available in industrial scale and commercialized by Air Liquide. Therefore, a simulation in ASPEN Plus can be omitted here and the literature figures of a standalone MtP plant are used. The process preconverts methanol into a Dimethylether (DME), which is subsequently transformed together with recycled olefins catalytically in three MtP reactors (two operating and one regenerating reactor) to ethylene (1.2 wt.- %) and propylene (28.4 wt.- %). The remainder is converted to the by-products fuel gas (1.4 wt.- %), LPG (2.2 wt.- %), gasoline (10.8 wt.- %), and water (56 wt.- %). The purity of propylene is reported to be 99.6 wt.- % (Rothaemel et al., 2016). Liquified Petrolum Gas (LPG) is considered in the butene product fraction. However, gasoline consists mainly of hydrocarbons in a range of C_5 to C_9 and is therefore considered as by-products (Henley et al., 2014). The MtP conversion energy demand is taken into account with 11 MJ/kg_{MeOH} as electrical energy demand (IEA, 2017).

2.7. Steam cracker unit

For olefine production, the Fischer–Tropsch product can be processed in a steam cracker and has proven to be an excellent feedstock. Karaba et al. investigated the conversion of the syncrude from renewable feedstock into chemicals (preferably high yields of ethylene and

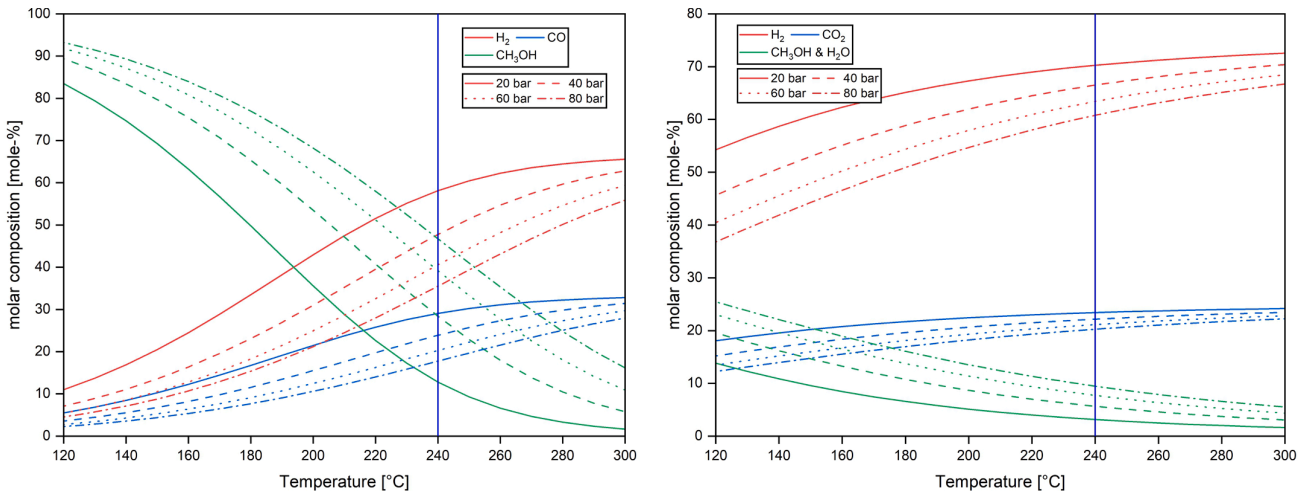

Fig. 4. Thermodynamic equilibrium of conventional methanol reaction via syngas (left) and CO_2 tolerant methanol synthesis (right).

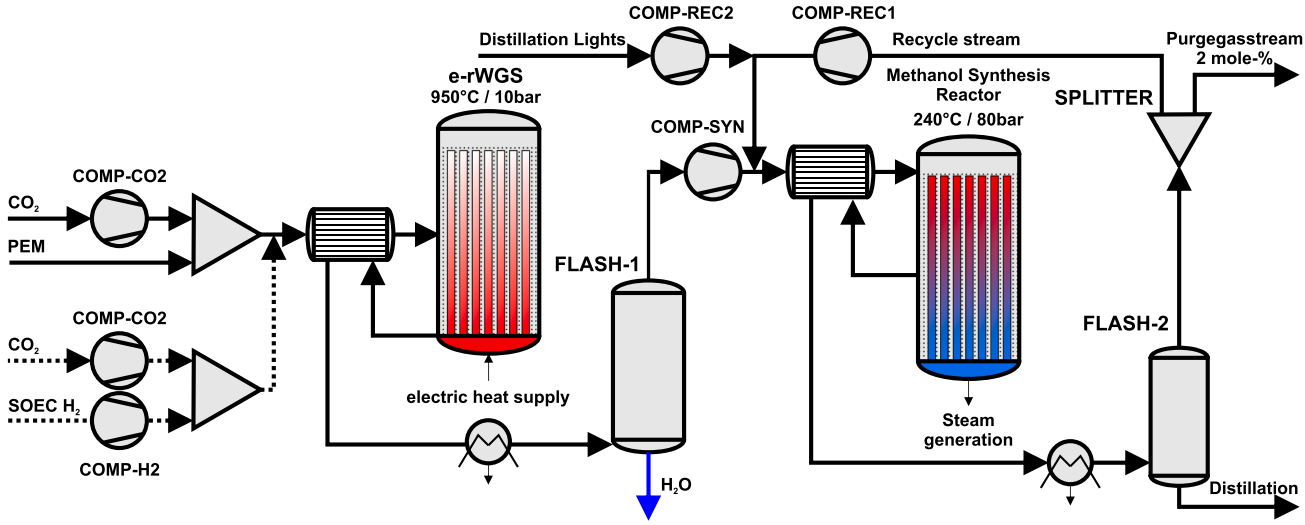

Fig. 5. Methanol production using a PEM/SOEC for hydrogen production, an rWGS reactor and a single stage methanol synthesis.

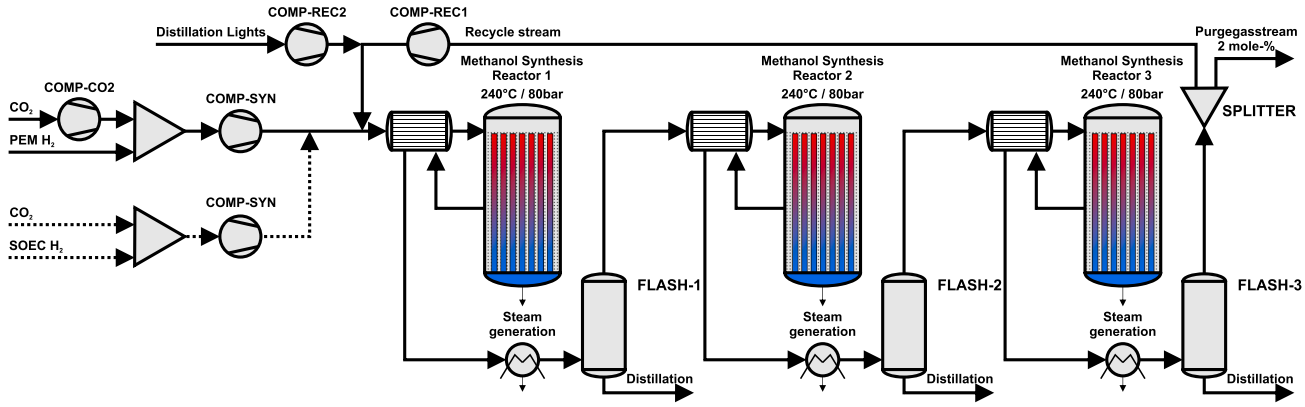

Fig. 6. Three-step methanol synthesis with PEM/SOEC for hydrogen production and intercooling for gas/liquid separation.

propylene) in a steam cracker. Again, the conversion yields and energy consumptions are taken from the literature, since these steam crackers are commercially available and standalone units (Karaba et al., 2021). The steam cracker operates at moderate pressures of 4 bar (g) and maximum temperatures of 815 °C. In Karaba et al. the feed fractions are divided into FT lights (FT L; C_5–C_{11}), FT middle distillate (FT MD; C_{10}–C_{23}) and vacuum residue (FT VR; C_{18}–C_{43}), the overall product is described as FT crude (FT Cr). The conversion yields are given for each fraction. The lower C_2–C_4 olefins consist of ethylene, propylene, but-1-ene, i-butene and butadiene (Karaba et al., 2021). In this elaboration, all other products are treated as by-products. The electrical energy demand for the steam cracker is assumed to be 15 MJ/$kg_{FT\text{-}Product}$ (IEA, 2017).

3. Simulation

The power to lower olefin plant is simulated in ASPEN Plus® V12.1. The ASPEN Plus simulation consists of the amine scrubber unit, the electrolysis and the Fischer–Tropsch or methanol synthesis. The amine scrubber unit is implemented in an electrolyte non-random two-liquid (ELECNRTL) section considering Henry coefficients for carbon dioxide, nitrogen and oxygen. The electrolysis and synthesis are simulated in a Peng-Robinson (PENG-ROB) section, and the distillation units of the methanol synthesis are furthermore run in a non-random-two-liquid (NRTL) model. Fig. 7 shows the flow sheet of the Fischer–Tropsch process chain with low temperature PEM electrolysis. The amine scrubber unit and electrolysis do not differ in each scenario. The consideration of heat integration is essential. Therefore, ASPEN Energy Analyzer® is used for the generation of a pinch analysis, which allows the calculation of required steam and cooling demand for a heat integrated process. The post-processing equipment (steam cracker and MtP unit) is not modeled in ASPEN Plus®, as its process setup is commercially available and a fully developed, standalone technology with available literature data for mass, energy and product yield figures. However, in order to take into account the influences of these facilities on the total performance of the different process chains, they were included as a black box in the mass and energy balance, but are considered in the cost calculation. The operation conditions for the main equipment are summarized in Table 1.

The scenarios are defined in Table 2 for each process route (Fig. 1), as the comparison of the Fischer–Tropsch and methanol synthesis, the electrolysis technology PEM and SOEC, as well as newly erected and existing steam cracker and MtP equipment should be considered.

For a technological comparison, key performance indicators (PtL, global efficiency and carbon conversion (Eq. (12) to Eq. (17)), and the specific energy consumption (Eq. (18) and Eq. (19))) as well as product quantities are calculated for each investigated scenario. The total operating time is assumed to be equal with the cement plant (7884 h per year).

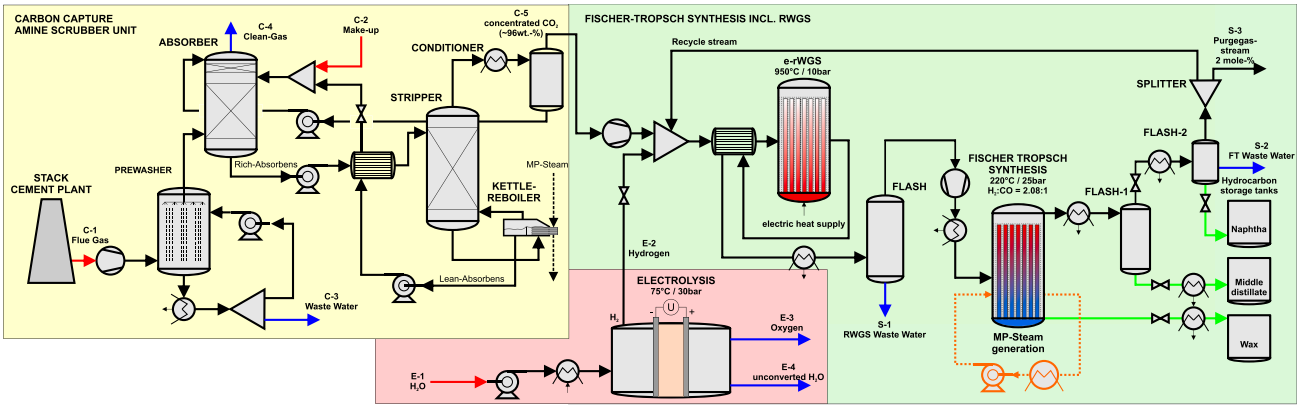

Fig. 7. Flow sheet of the Fischer–Tropsch process chain in a cement plant to capture 10,000 tons of CO2 per year.

Table 1
Operation conditions of the modeled operation units.

Equipment	Operating temperature [°C]	Operating pressure [bar (g)]
Pre-washer	40	0.4
Absorber column	40	0.4
Desorber column	110	0.1
PEM electrolysis	75	30
SOEC electrolysis	700–900	0.1
rWGS reactor	950	10
Methanol reactor	240	80
Fischer–Tropsch reactor	220	25

Table 2
Definition of synthesis, electrolysis and post-processing equipment for scenarios 1 to 8.

Scenario	Synthesis	Electrolysis	Post-processing equipment
1	Fischer–Tropsch with rWGS reactor	PEM	new steam cracker
2	Fischer–Tropsch with rWGS reactor	SOEC	new steam cracker
3	Fischer–Tropsch with rWGS reactor	PEM	existing steam cracker
4	Fischer–Tropsch with rWGS reactor	SOEC	existing steam cracker
5	Methanol synthesis with rWGS reactor	PEM	new MtP
6	Methanol synthesis with rWGS reactor	SOEC	new MtP
7	CO_2 tolerant methanol synthesis	PEM	new MtP
8	CO_2 tolerant methanol synthesis	SOEC	new MtP

The PtL efficiency η_{PtL} (Eq. (12) and Eq. (13)) is calculated by multiplying the lower heating value (LHV_i in kWh/kg) of the product fractions i with the associated product quantity ($\dot{m}_i$ in kg/h) divided by the total electrical energy demand, which is composed of the electrolysis energy (P_{el} in kW), the utilities electricity demand (P_U in kW) and in case of $\eta_{PtL,2}$ also the post-processing electrical demand (P_{post} in kW). Equipment such as pumps and compressors are considered in the utility category, therefore, P_U is the sum of the power demand of each equipment k (Eq. (11)). In this elaboration, $\eta_{PtL,1}$ is assigned to the intermediate product syncrude and methanol, whereas $\eta_{PtL,2}$ defines the PtL efficiency refered to the low chain hydrocarbon (C_2–C_4) product.

$$P_U = \sum_k P_{Uk} \tag{11}$$

$$\eta_{PtL,1} = \frac{\sum(\dot{m}_i * LHV_i)}{P_{el} + P_u} \tag{12}$$

$$\eta_{PtL,2} = \frac{\sum(\dot{m}_i * LHV_i)}{P_{el} + P_u + P_{post}} \tag{13}$$

The global efficiency η_{global} (Eq. (14) and Eq. (15)) includes not only the electrical power demand, but also the excess steam generation ($\dot{Q}_{heat}$ in kW) from the FTS reactor, or steam demand in case of methanol synthesis. If the possibility of steam export exists, the global efficiency is positively influenced. Steam generation lowers the global efficiency. Once again, the indices 1 and 2 define the intermediate or low chain hydrocarbon product, respectively.

$$\eta_{global,1} = \frac{\sum(\dot{m}_i * LHV_i)}{P_{el} + P_u + \dot{Q}_{heat}} \tag{14}$$

$$\eta_{global,2} = \frac{\sum(\dot{m}_i * LHV_i)}{P_{el} + P_u + P_{post} + \dot{Q}_{heat}} \tag{15}$$

The carbon efficiency η_{carbon} (Eq. (16) and Eq. (17)) describes the carbon yield in all products in relation to the carbon feed. It is defined as the ratio of carbon atoms present in the syncrude product fractions ($\sum \dot{n}_{c,prod,\,i}$) or low carbon chain product behind the post-processing units ($\dot{n}_{c,prod,C_2-C_4}$) to the carbon atoms fed to the PtL plant involving the carbon capture unit ($\dot{n}_{c,feed}$). Index 1 indicates the intermediate product syncrude or methanol, index 2 includes the post processing units and considers the products C_2 to C_4.

$$\eta_{carbon,1} = \frac{\sum \dot{n}_{c,prod,\,i}}{\dot{n}_{c,feed}} \tag{16}$$

$$\eta_{carbon,2} = \frac{\dot{n}_{c,prod,\,C_2-C_4}}{\dot{n}_{c,feed}} \tag{17}$$

The specific energy consumption (SEC, Eq. (18) and Eq. (19)) devides the total electrical energy input (P_{el} in kW) by the product quantity ($\dot{m}_{product}$ in kg/h). Index 1 considers only the intermediate product production, index 2 considers the complete process chain. However, caution must be paid for the intermediate product, as the entire electricity demand is also used in this calculation.

$$SEC_1 = \frac{P_{el} + P_u}{\dot{m}_{product,FT\ or\ MeOH}} \tag{18}$$

$$SEC_2 = \frac{P_{el} + P_u + P_{post}}{\dot{m}_{product,C2-C4}} \quad (19)$$

4. Economic calculation

Apart from the technological evaluation, the economics need to be considered when determining the most appropriate process route. Due to the stage of planning and several uncertainties in on-site utilities, the capital expenditures (CAPEX) estimation class 5 is selected, allowing for variations of +100/−50 % (AACE International Recommended Practices, 2020). Capital costs are calculated for inside battery limit (ISBL) equipment, which includes e.g., heat exchangers, compressors and multitube reactors (Fischer–Tropsch or methanol). Outside battery limit (OSBL) equipment, including cooling facilities or steam generation, is not considered in the investment cost calculation, however they are reflected in the operating costs. The operational expenditures (OPEX) include the main utility costs, such as electricity, operation and maintenance as well as labor costs. In the following subchapters, the CAPEX and OPEX calculation is carried out to calculate and compare the net production costs of the lower olefin product.

4.1. Capital cost calculation

ASPEN Process Economic Analyzer® V12.1 (APEA) calculates the major equipment costs (EC in EUR, base year 2019) according to the simulation performed, including e.g., heat exchangers, compressors, pumps, columns, etc. The investment costs and stack lifetime for the SOEC and PEM electrolysis are given in Table 3 (Herz et al., 2021).

The rWGS reactor is not a proven technology that is being integrated in such systems on large scale, therefore other literature data are considered. The design of the rWGS reactor is similar to a steam reforming reactor (high temperature level of 800–900 °C). For small steam reformers (0.15–15 MW), the investment costs are reported to be 3000 to 5000 USD_{2016}/kW (IEA, 2021). Since the electrified rWGS reactor has the advantage of smaller dimensions due to improved thermal management, the investment costs are reduced by approximately one third to 2000 EUR_{2016}/kW (IEA, 2021; Wismann et al., 2019).

The equipment costs (EC_{FT} in EUR) for the Fischer–Tropsch reactor are calculated by downscaling of available literature data from Herz et al. according to Eq. (20), whereas the base costs (EC_{ref} in EUR) are 18.93 $MEURR_{2019}$R, the base molar flow (S_{ref} in kmol/s) is 2.7 kmol/s and the scaling factor (d) is 0.85 (Herz et al., 2018). The occurring mole flow (S in kmol/s) is taken from the simulation results performed in this work.

$$EC_{FT} = EC_{FT,ref} * \left(\frac{S}{S_{ref}}\right)^d \quad (20)$$

The equipment costs for the steam cracker and MtP unit are taken with 2050 USD_{2018} and 1000 USD_{2018} per ton high value chemicals (syncrude or methanol), respectively, as a specific value from an IEA report (IEA, 2017). A distinction between US Dollar and Euro is not required in this investigation, due to the negligible difference in the current exchange rate (Finanzen.net, 2022).

The aforementioned prices differ in the year of publication, e.g., APEA databank uses the base year 2019. Therefore, it is necessary to align the equipment costs to actual market prices. The application of the "Chemical Engineering Plant Cost Index (CEPCI)" enables the calculation (Eq. (21)) of each equipment's actual market price (EC_{real}) based on February 2022 (e.g., the CEPCI figure is 801.3 for February 2022, for the APEA database it is 607.5 for the year 2019) (Towering Skills, 2022).

$$EC = EC_{ref} * \frac{CEPCI_{Feb,2022}}{CEPCI_{ref}} \quad (21)$$

The fixed capital investment costs (FCI) are composed of direct plant costs (D), indirect plant costs (I) and additional costs (AC). In Table 4, typical values for additional factors (ratio factor R) are listed, considering the impact purposes. The FCI calculation is applied by factor multiplication according to Eq. (19) (Herz et al., 2021). The ratio factor method is not fully used for electrolysis calculation, whereas only the factors 1, 6, 10, 11 and 12 are applied (Albrecht et al., 2017). For electrolysis, only factors R1, R6, R10, R11, and R12 are considered because the plant is installed in a modular design and the remaining factors are already considered in the CAPEX.

$$FCI = EC * \sum R_j \quad (22)$$

The working capital (WC) is assumed to be 10 % of total capital investment (TCI), since capital is needed for commissioning and startup.

$$TCI = FCI + WC \quad (23)$$

For an assumed rate of interest (IR) of 7 % and a pilot plant lifetime (PL) of 20 years, the annual depreciation ACC is calculated according to (Herz et al., 2021):

$$ACC = (FCI + WC) * \frac{IR * (1 + IR)^{PL}}{(1 + IR)^{PL} - 1} - \frac{WC}{PL} \quad (24)$$

4.2. Operational expenditures

The operational expenditures (OPEX) include the costs for operating labor (OL) as well as the ones for direct and indirect production.

The operating labor (OL) costs are calculated by multiplying the amount of labor hours (h_{labor}) with the specific labor costs (c_{labor}). The latter ones are taken from Albrecht et al. (Albrecht et al., 2017; Peters et al., 2004). According to Peters et al. the person hours can be estimated on the basis of the capacity of the plant and the number of units applied (Peters et al., 2004). The plant capacity is the total product quantity, syncrude or methanol quantity in kg/h, respectively. The plant operating time ($h_{plant,operation}$) is estimated to be 7884 h per year, according to the yearly operating time of the cement plant.

$$h_{labor} = 2.13 * \text{plant capacity}^{0.242} * n_{process_{steps}} * \frac{h_{plant_{operation}}}{24} \quad (25)$$

$$OL = h_{labor} * c_{labor} \quad (26)$$

Table 3
Investment costs and lifetime prediction of SOEC and PEM electrolysis for 2020 and 2050 (Herz et al., 2021).

Electrolysis type	SOEC		PEM	
Reference year	2020	2050	2020	2050
Specific investment cost [EUR_{2020}/kW]	1906	257	1287	296
Lifetime [h]	45,473	88,700	66,709	89,509

Table 4
Additional factors for fixed capital investment cost (FCI) calculation of fluid chemical plants (Herz et al., 2021).

Fixed capital costs (FCI)	j	Basis	Typical Value R
Total direct plant costs (D)			
Equipment installation	1	EC	0.47
Instrumentation and control	2	EC	0.36
Piping (installed)	3	EC	0.68
Electrical (installed)	4	EC	0.11
Buildings including services	5	EC	0.24
Yard improvements	6	EC	0.1
Service facilities (installed)	7	EC	0.55
Total indirect plant costs (I)			
Engineering and supervision	8	EC	0.33
Construction expenses	9	EC	0.41
Legal expenses	10	EC	0.04
As a function of total direct and indirect costs (AC)			
Contractor's fee	11	$D + I$	0.05
Contingency	12	$D + I$	0.1

The number of units ($n_{process,steps}$) is defined as any unit, unit process or combination, where thermodynamic or chemical changes occur (Albrecht et al., 2017). In this work, the numbers of process steps for each scenario are listed in Table 5. "Balance of plant" is also included as a process step, as it should include the interconnection of all process units.

The OL are taken as basis for additional fixed operating costs (FixOPEX) by applying the ratio factor method as performed for FCI. The used ratio factors for direct and indirect production costs and general expenses are taken from Albrecht et al. and are listed in Table 4 (Herz et al., 2021; Albrecht et al., 2017). The number of electrolysis stack replacement cycles (SR) is calculated by Eq. (27) and depends on the stack lifetime (SL in h, Table 3) and plant lifetime (PL).

$$SR = \text{rounddown}\left(\frac{PL * h_{plant,operation}}{SL} - 1\right) \quad (27)$$

It is assumed, stacks are replaced after lifetime, the costs are distributed over the entire life cycle. The depreciation is included in the calculation as sawtooth depreciation. Derived from this, annual replacement costs (Eq. (28), ARC in EUR/year) account for operating costs and are calculated with the ratio factor (R7 of Table 6) as followed:

$$ARC = \frac{SR * EC * R_7}{LT} \quad (28)$$

The main cost drivers are electricity costs for electrolysis and compressor, which are assumed to be 200 EUR/MWh (average of Q1 and Q2/2022) (E-Control Austria für die Regulierung der Elektrizitäts- und Erdgaswirtschaft, 2022). Water as a feedstock must also be considered, with a local cost of 1.85 EUR/m^3 (Hof am Leithaberge, 2022). Medium pressure steam is purchased for 26.3 EUR/t, the revenue in case of steam export is assumed as the same value (Albrecht et al., 2017). Since the export of oxygen is not economical to this extent, it is assumed that it is released into the atmosphere or fed to the cement plant's rotary kiln. Therefore, revenues from oxygen are not considered in the calculation.

The total OPEX are composed of FixOPEX, the variable OPEX including utility costs and revenues from by-products or export products.

4.3. Net production costs (NPC)

The net production costs (NPC in EUR/year) are composed of annualized capital costs (ACC in EUR/year) and operational expenditures (OPEX in EUR/year). For the calculation of NPC, the methodology of Peters et al. is applied (Peters et al., 2004). The specific NPC_{pr} (Eq. (29), in EUR/kg) is calculated for the liquid intermediate product syncrude and methanol as well as for the lower olefine product (C_2–C_4) to set a basis for the scenario comparison.

Table 5
Process step definition for each scenario for labor hour calculation.

Number of unit $n_{process,steps}$	Scenario number		
	1–4 Fischer–Tropsch	*5–6 MeOH with rWGS*	*7–8 CO_2tolerant MeOH*
1	Carbon capture unit	Carbon capture unit	Carbon capture unit
2	Electrolysis unit	Electrolysis unit	Electrolysis unit
3	rWGS reactor	rWGS reactor	MeOH synthesis reactor 1
4	Fischer–Tropsch reactor	MeOH synthesis	MeOH synthesis reactor 2
5	Product separation	Product Separation	MeOH synthesis reactor 3
6	Steam cracker unit	Methanol-to-propylene unit	Product separation
7	Balance of plant	Balance of plant	Methanol-to-propylene unit
8			Balance of plant

Table 6
Ratio factors for fixed operational expenditures (OPEX) calculation.

Fixed operational expenditures FixOPEX	j	Basis	Typical value R
Direct production costs			
Operating labor [OL]	1	OL	1
Operating supervision	2	OL	0.15
Maintenance labor	3	FCI	0.02
Maintenance material	4	FCI	0.02
Operating supplies	5	M[1]	0.15
Laboratory charges	6	OL	0.2
Electrolysis stack replacement	7	EC	0.77
Indirect production costs			
Insurance and taxes	8	FCI	0.02
Plant overhead costs [PO]	9	TLC[2]	0.6
General expenses			
Administrative costs	10	PO	0.25

[1]M = Maintenance labor (R3) + maintenance material (R4).
[2]PLC = Total labor costs = operating labor (R1) + operating supervision (R2) + maintenance labor (R3).

$$NPC_{pr} = \frac{ACC + OPEX}{\dot{m}_{chemical}} \quad (29)$$

4.4. Sensitivity analysis of assumed market prices

A sensitivity study of assumed market prices is crucial now, as equipment and electricity costs are coupled to a turbulence market situation. Therefore, an optimistic and pessimistic case are defined in Table 7 for these categories, as they include changes in the process design (equipment costs) and also the major utility costs (electricity). Beside the market assumptions, the investment costs of the electrolysis technology will decrease as stated in Table 3 (Herz et al., 2021). For all these assumptions, the net productions costs are recalculated, and the deviation to the base cases of each scenario are elaborated.

5. Results

The simulation and calculation results of the defined scenarios with intermediate products syncrude and methanol and subsequent steam cracker or MtP unit are divided into the sections mass (chapter 5.1) and energy balance (chapter 5.2), investment, operating and net production costs (chapter 5.3) and sensitivity analysis (chapter 5.4). The comparison is generally based on the final product lower olefins (C_2–C_4) to achieve high product yields and low specific net production costs, and guarantee an unobstructed process selection too. The ASPEN Flowsheets incl. mass balance are available in the supplementary material.

5.1. Investigation of the mass balance

The mass balance for the carbon capture unit is given in Table 8. Because the same quantity of annual 10,000 tons of CO_2 (C-5) is captured, the mass balance of the amine scrubbing unit is the same for all scenarios. The CO_2 separation efficiency is calculated with 90.5 % which corresponds to the findings of Madeddu et al., who specified a value of 90 % (Madeddu et al., 2019). The separated CO_2 is concentrated at 96.8 wt.- % (wet) or 99.9 wt.- % (dry) and therefore suitable for utilization. A minor MEA stream is discharged in the absorber tower by the clean gas stream C-4. This is fed by an additional makeup stream C-2 (0.03 kg/h) to keep the concentration of MEA solution at 30 wt.- %. The

Table 7
Assumptions for the sensitivity analysis.

Utility or ratio	Optimistic case	Base case	Pessimistic case
Equipment costs	50 %	100 %	200 %
Electricity price	100 EUR/MWh	200 EUR/MWh	400 EUR/MWh
PEM/SOEC	296 / 257 EUR/kW	1906 / 1209 EUR/kW	–

Table 8
Mass balance of the carbon capture unit for all scenarios.

Mass balance		Inlet		Outlet		
Carbon capture unit		C-1 Flue gas	C-2 Makeup amine	C-3 Pre-washer wastewater	C-4 Clean gas	C-5 Concentrated CO_2
Total	**kg/h**	**6686**	**785.03**	**243**	**5926**	**1302**
H_2O	*kg/h*	*504*	*785*	*243*	*1006*	*41*
CO_2	*kg/h*	*1391*			*130*	*1260*
N_2	*kg/h*	*4049*			*4048*	*1*
O_2	*kg/h*	*742*			*742*	
MEA	*kg/h*		*0.03*		*0.03*	

lean amine solvent has a composition of 0.29 mol_{CO2}/mol_{MEA} and corresponds to the validated values with a range of 0.28–0.35 mol_{CO2}/mol_{MEA} from Sakwattanapong et al. (Sakwattanapong et al., 2005).

The mass balance for the electrolysis unit is given in Table 9. The type of electrolysis for scenario 1 to 8 has no affect in the mass balance, as operation conditions are decisive in these comparisons. Depending on the considered synthesis in the downstream process, the hydrogen demand is 2 and 3 kg/h higher for the FTS (176 kg_{H2}/h) compared to the methanol synthesis (173 kg/h in scenario 5 and 6, 174 kg/h in scenario 7 and 8). The deviations stem from the H_2:CO ratio downstream of the rWGS reactor, as the recycle stream composition differs for methanol and FTS.

The mass balance for the PtL process route from CO_2 and hydrogen as input streams to the intermediate products syncrude and methanol is given in Table 10. The main product in Fischer–Tropsch processes (scenarios 1 to 4) are hydrocarbons, which are divided into lights (C_1–C_4), naphtha (C_5–C_{10}), middle distillate (C_{11}–C_{22}) and waxes (>C_{22}), resulting from the ASF distribution, whereas methanol is the product in scenarios 5 to 8. Scenarios 1 to 6 are operated with a rWGS reactor, whereas an intermediate water condensing step is indispensable in the process to shift the thermodynamics for the downstream synthesis part. The main product consists of 381 $kg_{syncrude}$/h for the FTS (scenarios 1 to 4), 881 kg/h (scenarios 5 and 6) and 894 kg/h (scenarios 7 and 8), respectively, for methanol synthesis. Scenarios 5 and 6 with an implemented rWGS reactor produce 13 kg/h less methanol compared to the CO_2 tolerant methanol synthesis in scenarios 7 and 8. This is a result of the combination of two different synthesis technologies (rWGS and MeOH synthesis), as the rWGS reaction produces methane within a side reaction (Eq. (3)). Even small quantities lead to lower product, as methane is treated inert in the methanol synthesis, which lowers the product output. A comparison of product quantities is not appropriate, as the composition and lower heating value (LHV) of syncrude and methanol is not comparable. For methanol, an LHV of 5.53 kWh/kg_{MeOH} is assumed, the LHV for the Fischer–Tropsch product is calculated for each fraction according to Boie and averages at 44.1 $MJ/kg_{FT\text{-}Product}$ (McAllister, 2011). In the methanol synthesis scenarios 5 to 8, the purge gas stream consists only of methane and unconverted gasses. In contrast, the purge gas of the Fischer–Tropsch process (scenarios 1 to 4) consists of additional higher order, gaseous hydrocarbons which are linked upstream to the rWGS reactor. In scenarios 1 to 4, possible side reactions occur in the rWGS reactor (see chapter 2.3), whereas the H_2:CO = 2.08:1 ratio is maintained by adjusting the hydrogen feed for both syntheses. If downstream processing units (steam cracker or MtP) would not be available on site of syncrude or methanol production, the up to 2.3 times higher amount of methanol compared to the Fischer–Tropsch product would lead to the disadvantage of larger required storage volumes and higher transportation costs.

Lower olefins (ethylene, propylene and butene) are considered as desired main products in this study, as they are the basis for further conversion into polyolefins. The product yields achieved with post-processing units via a steam cracker for the Fischer–Tropsch product and MtP for methanol are given in Table 11. The LPG fraction of the MtP process is accounted for the butene fraction (raw C_4), and the remainder (gasoline) counts for higher hydrocarbons and is attributed to others. Methanol consists of carbon and hydrogen plus oxygen. The latter one is not converted into olefins, whereas water is produced in the MtP plant, which leads to the requirement of higher wastewater treatment capacities. The lower olefin product yield (C_2–C_4) of the steam cracker is higher compared to the MtP process (4 and 6 wt.- %, respectively, difference to the product yield of the MtP process). Scenarios 1 to 4 are the best-case scenarios with an achieved product quantity of 297 kg/h. The

Table 9
Mass balance of the electrolysis unit for all scenarios.

Mass balance - electrolysis			Scenario number		
			1–4	5–6	7–8
Inlet					
E-1 Water	H_2O	kg/h	1652	1641	1631
Outlet					
E-2 Hydrogen	H_2	kg/h	176	174	173
E-3 Oxygen	O_2	kg/h	1394	1385	1376
E-4 Unconverted water	H_2O	kg/h	83	82	82

Table 10
Mass balance of the synthesis unit for all scenarios.

Mass balance - synthesis			Scenario number		
			1–4	5–6	7–8
Inlet					
C-5 Concentrated CO_2	**Total**	**kg/h**	**1302**		
	H_2O	*kg/h*	*41*		
	CO_2	*kg/h*	*1260*		
	N_2	*kg/h*	*1*		
E-2 Hydrogen	**H_2**	**kg/h**	**176**	**174**	**173**
Outlet					
S-1 rWGS wastewater	**H_2O**	**kg/h**	**376**	**456**	**0**
S-2 Synthesis wastewater	**H_2O**	**kg/h**	**670**	**104**	**548**
S-3 Purge gas	**Total**	**kg/h**	**48**	**35**	**32**
	CO	*kg/h*	*31*	*3*	*2*
	H_2	*kg/h*	*4*	*3*	*4*
	CO_2	*kg/h*	*6*	*19*	*25*
	N_2	*kg/h*	*1*	*1*	*1*
	CH_4	*kg/h*	*5*	*9*	*0*
	$>C_1$	*kg/h*	*1*	*0*	*0*
S-4 Product	**Total**	**kg/h**	**383**	**881**	**894**
	CH_3OH	*kg/h*	*0*	*881*	*894*
	H_2O	*kg/h*	*2*	*0*	*0*
	C_5–C_{10}	*kg/h*	*41*	*0*	*0*
	C_{11}–C_{22}	*kg/h*	*149*	*0*	*0*
	$>C_{22}$	*kg/h*	*191*	*0*	*0*
	Total C_5–C_{22+}	**kg/h**	*381*	*0*	*0*

Table 11
Product yield of post-processing steam cracker (syncrude) and MtP units (methanol).

Mass balance – post-processing unit			Scenario number		
			1–4	5–6	7–8
Inlet					
Product Syncrude/MeOH	**Total**	**kg/h**	**383**	**881**	**894**
Outlet					
Products C_2–C_4	**Total**	**kg/h**	297	280	284
Ethylene	C_2H_4	kg/h	166	11	11
Propylene	C_3H_6	kg/h	70	250	254
Butene	C_4H_8	kg/h	61	19	19
Byproducts	**Total**	**kg/h**	86	0	0
Water	H_2O	kg/h	2	493	501
Other hydrocarbons/by-products		kg/h	84	107	109

main focus in scenarios 5 to 8 is in the propylene production, whereas total lower olefins of 280 kg/h and 284 kg/h are achieved for scenarios 5 and 6, as well as 7 and 8, respectively. Concluding the mass balance, the analysis shows the best lower olefin yields for scenarios 1 to 4, consisting of an rWGS reactor, and an FTS with downstream steam cracker unit. The scenarios 5 and 6, consisting of a rWGS reactor for pre-conversion perform worst.

5.2. Investigation of energy balance

The energy balances for the whole process routes are given in Table 12, whereas the main utility used in all process routes is electricity. The main consumer is the electrolysis, followed by the electrified rWGS reactor (if applicable), the gas compression, and pumps. Heat integration is also carried out for each process route using ASPEN Energy Analyzer® V12.1. In the Fischer–Tropsch process, the highly exothermic reaction enables the generation of middle pressure steam, which is used to operate the desorber reboiler and preheat the SOEC input stream in scenarios 2, 4, 6 and 8 (water evaporation at 5 bar(g) from 10 °C to 165 °C). Methanol synthesis is exothermic; however, additional steam must be generated for the desorber and SOEC units due to the lower energy release in the methanol synthesis compared with FTS. If steam is required, it is imported and considered in the operational cost calculation as utility. The electrolysis has the highest electricity demand, which strongly depends on the specific energy consumption of the applied electrolysis technology (3.6 and 4.7 kWh/Nm^3_{H2} for SOEC and PEM, respectively).

For an appropriate technical comparison of each defined scenario, the evaluation basis must be defined. In this work, the key performance indicators (KPI) PtL efficiency (Eq. (12) and Eq. (13)), the global efficiency (Eq. (14) and Eq. (15)), the carbon efficiency (Eq. (16) and Eq. (17)) and the SEC (Eq. (18) and Eq. (19)) are calculated and listed in Table A.8 (supplementary material) and shown in Fig. 8. Whereas PtL efficiency only includes electrical energy, global efficiency emphasizes the importance of heat integration, since it also considers steam use or generation, which is an important factor for process decision. The PtL efficiency is best for methanol synthesis, however, regarding to global efficiencies as well as SEC, the best process scenarios consist of the FTS with hydrogen production via an SOEC (scenarios 2 and 4) with a PtL efficiency of 37.5 %, a global efficiency of 38.2 %, a carbon efficiency of 85.1 % and an SEC of 34.4 kWh/$kg_{C_2-C_4}$. A disadvantage is the 2–3 % lower carbon efficiency compared to the methanol routes which achieve best KPIs in scenario 8, with a PtL efficiency of 64.3 % and global efficiency of 51.1 %. Since the supply of renewable electricity remains as a bottleneck in the upcoming years, high PtL efficiencies of the processes are particularly important for a production with low energy input. The steam demand is expected to be produced electrically, which would decrease the PtL efficiency of the methanol syntheses. Therefore, global efficiency is considered in this case specifically. The comparison is based on the SEC_2 on the lower olefin product because the total product composition of Fischer–Tropsch and methanol routes is different, and thus the values would not be representative. In conclusion it can be summarized, that from a mass and energy perspective, scenario 2 and 4 seems to be the best option for a power-to-lower olefin plant with 34.4 kWh/$kg_{C_2-C_4}$, compared to the best methanol scenario 6 with 44.2 kWh/$kg_{C_2-C_4}$.

5.3. Economic study

To determine the most suitable process route, the investment and operational costs must be considered in addition to the technical assessment. Table 13 shows the estimated costs for the individual scenarios. The use of ASPEN Process Economic Analyzer® V12.1 allows the determination of the equipment costs for the amine scrubbing and synthesis including the product separation unit. The equipment and investment costs for the amine scrubber unit are the same for each process route, based on the same annual capture volume of 10,000 tons of CO_2. The TCI differs for each process and is strongly dependent on the used electrolysis type. The SOEC requires an additional hydrogen compressor for scenario 2, 4, 6 and 8, which results in much higher TCI as well as of ACC. The integration of an existing steam cracker unit reduces the investment costs radically, which is shown as a result for scenario 3. It has the lowest TCI with 77.4 MEUR.

Beside the investment costs, the operating costs are continuously ongoing, and therefore have to be considered in the economic evaluation. The utility costs are listed in Table 14, whereas the main cost driver is composed by the electricity costs, which accounts for more than 95 % of total utility costs in each scenario. Steam export has a positive influence on utility costs for Fischer–Tropsch processes (scenarios 1 to 4), however, steam use leads to additional costs for the methanol processes (scenarios 5 to 8).

The calculation results of the operational expenditures are shown in Table 15. As for the utility cost breakdown (Table 14), a more efficient electrolysis technology (SOEC instead of PEM) has a significant impact on the electricity demand and costs. Table 15 also shows the specific net production costs (NPC_{Pr}) for the Fischer–Tropsch and methanol synthesis, whereas scenario 3 has the lowest NPC_{Pr}. Analyzing scenario 3, the specific NPC_{Pr} of syncrude are 0.95 EUR/kWh, which equals to

Table 12
Summarized utility demand (electricity, steam and product energy content) of the scenarios.

Energy balance			Scenario number					
			1,3	2,4	5	6	7	8
Total electricity demand	$\mathbf{P_{total}}$	**kW**	**13,074**	**11,112**	**12,776**	**10,807**	**12,249**	**10,458**
Utilities – Total electricity demand	$\mathbf{P_u}$	**kW**	**1415**	**1605**	**697**	**866**	**423**	**757**
Compressors	P_{u1}	kW	519	714	425	599	519	714
Blower flue gas	P_{u1-1}	*kW*	*118*		*118*		*118*	
Compressor CO_2	P_{u1-2}	*kW*	*80*		*80*		*120*	*0*
Compressor H_2	P_{u1-3}	*kW*	*0*	*194*	*0*	*0*	*0*	*0*
Compressor synthesis	P_{u1-4}	*kW*	*321*		*218*		*138*	*598*
Compressor recycle 1	P_{u1-5}	*kW*	*0*		*4*	*9*	*9*	*9*
Compressor recycle 2	P_{u1-6}	*kW*	*0*		*5*	*2*	*2*	*2*
Pumps	P_{u2}	kW	6	6	6	1	6	1
Preheater+eRWGS	P_{u3}	kW	889		266		29	
Electrolysis	$\mathbf{P_{el}}$	**kW**	**9177**	**7030**	**9117**	**6983**	**9060**	**6939**
Steam cracker/MtP	$\mathbf{P_{post}}$	**kW**	**1587**		**2691**		**2732**	
Steam generation (-)/use (+)	$\mathbf{Q_{heat}}$	$\mathbf{kW_{th}}$	**−639**	**−182**	**1165**	**1682**	**787**	**1992**
Product energy content 1	**Total C_5-C_{22+}, Methanol**	**kW**	**4665**		**4872**		**4946**	
Product energy content 2	**Total C_2-C_4**	**kW**	**3831**		**3566**		**3621**	
Product Energy Content - ethylene	C_2H_4	*kW*	*2174*		*139*		*141*	
Product energy content - propylene	C_3H_6	*kW*	*893*		*3186*		*3235*	
Product energy content - butene	C_4H_8	*kW*	*764*		*242*		*245*	

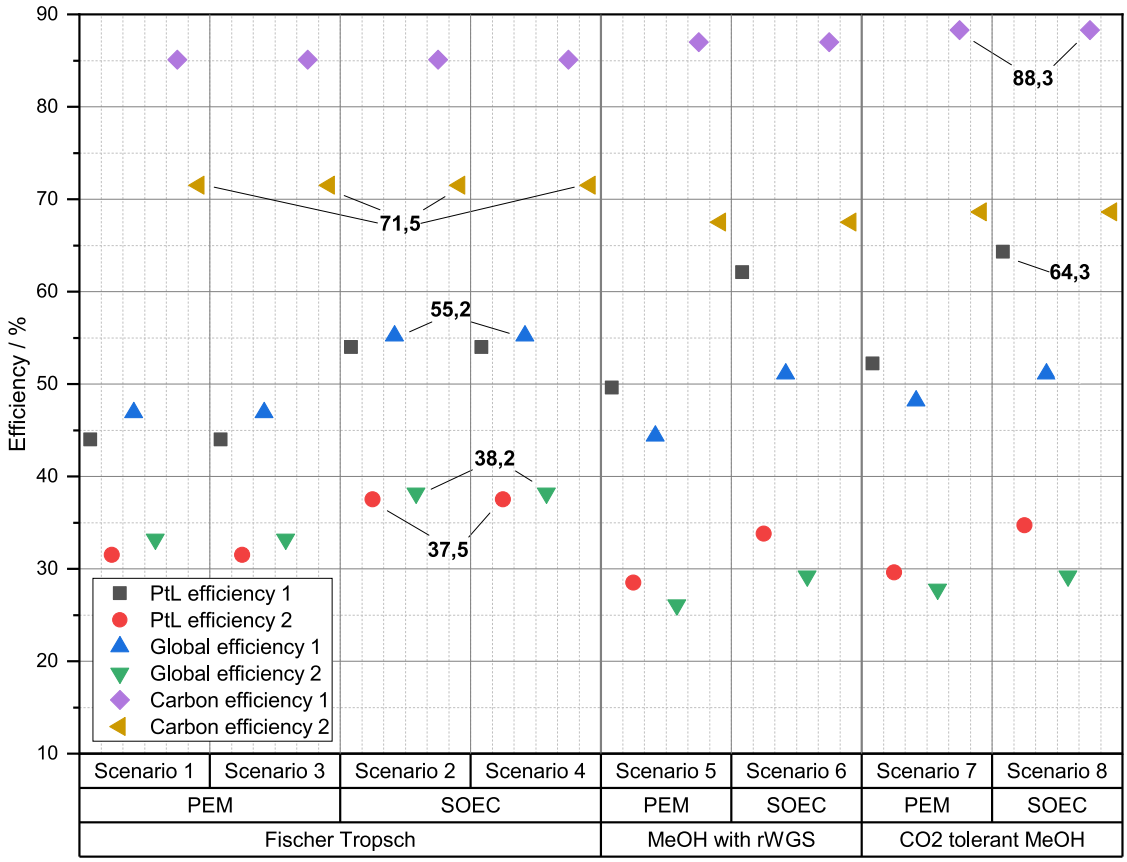

Fig. 8. Calculated efficiencies and indication of maximum values for each scenario.

Table 13
Capital investment calculation for fluid chemical production according to Peters et al. (Peters et al., 2004).

CAPEX – Investment costs		Scenario number							
		1	2	3	4	5	6	7	8
Direct capital costs [D]	MEUR	53.1	70.7	53.1	64.5	54.6	65.6	54.6	54.1
Indirect capital costs [I]	MEUR	7.5	9.5	7.5	9.5	7.9	9.8	7.9	7.2
Total direct and indirect costs [$D + I$]	**MEUR**	**60.6**	**74.0**	**60.6**	**74.0**	**62.5**	**75.4**	**62.5**	**61.3**
Additional costs [AC]	MEUR	9.1	11.1	9.1	11.1	9.4	11.3	9.4	9.2
Post processing investment costs	MEUR	6.2	6.2	0.0	0.0	6.9	6.9	7.0	7.0
Fixed capital investment [FCI]	**MEUR**	**75.8**	**91.2**	**69.7**	**85.1**	**78.8**	**93.6**	**78.9**	**77.5**
Working capital [WC]	MEUR	8.4	10.1	7.7	9.5	8.8	10.4	8.8	8.6
Total capital investment [TCI]	**MEUR**	**84.3**	**101.4**	**77.4**	**94.5**	**87.6**	**104.0**	**87.7**	**86.1**
Annualized capital cost [ACC]	**MEUR/year**	**7.5**	**9.1**	**6.9**	**8.4**	**7.8**	**9.3**	**7.8**	**7.7**

Table 14
Raw materials and utility costs of the process routes.

Raw materials and utilities (R&U)		Scenario number							
		1	2	3	4	5	6	7	8
Electricity	MEUR/year	19.24	16.15	19.24	16.15	21.91	19.79	20.74	20.20
Water	MEUR/year	0.05	0.05	0.05	0.05	0.05	0.05	0.05	0.05
Steam	MEUR/year	−0.17	−0.05	−0.17	−0.05	0.31	0.45	0.21	0.53
Cooling water	MEUR/year	0.10	0.04	0.10	0.04	0.11	0.04	0.10	0.05
Cooling water treatment	MEUR/year	0.01	0.00	0.01	0.00	0.01	0.00	0.01	0.00
Total raw materials and utility costs	**MEUR/year**	**19.23**	**16.20**	**19.23**	**16.20**	**22.39**	**20.34**	**21.10**	**20.83**

specific NPC_{Pr} 1.16 EUR/$kg_{C_2-C_4}$ or 15.03 EUR/$kg_{C_2-C_4}$ for the product lower olefins. The production of lower olefins via the methanol route (scenarios 5 to 8) results in higher NPC_{Pr} (up to 1.45 EUR/$kWh_{C_2-C_4}$ or 18.5 EUR/$kg_{C_2-C_4}$) compared to the Fischer–Tropsch routes (scenarios 1 to 4). The higher investment costs of SOEC compared to PEM turn out to be not as critical as first assumed, as the high electricity price has a strong impact on the operating costs. As a conclusion, the FTS in scenarios 3 and 4 turns out to be the best-case scenario in terms of economic

Table 15
Operational expenditures calculation for liquid chemical production according to Peters et al. (Peters et al., 2004).

OPEX – Operating costs		Scenario number							
		1	2	3	4	5	6	7	8
Direct production costs									
Operating labor [OL]	MEUR/year	0.77	0.77	0.77	0.77	0.94	0.94	1.08	1.08
Operating supervision	MEUR/year	0.12	0.12	0.12	0.12	0.14	0.14	0.16	0.16
Maintenance labor	MEUR/year	1.52	1.82	1.52	1.82	1.58	1.87	1.58	1.55
Maintenance material	MEUR/year	1.52	1.82	1.52	1.82	1.58	1.87	1.58	1.55
Operating supplies	MEUR/year	0.46	0.55	0.46	0.55	0.47	0.56	0.47	0.47
Laboratory charges	MEUR/year	0.15	0.15	0.15	0.15	0.19	0.19	0.22	0.22
Raw materials and utilities	MEUR/year	19.23	16.20	19.23	16.20	22.39	20.34	21.10	20.83
Electrolysis stack replacement [ARC]	MEUR/year	1.07	1.82	1.02	1.53	0.90	1.54	0.90	1.53
Indirect production costs									
Insurance and taxes	MEUR/year	1.52	1.82	1.39	1.70	1.58	1.87	1.58	1.55
Plant overhead costs [PO]	MEUR/year	1.44	1.63	1.44	1.63	1.60	1.77	1.69	1.68
Administrative costs	MEUR/year	0.36	0.41	0.36	0.41	0.40	0.44	0.42	0.42
Annuity [ACC]	MEUR/year	7.53	9.06	6.92	8.45	7.83	9.30	7.84	7.70
Net production costs [NPC]	**MEUR/year**	**35.67**	**36.17**	**34.89**	**35.14**	**39.59**	**40.85**	**38.62**	**38.73**
Specific NPC_{pr} – syncrude/MeOH	EUR/kg	11.88	12.04	11.61	11.70	5.71	5.89	5.48	5.50
Specific NPC_{pr} - syncrude/MeOH	EUR/kWh	0.97	0.98	0.95	0.96	1.03	1.06	0.99	0.99
Specific NPC_{pr}–C_2–C_4	EUR/kg	15.26	15.47	14.92	15.03	17.93	18.50	17.23	17.28
Specific NPC_{pr}–C_2–C_4	EUR/kWh	1.18	1.20	1.16	1.16	1.41	1.45	1.35	1.36

evaluation. However, also the calculation with a newly erected steam cracker (scenarios 1 and 2) would have better specific NPC_{Pr} compared to all methanol process routes. Furthermore, the implementation of a PEM electrolysis has a slight advantage in specific NPC_{Pr} (0.02 EUR/$kWh_{C_2–C_4}$).

As a validation of the process models, usually the specific NPC_{Pr} can be compared with other studies. As already stated in the introduction (chapter 1), several authors studied the conversion of CO_2 and H_2 to the final product kerosene or methanol, and not to lower olefins. However, they are not involving any post-processing steam cracker or MtP unit (Adelung et al., 2021; König et al., 2015; Herz et al., 2021; Ghosh et al., 2019).

Ghosh et al. compared two methanol synthesis processes, once with an rWGS reactor for pre-conversion and downstream methanol reactor, and a second one with a two-stage methanol synthesis (Ghosh et al., 2019). The process route with implemented rWGS reactor as pre-converter performs poor compared to the two-step reactor. This is also the result of this study, as the methanol product yield (881 and 894 kg/h) and global efficiency are lower for scenarios 5 and 6 with rWGS reactor. From an economic perspective, the representative specific NPC_{Pr} are about 0.06 and 0.10 $EUR_{2022}/kWh_{C_2–C_4}$ higher in scenarios 5 and 6, compared to scenarios 7 and 8, implementing a three-step methanol synthesis. This is also the case for the comparison of NPC_{Pr} of the intermediate product methanol. Ghosh et al. did not calculate NPC, which does not allow the comparison of costs.

König et al. simulated and evaluated a PtL process, converting CO_2 and H_2 in an rWGS reactor to syngas und furthermore in a downstream FTS and hydrocracker, to achieve high kerosene yields. Hydrogen is produced via a PEM electrolysis and a carbon capture unit is not included in investment costs. A main difference is the assumption of the electricity price, as it is assumed with 116 EUR/MWh. The calculated net production costs result in 0.46 EUR_{2015}/MWh (König, 2016). A recalculation of the NPC_{Pr} is done for this study with the electricity price from König et al. and without the investment costs of the amine scrubber unit. The NPC_{Pr} results for scenario 3 (including a PEM electrolysis and no steam cracker investment costs) in 0.51 $EUR_{2015}/kWh_{methanol}$ (König, 2016). This deviation is acceptable, because there may be the impact of the plant size, since a pilot plant is planned in this study and König et al. uses a process with 1.512 GW electrolysis, which could also reduce NPC.

Herz et al. also simulated a PtL process with a PEM (72.2 MW) and SOEC (67.8 MW) electrolysis, which converts CO_2 and H_2 to syncrude. A carbon capture unit is not included in their study. The electricity price is assumed with 54 EUR/MWh, which leads to NPC_{Pr} of 0.26_{PEM} and 0.20_{SOEC} $EUR_{2020}/kWh_{syncrude}$. A recalculation of this work's study with the electricity price of Herz et al. results in values of 0.49_{PEM} and 0.51_{SOEC} $EUR_{2020}/kWh_{syncrude}$. In this case, also a deviation is recognizable, as the FCI with 313.9 and 148.7 $MEUR_{2020}$ for the process route with PEM and SOEC, respectively, seems to be quite low compared to this work, as only main components (e.g., reactor, compressor) were considered, without performing a detailed equipment calculation.

Adelung et al. used the same process setup as König et al. for kerosene production (52–82 kt_{C5+}/year) (Adelung and Dietrich, 2022). In the economic comparison hydrogen costs are implemented between 2.3 to 7.6 EUR/kg_{H2}, which results in NPC_{Pr} varying between 1.81 and 5.47 EUR_{2021}/kg_{C5+}. Hydrogen is produced with a PEM electrolysis and an electricity price of 51 EUR/MWh. Updating this study with the electricity price of Adelung et al., the NPC_{Pr} are calculated to 5.62 $EUR_{2021}/kg_{syncrude}$, whereas the deviation is quite acceptable. The gap is comprehensible, when comparing the MEA absorption process, as it is assumed in their study with 31.8 $MEUR_{2005}$ investment costs for a 134.81 t_{CO2}/h carbon capture unit. The calculation of the carbon capture unit with the reference of Adelung et al. and a degression factor of 0.8 leads to 0.77 $MEUR_{2005}$, quite low compared to approximately 7 $MEUR_{2022}$ calculated in this study.

5.4. Sensitivity analysis of economic assumptions

Fluctuating market prices, especially rising equipment costs and high electricity prices, change the NPC calculation quickly, and makes it hard to give forecasts and predictions for the most suitable process route. Therefore, the deviation of recalculated NPC_{Pr} for the equipment costs, electricity price and future PEM/SOEC costs are given in Fig. 9 and Table A.9 (supplementary material). With the main driver being the electricity price, the NPC_{Pr} can change up to +55.6 % in scenario 3. However, the equipment cost variation results in only +40 % for scenario 2. Future PEM and SOEC equipment costs also have a major impact on total NPC, as they can reduce the costs up to −17.4 % in scenario 2. For the previous selected best-case scenario 4, rising equipment costs have an impact of +36.3 %, the rising electricity price +48.6 % and the lower PEM/SOEC future costs −14.6 % of NPC.

6. Conclusion

This study reveals a comparison of different process routes to convert 10,000 tons/year of CO_2 rich cement plant off-gas and H_2 catalytically to lower olefins. Fischer–Tropsch syncrude and methanol are considered as intermediate products, which are further converted in a downstream steam cracker or MtP unit to lower olefins. The technological evaluation

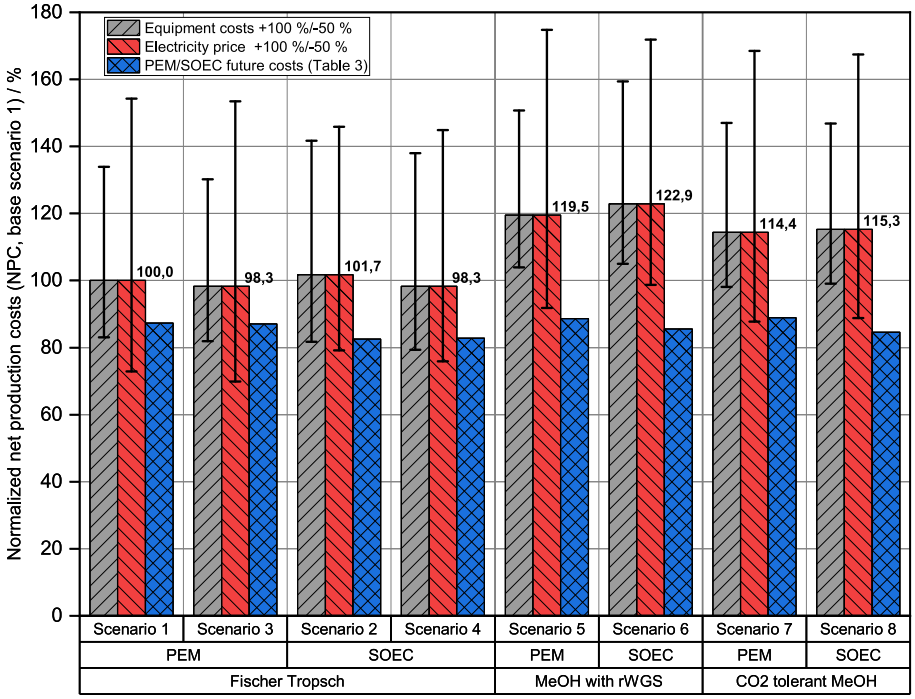

Fig. 9. Sensitivity study of the net production costs considering deviations from actual market prices related on equipment and utility costs (normalized to scenario 1).

indicates the importance of heat integration of the entire process chain, as the scenarios 1–4 which include a highly exothermic Fischer–Tropsch synthesis yield to overall higher global efficiencies. Lower steam production in the scenarios 5–8 with methanol synthesis require additional steam generation, which significantly decreases the global efficiency (33.2–38.2 % for FTS compared to 26.1–29.2 % for MeOH synthesis).

A high temperature electrolysis is only advantageous if excess steam is available on site. The lower SEC of the SOEC with 3.6 kWh/Nm^3_{H2} compared to PEM electrolysis leads to higher efficiencies (+5 % in scenarios 1–4, up to 3.1 % in scenarios 5–8) and lower electricity costs. Contrary to expectations, the rWGS reactor achieves due to its high temperature heat demand in combination with a PEM electrolysis a lower global efficiency compared to the CO_2 tolerant methanol synthesis (1.7 %). The yield of lower olefins is 5.7 % higher for the Fischer–-Tropsch and steam cracker route, compared to both methanol routes. Furthermore, if the synthesis location is separated from the downstream processing of the intermediates, the both mass and volume-related transportation quantity for methanol is approximately twice compared to syncrude. The outcome of the technological evaluation rates scenario 2 and 4 as preferred process routes. From an economic point of view and the consideration of various cost factors (electricity price, operating and maintenance, depreciation, …), the net production costs for scenario 3 and 4 (Fischer–Tropsch synthesis) are the lowest in the entire assessment. The NPC increases for the methanol routes up to 14.4–22.9 %. While the investment costs for the methanol route are quite similar to the Fischer–Tropsch route, a main distinction lies in the electricity demand. Despite a proper heat integration, there is a significant requirement of additional, electrically provided steam, due to the lower exothermicity of the methanol reaction. Furthermore, the amine scrubber unit has a major impact on the NPC_{Pr}, an important impact often omitted in other literature. The Fischer–Tropsch process route with PEM electrolysis and existing steam cracker (scenario 3) is evaluated as the best power-to-lower olefin route with specific NPC_{Pr} of 14.92 EUR/$kg_{C_2-C_4}$, directly followed by the same synthesis with SOEC (scenario 4) and NPC_{Pr} of 15.03 EUR/$kg_{C_2-C_4}$. Furthermore, the integration of a new steam cracker (scenarios 1 and 2) has also high potential (15.26–15.47 EUR/$kg_{C_2-C_4}$), compared to the methanol synthesis with MtP unit (scenarios 5 to 8, 17.23–18.50 EUR/$kg_{C_2-C_4}$).

As a conclusion, the assessment of the different polyolefin production routes shows the best efficiencies and cost calculation for the FTS with PEM electrolysis for this scale of plant. As shown in the sensitivity analysis, higher electricity prices will shift the choice of electrolysis technology to SOEC, as the NPC_{Pr} are getting lower. However, the lower equipment costs and longer stack lifetime currently favor the PEM electrolysis, but future development of electrolysis stacks resulting in longer lifetime and lower stack replacement costs may favor the SOEC technology. Summarizing all advantages and disadvantages, the FTS with PEM electrolysis and the implementation of an existing steam cracker (scenario 3) is selected as the best scenario due to lower net production costs in this context.

CRediT authorship contribution statement

Christoph Markowitsch: Conceptualization, Project administration, Methodology, Software, Investigation, Validation, Writing – original draft, Writing – review & editing. **Markus Lehner:** Conceptualization, Methodology, Supervision, Validation, Writing – review & editing. **Markus Maly:** Conceptualization, Validation, Supervision, Writing – review & editing.

Declaration of Competing Interest

The authors declare that they have no known competing financial interests or personal relationships that could have appeared to influence the work reported in this paper.

Data availability

Data will be made available on request.

Acknowledgments

This research was developed as a part of the "C2PAT – Carbon to product Austria" project. The financial support by Holcim Technology Ltd., Verbund Energy4Business GmbH, OMV AG and Borealis Polyolefine GmbH is gratefully acknowledged.

Supplementary materials

Supplementary material associated with this article can be found, in the online version, at doi:10.1016/j.ijggc.2023.103985.

References

AACE International Recommended Practices, 2020. Cost Estimate Classification System: AACE International Recommended Practice No. 18R-97.

Adams II, T.A., Thatho, T., Le Feuvre, M.C., Swartz, C.L.E., 2018. The optimal design of a distillation system for the flexible polygeneration of dimethyl ether and methanol under uncertainty. Front. Energy Res. 6, 41. https://doi.org/10.3389/fenrg.2018.00041.

Adelung, S., Dietrich, R.-U., 2022. Impact of the reverse water-gas shift operating conditions on the Power-to-Liquid fuel production cost. Fuel 317, 123440. https://doi.org/10.1016/j.fuel.2022.123440.

Adelung, S., Maier, S., Dietrich, R.-U., 2021. Impact of the reverse water-gas shift operating conditions on the Power-to-Liquid process efficiency. Sustain. Energy Technolog. Assessm. 43, 100897 https://doi.org/10.1016/j.seta.2020.100897.

Albrecht, F.G., König, D.H., Baucks, N., Dietrich, R.-U., 2017. A standardized methodology for the techno-economic evaluation of alternative fuels – a case study. Fuel 194, 511–526. https://doi.org/10.1016/j.fuel.2016.12.003.

Allen, J., Panquet, S., Bastiani, A., 2021. Electrochemical ammonia: power to ammonia ratio and balance of plant requirements for two different electrolysis approaches. Front. Chem. Eng. 3, 67. https://doi.org/10.3389/fceng.2021.765457.

Anicic, B., Trop, P., Goricanec, D., 2014. Comparison between two methods of methanol production from carbon dioxide. Energy 77, 279–289. https://doi.org/10.1016/j.energy.2014.09.069.

Bisotti, F., Fedeli, M., Prifti, K., Galeazzi, A., Dell`Angelo, A., Manenti, F., 2022. Impact of kinetic models on methanol synthesis reactor predictions: in silico assessment and comparison with industrial data. Ind. Eng. Chem. Res. 61 (5), 2206–2226. https://doi.org/10.1021/acs.iecr.1c04476.

Boudier, M., 2021. Synkero builds facility in the port of Amsterdam, producing sustainable aviation fuel from CO_2. Synkero, 8 February 2021; Available from. https://synkero.com/synkero-builds-facility-in-the-port-of-amsterdam-producing-sustainable-aviation-fuel-from-co2/ [October 28, 2022].

Brübach, L., Hodonj, D., Biffar, L., Pfeifer, P., 2022. Detailed kinetic modeling of CO_2-based Fischer–Tropsch synthesis. Catalysts 12 (6), 630. https://doi.org/10.3390/catal12060630.

Bundesministerium für Digitalisierung und Wirtschaftsstandort, 2022. Die österreichische Klimaschutzstrategie/Politik. (January 18, 2022) Available from: https://www.oesterreich.gv.at/themen/bauen_wohnen_und_umwelt/klimaschutz/1/Seite.1000310.html.

Bussche, K., Froment, G.F., 1996. A steady-state kinetic model for methanol synthesis and the water gas shift reaction on a commercial Cu/ZnO/Al_2O_3 Catalyst. J. Catal. 161 (1), 1–10. https://doi.org/10.1006/jcat.1996.0156.

E-Control Austria für die Regulierung der Elektrizitäts- und Erdgaswirtschaft, 2022. *Aktueller Marktpreis gemäß § 41 Ökostromgesetz*. (October 13, 2022). Available from: https://www.e-control.at/industrie/oeko-energie/oekostrommarkt/marktpreise-gem-paragraph-20.

Trading Economics, 2022. EU- Carbon Permits (EUR). (January 15, 2022). Available from: https://tradingeconomics.com/commodity/carbon%20(13.01.2022).

Europäisches Parlament, 2022. Plastikmüll und Recycling in der EU: Zahlen und Fakten. (January 18, 2022). Available from: https://www.europarl.europa.eu/news/de/headlines/society/20181212STO21610/plastikmull-und-recycling-in-der-eu-zahlen-und-fakten.

Finanzen.net, 2022. Euro Dollar Wechselkurs (EUR/USD). [December 07, 2022]; Available from: https://www.finanzen.net/devisen/dollarkurs.

Ghosh, S., Uday, V., Giri, A., Srinivas, S., 2019. Biogas to methanol: a comparison of conversion processes involving direct carbon dioxide hydrogenation and via reverse water gas shift reaction. J. Clean. Prod. 217, 615–626. https://doi.org/10.1016/j.jclepro.2019.01.171.

GLOBAL 2000, 2022. Plastikatlas 2019: Daten und Fakten über eine Welt voller Kunststoffe. (January 18, 2022). Available from: https://www.global2000.at/sites/global/files/2019-Plastikatlas-Oesterreich.pdf.

Henley, M., Letinski, D.J., Carr, J., Caro, M.L., Daughtrey, W., White, R., 2014. Health assessment of gasoline and fuel oxygenate vapors: generation and characterization of test materials. Regul. Toxicol. Pharmacol. 70 (2 Suppl), S13–S17. https://doi.org/10.1016/j.yrtph.2014.05.012.

Herz, G., Reichelt, E., Jahn, M., 2018. Techno-economic analysis of a co-electrolysis-based synthesis process for the production of hydrocarbons. Appl. Energy 215, 309–320. https://doi.org/10.1016/j.apenergy.2018.02.007.

Herz, G., Rix, C., Jacobasch, E., Müller, N., Reichelt, E., Jahn, M., et al., 2021. Economic assessment of Power-to-Liquid processes – influence of electrolysis technology and operating conditions. Appl. Energy 292, 116655. https://doi.org/10.1016/j.apenergy.2021.116655.

Hof am Leithaberge, 2022. Wasserbezugsgebühr 2022. (January 15, 2022). Available from: http://www.hof-leithaberge.gv.at/Wasserbezugsgebuehr.

IEA, 2017. Simplified levelised cost of petrochemicals for selected feedstocks and regions. (October 31, 2022). Available from: www.iea.org.

IEA, 2021. Technology Roadmap Hydrogen and Fuel Cells. (December 22, 2021). Available from: https://www.iea.org/reports/technology-roadmap-hydrogen-and-fuel-cells.

International Methanol Producers & Consumers Association, 2015. IMPCA Methanol Reference Specifications. (March 25, 2022). Available from: https://www.methanol.org/wp-content/uploads/2016/07/IMPCA-Ref-Spec-08-December-2015.pdf.

Karaba, A., Rozhon, J., Patera, J., Hájek, J., Zámostný, P., 2021. Fischer–Tropsch wax from renewable resources as an excellent feedstock for the steam-cracking process. Chem. Eng. Technol. 44 (2), 329–338. https://doi.org/10.1002/ceat.202000400.

Kearns, D., Liu, H., Consoli, C., 2021. Technology Readiness and Costs for CCS. ACAMH.

Klerk, A de, 2011. Fischer–Tropsch Refining, 1st ed. Wiley, Hoboken, NJ, Weinheim.

König, D.H., Baucks, N., Dietrich, R.-U., Wörner, A., 2015. Simulation and evaluation of a process concept for the generation of synthetic fuel from CO_2 and H_2. Energy 91, 833–841. https://doi.org/10.1016/j.energy.2015.08.099.

König, D.H., 2016. Techno-ökonomische Prozessbewertung der Herstellung synthetischen Flugturbinentreibstoffes aus CO_2 und H_2. Universitätsbibliothek der Universität Stuttgart, Stuttgart [Dissertation].

Madeddu, C., Errico, M., Baratti, R., 2019. CO2 Capture by Reactive Absorption-Stripping: Modeling, Analysis and Design. Springer International Publishing, Cham.

Markowitsch, C., Lehner, M., 2023. Impact of the operation conditions on the reverse-water-gas shift reaction. In: Benítez-Andrades, J.A., García-Llamas, P., Taboada, Á, Estévez-Mauriz, L., Baelo, R. (Eds.), Global Challenges for a Sustainable Society: EURECA-PRO The European University for Responsible Consumption and Production, 1st ed. Springer International Publishing; Imprint Springer, Cham, pp. 66–76.

Markowitsch C., Lehner M., Kitzweger J., Haider W., Ivanovici S., Unfried M., Maly M., 2022. Conference EnInnov 2022 TU Graz. C2PAT - Carbon to Product Austria. [February 18, 2022]; Available from: https://www.tugraz.at/fileadmin/user_upload/tugrazExternal/738639ca-39a0-4129-b0f0-38b384c12b57/files/lf/Session_D6/464_LF_Markowitsch.pdf.

Markowitsch, C., Lehner, M., Maly, M., 2023. Evaluation of process structures and reactor technologies of an integrated power-to-liquid plant at a cement factory. J. CO2 Utilizat. 70, 102449 https://doi.org/10.1016/j.jcou.2023.102449.

Mauschitz, G., 2021. Emissionen Aus Anlagen der österreichischen Zementindustrie - Berichtsjahr 2020. Wien.

McAllister, S., 2011. Fundamentals of Combustion Processes. Springer New York, New York, NY.

Oelmann T., Schuhmann T., Drosdzol C., Haag S., Castillo-Welter F. A New Reactor Concept for Conversion of CO2 to Methanol (AirLiquide) 2020.

Parlament Österreich, 2022. Ökosoziales Steuerreformgesetz 2022 Teil 1. (January 15, 2022). Available from: https://www.parlament.gv.at/PAKT/VHG/XXVII/ME/ME_00158/#.

Peters, M.S., Timmerhaus, K.D., West, R.E., 2004. Plant Design and Economics For Chemical Engineers, 5th ed. McGraw-Hill, Boston.

Pratschner, S., Hammerschmid, M., Müller, S., Winter, F., 2023. Evaluation of CO_2 sources for Power-to-Liquid plants producing Fischer–Tropsch products. J. CO2 Utilizat. 72, 102508 https://doi.org/10.1016/j.jcou.2023.102508.

Rochelle, G.T., 2012. Thermal degradation of amines for CO_2 capture. Curr. Opin. Chem. Eng. 1 (2), 183–190. https://doi.org/10.1016/j.coche.2012.02.004.

Rothaemel M., Gorny M., Haag S. Methanol-to-Propylene (MTP®), 2016. A proven technology for on-purpose propylene production.

SAF+ Consortium, 2022. Providing a sustainable solution for low-carbon flying. (October 28, 2022). Available from: https://safplusconsortium.com/.

Sakwattanapong, R., Aroonwilas, A., Veawab, A., 2005. Behavior of reboiler heat duty for CO_2 capture plants using regenerable single and blended alkanolamines. Ind. Eng. Chem. Res. 44 (12), 4465–4473. https://doi.org/10.1021/ie050063w.

Schemme, S., Breuer, J.L., Köller, M., Meschede, S., Walman, F., Samsun, R.C., et al., 2020. H2-based synthetic fuels: a techno-economic comparison of alcohol, ether and hydrocarbon production. Int. J. Hydrogen Energy 45 (8), 5395–5414. https://doi.org/10.1016/j.ijhydene.2019.05.028.

Spaun, S., Bauer, C., Dankl, C., Friedle, R., Papsch, F., 2022. Roadmap Zur CO_2-Neutralität Der österreichischen Zementindustrie Bis 2050. Wien.

Sunfire GmbH, 2022. Sunfire Factsheet HyLink SOEC. (February 05, 2022). Available from: https://www.sunfire.de/files/sunfire/images/content/Sunfire.de%20(neu)/Sunfire-Factsheet-HyLink-SOEC-20210303.pdf.

Tiktak, W.J., 2019. Heat Management of PEM Electrolysis. Delft University of Technology, Amsterdam, Netherlands [Master thesis].

Towering Skills LLC, 2022. Cost Indices – Towering Skills. (May 05, 2022). Available from: https://www.toweringskills.com/financial-analysis/cost-indices/#cepci-2001-to-present.

Trattner, A., Höglinger, M., Macherhammer, M.-G., Sartory, M., 2021. Renewable hydrogen: modular concepts from production over storage to the consumer. Chemie Ingenieur Technik 93 (4), 706–716. https://doi.org/10.1002/cite.202000197.

Unde, R.B., 2012. Kinetics and Reaction Engineering Aspects of Syngas Production By the Heterogeneously Catalysed Reverse Water Gas Shift Reaction. Universität Bayreuth, Bayreuth [Dissertation].

Vervloet, D., Kapteijn, F., Nijenhuis, J., van Ommen, J.R., 2012. Fischer–Tropsch reaction–diffusion in a cobalt catalyst particle: aspects of activity and selectivity for a

variable chain growth probability. Catal. Sci. Technol. 2 (6), 1221. https://doi.org/10.1039/C2CY20060K.
Wismann, S.T., Engbæk, J.S., Vendelbo, S.B., Bendixen, F.B., Eriksen, W.L., Aasberg-Petersen, K., et al., 2019. Electrified methane reforming: a compact approach to greener industrial hydrogen production. Science 364 (6442), 756–759. https://doi.org/10.1126/science.aaw8775.
Zhou, S., Wang, S., Sun, C., Chen, C., 2013. SO2 effect on degradation of MEA and some other amines. Energy Procedia 37, 896–904. https://doi.org/10.1016/j.egypro.2013.05.184.

Comparison and techno-economic evaluation of process routes for lower olefin production via Fischer-Tropsch and methanol synthesis

Christoph Markowitsch, Markus Lehner, Markus Maly

Supplementary Material

This supplementary material includes detailed ASPEN flow sheets inclusive their stream description. The results of the detailed efficiency calculation and sensitivity study of the net production costs are listed in Tables A.8 and A.9. Since 10,000 tons/year of CO_2 are captured in all scenarios, one carbon capture flow sheet inclusive mass balance for the carbon capture plant can be created for all scenarios.

1. Simulation of the carbon capture unit

The carbon capture unit is designed to separate CO_2 from the cement-plant exhaust gas with a capacity of 10,000 tons per year and an annual plant operation time of 7,880 hours. The simulation is carried out with ASPEN Plus 12.1 ®. In Figure A.1 the ASPEN flowsheet is depicted with associated mass balance in Table A.1.

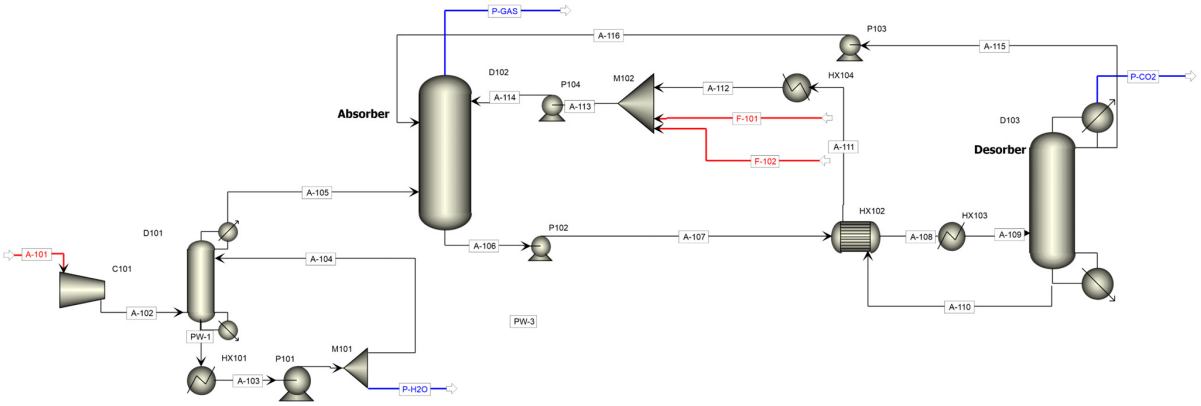

Figure A.1: Flow sheet of the amine scrubber unit to capture 10,000 tons CO_2 per year

Table A.1: Mass balance of the amine scrubber unit

	Units	A-101	A-102	A-103	A-104	A-105	A-106	A-107	A-108	A-109	A-110	A-111	A-112	A-113	A-114	A-115	A-116	F-101	F-102	P-CO2	P-GAS	P-H2O
Temperature	C	110	169	20	20	40	46	45	94	85	104	100	40	39	39	40	40	20	20	40	65	20
Pressure	barg	0	1	0,1	1	0	0	0	0	0	0	0	0	0	0	0	0	0	0	0	0	1
Molar Vapor Fraction		1,00	1,00	0,00	0,00	1,00	0,00	0,00	0,42	0,24	0,98	0,65	0,06	0,00	0,00	0,00	0,00	0,00	0,00	1,00	1,00	0,00
Enthalpy Flow	kW	-5167	-5049	-39895	-38825	-4404	-74026	-58719	-55502	-57405	-52877	-56094	-63058	-72779	-72779	-842	-842	-3463	0	-3279	-3999	-1070
Mass Flows	kg/h	6686	6686	9041	8798	6443	22098	22098	22098	22098	20604	20604	20604	21389	21389	192	192	785	0,03	1302	5926	243
CO	kg/h	0	0	0	0	0	0	0	0	0	0	0	0	0	0	0	0	0	0	0	0	0
H2	kg/h	0	0	0	0	0	0	0	0	0	0	0	0	0	0	0	0	0	0	0	0	0
H2O	kg/h	504	504	9040	8797	263	13417	13354	13354	13354	13254	13254	13254	14045	14045	192	191	785	0	42	1006	243
CO2	kg/h	1391	1391	1	1	1390	2	1	1	1	134	134	134	0	0	0	0	0	0	1259	130	0
N2	kg/h	4049	4049	0	0	4049	1	1	1	1	0	0	0	0	0	0	0	0	0	1	4048	0
O2	kg/h	742	742	0	0	742	0	0	0	0	0	0	0	0	0	0	0	0	0	0	742	0
C	kg/h	0	0	0	0	0	0	0	0	0	0	0	0	0	0	0	0	0	0	0	0	0
H2S	kg/h	0	0	0	0	0	0	0	0	0	0	0	0	0	0	0	0	0	0	0	0	0
MEA	kg/h	0	0	0	0	0	226	386	386	386	3872	3872	3872	3457	3457	0	0	0	0,03	0	0	0
MEA+	kg/h	0	0	0	0	0	3257	3309	3309	3309	1271	1271	1271	1481	1481	0	0	0	0	0	0	0
MEACOO-	kg/h	0	0	0	0	0	4891	4530	4530	4530	2007	2007	2007	2361	2361	0	0	0	0	0	0	0
HCO3-	kg/h	0	0	0	0	0	276	440	440	440	60	60	60	18	18	0	0	0	0	0	0	0
CO3-2	kg/h	0	0	0	0	0	28	77	77	77	6	6	6	26	26	0	0	0	0	0	0	0

2. Simulation of the Fischer-Tropsch unit

The Fischer Tropsch process routes includes scenarios 1 to 4 with a rWGS reactor and the Fischer Tropsch synthesis incl. product separation into the fractions naphtha, middle distallte, waxes and unconverted gases. The main distinction is the electrolysis technology, whereas scenarios 1 and 3 (Figure A.2) uses a PEM electrolysis, scenarios 2 and 4 (Figure A.3) have implemented a SOEC. The mass balance for scenario 1/3 and 2/4 is given in Table A.2 and Table A.3, respectively.
The feed water for the PEM electorlysis is compressed, preheated and converted in a stoichiometric reactor (0.5 H_2O → H_2 + 0.5 O_2) to hydrogen and oxygen. In case of a SOEC, the reactor cooling system of the Fischer-Tropsch unit is also used for feed water heating. Furthermore, an additional compressor for hydrogen compression is implemented in scenarios 2&4.
CO_2 and H_2 is mixed and fed to the rWGS reactor. The rWGS reactor is modeled as GIBBS reactor, reaching thermodynamic equilibrium at 950 °C and 10 barg. The waste heat is used to preheat the feedgas mixture. The Fischer Tropsch reactor is modeled as stoichiometric reactor, whereas the product composition follows the Anderson-Schulz-Flory distribution with a chain growth probabiltiy of 0.92 and a single CO conversion of 40 %. Heat integration is performed with ASPEN Energy Analyzer.

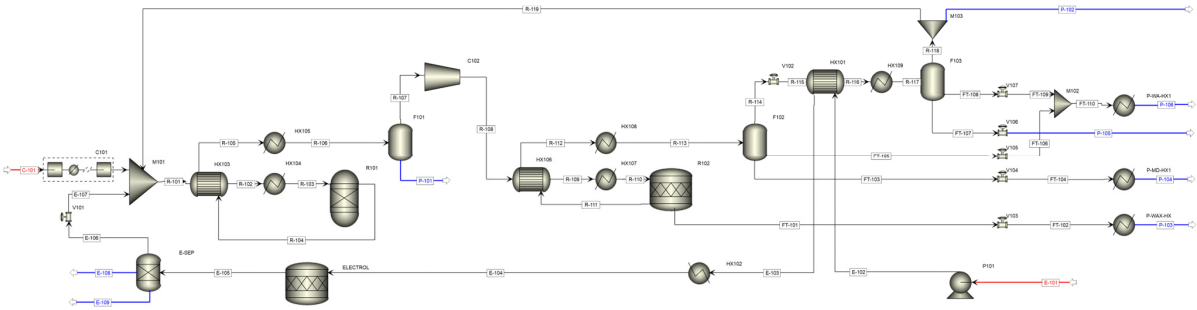

Figure A.2: Flow sheet of scenario 1 and 3 (includes PEM electrolysis, rWGS reactor, Fischer Tropsch synthesis)

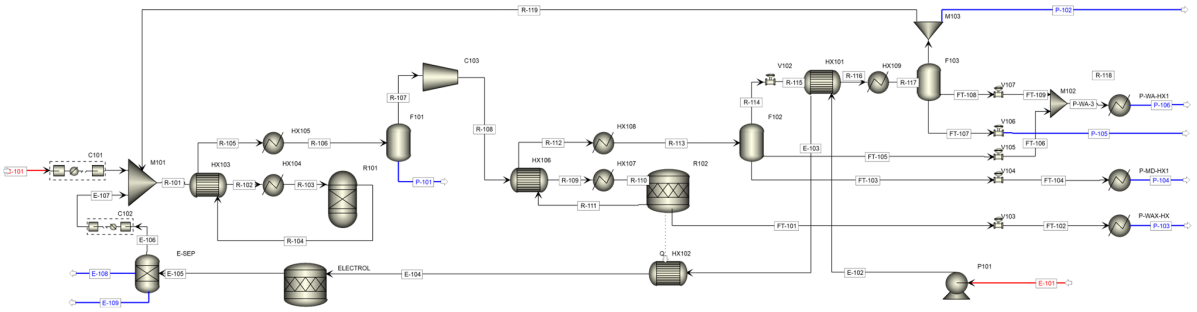

Figure A.3: Flow sheet of scenario 2 and 4 (includes SOEC electrolysis, rWGS reactor, Fischer Tropsch synthesis)

Table A.2: Mass balance of Scenario 1 and 3 (PEM-rWGS-FTS)

	Units	C-101	C-102	E-101	E-102	E-103	E-104	E-105	E-106	E-107	E-108	E-109	R-101	R-102	R-103	R-104	R-105	R-106	R-107	R-108	R-109	R-110	R-111	R-112	R-113
Temperature	C	43	379	10	12	89	75	75	75	76	75	75	84	930	950	950	98	30	30	159	210	240	220	162	150
Pressure	barg	0	10	1,5	32	32	32	32	32	10	32	32	10	10	10	10	10	10	9	25	25	25	25	25	25
Molar Vapor Fraction		1,00	1,00	0,00	0,00	0,00	0,00		1,00	1,00	1,00	0,00	1,00	1,00	1,00	1,00	1,00	0,94	1,00	1,00	1,00	1,00	1,00	1,00	1,00
Enthalpy Flow	kW	-3279	-3153	-7767	-7762	-7592	-7623		36	36	15	-762	-5924	-3436	-3372	-2570	-5058	-5498	-3871	-3545	-3415	-3338	-5051	-5181	-5204
Mass Flows	kg/h	1302,2	1302,2	1743,2	1743,2	1743,2	1743,2	1743,2	175,6	175,6	1393,3	174,3	3870,4	3870,4	3870,4	3870,4	3870,4	3870,4	3503,4	3503,4	3503,4	3503,4	3272,7	3272,7	3272,7
CO	kg/h	0	0	0	0	0	0	0	0	0	0	0	1521	1521	1521	2588	2588	2588	2588	2588	2588	2588	1552	1552	1552
H2	kg/h	0	0	0	0	0	0	176	176	176	0	0	393	393	393	387	387	387	387	387	387	387	222	222	222
H2O	kg/h	42	42	1743	1743	1743	1743	174	0	0	0	174	47	47	47	387	387	387	20	20	20	20	685	685	685
CO2	kg/h	1259	1259	0	0	0	0	0	0	0	0	0	1566	1566	1566	313	313	313	313	313	313	313	313	313	313
N2	kg/h	1	1	0	0	0	0	0	0	0	0	0	46	46	46	46	46	46	46	46	46	46	46	46	46
O2	kg/h	0	0	0	0	0	0	1393	0	0	1393	0	0	0	0	0	0	0	0	0	0	0	0	0	0
CH4	kg/h	0	0	0	0	0	0	0	0	0	0	0	239	239	239	149	149	149	149	149	149	149	244	244	244
C2H6	kg/h	0	0	0	0	0	0	0	0	0	0	0	5	5	5	0	0	0	0	0	0	0	6	6	6
C3H8	kg/h	0	0	0	0	0	0	0	0	0	0	0	7	7	7	0	0	0	0	0	0	0	7	7	7
C4H10	kg/h	0	0	0	0	0	0	0	0	0	0	0	9	9	9	0	0	0	0	0	0	0	9	9	9
C5H12	kg/h	0	0	0	0	0	0	0	0	0	0	0	10	10	10	0	0	0	0	0	0	0	10	10	10
C6H14	kg/h	0	0	0	0	0	0	0	0	0	0	0	10	10	10	0	0	0	0	0	0	0	11	11	11
C7H16	kg/h	0	0	0	0	0	0	0	0	0	0	0	8	8	8	0	0	0	0	0	0	0	12	12	12
C8H18	kg/h	0	0	0	0	0	0	0	0	0	0	0	5	5	5	0	0	0	0	0	0	0	13	13	13
C9H20	kg/h	0	0	0	0	0	0	0	0	0	0	0	2	2	2	0	0	0	0	0	0	0	13	13	13
C10H22	kg/h	0	0	0	0	0	0	0	0	0	0	0	1	1	1	0	0	0	0	0	0	0	13	13	13
C11H24	kg/h	0	0	0	0	0	0	0	0	0	0	0	0	0	0	0	0	0	0	0	0	0	13	13	13
C12H26	kg/h	0	0	0	0	0	0	0	0	0	0	0	0	0	0	0	0	0	0	0	0	0	13	13	13
C13H28	kg/h	0	0	0	0	0	0	0	0	0	0	0	0	0	0	0	0	0	0	0	0	0	13	13	13
C14H30	kg/h	0	0	0	0	0	0	0	0	0	0	0	0	0	0	0	0	0	0	0	0	0	12	12	12
C15H32	kg/h	0	0	0	0	0	0	0	0	0	0	0	0	0	0	0	0	0	0	0	0	0	11	11	11
C16H34	kg/h	0	0	0	0	0	0	0	0	0	0	0	0	0	0	0	0	0	0	0	0	0	10	10	10
C17H36	kg/h	0	0	0	0	0	0	0	0	0	0	0	0	0	0	0	0	0	0	0	0	0	9	9	9
C18H38	kg/h	0	0	0	0	0	0	0	0	0	0	0	0	0	0	0	0	0	0	0	0	0	8	8	8
C19H40	kg/h	0	0	0	0	0	0	0	0	0	0	0	0	0	0	0	0	0	0	0	0	0	7	7	7
C20H42	kg/h	0	0	0	0	0	0	0	0	0	0	0	0	0	0	0	0	0	0	0	0	0	5	5	5
C21H44	kg/h	0	0	0	0	0	0	0	0	0	0	0	0	0	0	0	0	0	0	0	0	0	4	4	4
C22H46	kg/h	0	0	0	0	0	0	0	0	0	0	0	0	0	0	0	0	0	0	0	0	0	3	3	3
C23H48	kg/h	0	0	0	0	0	0	0	0	0	0	0	0	0	0	0	0	0	0	0	0	0	2	2	2
C24H50	kg/h	0	0	0	0	0	0	0	0	0	0	0	0	0	0	0	0	0	0	0	0	0	2	2	2
C25H52	kg/h	0	0	0	0	0	0	0	0	0	0	0	0	0	0	0	0	0	0	0	0	0	1	1	1
C26H54	kg/h	0	0	0	0	0	0	0	0	0	0	0	0	0	0	0	0	0	0	0	0	0	1	1	1
C27H56	kg/h	0	0	0	0	0	0	0	0	0	0	0	0	0	0	0	0	0	0	0	0	0	1	1	1
C29H60	kg/h	0	0	0	0	0	0	0	0	0	0	0	0	0	0	0	0	0	0	0	0	0	0	0	0
C30H62	kg/h	0	0	0	0	0	0	0	0	0	0	0	0	0	0	0	0	0	0	0	0	0	0	0	0
C30+	kg/h	0	0	0	0	0	0	0	0	0	0	0	0	0	0	0	0	0	0	0	0	0	0	0	0

	R-114	R-115	R-116	R-117	R-118	R-119	FT-101	FT-102	FT-103	FT-104	FT-105	FT-106	FT-107	FT-108	FT-109	FT-110	P-101	P-102	P-103	P-104	P-105	P-106
Temperature	100	99	46	20	20	20	220	220	100	101	100	100	20	20	20	85	30	20	40	40	20	60
Pressure	25	11	11	11	11	11	25	4	25	4	25	4	11	11	4	4	9	11	0	4	4	4
Molar Vapor Fra	1,00	1,00	0,97	0,96	1,00	1,00	0,00	0,07	0,00	0,04	0,00	0,00	0,00	0,00	0,00	0,00	0,00	1,00	0,05	0,03	0,01	0,00
Enthalpy Flow	-3244	-3244	-3414	-3475	-2859	-2802	-100	-100	-59	-59	-2365	-2365	-24	-595	-595	-2960	-1626	-57	-127	-64	-24	-2981
Mass Flows	2616,0	2616,0	2616,0	2616,0	2441,5	2392,7	230,9	230,9	112,0	112,0	544,7	544,7	40,5	134,0	134,0	678,7	367,0	48,8	230,9	112,0	40,5	678,7
CO	1552	1552	1552	1552	1552	1521	0	0	0	0	0	0	0	0	0	0	0	31	0	0	0	0
H2	222	222	222	222	222	217	0	0	0	0	0	0	0	0	0	0	0	4	0	0	0	0
H2O	140	140	140	140	6	6	1	1	1	1	545	545	0	134	134	679	367	0	1	1	0	679
CO2	313	313	313	313	313	307	0	0	0	0	0	0	0	0	0	0	0	6	0	0	0	0
N2	46	46	46	46	46	45	0	0	0	0	0	0	0	0	0	0	0	1	0	0	0	0
O2	0	0	0	0	0	0	0	0	0	0	0	0	0	0	0	0	0	0	0	0	0	0
CH4	244	244	244	244	244	239	0	0	0	0	0	0	0	0	0	0	0	5	0	0	0	0
C2H6	6	6	6	6	6	5	0	0	0	0	0	0	0	0	0	0	0	0	0	0	0	0
C3H8	7	7	7	7	7	7	0	0	0	0	0	0	0	0	0	0	0	0	0	0	0	0
C4H10	9	9	9	9	9	9	0	0	0	0	0	0	0	0	0	0	0	0	0	0	0	0
C5H12	10	10	10	10	10	10	0	0	0	0	0	0	0	0	0	0	0	0	0	0	0	0
C6H14	11	11	11	11	10	10	0	0	0	0	0	0	1	0	0	0	0	0	0	0	1	0
C7H16	11	11	11	11	9	8	0	0	1	1	0	0	3	0	0	0	0	0	0	1	3	0
C8H18	11	11	11	11	5	5	0	0	1	1	0	0	6	0	0	0	0	0	0	1	6	0
C9H20	10	10	10	10	2	2	0	0	3	3	0	0	8	0	0	0	0	0	0	3	8	0
C10H22	9	9	9	9	1	1	0	0	5	5	0	0	8	0	0	0	0	0	0	5	8	0
C11H24	6	6	6	6	0	0	0	0	7	7	0	0	6	0	0	0	0	0	0	7	6	0
C12H26	4	4	4	4	0	0	1	1	9	9	0	0	4	0	0	0	0	0	1	9	4	0
C13H28	2	2	2	2	0	0	1	1	10	10	0	0	2	0	0	0	0	0	1	10	2	0
C14H30	1	1	1	1	0	0	1	1	11	11	0	0	1	0	0	0	0	0	1	11	1	0
C15H32	1	1	1	1	0	0	2	2	11	11	0	0	1	0	0	0	0	0	2	11	1	0
C16H34	0	0	0	0	0	0	3	3	10	10	0	0	0	0	0	0	0	0	3	10	0	0
C17H36	0	0	0	0	0	0	4	4	9	9	0	0	0	0	0	0	0	0	4	9	0	0
C18H38	0	0	0	0	0	0	4	4	8	8	0	0	0	0	0	0	0	0	4	8	0	0
C19H40	0	0	0	0	0	0	5	5	7	7	0	0	0	0	0	0	0	0	5	7	0	0
C20H42	0	0	0	0	0	0	6	6	5	5	0	0	0	0	0	0	0	0	6	5	0	0
C21H44	0	0	0	0	0	0	7	7	4	4	0	0	0	0	0	0	0	0	7	4	0	0
C22H46	0	0	0	0	0	0	8	8	3	3	0	0	0	0	0	0	0	0	8	3	0	0
C23H48	0	0	0	0	0	0	8	8	2	2	0	0	0	0	0	0	0	0	8	2	0	0
C24H50	0	0	0	0	0	0	8	8	2	2	0	0	0	0	0	0	0	0	8	2	0	0
C25H52	0	0	0	0	0	0	8	8	1	1	0	0	0	0	0	0	0	0	8	1	0	0
C26H54	0	0	0	0	0	0	8	8	1	1	0	0	0	0	0	0	0	0	8	1	0	0
C27H56	0	0	0	0	0	0	8	8	1	1	0	0	0	0	0	0	0	0	8	1	0	0
C29H60	0	0	0	0	0	0	8	8	0	0	0	0	0	0	0	0	0	0	8	0	0	0
C30H62	0	0	0	0	0	0	7	7	0	0	0	0	0	0	0	0	0	0	7	0	0	0
C30+	0	0	0	0	0	0	122	122	0	0	0	0	0	0	0	0	0	0	122	0	0	0

Table A.3: Mass balance of Scenario 2 and 4 (SOEC-rWGS-FTS)

	Units	C-101	C-102	E-101	E-102	E-103	E-104	E-105	E-106	E-107	E-108	E-109	R-101	R-102	R-103	R-104	R-105	R-106	R-107	R-108	R-109	R-110	R-111	R-112	R-113
Temperature	C	43	379	10	12	89	160	75	75	242	75	75	84	930	950	950	98	30	30	159	210	240	220	162	150
Pressure	barg	0	10	1,5	5	5	5	1	1	10	1	1	10	10	10	10	10	10	9	25	25	25	25	25	25
Molar Vapor Fraction		1,00	1,00	0,00	0,00	0,00	1,00		1,00	1,00	1,00	0,00	1,00	1,00	1,00	1,00	1,00	0,94	1,00	1,00	1,00	1,00	1,00	1,00	1,00
Enthalpy Flow	kW	-3279	-3153	-7767	-7762	-7592	-6365		35	153	18	-760	-5924	-3436	-3372	-2570	-5058	-5498	-3871	-3545	-3415	-3338	-5051	-5181	-5204
Mass Flows	kg/h	1302,2	1302,2	1743,2	1743,2	1743,2	1743,2	1743,2	175,6	175,6	1393,3	173,8	3870,4	3870,4	3870,4	3870,4	3870,4	3870,4	3503,4	3503,4	3503,4	3503,4	3272,7	3272,7	3272,7
CO	kg/h	0	0	0	0	0	0	0	0	0	0	0	1521	1521	1521	2588	2588	2588	2588	2588	2588	2588	1552	1552	1552
H2	kg/h	0	0	0	0	0	0	176	176	176	0	0	393	393	393	387	387	387	387	387	387	387	222	222	222
H2O	kg/h	42	42	1743	1743	1743	1743	174	0	0	0	174	47	47	47	387	387	387	20	20	20	20	685	685	685
CO2	kg/h	1259	1259	0	0	0	0	0	0	0	0	0	1566	1566	1566	313	313	313	313	313	313	313	313	313	313
N2	kg/h	1	1	0	0	0	0	0	0	0	0	0	46	46	46	46	46	46	46	46	46	46	46	46	46
O2	kg/h	0	0	0	0	0	0	1393	0	0	1393	0	0	0	0	0	0	0	0	0	0	0	0	0	0
CH4	kg/h	0	0	0	0	0	0	0	0	0	0	0	239	239	239	149	149	149	149	149	149	149	244	244	244
C2H6	kg/h	0	0	0	0	0	0	0	0	0	0	0	5	5	5	0	0	0	0	0	0	0	6	6	6
C3H8	kg/h	0	0	0	0	0	0	0	0	0	0	0	7	7	7	0	0	0	0	0	0	0	7	7	7
C4H10	kg/h	0	0	0	0	0	0	0	0	0	0	0	9	9	9	0	0	0	0	0	0	0	9	9	9
C5H12	kg/h	0	0	0	0	0	0	0	0	0	0	0	10	10	10	0	0	0	0	0	0	0	10	10	10
C6H14	kg/h	0	0	0	0	0	0	0	0	0	0	0	10	10	10	0	0	0	0	0	0	0	11	11	11
C7H16	kg/h	0	0	0	0	0	0	0	0	0	0	0	8	8	8	0	0	0	0	0	0	0	12	12	12
C8H18	kg/h	0	0	0	0	0	0	0	0	0	0	0	5	5	5	0	0	0	0	0	0	0	13	13	13
C9H20	kg/h	0	0	0	0	0	0	0	0	0	0	0	2	2	2	0	0	0	0	0	0	0	13	13	13
C10H22	kg/h	0	0	0	0	0	0	0	0	0	0	0	1	1	1	0	0	0	0	0	0	0	13	13	13
C11H24	kg/h	0	0	0	0	0	0	0	0	0	0	0	0	0	0	0	0	0	0	0	0	0	13	13	13
C12H26	kg/h	0	0	0	0	0	0	0	0	0	0	0	0	0	0	0	0	0	0	0	0	0	13	13	13
C13H28	kg/h	0	0	0	0	0	0	0	0	0	0	0	0	0	0	0	0	0	0	0	0	0	13	13	13
C14H30	kg/h	0	0	0	0	0	0	0	0	0	0	0	0	0	0	0	0	0	0	0	0	0	12	12	12
C15H32	kg/h	0	0	0	0	0	0	0	0	0	0	0	0	0	0	0	0	0	0	0	0	0	11	11	11
C16H34	kg/h	0	0	0	0	0	0	0	0	0	0	0	0	0	0	0	0	0	0	0	0	0	10	10	10
C17H36	kg/h	0	0	0	0	0	0	0	0	0	0	0	0	0	0	0	0	0	0	0	0	0	9	9	9
C18H38	kg/h	0	0	0	0	0	0	0	0	0	0	0	0	0	0	0	0	0	0	0	0	0	8	8	8
C19H40	kg/h	0	0	0	0	0	0	0	0	0	0	0	0	0	0	0	0	0	0	0	0	0	7	7	7
C20H42	kg/h	0	0	0	0	0	0	0	0	0	0	0	0	0	0	0	0	0	0	0	0	0	5	5	5
C21H44	kg/h	0	0	0	0	0	0	0	0	0	0	0	0	0	0	0	0	0	0	0	0	0	4	4	4
C22H46	kg/h	0	0	0	0	0	0	0	0	0	0	0	0	0	0	0	0	0	0	0	0	0	3	3	3
C23H48	kg/h	0	0	0	0	0	0	0	0	0	0	0	0	0	0	0	0	0	0	0	0	0	2	2	2
C24H50	kg/h	0	0	0	0	0	0	0	0	0	0	0	0	0	0	0	0	0	0	0	0	0	2	2	2
C25H52	kg/h	0	0	0	0	0	0	0	0	0	0	0	0	0	0	0	0	0	0	0	0	0	1	1	1
C26H54	kg/h	0	0	0	0	0	0	0	0	0	0	0	0	0	0	0	0	0	0	0	0	0	1	1	1
C27H56	kg/h	0	0	0	0	0	0	0	0	0	0	0	0	0	0	0	0	0	0	0	0	0	1	1	1
C29H60	kg/h	0	0	0	0	0	0	0	0	0	0	0	0	0	0	0	0	0	0	0	0	0	0	0	0
C30H62	kg/h	0	0	0	0	0	0	0	0	0	0	0	0	0	0	0	0	0	0	0	0	0	0	0	0
C30+	kg/h	0	0	0	0	0	0	0	0	0	0	0	0	0	0	0	0	0	0	0	0	0	0	0	0

	R-114	R-115	R-116	R-117	R-118	R-119	FT-101	FT-102	FT-103	FT-104	FT-105	FT-106	FT-107	FT-108	FT-109	FT-110	P-101	P-102	P-103	P-104	P-105	P-106
Temperature	100	99	46	20	20	20	220	220	100	101	100	100	20	20	20	85	30	20	40	40	20	60
Pressure	25	11	11	11	11	11	25	4	25	4	25	4	11	11	4	4	9	11	0	4	4	4
Molar Vapor Fra	1,00	1,00	0,97	0,96	1,00	1,00	0,00	0,07	0,00	0,04	0,00	0,00	0,00	0,00	0,00	0,00	0,00	1,00	0,05	0,03	0,01	0,00
Enthalpy Flow	-3244	-3244	-3414	-3475	-2859	-2802	-100	-100	-59	-59	-2365	-2365	-24	-595	-595	-2960	-1626	-57	-127	-64	-24	-2981
Mass Flows	2616,0	2616,0	2616,0	2616,0	2441,5	2392,7	230,9	230,9	112,0	112,0	544,7	544,7	40,5	134,0	134,0	678,7	367,0	48,8	230,9	112,0	40,5	678,7
CO	1552	1552	1552	1552	1552	1521	0	0	0	0	0	0	0	0	0	0	0	31	0	0	0	0
H2	222	222	222	222	222	217	0	0	0	0	0	0	0	0	0	0	0	4	0	0	0	0
H2O	140	140	140	140	6	6	1	1	1	1	545	545	0	134	134	679	367	0	1	1	0	679
CO2	313	313	313	313	313	307	0	0	0	0	0	0	0	0	0	0	0	6	0	0	0	0
N2	46	46	46	46	46	45	0	0	0	0	0	0	0	0	0	0	0	1	0	0	0	0
O2	0	0	0	0	0	0	0	0	0	0	0	0	0	0	0	0	0	0	0	0	0	0
CH4	244	244	244	244	244	239	0	0	0	0	0	0	0	0	0	0	0	5	0	0	0	0
C2H6	6	6	6	6	6	5	0	0	0	0	0	0	0	0	0	0	0	0	0	0	0	0
C3H8	7	7	7	7	7	7	0	0	0	0	0	0	0	0	0	0	0	0	0	0	0	0
C4H10	9	9	9	9	9	9	0	0	0	0	0	0	0	0	0	0	0	0	0	0	0	0
C5H12	10	10	10	10	10	10	0	0	0	0	0	0	0	0	0	0	0	0	0	0	0	0
C6H14	11	11	11	11	10	10	0	0	0	0	0	0	1	0	0	0	0	0	0	0	1	0
C7H16	11	11	11	11	9	8	0	0	1	1	0	0	3	0	0	0	0	0	0	1	3	0
C8H18	11	11	11	11	5	5	0	0	1	1	0	0	6	0	0	0	0	0	0	1	6	0
C9H20	10	10	10	10	2	2	0	0	3	3	0	0	8	0	0	0	0	0	0	3	8	0
C10H22	9	9	9	9	1	1	0	0	5	5	0	0	8	0	0	0	0	0	0	5	8	0
C11H24	6	6	6	6	0	0	0	0	7	7	0	0	6	0	0	0	0	0	0	7	6	0
C12H26	4	4	4	4	0	0	1	1	9	9	0	0	4	0	0	0	0	0	1	9	4	0
C13H28	2	2	2	2	0	0	1	1	10	10	0	0	2	0	0	0	0	0	1	10	2	0
C14H30	1	1	1	1	0	0	1	1	11	11	0	0	1	0	0	0	0	0	1	11	1	0
C15H32	1	1	1	1	0	0	2	2	11	11	0	0	1	0	0	0	0	0	2	11	1	0
C16H34	0	0	0	0	0	0	3	3	10	10	0	0	0	0	0	0	0	0	3	10	0	0
C17H36	0	0	0	0	0	0	4	4	9	9	0	0	0	0	0	0	0	0	4	9	0	0
C18H38	0	0	0	0	0	0	4	4	8	8	0	0	0	0	0	0	0	0	4	8	0	0
C19H40	0	0	0	0	0	0	5	5	7	7	0	0	0	0	0	0	0	0	5	7	0	0
C20H42	0	0	0	0	0	0	6	6	5	5	0	0	0	0	0	0	0	0	6	5	0	0
C21H44	0	0	0	0	0	0	7	7	4	4	0	0	0	0	0	0	0	0	7	4	0	0
C22H46	0	0	0	0	0	0	8	8	3	3	0	0	0	0	0	0	0	0	8	3	0	0
C23H48	0	0	0	0	0	0	8	8	2	2	0	0	0	0	0	0	0	0	8	2	0	0
C24H50	0	0	0	0	0	0	8	8	2	2	0	0	0	0	0	0	0	0	8	2	0	0
C25H52	0	0	0	0	0	0	8	8	1	1	0	0	0	0	0	0	0	0	8	1	0	0
C26H54	0	0	0	0	0	0	8	8	1	1	0	0	0	0	0	0	0	0	8	1	0	0
C27H56	0	0	0	0	0	0	8	8	1	1	0	0	0	0	0	0	0	0	8	1	0	0
C29H60	0	0	0	0	0	0	8	8	0	0	0	0	0	0	0	0	0	0	8	0	0	0
C30H62	0	0	0	0	0	0	7	7	0	0	0	0	0	0	0	0	0	0	7	0	0	0
C30+	0	0	0	0	0	0	122	122	0	0	0	0	0	0	0	0	0	0	122	0	0	0

3. Simulation of the conventional methanol synthesis unit

Scenarios 5 and 6 include a conventional methanol synthesis, which converts syngas (a gas mixture mainly consisting of H_2 and CO) in a single step reactor setup to methanol. In case of CO_2 as feedgas, a pre-conversion in a rWGS reactor is mandatory to produce syngas. The distinction between scenario 5 and 6 is the production of hydrogen, using the PEM (scenario 5) and SOEC (scenario 6) techniques, which are described in section 2 (Fischer Tropsch simulation).
The methanol synthesis is implemented as a kinetic, plug flow reactor, operating at 240 °C and 80 barg. The pressure drop is calculated by ASPEN Plus, using the "Ergun" equation. The tubes are assumed to have a length of 7 m and a diameter of 0.04 m. The distillation unit consists of a high (10 barg) and atmospheric pressure unit to achieve high and pure methanol yields. Heat integration is performed with ASPEN Energy Analyzer.
Figure A.4/Table A.4 and Figure A.5/Table A.5 show the flowsheets and mass balances of scenarios 5 and 6, respectively.

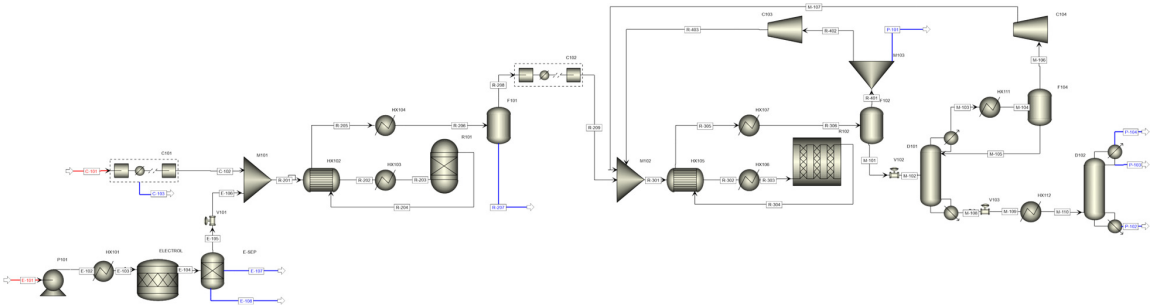

Figure A.4: Flow sheet of scenario 5 (includes PEM electrolysis, rWGS reactor, methanol synthesis)

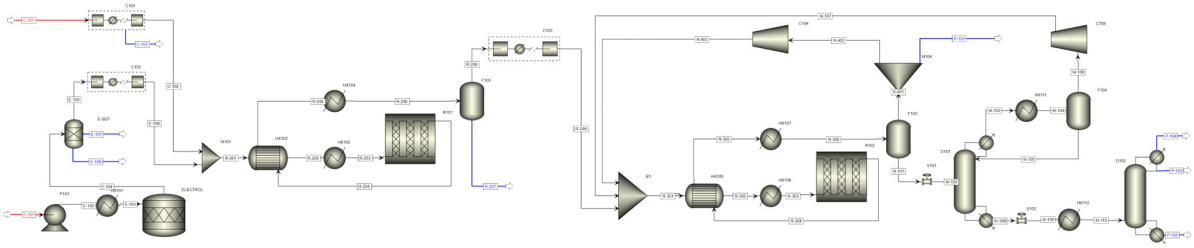

Figure A.5: Flow sheet of scenario 6 (includes SOEC electrolysis, rWGS reactor, methanol synthesis)

Table A.4: Mass balance of Scenario 5 (PEM-rWGS-methanol synthesis)

	Units	C-101	C-102	C-103	E-101	E-102	E-103	E-104	E-105	E-106	E-107	E-108	R-201	R-202	R-203	R-204	R-205	R-206	R-207	R-208	R-209	R-301	R-302	R-303
Temperature	C	43	151	30	10	10	160	75	75	146	75	75	146	900	950	950	155	30	30	30	30	34	170	240
Pressure	barg	0	10	2	2	5	5	1	1	10	1	1	10	10	10	10	10	10	9	9	80	80	80	80
Molar Vapor Fraction		1,00	1,00	0,00	0,00	0,00	1,00		1,00	1,00	1,00	0,00	1,00	1,00	1,00	1,00	1,00	0,80	0,00	1,00	1,00	1,00	1,00	1,00
Enthalpy Flow	kW	-3278	-3111	-159	-7718	-7717	-6345		35	85	18	-758	-3026	-2179	-2119	-1949	-2796	-3213	-1862	-1351	-1353	-6483	-6082	-5872
Mass Flows	kg/h	1302,1	1266,3	35,8	1732,2	1732,2	1732,2	1732,2	174,4	174,4	1384,5	173,2	1440,7	1440,7	1440,7	1440,7	1440,7	1440,7	420,3	1020,4	1020,4	3893,3	3893,3	3892,8
CO	kg/h	0	0	0	0	0	0	0	0	0	0	0	0	0	0	623	623	623	0	623	623	860	860	860
H2	kg/h	0	0	0	0	0	0	174	174	174	0	0	174	174	174	125	125	125	0	125	125	387	387	387
H2O	kg/h	42	6	36	1732	1732	1732	173	0	0	0	173	6	6	6	426	426	426	420	6	6	7	7	7
CO2	kg/h	1259	1259	0	0	0	0	0	0	0	0	0	1259	1259	1259	257	257	257	0	257	257	1834	1834	1833
N2	kg/h	1	1	0	0	0	0	0	0	0	0	0	1	1	1	1	1	1	0	1	1	74	74	74
O2	kg/h	0	0	0	0	0	0	1385	0	0	1385	0	0	0	0	0	0	0	0	0	0	0	0	0
CH4	kg/h	0	0	0	0	0	0	0	0	0	0	0	0	0	0	9	9	9	0	9	9	702	702	701
CH3OH	kg/h	0	0	0	0	0	0	0	0	0	0	0	0	0	0	0	0	0	0	0	0	29	29	29

	Units	R-304	R-305	R-306	R-401	R-402	R-403	M-101	M-102	M-103	M-104	M-105	M-106	M-107	M-108	M-109	M-110	P-101	P-102	P-103	P-104
Temperature	C	240	123	30	30	30	32	30	31	110	30	30	30	246	143	120	120	30	100	62	62
Pressure	barg	79	79	79	79	79	80	79	11	10	10	10	10	80	10	5	5	79	0	0	0
Molar Vapor Fraction		1,00	0,97	0,86	1,00	1,00	1,00	0,00	0,02	1,00	0,51	0,00	1,00	1,00	0,00	0,09	0,09	1,00	0,00	0,00	1,00
Enthalpy Flow	kW	-6582	-6983	-7498	-5005	-4943	-4940	-2492	-2492	-305	-329	-135	-194	-190	-2175	-2175	-2175	-62	-445	-1794	-2
Mass Flows	kg/h	3892,8	3892,8	3893,1	2827,7	2792,7	2792,7	1065,4	1065,4	142,2	142,2	62,0	80,3	80,3	985,1	985,1	985,1	35,0	103,1	881,0	1,0
CO	kg/h	241	241	241	240	237	237	0	0	0	0	0	0	0	0	0	0	3	0	0	0
H2	kg/h	266	266	266	265	262	262	0	0	0	0	0	0	0	0	0	0	3	0	0	0
H2O	kg/h	104	104	104	1	1	1	103	103	1	1	1	0	0	103	103	103	0	103	0	0
CO2	kg/h	1596	1596	1596	1520	1501	1501	76	76	82	82	6	76	76	0	0	0	19	0	0	0
N2	kg/h	74	74	74	74	73	73	0	0	0	0	0	0	0	0	0	0	1	0	0	0
O2	kg/h	0	0	0	0	0	0	0	0	0	0	0	0	0	0	0	0	0	0	0	0
CH4	kg/h	701	701	702	699	690	690	3	3	3	3	0	3	3	0	0	0	9	0	0	0
CH3OH	kg/h	911	911	911	28	28	28	883	883	56	56	55	1	1	882	882	882	0	0	881	1

Table A.5: Mass balance of Scenario 6 (SOEC-rWGS-methanol synthesis)

	Units	C-101	C-102	C-103	E-101	E-102	E-103	E-104	E-105	E-106	E-107	E-108	R-201	R-202	R-203	R-204	R-205	R-206	R-207	R-208	R-209	R-301	R-302	R-303
Temperature	C	43	151	30	10	12	75	75	75	76	75	75	146	900	950	950	155	30	30	30	30	34	170	240
Pressure	barg	0	10	2	2	32	32	32	32	9	32	32	10	10	10	10	10	10	9	9	80	80	80	80
Molar Vapor Fraction		1,00	1,00	0,00	0,00	0,00	0,00		1,00	1,00	1,00	0,00	1,00	1,00	1,00	1,00	1,00	0,80	0,00	1,00	1,00	1,00	1,00	1,00
Enthalpy Flow	kW	-3278	-3111	-159	-7718	-7713	-7575		35	35	15	-758	-3026	-2179	-2119	-1949	-2796	-3213	-1862	-1351	-1353	-6483	-6082	-5872
Mass Flows	kg/h	1302,1	1266,3	35,8	1732,3	1732,3	1732,3	1732,3	174,5	174,5	1384,6	173,2	1440,7	1440,7	1440,7	1440,7	1440,7	1440,7	420,3	1020,4	1020,4	3893,3	3893,3	3892,8
CO	kg/h	0	0	0	0	0	0	0	0	0	0	0	0	0	0	623	623	623	0	623	623	860	860	860
H2	kg/h	0	0	0	0	0	0	174	174	174	0	0	174	174	174	125	125	125	0	125	125	387	387	387
H2O	kg/h	42	6	36	1732	1732	1732	173	0	0	0	173	6	6	6	426	426	426	420	6	6	7	7	7
CO2	kg/h	1259	1259	0	0	0	0	0	0	0	0	0	1259	1259	1259	257	257	257	0	257	257	1834	1834	1833
N2	kg/h	1	1	0	0	0	0	0	0	0	0	0	1	1	1	1	1	1	0	1	1	74	74	74
O2	kg/h	0	0	0	0	0	0	1385	0	0	1385	0	0	0	0	0	0	0	0	0	0	0	0	0
CH4	kg/h	0	0	0	0	0	0	0	0	0	0	0	0	0	0	9	9	9	0	9	9	702	702	701
CH3OH	kg/h	0	0	0	0	0	0	0	0	0	0	0	0	0	0	0	0	0	0	0	0	29	29	29

	Units	R-304	R-305	R-306	R-401	R-402	R-403	M-101	M-102	M-103	M-104	M-105	M-106	M-107	M-108	M-109	M-110	P-101	P-102	P-103	P-104
Temperature	C	240	123	30	30	30	32	30	31	110	30	30	30	246	143	120	120	30	100	62	62
Pressure	barg	79	79	79	79	79	80	79	11	10	10	10	10	80	10	5	5	79	0	0	0
Molar Vapor Fraction		1,00	0,97	0,86	1,00	1,00	1,00	0,00	0,02	1,00	0,51	0,00	1,00	1,00	0,00	0,09	0,09	1,00	0,00	0,00	1,00
Enthalpy Flow	kW	-6582	-6983	-7498	-5005	-4943	-4940	-2492	-2492	-305	-329	-135	-194	-190	-2175	-2175	-2175	-62	-445	-1794	-2
Mass Flows	kg/h	3892,8	3892,8	3893,1	2827,7	2792,7	2792,7	1065,4	1065,4	142,2	142,2	62,0	80,3	80,3	985,1	985,1	985,1	35,0	103,1	881,0	1,0
CO	kg/h	241	241	241	240	237	237	0	0	0	0	0	0	0	0	0	0	3	0	0	0
H2	kg/h	266	266	266	265	262	262	0	0	0	0	0	0	0	0	0	0	3	0	0	0
H2O	kg/h	104	104	104	1	1	1	103	103	1	1	1	0	0	103	103	103	0	103	0	0
CO2	kg/h	1596	1596	1596	1520	1501	1501	76	76	82	82	6	76	76	0	0	0	19	0	0	0
N2	kg/h	74	74	74	74	73	73	0	0	0	0	0	0	0	0	0	0	1	0	0	0
O2	kg/h	0	0	0	0	0	0	0	0	0	0	0	0	0	0	0	0	0	0	0	0
CH4	kg/h	701	701	702	699	690	690	3	3	3	3	0	3	3	0	0	0	9	0	0	0
CH3OH	kg/h	911	911	911	28	28	28	883	883	56	56	55	1	1	882	882	882	0	0	881	1

4. Simulation of the CO_2 tolerant methanol synthesis unit

Scenarios 7 and 8 include a CO_2 tolerant methanol synthesis, which converts CO_2 and H_2 directly in a series of three reactors to methanol. The assumptions of the reactor properties are the same as for the conventional methanol synthesis (section 4). The intermedate methanol-water mixture is separated between each methanol reactor and fed to the distillation unit. The main distinction between scenario 7 and 8 is the production of hydrogen, using the PEM (scenario 7) and SOEC (scenario 8) techniques, which are described in section 2 (Fischer Tropsch simulation). Heat integration is performed with ASPEN Energy Analyzer.
Figure A.6/Table A.6 and Figure A.7/Table A.7 show the flowsheets and mass balances of scenarios 7 and 8, respectively.

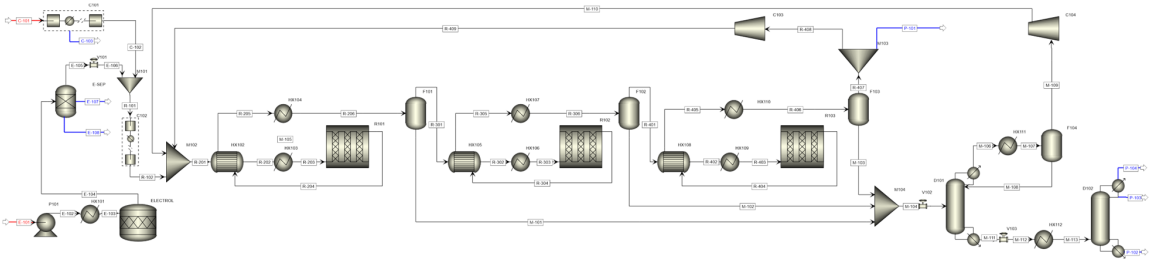

Figure A.6: Flow sheet of scenario 7 (includes PEM electrolysis, 3-stage methanol synthesis)

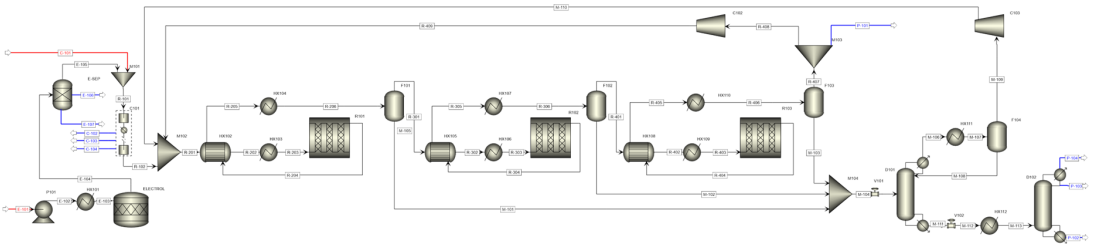

Figure A.7: Flow sheet of scenario 8 (includes SOEC electrolysis, 3-stage methanol synthesis)

Table A.6: Mass balance of Scenario 7 (PEM – three-stage methanol synthesis)

	Units	C-101	C-102	C-103	M-106	M-107	M-108	E-101	E-102	E-103	E-104	E-105	E-106	E-107	E-108	M-109	M-110	M-111	M-113	M-112	M-101	M-102	M-103	M-105	M-104	P-104	P-103	P-102
Temperature	°C	43	30	30	126	30	30	10	12	75	75	75	75	75	75	30	246	152	129	129	30	30	30	32	30	64	64	100
Pressure	barg	0	30	5	10	10	10	2	32	32	32	32	30	32	32	10	80	10	5	5	78	77	75	11	75	0	0	0
Molar Vapor Fraction		1,0	1,0	0,0	1,0	0,3	0,0	0,0	0,0	0,0		1,0	1,0	1,0	0,0	1,0	1,0	0,0	0,1	0,1	0,0	0,0	0,0	0,0	0,0	1,0	0,0	0,0
Enthalpy Flow	kW	-3278	-3153	-169	-234	-260	-152	-7669	-7665	-7527		35	35	15	-753	-109	-106	-3919	-3919	-3919	-1674	-1410	-1140	-4224	-4224	-2	-1818	-2200
Mass Flows	kg/h	1302	1264	38	111	111	67	1721	1721	1721	1721	173	173	1376	172	44	44	1405	1405	1405	556	492	401	1449	1449	1	894	510
CO	kg/h	0	0	0	0	0	0	0	0	0	0	0	0	0	0	0	0	0	0	0	0	0	0	0	0	0	0	0
H2	kg/h	0	0	0	0	0	0	0	0	0	0	173	173	0	0	0	0	0	0	0	0	0	0	0	0	0	0	0
H2O	kg/h	42	3	38	4	4	4	1721	1721	1721	172	0	0	0	172	0	0	509	509	509	218	163	128	509	509	0	0	509
CO2	kg/h	1259	1259	0	49	49	6	0	0	0	0	0	0	0	0	43	43	0	0	0	14	16	13	43	43	0	0	0
N2	kg/h	1	1	0	0	0	0	0	0	0	0	0	0	0	0	0	0	0	0	0	0	0	0	0	0	0	0	0
O2	kg/h	0	0	0	0	0	0	0	0	0	1376	0	0	1376	0	0	0	0	0	0	0	0	0	0	0	0	0	0
CH3OH	kg/h	0	0	0	57	57	57	0	0	0	0	0	0	0	0	1	1	896	896	896	324	313	259	897	897	1	894	1

	Units	P-101	R-101	R-102	R-201	R-202	R-203	R-204	R-205	R-206	R-301	R-302	R-303	R-304	R-305	R-306	R-401	R-402	R-403	R-404	R-405	R-406	R-407	R-408	R-409
Temperature	°C	30	52	186	108	180	240	240	166	30	30	180	240	240	121	30	30	180	240	240	120	30	30	30	38
Pressure	barg	75	30	83	80	80	80	78	78	78	78	78	78	77	77	77	77	77	77	75	75	75	75	75	80
Molar Vapor Fraction		1,0	1,0	1,0	1,0	1,0	1,0	1,0	1,0	0,9	1,0	1,0	1,0	1,0	1,0	0,9	1,0	1,0	1,0	1,0	1,0	0,9	1,0	1,0	1,0
Enthalpy Flow	kW	-65	-3117	-2979	-6245	-6078	-5939	-6094	-6261	-6802	-5128	-4845	-4730	-4903	-5186	-5487	-4077	-3847	-3754	-3900	-4130	-4373	-3233	-3168	-3159
Mass Flows	kg/h	33	1437	1437	3083	3083	3083	3083	3083	3083	2527	2527	2527	2527	2527	2527	2036	2036	2036	2036	2036	2036	1635	1602	1602
CO	kg/h	2	0	0	116	116	116	164	164	164	164	164	164	144	144	144	144	144	144	118	118	118	118	116	116
H2	kg/h	4	173	173	372	372	372	307	307	307	307	307	307	250	250	250	250	250	250	203	203	203	203	199	199
H2O	kg/h	0	3	3	5	5	5	220	220	220	2	2	2	164	164	164	1	1	1	129	129	129	1	1	1
CO2	kg/h	25	1259	1259	2516	2516	2516	1990	1990	1990	1977	1977	1977	1581	1581	1581	1565	1565	1565	1252	1252	1252	1239	1214	1214
N2	kg/h	1	1	1	47	47	47	47	47	47	47	47	47	47	47	47	47	47	47	47	47	47	47	46	46
O2	kg/h	0	0	0	16	16	16	16	16	16	16	16	16	16	16	16	16	16	16	16	16	16	16	16	16
CH3OH	kg/h	0	0	0	12	12	12	339	339	339	15	15	15	326	326	326	14	14	14	271	271	271	11	11	11

Table A.7: Mass balance of Scenario 6 (SOEC – three-stage methanol synthesis)

	Units	C-101	C-102	C-103	C-104	C-105	M-106	M-107	M-108	E-101	E-102	E-103	E-104	E-105	E-106	E-107	M-109	M-110	M-111	M-113	M-112	M-101	M-102	M-103	M-105	M-104	P-104	P-103
Temperature	°C	43	30	30	30	30	126	30	30	10	10	160	75	75	75	75	30	246	152	129	129	30	30	30	32	30	64	64
Pressure	barg	0	30	2	8	27	10	10	10	2	5	5	1	1	1	1	10	80	10	5	5	78	77	75	11	75	0	0
Molar Vapor Fraction		1,0	1,0	0,0	0,0	0,0	1,0	0,3	0,0	0,0	0,0	1,0		1,0	1,0	0,0	1,0	1,0	0,0	0,1	0,1	0,0	0,0	0,0	0,0	0,0	1,0	0,0
Enthalpy Flow	kW	-3278	-3153	-75	-72	-24	-234	-260	-152	-7670	-7669	-6306		35	17	-753	-109	-106	-3919	-3919	-3919	-1674	-1410	-1140	-4224	-4224	-2	-1818
Mass Flows	kg/h	1302	1264	17	16	5	111	111	67	1721	1721	1721	1721	173	1376	172	44	44	1405	1405	1405	556	492	401	1449	1449	1	894
CO	kg/h	0	0	0	0	0	0	0	0	0	0	0	0	0	0	0	0	0	0	0	0	0	0	0	0	0	0	0
H2	kg/h	0	0	0	0	0	0	0	0	0	0	0	173	173	0	0	0	0	0	0	0	0	0	0	0	0	0	0
H2O	kg/h	42	3	17	16	5	4	4	4	1721	1721	1721	172	0	0	172	0	0	509	509	509	218	163	128	509	509	0	0
CO2	kg/h	1259	1259	0	0	0	49	49	6	0	0	0	0	0	0	0	43	43	0	0	0	14	16	13	43	43	0	0
N2	kg/h	1	1	0	0	0	0	0	0	0	0	0	0	0	0	0	0	0	0	0	0	0	0	0	0	0	0	0
O2	kg/h	0	0	0	0	0	0	0	0	0	0	0	1376	0	1376	0	0	0	0	0	0	0	0	0	0	0	0	0
CH3OH	kg/h	0	0	0	0	0	57	57	57	0	0	0	0	0	0	0	1	1	896	896	896	324	313	259	897	897	1	894

	Units	P-102	P-101	R-101	R-102	R-201	R-202	R-203	R-204	R-205	R-206	R-301	R-302	R-303	R-304	R-305	R-306	R-401	R-402	R-403	R-404	R-405	R-406	R-407	R-408	R-409
Temperature	°C	100	30	64	186	108	180	240	240	166	30	30	180	240	240	121	30	30	180	240	240	120	30	30	30	38
Pressure	barg	0	75	0	83	80	80	80	78	78	78	78	78	78	77	77	77	77	77	77	75	75	75	75	75	80
Molar Vapor Fraction		0,0	1,0	1,0	1,0	1,0	1,0	1,0	1,0	1,0	0,9	1,0	1,0	1,0	1,0	1,0	0,9	1,0	1,0	1,0	1,0	1,0	0,9	1,0	1,0	1,0
Enthalpy Flow	kW	-2200	-65	-3244	-2979	-6245	-6078	-5939	-6094	-6261	-6802	-5128	-4845	-4730	-4903	-5186	-5487	-4077	-3847	-3754	-3900	-4130	-4373	-3233	-3168	-3159
Mass Flows	kg/h	510	33	1475	1437	3083	3083	3083	3083	3083	3083	2527	2527	2527	2527	2527	2527	2036	2036	2036	2036	2036	2036	1635	1602	1602
CO	kg/h	0	2	0	0	116	116	116	164	164	164	164	164	164	144	144	144	144	144	144	118	118	118	118	116	116
H2	kg/h	0	4	173	173	372	372	372	307	307	307	307	307	307	250	250	250	250	250	250	203	203	203	203	199	199
H2O	kg/h	509	0	42	3	5	5	5	220	220	220	2	2	2	164	164	164	1	1	1	129	129	129	1	1	1
CO2	kg/h	0	25	1259	1259	2516	2516	2516	1990	1990	1990	1977	1977	1977	1581	1581	1581	1565	1565	1565	1252	1252	1252	1239	1214	1214
N2	kg/h	0	1	1	1	47	47	47	47	47	47	47	47	47	47	47	47	47	47	47	47	47	47	47	46	46
O2	kg/h	0	0	0	0	16	16	16	16	16	16	16	16	16	16	16	16	16	16	16	16	16	16	16	16	16
CH3OH	kg/h	1	0	0	0	12	12	12	339	339	339	15	15	15	326	326	326	14	14	14	271	271	271	11	11	11

5. Additional tables

A list of the calculated efficiencies for all sections are given in Table A.8.

Table A.8: Calculated efficiencies and specific energy consumption for lower olefine production

Efficiencies			Scenario number							
			1	2	3	4	5	6	7	8
PtL efficiency 1	$\eta_{PtL,1}$	[%]	44.0	54.0	44.0	54.0	49.6	62.1	52.2	64.3
PtL efficiency 2	$\eta_{PtL,2}$	[%]	31.5	37.5	31.5	37.5	28.5	33.8	29.6	34.7
Global efficiency 1	$\eta_{global,1}$	[%]	46.9	55.2	46.9	55.2	44.4	51.1	48.2	51.1
Global efficiency 2	$\eta_{global,2}$	[%]	33.2	38.2	33.2	38.2	26.1	29.2	27.8	29.2
Carbon efficiency 1	$\eta_{carbon,}$	[%]	85.1	85.1	85.1	85.1	87.0	87.0	88.3	88.3
Carbon efficiency 2	$\eta_{carbon,}$	[%]	71.5	71.5	71.5	71.5	67.5	67.5	68.6	68.6
SEC (based on intermediate product)	SEC_1	[kWh/kg]	31.8	26.7	31.8	26.7	15.6	14.1	14.6	14.1
SEC (based on C_2-C_4 product fraction)	SEC_2	[kWh/kg]	41.0	34.4	41.0	34.4	49.2	44.2	46.0	44.4

The effect of the variation of the utility costs and the impact of the equipment costs on the net production costs is given in Table A.9.

Table A.9: Sensitivity study considering deviations from actual market prices related on equipment and utility costs

Sensitivity study – specific NPC_{C2-C4}		Scenario number							
		1	2	3	4	5	6	7	8
Base scenario – lower olefins C_2 – C_4	**EUR/kWh**	**1.18**	**1.20**	**1.16**	**1.16**	**1.41**	**1.45**	**1.35**	**1.36**
Equipment costs +100 %	EUR/kWh	1.58	1.68	1.53	1.62	1.85	1.98	1.79	1.79
Equipment costs -50 %	EUR/kWh	0.98	0.96	0.97	0.94	1.19	1.19	1.13	1.14
Electricity price +100 % (400 EUR/MWh)	EUR/kWh	1.82	1.73	1.80	1.70	2.19	2.16	2.08	2.07
Electricity price -50 % (100 EUR/MWh)	EUR/kWh	0.86	0.93	0.83	0.90	1.02	1.10	0.99	1.00
PEM/SOEC future costs **Fehler! Verweisquelle konnte nicht gefunden werden.**	EUR/kWh	1.03	0.99	1.01	0.96	1.25	1.24	1.20	1.15

Publication III

Impact of the Operation Conditions on the Reverse-Water-Gas Shift Reaction

Christoph Markowitsch, Markus Lehner

EURECA-PRO The European University for Responsible Consumption and Production. 1st ed. (2023)
DOI: 10.1007/978-3-031-25840-4_10

Conception and planning	Simulation	Analysis and interpretation	Manuscript preparation
90%	100%	90%	100%

Impact of the Operation Conditions on the Reverse-Water-Gas Shift Reaction

Christoph Markowitsch(✉) and Markus Lehner

Process Technology and Environmental Protection, Montanuniversitaet Leoben, 8700 Leoben, Austria
christoph.markowitsch@unileoben.ac.at

Abstract. The reverse water gas shift (rWGS) reaction represents a key technology to realize an end-to-end power-to-liquid process chain. In this work, experimental tests of a nickel catalyst are reported. The influence of operating temperature (650–950 °C), pressure (ambient pressure up to 6 bar_a) and gas hourly space velocity (6000–40 000 h^{-1}) on the conversion of CO_2 and hydrogen is investigated. The results of this experimental evaluation show that the rWGS reaction favors high temperatures and low pressures. Thermodynamic equilibrium is approached with the used catalyst. Higher gas hourly space velocities favor the rWGS reaction and inhibit methane formation.

Keywords: Carbon capture and utilization · Catalyst performance · Power-to-liquid · Reverse water gas shift

1 Introduction

The cement industry emitted 9 % of Austria's ETS (EU Emission Trading System) certified emissions, which corresponds to 3.3 % of Austria's carbon dioxide emissions in 2019 [1]. Austria's target is to reduce 40 % of greenhouse gas emissions by 2030 and achieve climate neutrality by 2040 [2]. In cement production process-related CO_2 emissions are unavoidable, which are generated by the decarbonization process of limestone and account for two-thirds of the total greenhouse gas emissions. [3]. One option for the reduction of CO_2 emissions is the implementation of a carbon capture and utilization (CCU) plant. A possible Power-to-Liquid route is a Fischer–Tropsch synthesis. The produced synthetic oil can be further converted in steam- and hydrocrackers to propylene or ethylene, which is the feedstock for polypropylene and polyethylene production [4]. The Fischer Tropsch synthesis requires syngas (a mixture of carbon monoxide and hydrogen) as feedstock, the direct hydrogenation of CO_2 is currently not yet commercially available [5].

Therefore, a pre-conversion of CO_2 to CO is required which can be achieved with the reverse water gas shift reaction. Basically, the rWGS reaction (Eq. 1) is endothermic and catalytically converts carbon dioxide with hydrogen to carbon monoxide and water (steam) [6, 7].

$$CO_2 + H_2 \leftrightarrow CO + H_2O \qquad \Delta H_r^{298K} = +41 kJ/mol \tag{1}$$

J. A. Benítez-Andrades et al. (eds.), *Global Challenges for a Sustainable Society*,
Springer Proceedings in Earth and Environmental Sciences, https://doi.org/10.1007/978-3-031-25840-4_10

The CO_2 conversion (X_{CO_2}) is defined as the ratio between the difference of inlet ($\dot{n}_{CO_2,in}$ in kmol/h) and outlet ($\dot{n}_{CO_2,out}$ in kmol/h) mole flow, and the CO_2 inlet mole flow as given in Eq. 2. Furthermore, Eq. 3 defines the CO selectivity (S_{CO}) as the ratio of the obtained CO mole flow ($\dot{n}_{CO}$ in kmol/h) in the product and the converted CO_2 [8].

$$X_{CO_2} = \frac{\dot{n}_{CO_2,in} - \dot{n}_{CO_2,out}}{\dot{n}_{CO_2,in}} \tag{2}$$

$$S_{CO} = \frac{\dot{n}_{CO,out} - \dot{n}_{CO,in}}{\dot{n}_{CO_2,in} - \dot{n}_{CO_2,out}} \tag{3}$$

Considering the thermodynamics of the reaction, a complete conversion of CO_2 is not feasible. Side reactions that occur, such as methanation, Bosch reaction or the Boudouard equilibrium, must also be taken into account in the catalytic conversion process. The last two lead to coke formation and deactivation of the catalyst. To counteract this and improve the CO_2 conversion, the equilibrium can be shifted by running the rWGS reaction with an over-stoichiometric ratio of H_2:CO_2 of 3:1 [9]. Thus, a syngas composition with a desired H_2:CO ratio of 2:1 is obtained. Figure 1 shows the thermodynamic equilibrium in a temperature range of 300–1100 °C and pressures of 1, 5 and 30 bar_g [10].

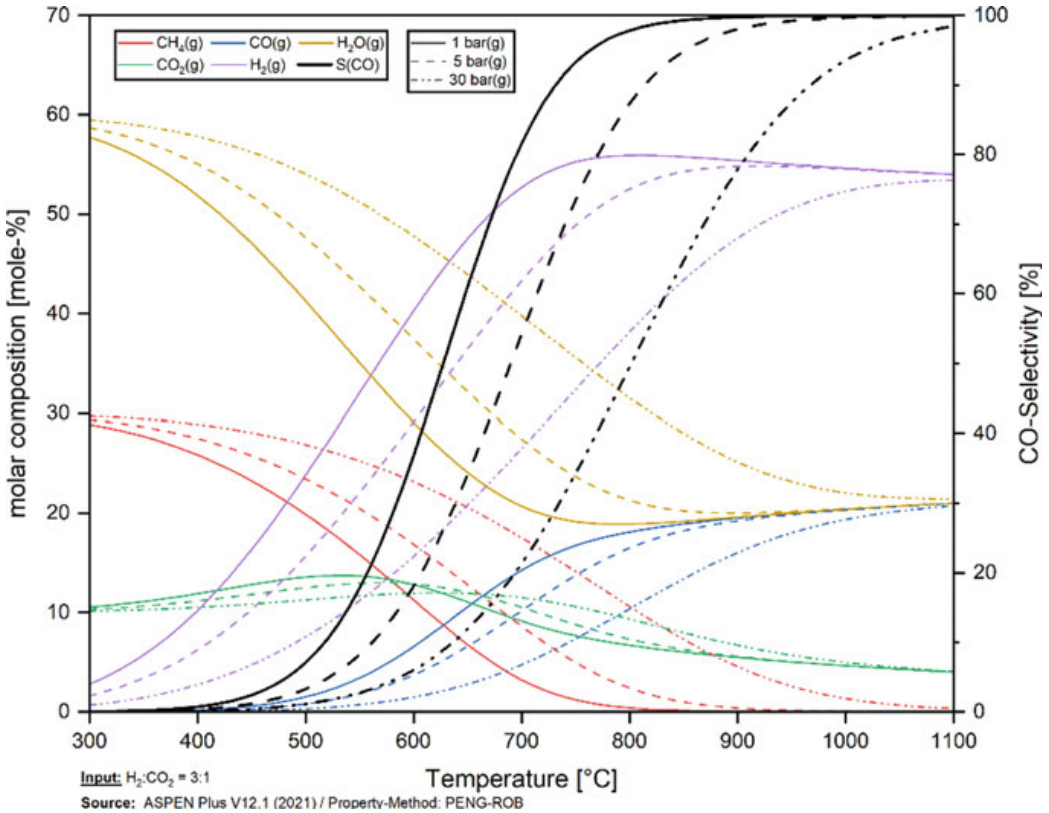

Fig. 1 Thermodynamic equilibrium considering an inlet ratio of H_2:CO_2 of 3:1 in a temperature range of 300–1100 °C and pressures of 1, 5, and 30 bar_g

In this work, an experimental investigation of the rWGS reaction is carried out. The experiments provide insights into temperature, pressure, and gas-hour-space-velocity (GHSV) dependence of the reaction. A comparison of the experimentally obtained product compositions with the thermodynamic equilibrium is performed.

2 Methods

2.1 Experimental setup

The experimental setup is constructed as shown in the P&ID diagram (Fig. 2), starting with a gas mixing station (X1, mass controller of hydrogen/0–12 Nl/min, carbon dioxide/0–10 Nl/min, and nitrogen/0–20 Nl/min), a quartz-glass reactor in a tube furnace, a cooling and water condenser unit, followed by the gas analysis and flare. The quartz glass is designed for an operating pressure of 10 bar_a and temperatures up to 1100 °C. The plant settings and the registration of the measured values are handled by the "Lookout" software. The pressure is controlled by adjusting the automatic valve (V038) at the reactor outlet.

The glass reactor has a length of 1700 mm and an inner diameter of 15 mm. The connections from the glass tube to the piping are made via crimp connectors, which allow a maximal operating inlet pressure of 6 bar_a. The gas mixture is fed directly to the crimp connectors without heating. To achieve high temperatures, the catalyst is located at the end of the reactor, while the furnace is also used as gas preheating unit. The nickel-based catalyst used has a cylindrical shape (3.2 mm × 3.2 mm). The catalyst bed has a length of 75 mm and a total bulk volume of 12.37 cm^3. The remaining volume of the glass tube is filled with inert balls, ensuring sufficient heat exchange in the preheating zone. Six thermocouples are implemented in the reactor to obtain the axial temperature profile. The position of the thermocouples is depicted in Fig. 3.

2.2 Catalyst tests

Activation of the catalyst started with heating the fixed bed to temperatures of 500 °C (thermocouple T3) in the furnace. Nitrogen at 10 Nl/min was used to purge the system. When the temperature was reached, the ratio of nitrogen to hydrogen was gradually changed and after 30 min, pure hydrogen was fed into the system for catalyst activation. After one hour, the temperature was increased to 950 °C and the catalyst was ready for catalyst testing.

In the initial experimental tests, the operation pressure was gradually increased from atmospheric pressure to 6 bar_a with a starting temperature of 950 °C (measured at thermocouple T3) and a constant GHSV of 20 000 h^{-1}. Temperature variation continued for 850, 750 and 650 °C according to the experimental design (Table 1). In the second series of catalyst tests, the effect of temperature and GHSV on the rWGS reaction was investigated. The experiments started with temperatures of 650 °C measured at the beginning of the catalyst bed (thermocouple T3), and the GHSV was varied between 6000 and 40 000 h^{-1}. The design for the second experimental test series is detailed in Table 2.

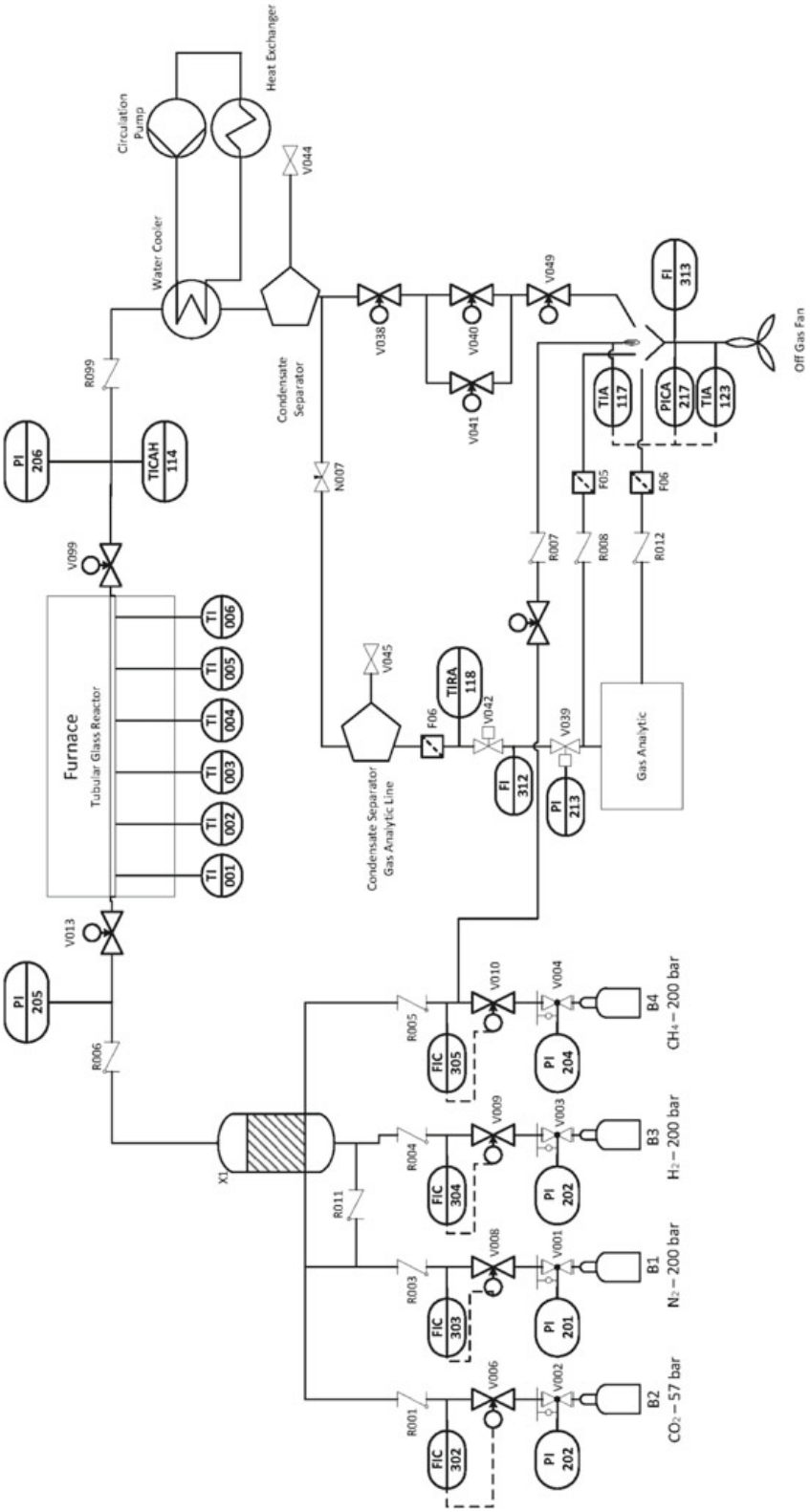

Fig. 2 P&ID of the experimental setup

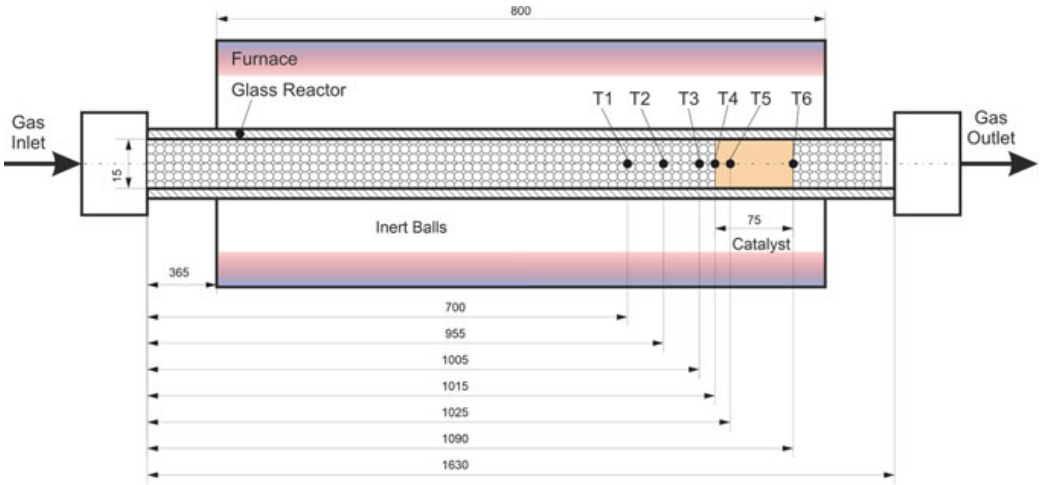

Fig. 3 Experimental setup and position of the thermocouples in the glass reactor

2.3 Evaluation of the experimental data and calculation of the thermodynamic equilibrium

The inlet flow of the feed gas is measured by mass flow meters, and the molar flow is subsequently calculated. The gas analyzer is implemented behind the water condenser (Fig. 2). It measures CO_2, CO, CH_4 and the ratio of H_2:N_2. The figures are registered in the "Lookout" software. The equilibrium conversions are calculated in ASPEN HYSYS V12, which implements a Gibbs reactor that minimizes the Gibbs-free energy. The values of the gas analysis are recalculated for the dry gas flow, and are directly compared with the equilibrium calculation from ASPEN.

3 Results

According to Fig. 1, the rWGS reaction generally favors high temperatures (900 °C) and low pressures for achieving the thermodynamic equilibrium. At pressures of 10 and 30 bar_g, even elevated temperatures of 950 °C and higher are necessary.

In the first experimental test series the influence of pressure on the rWGS reaction is investigated. Figure 4 compares the thermodynamic equilibrium with the experimental results for pressures of 1.4, 3 and 6 bar_a. The full lines describe the development of the molar fractions in thermodynamic equilibrium for the components CO, CO_2, CH_4 and H_2 calculated from ASPEN HYSYS. Here, steam is not included in the evaluation due to the separation upstream of the gas-analyzer. The comparison of the pressure influence is also shown in Fig. 4.

In the second experimental tests, the influence of the gas-hourly-space-velocity (GHSV) and temperature at ambient pressure is investigated. The deviation of experimental results from the thermodynamic calculation is shown in Fig. 5 for the GHSV values of 6000, 10 000, 20 000 and 40 000 h^{-1}. Again, the full lines describe the development of the molar fractions of CO, CO_2, CH_4 and H_2 in thermodynamic equilibrium. The absolute deviation of each GHSV value is shown in the last plot of Fig. 5.

Table 1 Design of experiments with variation of temperature and pressure at constant GHSV

Exp. number	Temperature	Pressure	GHSV	CO_2	H_2
#	(°C)	(bar_a)	(h^{-1})	(Nl/min)	(Nl/min)
1.1	950	1	20 000	1.1781	3.5343
1.2	950	2	20 000	1.1781	3.5343
1.3	950	3	20 000	1.1781	3.5343
1.4	950	4	20 000	1.1781	3.5343
1.5	950	5	20 000	1.1781	3.5343
1.6	950	6	20 000	1.1781	3.5343
1.7	850	1	20 000	1.1781	3.5343
1.8	850	2	20 000	1.1781	3.5343
1.9	850	3	20 000	1.1781	3.5343
1.10	850	4	20 000	1.1781	3.5343
1.11	850	5	20 000	1.1781	3.5343
1.12	850	6	20 000	1.1781	3.5343
1.13	750	1	20 000	1.1781	3.5343
1.14	750	2	20 000	1.1781	3.5343
1.15	750	3	20 000	1.1781	3.5343
1.16	750	4	20 000	1.1781	3.5343
1.17	750	5	20 000	1.1781	3.5343
1.18	750	6	20 000	1.1781	3.5343
1.19	650	1	20 000	1.1781	3.5343
1.20	650	2	20 000	1.1781	3.5343
1.21	650	3	20 000	1.1781	3.5343
1.22	650	4	20 000	1.1781	3.5343
1.23	650	5	20 000	1.1781	3.5343
1.24	650	6	20 000	1.1781	3.5343

The measured temperatures of thermocouples are shown in Fig. 6. The reactor temperature profile is shown for a catalyst bed inlet temperature of 650 °C and 950 °C as well as for gas hourly space velocities of 6000, 10 000, 20 000 and 40 000 h^{-1}.

4 Discussion

The operating conditions, temperature, pressure and GHSV, influence conversion and yield of the rWGS reaction on a nickel catalyst significantly. The unwanted methanation reaction is suppressed by high temperatures and low pressure levels, as it can be seen in Fig. 4. The experimentally obtained product compositions approximate fairly good to

Table 2 Design of experiments with variation of temperature and GHSV at constant pressure

Exp. number	Temperature	Pressure	GHSV	CO_2	H_2
#	(°C)	(bar_a)	(h^{-1})	(Nl/min)	(Nl/min)
2.1	650	1	6000	0.3534	1.0603
2.2	650	1	8000	0.4712	1.4137
2.3	650	1	10 000	0.5890	1.7671
2.4	650	1	20 000	1.1781	3.5343
2.5	650	1	40 000	2.3562	7.0686
2.6	750	1	6000	0.3534	1.0603
2.7	750	1	8000	0.4712	1.4137
2.8	750	1	10 000	0.5890	1.7671
2.9	750	1	20 000	1.1781	3.5343
2.10	750	1	40 000	2.3562	7.0686
2.11	850	1	6000	0.3534	1.0603
2.12	850	1	8000	0.4712	1.4137
2.13	850	1	10 000	0.5890	1.7671
2.14	850	1	20 000	1.1781	3.5343
2.15	850	1	40 000	2.3562	7.0686
2.16	950	1	6000	0.3534	1.0603
2.17	950	1	8000	0.4712	1.4137
2.18	950	1	10 000	0.5890	1.7671
2.19	950	1	20 000	1.1781	3.5343
2.20	950	1	40 000	2.3562	7.0686

the thermodynamic equilibrium for each pressure level. Only at temperatures higher than 650 °C a larger deviation ca be observed for carbon monoxide, particularly in comparison to CO_2, CH_4, and H_2. Methane formation is below thermodynamic equilibrium at 650 °C. This may be caused by the exothermic nature of the methanation reaction which heats up the catalyst bed locally, and thus suppress methane formation. Nevertheless, the experimental investigation confirms that temperature and pressure have a corresponding influence on the conversion of CO_2 to the desired synthesis gas. Low pressure and high temperature favor the rWGS reaction, while high pressure and lower temperatures promote methane formation.

The influence of the GHSV value is not so decisive as temperature and pressure. The comparison of the experimental results of the five different GHSV values (Fig. 6, 6000, 10 000, 20 000, 40 000 h^{-1}) reveals that the methane content in the product gas decreases with increasing gas velocity. The temperature drops at a specific gas velocity of 40 000 h^{-1} to 900 °C (measured at thermocouple T4) what changes the thermodynamic equilibrium significantly in the direction of methanation. However, even at 900 °C,

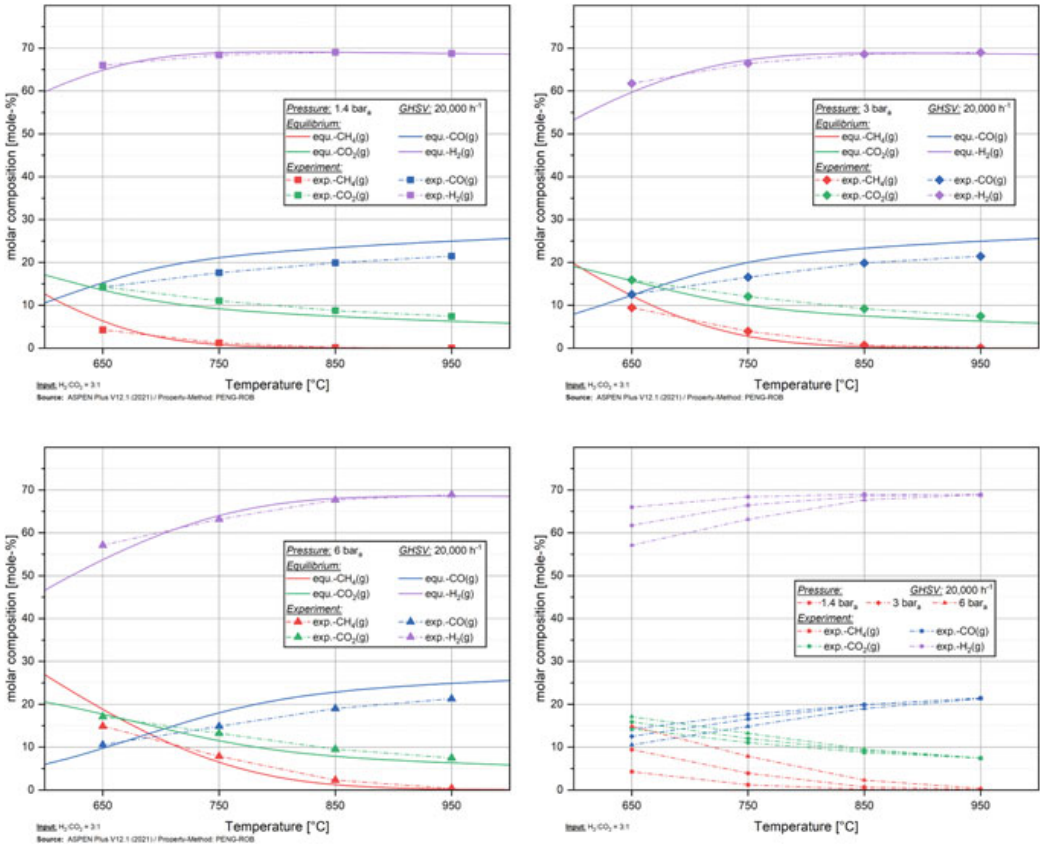

Fig. 4 Experimental results and thermodynamic equilibrium for constant GHSV values and variation of pressure levels (1.4, 3, 6 bar_a)

methane formation is very low. On the other hand, the higher gas velocity makes the flow in the reactor more turbulent, allowing better heat and mass transfer between the catalyst surface and the gas particles.

A similar trend can be observed at 650 °C, however due to the increased heat release by the exothermic methanation, the temperature deviations are less pronounced. As shown in Fig. 6, the higher gas velocity leads to higher heat generation in the catalyst and this also results in the shift of the thermodynamic equilibrium towards the endothermic rWGS reaction, which can also be seen by a small temperature drop at thermocouple T4. With higher pressure and increased methane formation, the temperature continues to increase. In order to maintain constant temperatures of 650 °C, the reactor would have to be cooled instead of heated in this case. Additionally, the higher GHSV value allows a higher exit temperature from the catalyst and thus a lower selectivity to CH_4. The CO content increases accordingly.

The second series of tests was carried out completely independently of the first series of tests. This allows validation of the product composition at temperatures 650, 750, 850 and 950 °C and ambient pressure for a GHSV value of 20 000 h^{-1}.

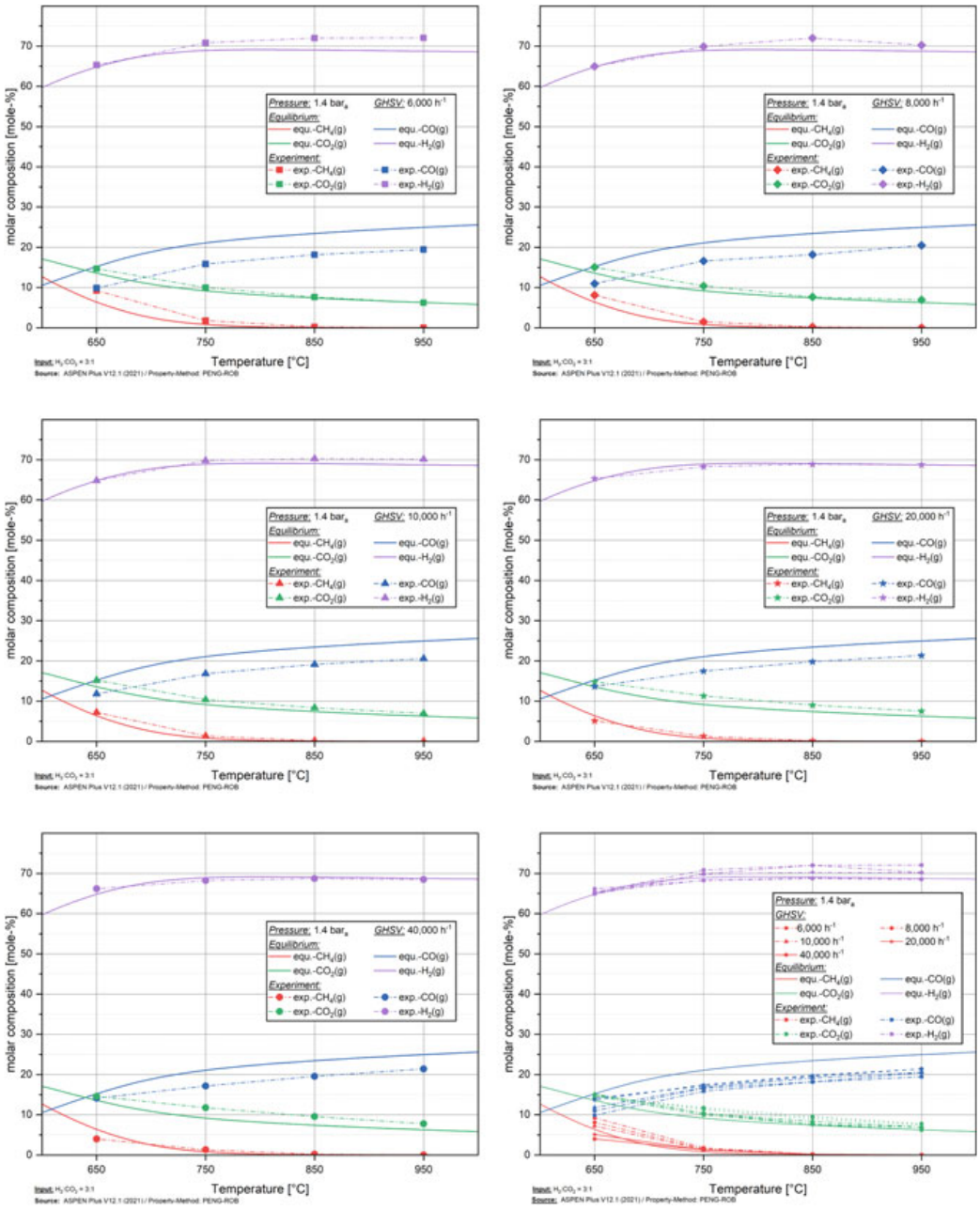

Fig. 5 Experimental results and thermodynamic equilibrium for ambient pressure and GHSV variation (6000, 8000, 10 000, 20 000, 40 000 h^{-1})

5 Conclusions

The reverse water gas shift reaction enables the conversion of CO_2 and hydrogen into synthesis gas, which is used as a feedstock for a wide variety of syntheses. The experimental results in this work show that the rWGS reaction can be performs on nickel catalysts. The conversion of CO_2 and hydrogen into synthesis gas is favored at higher temperatures and lower pressures, since methane formation is inhibited. Therefore, the rWGS reaction should be operated at temperatures higher than 900 °C and pressures

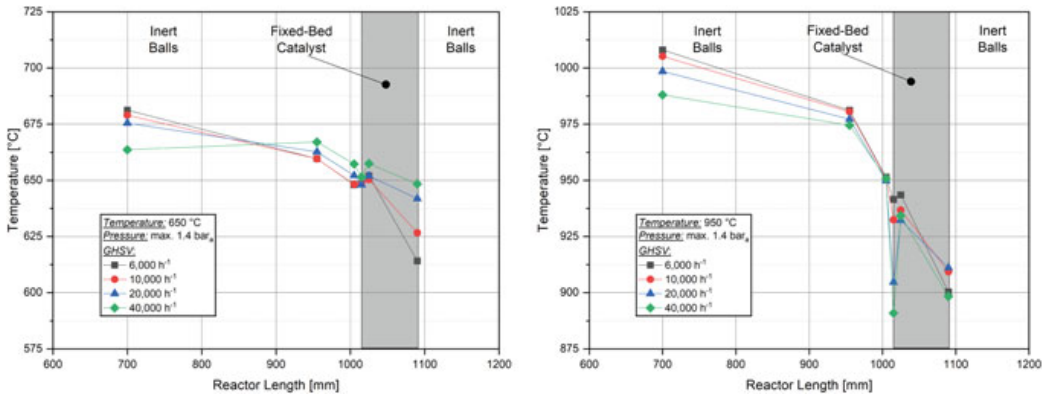

Fig. 6 Reactor temperature profile for 650 and 950 °C (measured at thermocouple T3) and GHSV values of 6000, 10 000, 20 000, 40 000 h^{-1}

lower than 6 bar_a to suppress undesired methane formation. However, the selection of the operating pressure level is also influenced by the pressure requirements of further downstream catalytic conversions.

The gas hourly space velocity in the fixed-bed reactor has only a minor effect on the CO_2 conversion. In this experimental study, higher gas velocities favor the rWGS reaction and inhibit methane formation. A general recommendation for an optimum gas hourly space velocity cannot be given, since the simplified experimental set-up does not allow for a transformation to industrial reactor systems.

Further studies should deal in particular with a more detailed analysis of the product gas stream for other by-products, as only CH_4 and no longer chain hydrocarbons were measured in these initial series of experiments. Furthermore, the influence of the over-stoichiometric hydrogen feed on coke formation, conversion, selectivity and the turbulence in the catalyst bulk should be investigated.

References

1. Umweltbundesamt Environment Agency Austria.: Austria's National Inventory Report 2021
2. Bundesministerium für Klimaschutz, Umwelt, Energie, Mobilität, Innovation und Technologie.: Das Übereinkommen von Paris (2022). https://www.oesterreich.gv.at/themen/bauen_wohnen_und_umwelt/klimaschutz/1/Seite.1000325.html. Accessed 02 Feb 2022
3. Mauschitz, G.: Emissionen aus Anlagen der österreichischen Zementindustrie - Berichtsjahr 2020. Wien (2021)
4. König, D.H.: Techno-ökonomische Prozessbewertung der Herstellung synthetischen Flugturbinentreibstoffes aus CO_2 und H_2. Dissertation, Universitätsbibliothek der Universität Stuttgart (2016)
5. Maitlis, P.M., de Klerk, A.: Greener Fischer-Tropsch processes for fuels and feedstocks, 1st edn. Wiley-VCH, Weinheim (2013)
6. König, D.H., Baucks, N., Dietrich, R.-U., et al.: Simulation and evaluation of a process concept for the generation of synthetic fuel from CO_2 and H_2. Energy **91**, 833–841 (2015). https://doi.org/10.1016/j.energy.2015.08.099
7. Unde, R.B.: Kinetics and Reaction Engineering Aspects of Syngas Production by the Heterogeneously Catalysed Reverse Water Gas Shift Reaction. Dissertation, Universität Bayreuth (2012)

8. Adelung, S., Maier, S., Dietrich, R.-U.: Impact of the reverse water-gas shift operating conditions on the Power-to-Liquid process efficiency. Sustain. Energ. Technol. Assess. **43**, 100897 (2021). https://doi.org/10.1016/j.seta.2020.100897
9. Escobar, W.F.: Study of the Reverse Water-Gas Shift and Dryreforming Reactions Conditions in a Fixed Bed Reactor. Dissertation, Universität Stuttgart (2015)
10. Markowitsch, C., Lehner, M., Kitzweger, J. et al.: Conference EnInnov 2022 TU Graz] C2PAT—Carbon to Product Austria (2022). https://www.tugraz.at/fileadmin/user_upload/tugrazExternal/738639ca-39a0-4129-b0f0-38b384c12b57/files/lf/Session_D6/464_LF_Markowitsch.pdf. Accessed 18 Feb 2022

Publication IV

Process intensification of the rWGS reaction by a perovskite-based catalyst

Christoph Markowitsch, Marion Andritz, Lorenz Lindenthal,
Thomas Cotter, Hedda Drexler, Christoph Rameshan, Markus Lehner

Submitted for review

Conception and planning	Simulation	Analysis and interpretation	Manuscript preparation
80%	90%	85%	90%

Process intensification of the rWGS reaction by a perovskite-based catalyst

Christoph Markowitsch[1]*, Marion Andritz[1], Lorenz Lindenthal [2], Thomas Cotter[2], Hedda Drexler[2], Christoph Rameshan[2], Markus Lehner[1]

[1]Chair of Process Technology and Environmental Protection, Montanuniversitaet Leoben, Franz-Josef-Str. 18, A-8700 Leoben, Austria

[2]Chair of Physical Chemistry, Montanuniversitaet Leoben, Franz-Josef-Str. 18, A-8700 Leoben, Austria

*Corresponding Author
christoph.markowitsch@unileoben.ac.at, 0043-676-4773442

Keywords: rWGS, catalyst performance, nickel catalyst, perovskite catalyst, rWGS process intensification

Abstract

The reverse water gas shift (rWGS) reaction represents a key technology for the utilization of CO_2. This study presents experimental results which compare the performance of a commercially available nickel catalyst, two novel perovskite catalysts and Al_2O_3. In addition to the variations of the input gas composition, the operating conditions have been adjusted between 550 and 950 °C and 1 to 8 bara. The results reveal, on the one hand, that the nickel catalyst achieves thermodynamic equilibrium, resulting in high selectivity toward CO formation at elevated temperatures (950 °C) and ambient pressure. Higher catalyst loads suppress methane formation. On the other hand, the perovskite catalyst prevents methane formation even at low temperature (550 °C) and higher pressures favor the CO formation. In consequence, methane formation is limited to less than 2 vol.-% at 650 °C and 8 bara and the CO content in the product gas is significantly higher compared with the nickel catalyst. Al_2O_3 also shows catalytic activity and achieves thermodynamic equilibrium at higher temperature (950 °C). The investigated novel perovskite catalysts have the potential to intensify the rWGS reaction towards a simpler reactor design and a highly efficient operation, also on a large-scale basis.

1. Introduction

The latest IPCC Synthesis Report 2023 shows that the earth has already warmed by 1.1 °C in average, compared to pre-industrial levels [1]. The goal of the Paris Agreement is to limit global warming to a maximum of 2 °C, with the ambition of not exceeding the 1.5 °C target [2]. An approach that could reduce industrial emissions as well as those of the transport sector, is to use emitted CO_2 as a resource to produce base-chemicals such as methanol or synthetic crude oil (syncrude) using a Fischer-Tropsch synthesis (FTS). These intermediates can be further used in upgrading processes (methanol-to-propylene or steam-/hydrocracker for syncrude) to produce polyolefins or fuels in a CO_2-neutral way. In this context, the rWGS reaction plays a crucial role, as CO_2 is catalytically converted with green hydrogen into the more reactive carbon monoxide. In a study of a power-to-liquid (PtL) plant different rWGS reactor and electrolysis technologies were evaluated [3]. The best process route was found to be an electrified rWGS reactor design in combination with a high-temperature electrolysis. The highest PtL efficiency was achieved with one recycling stream of the gaseous products upstream of the rWGS reactor. Several publications are focused on the production of renewable fuels (kerosene, diesel, etc.)

from CO_2 and green H_2 [4–6] in which a rWGS reactor is used to convert CO_2 and H_2 to synthesis gas, and finally via FTS to syncrude.

All these studies assume the rWGS reaction as a Gibbs reactor, which calculates the product output composition applying the minimum Gibbs energy methodology for a defined feed stream. With this approach, it is assumed that thermodynamic equilibrium is achieved, which is questionable in industrial processes. One motivation of our study was to verify this hypothesis by experiments. Furthermore, methane (CH_4) is an undesired by-product in rWGS reactors, which is preferably formed at low temperatures (< 700 °C). Its formation thermodynamically increases with elevated pressure. In downstream processes, such as FTS, methane is treated as inert gas [7]. Therefore, the share of CH_4 should be kept as low as possible, otherwise high recycle rates around the Fischer-Tropsch synthesis are necessary, reducing efficiencies, and increasing net production costs [8]. Adelung et al. simulated a complete PtL process route and performed a sensitivity analysis to obtain the optimized rWGS operation conditions at a temperature of 825 °C and pressure of 5 bar [6]. König et al. designed the rWGS reactor in the simulation as Gibbs-reactor as well, using an operating temperature of 900 °C, but they considered an elevated operation pressure (25 bar) to avoid the compression step between the rWGS and FTS units [9]. Applying these assumptions, methane formation is occurring. Markowitsch et al. selected a temperature of 950 °C and a pressure of 10 barg to achieve very high CO selectivity (98 %), which results in a low methane content in the product gas [10].

Some authors have already studied the rWGS reaction on laboratory scale. Wolf et al. and Unde operated the rWGS reaction in a glass tube reactor with an inner diameter of 20 mm [11,12]. They used a commercial Ni/Al_2O_3 catalyst (cylinders with 3 mm diameter) and performed a temperature variation between 600 and 1000 °C, at ambient pressure only. In their experimental setup, a CO_2 conversion of 80 % (compared to CO_2 content at thermodynamic equilibrium) was achieved at an operating temperature of 900 °C, atmospheric pressure and a residence time of less than 100 ms.

In comparison, Vázquez et al. operated the rWGS reaction in a thinner glass reactor with an inner diameter of 6 mm and 0.5 g of a Ni/Al_2O_3 catalyst (two different types with 15 and 2 wt.-% active metal) and $Rh/CeO_2/Al_2O_3$. The operating temperature was chosen between 500 and 850 °C, as well as pressures between 1 and 30 bara [13]. Vázquez et al. have already shown that the rWGS reaction follows the thermodynamic equilibrium for their comparatively small reactor. The applied geometry allows a homogeneous radial and axial temperature profile in the catalyst bed. In operation, the flow rate was limited to 2.087 NL/min with a nitrogen content of 42.5 vol.-%. The catalyst bed was blended with SiC balls (1:4), to avoid temperature peaks caused by the endothermic reaction throughout the reactor and the catalyst bed section. The SiC balls act as a heat reservoir.

Escobar published a study of the rWGS reaction on a $Rh/\gamma\text{-}Al_2O_3$ catalyst, operating at temperatures up to 1000 °C and at atmospheric pressure. The reactor was made of stainless steel and had a length of 330 mm and an inner diameter of 8 mm. Additionally, five output measurement zones were installed, to monitor the gas composition throughout the reactor bed. The feed gas stream was merged with N_2 (80 vol.-%), since the range of the gas analyzer was limited to 33 vol.-% CO_2. The CO_2 conversion was calculated for 850 and 1050 °C, resulting in conversions close to the equilibrium for both operating points. A conversion of CO_2 was already detected in the pre-heating zone. For the study of the catalyst performance, the issues with CO_2 conversion in the preheating tubes was solved by installing two separate heating tubes for CO_2 and H_2. The impact of the reactor material itself on the CO_2 conversion was not investigated in the study [14].

Although the previously described studies showed promising results, they were all carried out on small-scale constructions of rWGS testing facilities or, if an inner reactor diameter of 20 mm was used, the operation has been demonstrated only under atmospheric pressure [11,12]. Higher pressures of up to

30 bar were achieved with smaller reactor designs with an inner diameter of 6 mm [13]. In all studies, the use of a nickel catalyst indicates that thermodynamic equilibrium is reached at high temperatures, which has an important impact on the process and reactor design for large-scale realization. Due to the high operation temperatures of 1000 °C, the choice of an appropriate material of construction, the catalyst stability as well as the heat transfer must be evaluated [15,16]. Conversely, according to the state of the art, an operation below 700 °C leads to an increase in methane formation, which is additionally intensified by an increase in operating pressure [15]. Therefore, research is being conducted on catalyst materials that can be used at lower temperatures such as 300 – 700 °C without any formation of CH_4 but high CO selectivity. Bahmanpour et al. summarized tested mono- and bimetallic catalysts applied at various operating conditions [17]. Noble metals (such as Pt, Pd, Ru, Ir and Au) or Fe, Co, and Ni are the most used in metal-based catalysts for the rWGS reaction. The catalyst performance is also affected by promoters, the catalytic supports and particle size distribution [18–20].

A promising candidate for a catalyst at low temperature was identified by Lindenthal et al. [21]. They described a perovskite catalyst testing in a tubular flow reactor at ambient pressure utilizing different catalyst powders with a mass ranging from 20 to 75 mg [21]. The overall flow of gases (Ar, CO_2 and H_2) was limited to 12 mL/min and the tests were operated from 300 – 700 °C. It is noticeable that no CH_4 was detected in the product gas stream at these temperatures and CO formation already started at 400 °C. $Nd_{0.6}Ca_{0.4}Fe_{0.9}Co_{0.1}O_{3-\delta}$ was found to be the catalytically most active material [20,21].

The present study focuses on a comparison of different catalysts for the rWGS reaction within a quartz-glass reactor. An experimental test campaign with a commercially available nickel catalyst, two novel perovskite catalysts with differing loadings of active material, and the support material Al_2O_3 as a fourth catalyst is executed. In this study, the microreactor experiments performed by Lindenthal et al. are scaled up to laboratory size to analyze the influence of industry-relevant conditions, i.e. the use of shaped pellets (instead of powder) [21]. This work compares these four catalysts, based on the resulting product composition, with a variation of operation temperature (550 – 950 °C), pressure (1 – 8 bara) and gas hourly space velocity (GHSV, 8000 and 20 000 h^{-1}). Additionally, as the impact of pressure on the product composition was not investigated by Lindenthal et al., a more comprehensive understanding of the perovskite catalysts performance in the rWGS reaction is conducted [21]. The feed ratio of H_2:CO_2 is equal to 3:1 (without additional nitrogen dilution), which is adopted from the PtL simulations and a first experimental study described by Markowitsch [3,22,23]. The objective is to operate the rWGS reactor at low temperature, which positively affects the operating and investment costs due to less energy demand and lower requirements on the reactor design [24]. The application of perovskite catalysts is expected to suppress methane formation even at lower temperatures, and thereby facilitate their incorporation into reactors utilizing established technology. The experimentally determined product gas compositions are compared for each catalyst with the thermodynamic equilibrium to conclude whether a catalyst is suitable for the rWGS reaction or not.

2. Methodology

2.1. Thermodynamic considerations

The catalytic conversion of CO_2 and H_2 has been investigated theoretically in several studies [3,6,11–13]. The rWGS reaction is endothermic and is given in Equation 1 [10].

$$\mathrm{CO_2 + H_2 \leftrightarrow CO + H_2O} \qquad \Delta \mathrm{H_r^{298K}} = +41\ \mathrm{kJ/mol} \qquad \text{Equation 1}$$

Since the rWGS reaction (Equation 1) takes place under constant volume conditions, pressure is not expected to have an impact on the equilibrium conversion. However, all possible side reactions must be addressed, such as the methanation of CO (Equation 2) and CO_2 (Equation 3), dry reforming (Equation 4), the Bosch reaction (Equation 5), and the Boudouard reaction (Equation 6). Considering all these reactions, both temperature and pressure have an impact on the thermodynamic equilibrium [25]. The suppression of those side reactions can be achieved by either a high CO_2 concentration, a high H_2 concentration or the in-situ removal of water (reactor design) [26]. Additionally, undesired production of solid carbon (Equation 5, Equation 6 and Equation 7) needs to be suppressed to avoid catalyst deactivation [27]. To address all side reactions, the use of an over-stoichiometric feed of H_2 with a H_2:CO_2 ratio of 3:1 is favorable for the operation of the rWGS reaction, and additionally to provide a reasonable syngas quality for downstream processes which usually convert CO and H_2 in a ratio of 2:1 (e.g. Fischer-Tropsch synthesis [3]). Other oxygenates, such as dimethyl ether, alcohols, larger alkanes, which could also be produced as undesired side products, are not analyzed in this experimental investigation, since these compounds are produced in trace amounts, if any [28].

$$CO + 3H_2 \leftrightarrow CH_4 + H_2O \qquad \Delta H_r^{298K} = -206\ \mathrm{kJ/mol} \qquad \text{Equation 2}$$

$$CO_2 + 4H_2 \leftrightarrow CH_4 + 2H_2O \qquad \Delta H_r^{298K} = -165\ \mathrm{kJ/mol} \qquad \text{Equation 3}$$

$$CH_4 + CO_2 \leftrightarrow 2CO + 2H_2 \qquad \Delta H_r^{298K} = +247\ \mathrm{kJ/mol} \qquad \text{Equation 4}$$

$$CO_2 + 2H_2 \leftrightarrow C_{(s)} + 2H_2O \qquad \Delta H_r^{298K} = -91\ \mathrm{kJ/mol} \qquad \text{Equation 5}$$

$$2CO \leftrightarrow CO_2 + C_{(s)} \qquad \Delta H_r^{298K} = -172\ \mathrm{kJ/mol} \qquad \text{Equation 6}$$

$$CH_4 \leftrightarrow C_{(s)} + 2H_2 \qquad \Delta H_r^{298K} = +75\ \mathrm{kJ/mol} \qquad \text{Equation 7}$$

The selectivity S(CO) is defined in Equation 8 as the ratio of produced molar stream of CO to the converted molar stream of CO_2.

$$S(CO) = \frac{\dot{n}_{CO,out} - \dot{n}_{CO,in}}{\dot{n}_{CO_2,in} - \dot{n}_{CO_2,out}} \qquad \text{Equation 8}$$

The thermodynamic equilibrium is calculated using ASPEN Plus V12.1® [29], by minimizing the Gibbs free energy. In the simulation, all possible reactions are implemented in a Gibbs Reactor considering the species CO, CO_2, H_2, H_2O, CH_4 and solid carbon ($C_{(s)}$). The feed consists of the aforementioned binary mixture of H_2 and CO_2 with a H_2:CO_2 ratio of 3:1. In Figure 1, the simulated equilibrium is given for a temperature range between 300 and 1100 °C and pressures of 1, 10 and 30 bara. As depicted, CO selectivity is affected by the operating temperature and pressure. Temperatures below 800 °C lead to reduced CO production, but promote methane formation. This is further increased by elevated pressure (e.g., 30 bara), where methane formation also occurs at 950 °C and diminishes the CO selectivity significantly. Solid carbon formation is suppressed due to the over-stoichiometric feed gas composition.

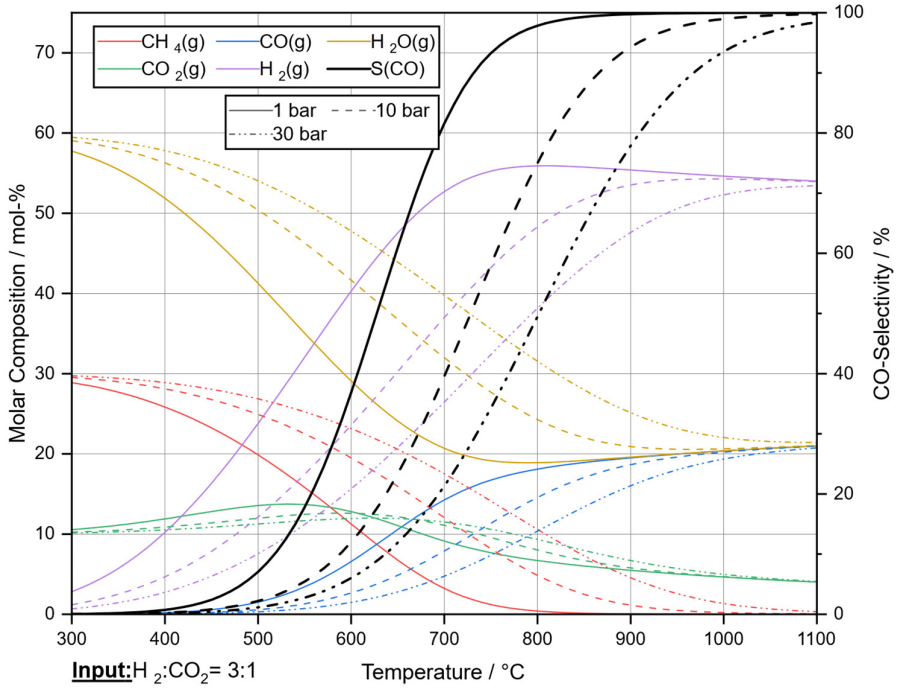

Figure 1: Thermodynamic equilibrium for a H_2:CO_2 feed ratio of 3:1, calculated for a temperature range from 300 - 1100 °C and pressures of 1, 10 and 30 bara

2.2. Experimental setup

The experimental setup used throughout this study consists of three sections, the quartz glass tube reactor, the furnace for the heat supply and the required auxiliary infrastructure. The P&ID scheme of the reactor setup is shown in Figure 2.

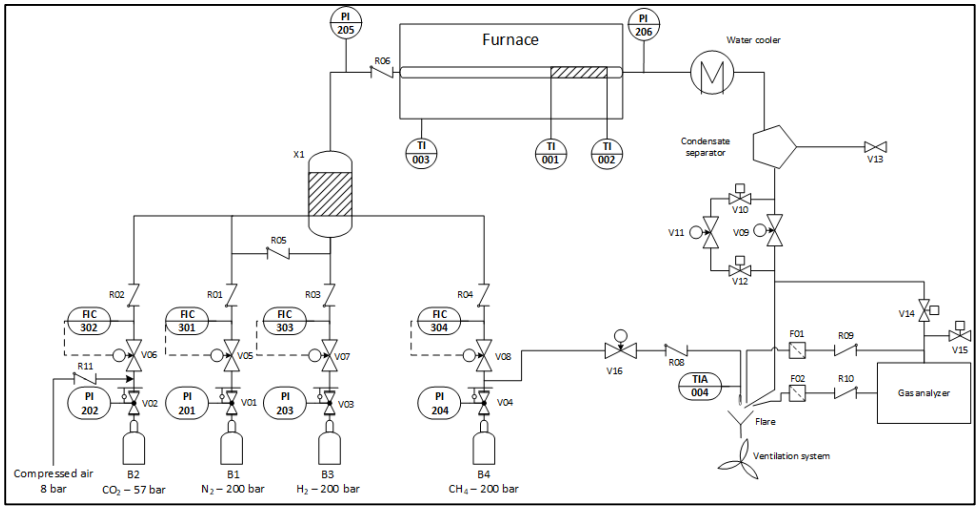

Figure 2: P&ID of the experimental reactor setup including the gas supply station, the furnace with integrated fix-bed-tube-reactor, gas analyzer and flare

The laboratory plant is supplied with highly purified gases from external gas bottles (CO_2, H_2, N_2) and a compressed air supply. Methane (CH_4) serves as the fuel source for the operation of the flare. Compressed air and nitrogen are used to dilute the input stream for catalyst activation procedures and to purge the reactor for stand-by mode. The mass flow controllers (Bronkhorst Deutschland Nord GmbH) installed for all gases allow a flow rate between 0.5 and 45 NL/min (FIC301 to FIC304). The gases are blended in a mixing station (X1). Normally, in the pre-heating tube the mixed gases are heated up to a maximum temperature of 350 °C prior to the quartz glass reactor inlet. During first test runs with a catalyst, already in the preheating zone at 350 °C (stainless steel tubes) methanation reaction (Equation 3) has been observed. Consequently, preheating was not used in the rWGS experiments described in this study and the feed gas was fed directly to the quartz glass reactor. Since the preheating step is omitted, the feed gas volume flow is also limited (GHSV < 20 000 h^{-1}). Blank tests were carried out and no methane formation could be detected in the blank set-up.

The quartz glass tube reactor has a total length of 1500 mm, an inner diameter of 15 mm and a wall thickness of 2.5 mm. The tube is crimp-connected through a perfluoroelastomeric (FFKM) seal with stainless-steel flanges that connect the gas inlet and outlet via 6 mm stainless steel tubing. The glass is fixed and has been tested up to an operating pressure of 8 bara for temperatures between 550 and 650 °C, and at 6 bara for 750, 850 and 950 °C. The quartz glass tube is positioned on ceramic supports of the tube furnace, which is temperature controlled by TI3 and guarantees a constant temperature over a defined heating zone of 550 mm. The catalyst fixed bed has a total length of 200 mm and is placed at the end of the furnace. To achieve elevated temperatures in the catalyst bed, the front zone in the furnace is used as a preheating unit as shown in Figure 3. Additionally, inert balls placed upstream of the catalyst bed guarantee sufficient heat transfer within the furnace. The inert balls positioned behind the catalyst bed are used for fixation, preventing the catalyst material from being blown out of the reactor. For measurement of the catalyst inlet and outlet temperature, Figure 3 also shows the axial position of two thermocouples (TI1 and TI2) placed in the bed. Pressure indicators (PI205 and PI206) in front of and behind the reactor allow the monitoring of the pressure drop over the reactor (catalyst bed and inert balls). For the described experimental set up, a contact time with the catalyst of at least 180 ms (GHSV < 20 000 h^{-1}) is achieved.

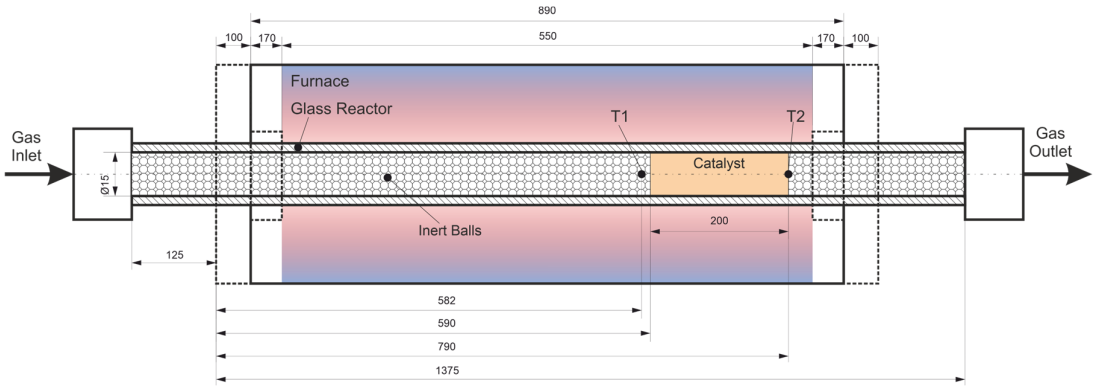

Figure 3: Setup of the quartz glass tube reactor in the furnace and position of the catalyst bed including thermocouples (not to scale)

The product gas contains steam which is condensed by a water-cooler and separated downstream of the rWGS reactor. To adjust the pressure in the reactor, a control valve (V11 in Figure 2) is used downstream of the gas cooler. The entire test rig is controlled and visualized by the software Labview 2019. A gas analyzer (Type ABB AO2020, ABB AG) is implemented in the product gas stream to obtain the online gas composition via ND-IR (CO_2, CO, CH_4) and thermal conductivity analyzer (H_2:N_2 ratio). The off-gas is combusted in a flare (stable CH_4 flame) and released to the ventilation system.

2.3. Catalyst description

Four different catalyst materials are used for the experimental tests. The first catalyst is a commercially available nickel-based catalyst, the second and third are based on a proprietary perovskite oxide catalyst mixed with different amounts of Al_2O_3 [20,21,30] and the last comprises solely the support material Al_2O_3. The compositions and geometric forms are given in Table 1.

Table 1: Catalysts used for experimental tests

Catalyst number	Catalyst composition	Catalyst geometry
Catalyst 1 - Nickel	Commercial nickel-catalyst	Cylinders 3.2 mm diameter, 3.2 mm height
Catalyst 2 - Perovskite 80/20	Perovskite catalyst, 20 wt.-% Al_2O_3	Pellets 6.0 mm diameter, 1.4 mm height
Catalyst 3 - Perovskite 50/50	Perovskite catalyst, 50 wt.-% Al_2O_3	Pellets 6.0 mm diameter, 2.2 mm height
Catalyst 4 - Al_2O_3	Aluminum oxide Al_2O_3	Pellets 5.8 mm diameter, 4.2 mm height

The perovskite oxide used for catalyst 2 and 3 was previously found to be a promising material for rWGS [21]. It has the composition $Nd_{0.6}Ca_{0.4}Fe_{0.9}Co_{0.1}O_{3-\delta}$ (resulting in a Co-content of ca. 3 wt.-%) and exhibits the property of exsolution. During this process, upon reductive treatment, the Co is selectively reduced and migrates to the surface, where Co-rich nanoparticles well anchored in the support material are formed. These nanoparticles are highly active for rWGS.

For the use in the reactor setup described in section 2.2., the synthesized perovskite powder (prepared as described in [21]) was tableted. For this, it was mixed with boehmite (γ-AlO(OH), provided by Sasol) acting as a binder, pressed into shape and sintered (which transforms the boehmite to Al_2O_3). The ratio of perovskite to boehmite was varied between catalyst 2 and 3 (cf. Table 1). Catalyst 4 was produced in the same way from pure boehmite.

3. Experimental tests

Before starting the series of experiments, the catalysts need to be activated. For this purpose, the manufacturer has defined an activation procedure for catalyst 1. Similarly, a procedure has been inferred for catalysts 2 and 3, based on previous results [30].

- Nickel-catalyst (catalyst 1): After placing the catalyst into the reactor, the system is flushed with nitrogen (10 NL/min) to remove all undesired gases (especially O_2). The reactor is heated to a temperature of 550 °C. Once the temperature is reached, the gas composition is gradually changed from 100 vol.-% nitrogen to 100 vol.-% hydrogen within 20 minutes. The catalyst is then activated at 550 °C for 1.5 h at a constant temperature and ambient pressure.
- Perovskite and Al_2O_3-catalysts (catalyst 2 to 4): The catalysts are flushed with air (5 NL/min) for 0.5 h up to 420 °C. Once the temperature of 420 °C is reached, the air is replaced by nitrogen (5 NL/min) for 10 minutes and then the catalyst is activated for 2 h with a gas flow of 10 NL/min and a composition of N_2:H_2 of 9.5:0.5 (5 vol.-% H_2 in N_2) at 625 °C and ambient pressure. To enable a direct and meaningful comparison, the Al_2O_3 material is also activated, although no active metals are placed on the material surface.

The temperature is varied for the nickel (catalyst 1) and Al_2O_3 catalyst (catalyst 4) from 550 – 950 °C, and for the perovskite catalysts (catalysts 2 and 3) from 550 – 850 °C, according to instructions of the manufacturers. The temperature is increased stepwise by 100 °C. Due to the flange connections used, the maximum pressure is set to 8 bara for the experiments with temperatures between 550 and 650 °C, and 6 bara for higher temperatures. Higher pressures are not possible with the applied set-up, due to the limitation of the quartz glass material. Operating pressures of 1, 3, 6 and 8 bara are used for the catalyst tests.

The impact of the GHSV on the product composition is also important to obtain a reactor design know-how, especially for the required catalyst bed length. The catalysts are operated at GHSV values of 8000 and 20 000 h^{-1} which corresponds to 4.71 NL/min and 11.78 NL/min, respectively, for the applied catalyst bed length of 200 mm. The temperature within the catalyst bed is strongly dependent on the volume flow of the gases. Therefore, the operation with GHSV values higher than 20 000 h^{-1} are not feasible, since heat transfer to the reactor is limited, and for higher GHSV the achieved temperature level is not sufficient.

The influence of temperature, pressure and GHSV is investigated for all catalysts (cf. Table 1). Based on the considerations for the main influencing operation parameters, the experimental plan for the respective catalysts is listed in Table 2.

Table 2: Design of experiments for a H_2:CO_2 inlet ratio of 3:1

Catalyst name	Temperature in °C	Pressure in bar_a	GHSV in h^{-1}
Catalyst 1 – Nickel	550, 650, 750, 850, 950	1, 3 and 6 (550-950 °C) 8 (550 and 650 °C)	8000, 20 000
Catalyst 2 – Perovskite 80/20	550, 650, 750, 850	1, 3 and 6 (550-850 °C) 8 (550 and 650 °C)	8000, 20 000
Catalyst 3 – Perovskite 50/50	550, 650, 750, 850	1, 3 and 6 (550-850 °C) 8 (550 and 650 °C)	8000, 20 000
Catalyst 4 – Al_2O_3	550, 650, 750, 850, 950	1, 3 and 6 (550-950 °C) 8 (550 and 650 °C)	8000, 20 000

4. Results and discussion

In this chapter, the results of the experimental tests of the four catalysts are presented and the influence of temperature, pressure and GHSV on the product composition are compared with the thermodynamic equilibrium. A detailed description of the mass and atom balance (inclusive error calculation) is provided in the supplementary material. Furthermore, a characterization of the used perovskite catalysts was performed, and the results are discussed in the supplementary material.

4.1. Results of catalyst 1 – nickel based

The experimental results obtained with catalyst 1 are shown in Figure 4, where the dry product gas composition is depicted as data points, and the corresponding theoretical thermodynamic composition as lines. Figure 4 summarizes the results obtained for GHSV 8000 h^{-1}, temperatures of 550, 650, 750, 850, and 950 °C, and pressures of 1, 3, 6 and 8 bara.

The methane content exhibits a noticeable increase with decreasing temperature (< 750 °C) and rising pressure. This correlation was already predicted by the thermodynamic analysis conducted prior to the experiments. Moreover, it is worth mentioning that the reaction approaches thermodynamic equilibrium when operating at 650 °C (or higher) and a GHSV of 8000 h^{-1}, but visibly

the convergence decreases at 550 °C. At 650 °C, convergence is also less complete with increasing pressure. The formation of methane is increasing with higher pressures for all temperatures. However, at 550 °C a significant lower CH_4 formation is observed as predicted by the thermodynamic equilibrium. Consequently, CO is overproduced and exceeds the equilibrium line. This could be attributed to the GHSV, because the increase of GHSV (Figure 5) results in lower methane formation and in increasing CO formation for all operating pressures (1, 6 and 8 bara) and temperatures of 550 and 650 °C. At these temperatures, the equilibrium is not fully reached, but there is a noticeable decrease in methane content observed with higher GHSV. The suppression of methane formation at higher GHSV values is a clear indication for the slower kinetics of this reaction compared to the obviously fast CO formation by the rWGS reaction. Methanation is slower due to the two-step reaction mechanism of CO_2 to CH_4 with an intermediate CO formation in the rWGS reaction [31]. As the residence time is not sufficient for full conversion, the faster CO formation is favored, which is evident by the higher CO concentration in the product gas at GHSV values of 20 000 h^{-1}. However, where no methane is formed, such as at temperatures of 950 °C, the lower resident times of the gas in the catalyst bed do not have an influence. Thermodynamic equilibrium is then reached for both GHSVs. With increasing temperature, the methane production diminishes from a thermodynamic perspective, and the kinetic of CO formation in the rWGS reaction is so fast that no influence of GHSV can be observed under the investigated conditions.

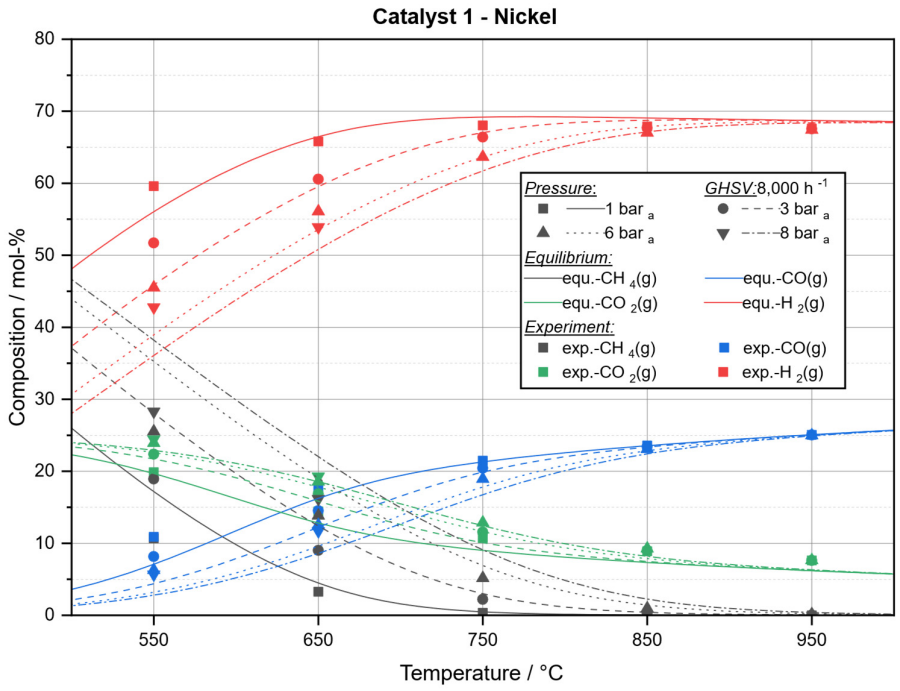

Figure 4: Product composition and thermodynamic equilibrium in a temperature range of 550 to 950 °C and 1, 3, 6 bara, and additional for 550 and 650 °C at 8 bara for catalyst 1 (Nickel-based) and GHSV 8000 h^{-1}

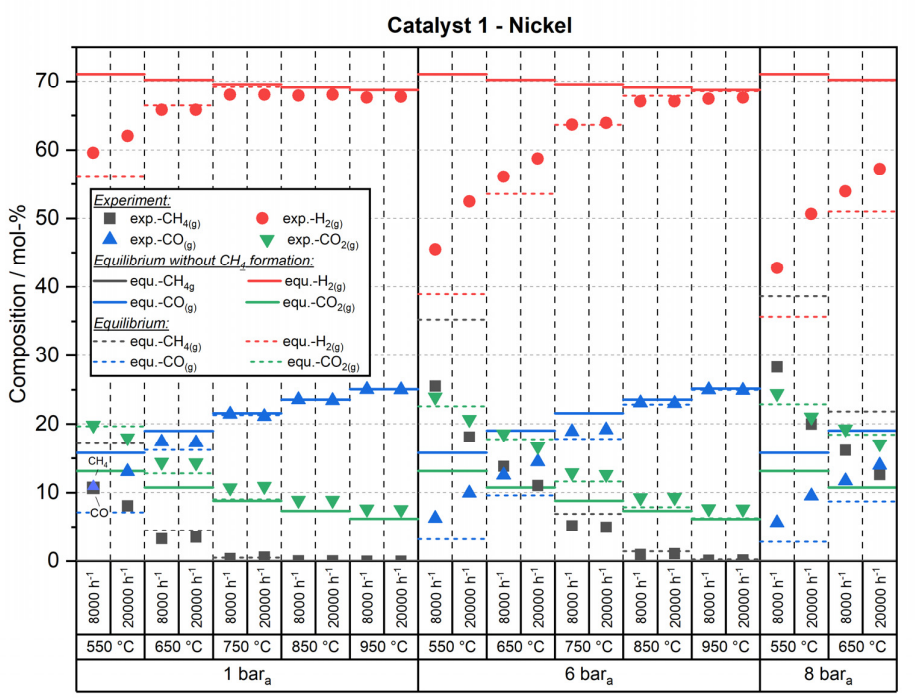

Figure 5: Product composition and thermodynamic equilibrium for GHSVs 8000 and 20 000 h^{-1} at temperatures of 550, 650, 750, 850 and 950 °C and 1, 6 and 8 bara for catalyst 1 (nickel-based)

For catalyst 1, it can be concluded that the reverse water-gas shift reaction tends to approach thermodynamic equilibrium for all investigated operating conditions, where no methane is produced (in particular high temperatures). Methane production increases at lower temperature and elevated pressure which is attributed to thermodynamics of the methane formation reaction. Therefore, CO formation exceeding equilibrium is comprehensible in the temperature range between 550 and 750 °C. The nickel catalyst is highly active for rWGS reaction at high temperatures (equilibrium at GHSV 20 000 h^{-1}), but not selective if CH_4 formation is thermodynamically favored. However, higher gas velocities, especially at lower temperatures and increasing pressure, suppress methane formation while favoring the rWGS reaction, due to the slow kinetics of methane formation.

4.2. Results of catalyst 2 – perovskite catalyst 80/20

The product composition for the experiments with catalyst 2 is depicted in Figure 6a and Figure 6b. Methane formation is almost completely suppressed, even at the temperature of 550 °C, where a methane fraction between 17.5 and 38 vol.-% is thermodynamically expected. In Figure 6b, CH_4 formation is neglected in the thermodynamic equilibrium calculation (Gibbs reactor with suppressed methane formation, no pressure dependency). However, the experimental results show that the increase in pressure from 1 to 3, 6 and 8 bara promotes the CO formation in a first step. At temperatures of 750 and 850 °C, the thermodynamic equilibrium without CH_4 formation is reached. The experiments confirm that methane formation is basically negligible here (< 1 vol.-%). At lower temperatures, CO formation is enhanced when the pressure is elevated to 3 bara at constant temperature (e.g., 550 °C), and remains stable with further increasing pressure just below equilibrium (about 13.8 vol.-%). Methane formation is recognizable at this point, particularly when exceeding a pressure of 6 bara. Here, methane formation rises significantly from 0 and 0.2 vol.-% at 1 and 3 bara to 1.2 and 2.7 vol.-% at 6 and 8 bara, respectively. Therefore, the optimum operating conditions for this catalyst are in a temperature range between 550 and 650 °C up to a pressure of

6 bara. At these conditions, the CH_4 formation is almost completely suppressed and the experimental results can be sufficiently described as a sole rWGS reaction.

Overall, the initial experimental results are promising as the suppression of methane formation leads to a relatively high concentration of hydrogen in the product gas, since less hydrogen is consumed for undesired methane formation. It is also encouraging that the CO formation at temperatures below 650 °C is close to the thermodynamic equilibrium of the rWGS reaction. Applying higher pressure up to 6 bara has a slight positive effect on CO formation at a temperature of 550 °C (10.8 for 1 bara and 13.9 mol-% for 6 and 8 bara), which can be attributed to the increasing reaction rate with higher partial pressure of the reactants.

One drawback is that higher pressure also slightly promotes the formation of methane. The pressure level does not significantly influence the conversion to CO at higher temperature levels (750 and 850 °C), as methane is not produced in these operating modes (thermodynamically lower methane formation at higher temperature) and higher temperature increases the reaction rate of CO formation according to the Arrhenius law. The thermodynamic equilibrium is reached in the experiments with temperatures above 650°C. This finding confirms that the assumption of a Gibbs reactor is feasible in process simulations with catalyst 2, where the small amount of formed methane can be neglected or treated as an inert gas (e.g., process chain optimization, where kinetics are not important). In these cases, the rWGS reaction can be simulated as a thermodynamically limited reaction, and needs no kinetic equation for this type of catalyst.

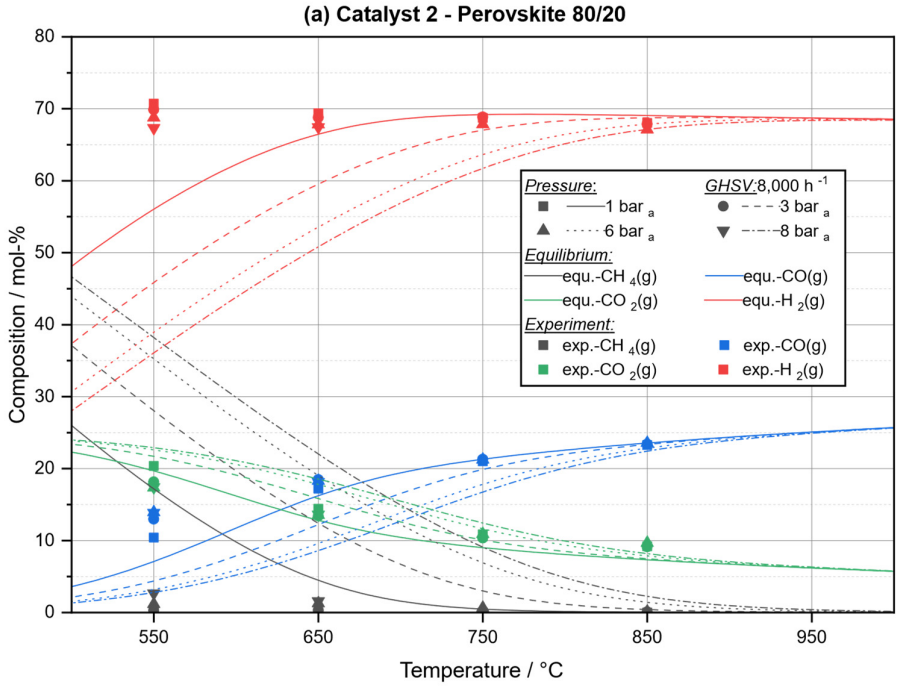

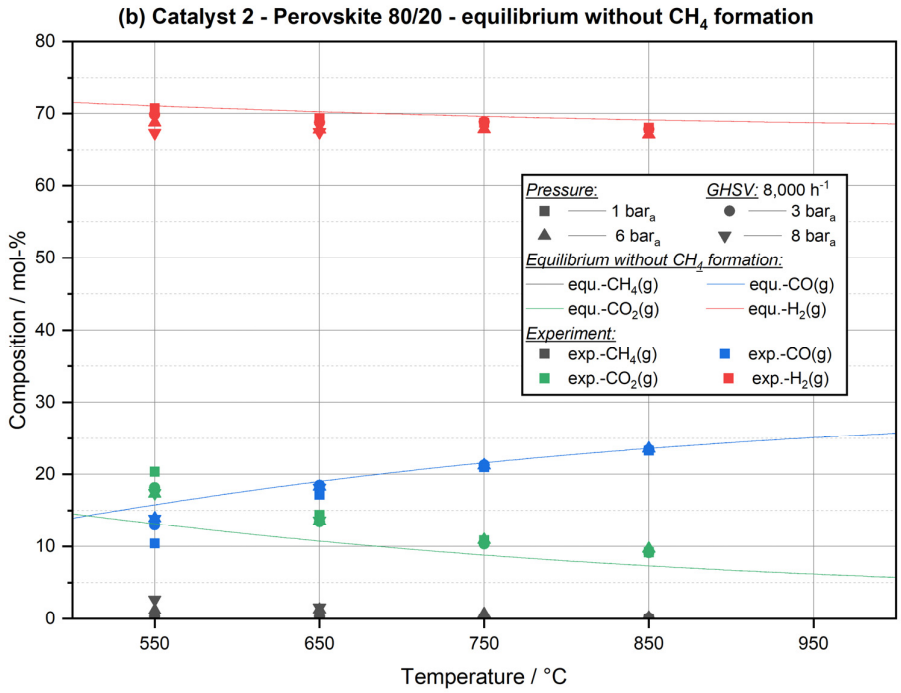

Figure 6: Product composition and thermodynamic equilibrium (a) with and (b) without consideration of methane formation in a temperature range of 550 to 850 °C and 1, 3, 6 bara, and additional for 550 and 650 °C at 8 bara for catalyst 2 (perovskite catalyst 80/20) and GHSV 8000 h^{-1}

The GHSV significantly influences the gas composition of catalyst 2 (illustrated in Figure 7). Higher GHSV values result in a decrease in CO formation (e.g., 550 °C, 1 bara: 10.4 mol-% at 8000 h^{-1} to 7.7 mol-% at 20 000 h^{-1}). This trend is also noticeable in the methane formation, as it slightly decreases at 8 bara with higher GHSV and low temperature (2.7 mol-% at 550 °C and 8000 h^{-1} to 1.9 mol-% at 550 °C and 20 000 h^{-1}). However, the thermodynamic equilibrium is achieved for GHSV 8000 h^{-1} and temperatures of 750 and 850 °C and all investigated pressures.

There is a conspicuous deviation in carbon monoxide (CO) formation from the thermodynamic predictions at lower temperatures and both gas hourly space velocity (GHSV) values. This deviation could be attributed to kinetics, as the reaction rate increases with higher temperatures, reflecting the influence of temperature on the reaction rate constant. While the selectivity of CO of the catalyst is remarkable high at all tested conditions, the reduced conversion of CO_2 to CO at higher GHSV values indicates that the activity of the catalyst can still be optimized.

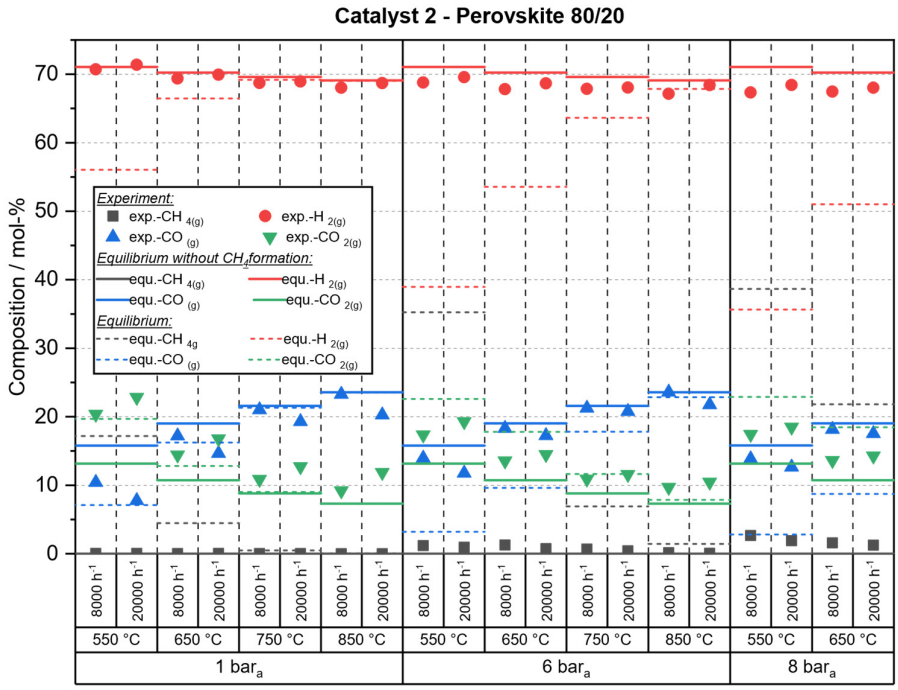

Figure 7: Product composition and thermodynamic equilibrium (with and without consideration of methane formation) for different GHSV 8000 and 20 000 h^{-1}, at temperatures of 550, 650, 750 and 850 °C and 1, 6 and 8 bara for catalyst 2 (perovskite catalyst 80/20)

4.3. Results of catalyst 3 – perovskite catalyst 50/50

The evaluation of the results for catalyst 3 illustrates some minor differences compared to catalyst 2. Figure 8 compares the dry product gas composition with the thermodynamic equilibrium with (Figure 8a) and without (Figure 8b) consideration of CH_4 formation. As can be observed in Figure 8a, the composition of the dry product does not align with the thermodynamic equilibrium, including CH_4 formation. The methane formation is overestimated for the temperatures 550 and 650 °C and all investigated pressures. It becomes evident that the thermodynamic equilibrium without consideration of CH_4 formation is achieved for 750 and 850 °C, where also thermodynamically no methane formation occurs. For lower temperatures of 550 and 650 °C, the equilibrium is approached with elevated pressure, but methane formation is also favored at higher pressure. At a moderate temperature of 550 °C the rate of CO formation is reduced according to Arrhenius' law. However, higher partial pressures of CO_2 and H_2 increase the reaction rate of CO formation, bringing it closer to equilibrium (without CH_4 formation). This becomes evident in Figure 8b, because thermodynamic equilibrium of CO formation is reached at 650°C at 6 bara compared to 750°C at 1 bara. The maximum CH_4 content with 2.4 vol.-% is obtained for a pressure of 8 bara, an operating temperature of 550 °C and GHSV of 8000 h^{-1}. A comparison of Figure 8a and 8b shows that the assumption of neglecting methane formation is approximately valid, since the formation of CH_4 is low (< 2.4 vol.-%) and the product composition follows the trend shown in Figure 8b.

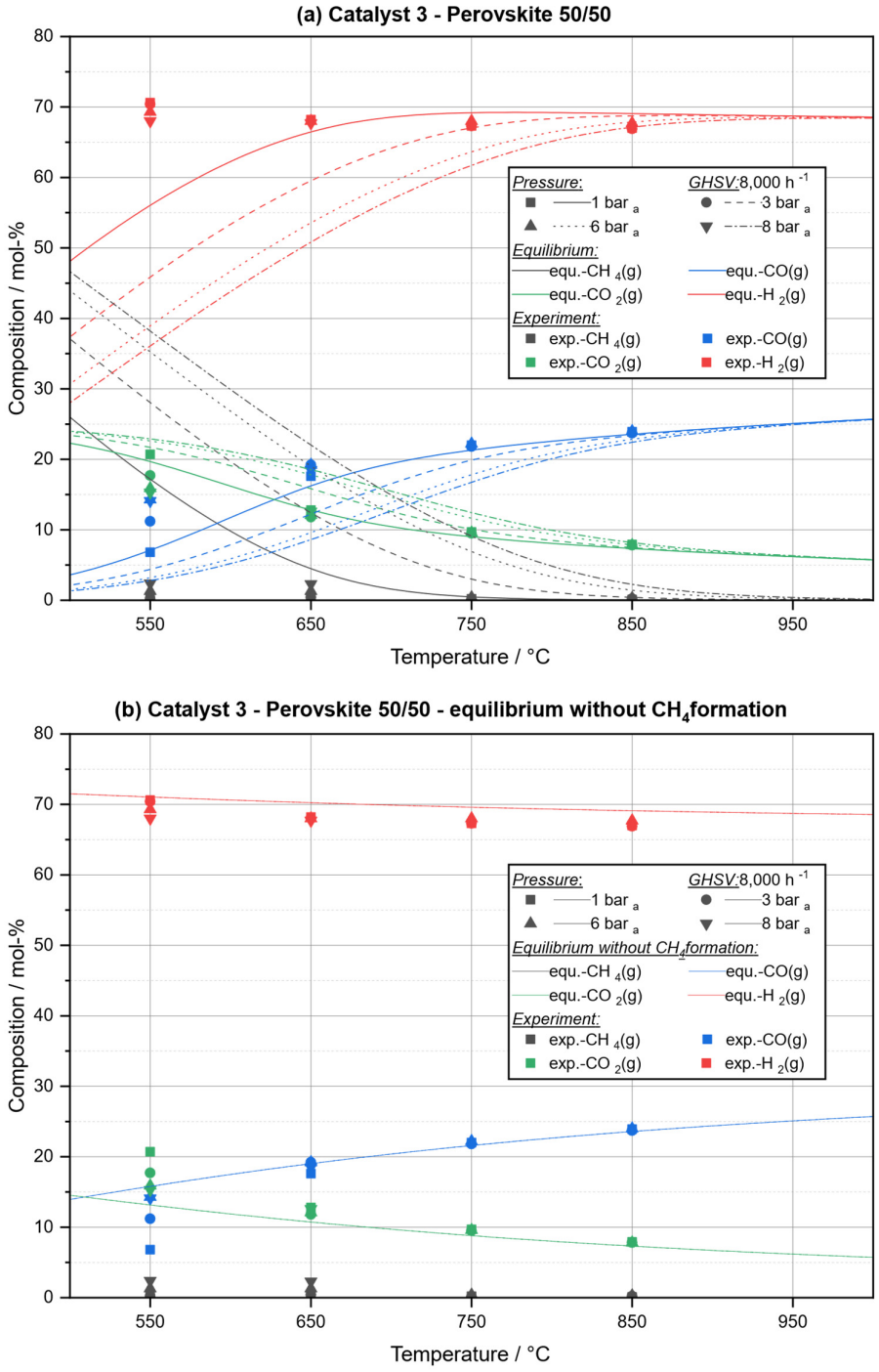

Figure 8: Product composition and thermodynamic equilibrium (a) with and (b) without consideration of methane formation in a temperature range of 550 to 850 °C and 1, 3, 6 bara, and additional for 550 and 650 °C at 8 bara for catalyst 3 (perovskite catalyst 50/50) and GHSV 8000 h^{-1}

The influence of GHSV (Figure 9) is also similar as observed with catalyst 2. With increasing GHSV values, CH_4 and CO formation decreases. However, the influence of GHSV decreases with higher pressures, probably due to the higher reaction rate related to an increased rate constant at higher temperatures. Catalyst 3 shows a stronger dependence on the GHSV than catalyst 2, indicated by a significant decrease of the CO formation at lower pressures and temperatures. For example, the

thermodynamic equilibrium is not reached for a GHSV value of 20 000 h^{-1} at 1 bara and lower than 850 °C, at 6 bara lower than 750 °C, and for 8 bara, it is not reached for both temperatures (550 and 650 °C). This may be caused by the different catalyst composition (higher proportion of Al_2O_3), which also means that the catalytically active surface is lower than for catalyst 2. Lower catalytic surface at higher GHSVs leads to a lower probability of contact between active centers and gas molecules. Nevertheless, thermodynamic equilibrium is reached for both GHSV values at 1 bara and 850 °C and at 6 bara already with 750 °C.

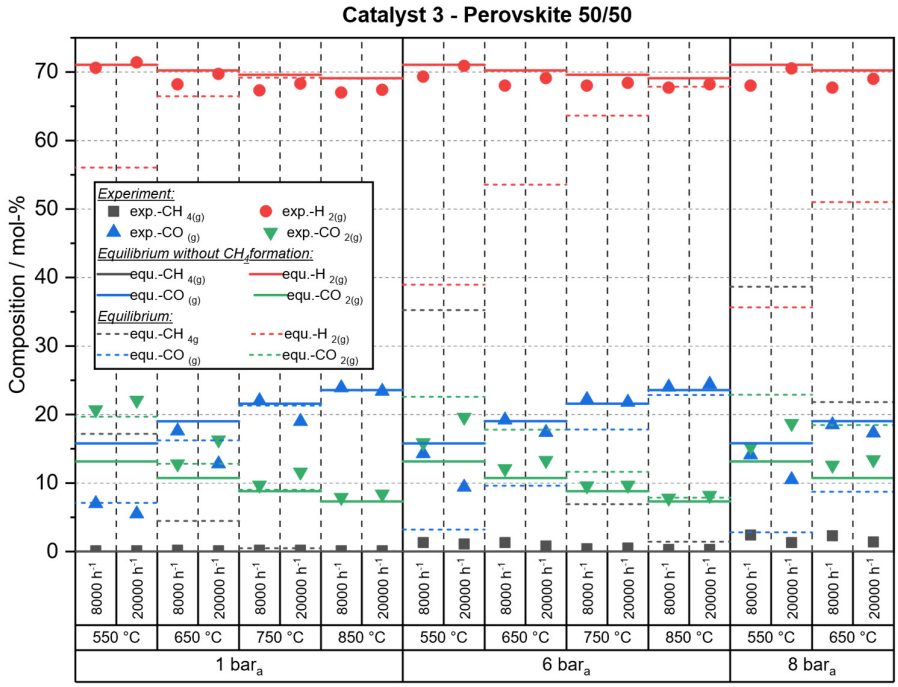

Figure 9: Product composition and thermodynamic equilibrium for GHSV 8000 and 20 000 h^{-1} at temperatures of 550, 650, 750 and 850 °C and 1, 6 and 8 bara for catalyst 3 (perovskite catalyst 50/50)

4.4. Results of catalyst 4 – aluminum oxide

Catalyst 4 reveals a completely different reaction behavior compared to the three other catalysts 1, 2 and 3. The catalyst based on aluminum oxide is usually used as a support material [32]. Figure 10a again depicts the comparison of the experimentally determined gas composition with the thermodynamic equilibrium for the case with and Figure 10b for the case without methane formation. It is remarkable that no methane is produced at any of the operating temperatures and pressures across all experimental test points. Particularly and in contrast to the nickel catalyst, low temperature and high pressure have no impact on methane formation. As expected, catalyst 4 has no activity for methane formation since catalytically active materials promoting this reaction are lacking. Increased CO formation with higher pressure is also noticeable with this catalyst, but only weakly at 550 °C. This means that the activation energy for the reaction is not sufficiently reduced by the catalyst at low temperatures and therefore there is insufficient conversion. The production of CO becomes more pronounced at higher temperatures. The support material Al_2O_3 is observed as an active material for rWGS, which could be caused by the ability of CO_2 adsorption described in literature [33]. The thermodynamic equilibrium is closely reached for a temperature of 950 °C and

pressure of 6 bara. However, the CO production starts already at temperatures of 550 °C (1.4 vol.-% at 1 bara) and 650 °C (3.2 vol.-% at 1 bara), and significantly increases at elevated pressures and temperatures, e.g. up to 23.6 vol.-% at 950 °C and 6 bara.

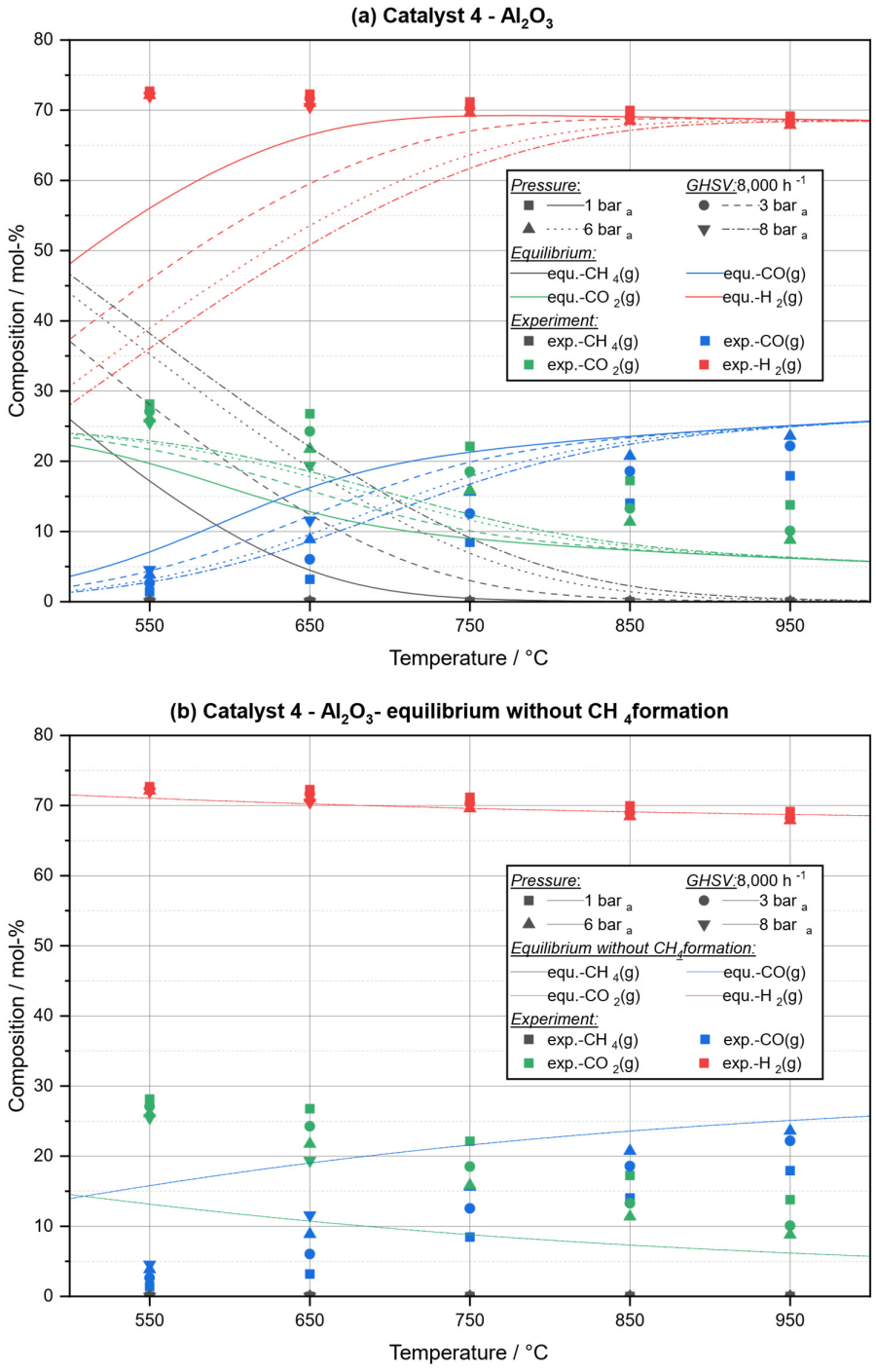

Figure 10: Product composition and thermodynamic equilibrium (a) with and (b) without consideration of methane formation in a temperature range of 550 to 950 °C and 1, 3, 6 bara, and additional for 550 and 650 °C at 8 bara for catalyst 4 (aluminum oxide) and GHSV 8000 h^{-1}

The GHSV has a more pronounced impact on the CO formation compared to all other catalysts, as it is shown for catalyst 4 in Figure 11. On the one hand, higher GHSV reduces the CO production, but,

on the other hand, throughout all tests and independent of the GHSV, no methane is formed. Catalyst 4 is very selective for rWGS, however, at the same time not very active. Thus, shorter residence times with higher GHSV reduce the conversion drastically due to the non-satisfying promotion of the kinetics. The thermodynamic equilibrium is almost reached only at higher pressures (> 6 bara), 950 °C and a GHSV of 8000 h^{-1}.

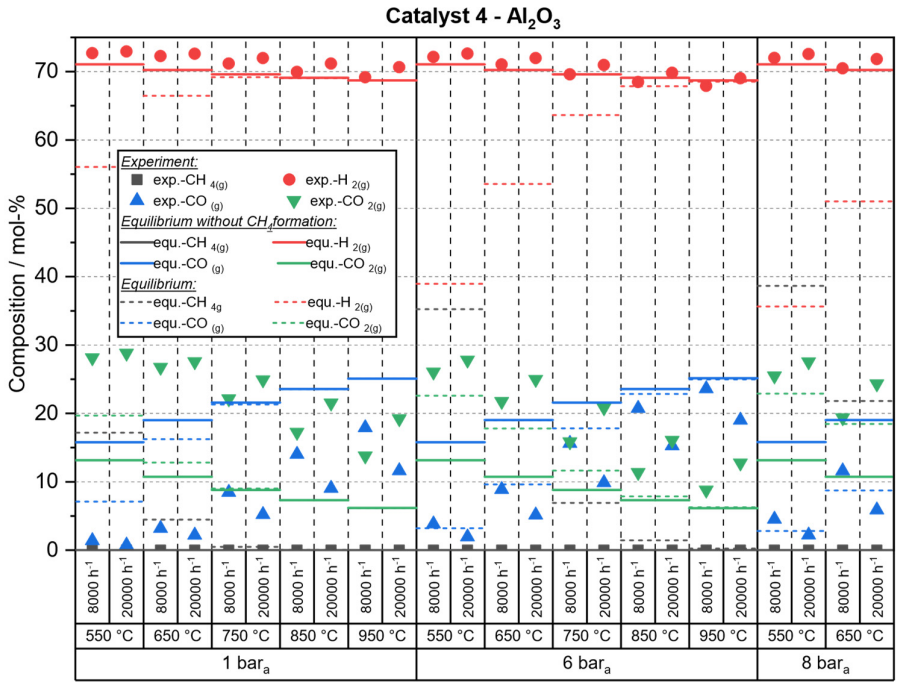

Figure 11: Product composition and thermodynamic equilibrium for different GHSV at temperatures of 550, 650, 750, 850 and 950 °C and 1, 6 and 8 bara for catalyst 4 (aluminum oxide)

4.5. Summary and comparison of the four catalysts used in this study

5. Conclusion and outlook

For the utilization of an rWGS reactor, it is evident that the catalyst selection, process design and the optimization of the operation conditions are of high importance. The conventional nickel catalyst requires high temperatures and low pressures for the suppression of methane formation. Consequently, the requirements for reactor design are demanding particularly in terms of material selection, but also for the heat management. The undesired methane formation at lower temperatures and higher pressures leads to increased hydrogen demand for an unwanted by-product, thereby reducing the overall efficiency of the process chain further. It is also crucial to consider how downstream processes (such as Fischer-Tropsch or methanol synthesis) are affected by the undesired components (specifically methane) and whether additional purification efforts are imposed. The evaluations for the nickel catalyst performed in this study show that a minimal amount of CH_4 is produced at operating conditions of 950 °C and 1 to 6 bara, which brings the experimental results almost in line with the theoretical thermodynamic equilibrium. This justifies the assumption of a Gibbs reactor used for many simulations in literature [3,5,6,9]. Additionally, higher values for GHSV have a negative influence on methane formation, which is advantageous in these applications.

The utilization of the novel perovskite catalysts enables a fundamentally simpler process design compared to catalyst 1 (nickel-based). When using the perovskite catalysts, the rWGS reaction occurs

dominantly already at lower temperatures around 550 °C, however, due to the thermodynamic equilibrium, the maximum possible CO_2 conversion is smaller at this temperature. The formation of methane increases with growing pressure for both perovskite catalysts (catalyst 2 and 3) for temperatures of 550 and 650 °C, but the content in the product gas is always significantly smaller compared to the nickel catalyst (catalyst 1). The CO concentration in the product gas remains constant independent from the operating pressure, thus following solely the rWGS reaction due to the suppression of possible side reactions. Reducing the catalyst contact time, indicated by a higher GHSV, negatively impacts CO production and subsequently reduces CO_2 conversion at lower temperatures. This suggests that the reaction kinetics are slow and that these catalysts have potential for improvement. Additionally, enhancing the geometry and surface area of catalysts 2 and 3 could increase the contact probability between the catalytically active phases and gas molecules, thereby improving their performance.

The Al_2O_3 material is also found to be catalytically active for the rWGS reaction at high temperature. With increasing temperature and pressure, the CO product concentration approaches thermodynamic equilibrium. It is almost achieved at 950 °C and 6 bara. Consequently, at these high temperatures, specially prepared nickel catalysts could be omitted and the better available and lower cost Al_2O_3 could be used. Increasing GHSV has a significant negative effect on the CO formation for this catalyst, but CH_4 formation remains suppressed for all operating points, independent of pressure, temperature or GHSV.

In the first tests using the pre-heating tube, methane was produced due to the catalytic activity of the stainless-steel tube at temperatures of 350 °C. The experiments revealed that CH_4 in the feed gas is not converted to CO and H_2 by the perovskite catalysts and Al_2O_3, but steam reforming occurs on the nickel catalyst. Therefore, CH_4 can be treated as an unreactive (inert) gas for catalysts 2, 3 and 4, which means that CH_4 fed to the reactor is neither produced (or only small amounts) nor converted. This is a very important insight, as CH_4 and higher gaseous hydrocarbons are usually recycled to the rWGS reactor from downstream processes like the Fischer Tropsch tail gas stream [3,6,9]. In the case of using these novel perovskite catalysts, the process design needs to be adjusted to avoid CH_4 in the feed stream to the rWGS reactor, for example by implementing a reformer in the recycle.

Further to the presented results, subsequent experiments will be designed to determine the kinetics of the rWGS reaction with the tested catalysts, compare them with existing literature, and simulate the corresponding plug flow reactor in ASPEN Plus. Moreover, further research will be dedicated to the production of perovskite catalysts, including surface enhancement and improved catalytic activity to obtain thermodynamic equilibrium also with higher GHSV. On the process operation side, the next step will involve adapting the existing experimental setup to target pressures up to 15 bara to obtain additional experimental results for both catalyst types at elevated pressures. Higher pressures are of particular interest, since industrial plants will be operated most likely with pressures around 15 – 20 bara. Furthermore, higher pressures promote undesired side reactions. In addition, catalyst performance tests should be conducted over an extended period of time to analyze the thermal and performance stability of the catalyst material. These investigations will also have a higher impact on understanding catalyst behavior and provide extensive experience for the industrial application of the rWGS reaction.

6. Highlights (max. 85 characters incl. spaces)

- Comparison of nickel, perovskite and Al_2O_3 catalysts for rWGS reaction
- Quartz-glass reactor setup for temperatures up to 950 °C and pressures up to 8 bara
- Impact of operating conditions on CO and CH_4 formation for four catalysts
- Identification of optimum operation conditions to minimize CH_4 and maximize CO in product gas

7. Declaration of competing interest

The authors declare that the research was conducted in the absence of any commercial or financial relationships that could be construed as a potential conflict of interest.

8. Authors contribution

C. Markowitsch: Conceptualization, Project administration, Methodology, Software, Evaluation, Investigation, Validation, Roles/Writing – original draft; Writing – review & editing

M. Andritz: Investigation, Writing – review & editing

T. Cotter: Investigation, Writing – review & editing

H. Drexler: Investigation, Writing – review & editing

L. Lindenthal: Investigation, Writing – review & editing

C. Rameshan: Resources, Writing – review & editing

M. Lehner: Conceptualization, Methodology, Evaluation, Resources, Validation, Writing – review & editing

9. Acknowledgements

We acknowledge Sasol for providing us with the boehmite material used in the catalyst preparation. This project has received funding from the European Research Council (ERC) under the European Union's Horizon Europe research and innovation program (grant agreement n° 101068557/ERC-proof of Concept Grant TUCAS-CO2).

10.Abbreviations

ND-IR	Nondispersive infrared sensor
FT	Fischer-Tropsch
FTS	Fischer-Tropsch synthesis
GHSV	Gas hourly space velocity [h^{-1}]
IPCC	International Panel on Climate Change
PtL	Power-to-liquid
rWGS	reverse water-gas shift
S(CO)	Selectivity of CO [-]
S(CH_4)	Selectivity of CH_4 [-]

11. References

[1] IPCC. Climate Change 2023: AR6 Synthesis Report; 2023.

[2] Climate Action. Übereinkommen von Paris. [February 02, 2022]; Available from: https://ec.europa.eu/clima/eu-action/international-action-climate-change/climate-negotiations/paris-agreement_de.

[3] Markowitsch C, Lehner M, Maly M. Evaluation of process structures and reactor technologies of an integrated power-to-liquid plant at a cement factory. Journal of CO2 Utilization 2023;70:102449.

[4] König DH. Techno-ökonomische Prozessbewertung der Herstellung synthetischen Flugturbinentreibstoffes aus CO2 und H2. Dissertation. Stuttgart; 2016.

[5] Albrecht FG, König DH, Baucks N, Dietrich R-U. A standardized methodology for the techno-economic evaluation of alternative fuels – A case study. Fuel 2017;194:511–26.

[6] Adelung S, Maier S, Dietrich R-U. Impact of the reverse water-gas shift operating conditions on the Power-to-Liquid process efficiency. Sustainable Energy Technologies and Assessments 2021;43:100897.

[7] Maitlis PM, Klerk A de. Greener Fischer-Tropsch processes for fuels and feedstocks. 1st ed. Weinheim: Wiley-VCH; 2013.

[8] González-Castaño M, Dorneanu B, Arellano-García H. The reverse water gas shift reaction: a process systems engineering perspective. React. Chem. Eng. 2021;6(6):954–76.

[9] König DH, Freiberg M, Dietrich R-U, Wörner A. Techno-economic study of the storage of fluctuating renewable energy in liquid hydrocarbons. Fuel 2015;159:289–97.

[10] Markowitsch C, Lehner M, Kitzweger J, Haider W, Ivanovici S, Unfried M et al. [Conference EnInnov 2022 TU Graz] C2PAT - Carbon to Product Austria. [February 18, 2022]; Available from: https://www.tugraz.at/fileadmin/user_upload/tugrazExternal/738639ca-39a0-4129-b0f0-38b384c12b57/files/lf/Session_D6/464_LF_Markowitsch.pdf.

[11] Wolf A, Jess A, Kern C. Syngas Production via Reverse Water-Gas Shift Reaction over a Ni-Al 2 O 3 Catalyst: Catalyst Stability, Reaction Kinetics, and Modeling. Chem. Eng. Technol. 2016;39(6):1040–8.

[12] Unde RB. Kinetics and Reaction Engineering Aspects of Syngas Production by the Heterogeneously Catalysed Reverse Water Gas Shift Reaction. Dissertation. Bayreuth; 2012.

[13] Vidal Vázquez F, Pfeifer P, Lehtonen J, Piermartini P, Simell P, Alopaeus V. Catalyst Screening and Kinetic Modeling for CO Production by High Pressure and Temperature Reverse Water Gas Shift for Fischer–Tropsch Applications. Ind. Eng. Chem. Res. 2017;56(45):13262–72.

[14] Escobar WF. Study of the reverse water-gas shift and dryreforming reactions conditions in a fixed bed reactor. Dissertation. Stuttgart; 2015.

[15] González-Castaño M, Dorneanu B, Arellano-García H. The reverse water gas shift reaction: a process systems engineering perspective. React. Chem. Eng. 2021;6(6):954–76.

[16] Yang L, Pastor-Pérez L, Villora-Pico JJ, Gu S, Sepúlveda-Escribano A, Reina TR. CO2 valorisation via reverse water-gas shift reaction using promoted Fe/CeO2-Al2O3 catalysts: Showcasing the potential of advanced catalysts to explore new processes design. Applied Catalysis A: General 2020;593:117442.

[17] Bahmanpour AM, Signorile M, Kröcher O. Recent progress in syngas production via catalytic CO2 hydrogenation reaction. Applied Catalysis B: Environmental 2021;295:120319.

[18] Tawalbeh M, Javed RMN, Al-Othman A, Almomani F, Ajith S. Unlocking the potential of CO2 hydrogenation into valuable products using noble metal catalysts: A comprehensive review. Environmental Technology & Innovation 2023;31:103217.

[19] Tawalbeh M, Muhammad Nauman Javed R, Al-Othman A, Almomani F. The novel contribution of non-noble metal catalysts for intensified carbon dioxide hydrogenation: Recent challenges and opportunities. Energy Conversion and Management 2023;279:116755.
[20] Popovic J, Lindenthal L, Rameshan R, Ruh T, Nenning A, Löffler S et al. High Temperature Water Gas Shift Reactivity of Novel Perovskite Catalysts. Catalysts 2020;10(5):582.
[21] Lindenthal L, Popovic J, Rameshan R, Huber J, Schrenk F, Ruh T et al. Novel perovskite catalysts for CO2 utilization - Exsolution enhanced reverse water-gas shift activity. Applied Catalysis B: Environmental 2021;292:120183.
[22] Markowitsch C, Lehner M, Maly M. Comparison and Techno-Economic Evaluation of Power-to-Plastic Process Routes for Lower Olefin Production Via Fischer-Tropsch and Methanol Synthesis. SSRN Journal 2023.
[23] Markowitsch C, Lehner M. Impact of the Operation Conditions on the Reverse-Water-Gas Shift Reaction. In: Benítez-Andrades JA, García-Llamas P, Taboada Á, Estévez-Mauriz L, Baelo R, editors. Global Challenges for a Sustainable Society: EURECA-PRO The European University for Responsible Consumption and Production, 1st ed. Cham: Springer International Publishing; Imprint Springer; 2023, p. 66–76.
[24] Peters MS, Timmerhaus KD, West RE. Plant design and economics for chemical engineers. 5th ed. Boston: McGraw-Hill; 2004.
[25] Alam MI, Cheula R, Moroni G, Nardi L, Maestri M. Mechanistic and multiscale aspects of thermo-catalytic CO2 conversion to C1 products. Catal. Sci. Technol. 2021;11(20):6601–29.
[26] Ampelli C, Perathoner S, Centi G. CO2 utilization: an enabling element to move to a resource- and energy-efficient chemical and fuel production. Philosophical transactions. Series A, Mathematical, physical, and engineering sciences 2015;373(2037).
[27] Roiaz M, Monachino E, Dri C, Greiner M, Knop-Gericke A, Schlögl R et al. Reverse Water-Gas Shift or Sabatier Methanation on Ni(110)? Stable Surface Species at Near-Ambient Pressure. Journal of the American Chemical Society 2016;138(12):4146–54.
[28] Frontera P, Macario A, Ferraro M, Antonucci P. Supported Catalysts for CO2 Methanation: A Review. Catalysts 2017;7(2):59.
[29] Aspen Technology Inc. ASPEN Plus V12.1: Aspen Technology Inc; 2023.
[30] Lindenthal L, Ruh T, Rameshan R, Summerer H, Nenning A, Herzig C et al. Ca-doped rare earth perovskite materials for tailored exsolution of metal nanoparticles. Acta Cryst B 2020;76(Pt 6):1055–70.
[31] Whitlow JE. Operation, Modeling and Analysis of the Reverse Water Gas Shift Process. In: AIP Conference Proceedings: AIP; 2003, p. 1116–1123.
[32] Daza YA, Kuhn JN. CO 2 conversion by reverse water gas shift catalysis: comparison of catalysts, mechanisms and their consequences for CO 2 conversion to liquid fuels. RSC Adv. 2016;6(55):49675–91.
[33] Zhu M, Ge Q, Zhu X. Catalytic Reduction of CO2 to CO via Reverse Water Gas Shift Reaction: Recent Advances in the Design of Active and Selective Supported Metal Catalysts. Trans. Tianjin Univ. 2020;26(3):172–87.

Process intensification of the rWGS reaction by perovskite-based catalyst

Christoph Markowitsch[1]*, Marion Andritz[1], Lorenz Lindenthal[2], Thomas Cotter[2], Hedda Drexler[2], Christoph Rameshan[2], Markus Lehner[1]

*Corresponding author: christoph.markowitsch@unileoben.ac.at, Montanuniversität Leoben, Austria

Supplementary Material

The rWGS reaction and the resulting product gas composition are discussed in detail in the manuscript. This supplementary material should expand the manuscript with additional information regarding the carbon and mass balance of the reaction and the material analysis of the perovskite-based catalysts. In the first chapter, the calculation steps for the calculation of the carbon and mass balance are carried out, whereas the analysis of the materials is described in the second chapter.

1. Calculation of the carbon and mass balance of the reaction for each catalyst

In the results and discussion section of the manuscript (chapter 4), the product composition is described for all catalyst materials in detail and the impact of operation conditions (temperature, pressure and GHSV) on the product gas composition are discussed. Nevertheless, it is crucial to calculate the atom balance for carbon, hydrogen and oxygen, as well as the mass balance in order to investigate whether the analysis is correct and if carbon is formed during the process. Carbon formation has a strong influence on catalyst deactivation and must be largely prevented.

In this study, the product gas is analyzed with an online gas analyzer (ABB AO2020, ABB AG). The device analyzes the components CO_2, CO and CH_4 via ND-IR, whereas H_2 is determined with a thermal conductivity analyzer. The data of the gas analyzer only provides the volumetric ratio of the output gases ($x_{CO2,dry}$, $x_{CO,dry}$, $x_{CH4,dry}$, $x_{H2,dry}$), without any quantification of these products. The accuracy of the gas analysis is limited to max. +/-1 vol.-% for all gases. The mass flow controllers (Bronkhorst) guarantee an accuracy of max. +/- 0.5 % for the feed gases H_2 and CO_2, which leads to a possible deviation of 0.225 NL/min. The thermodynamic equilibrium is investigated (Figure 1, detailed description is in chapter 2.1 in the manuscript) for an input gas composition of H_2:CO_2 equal to 3:1.

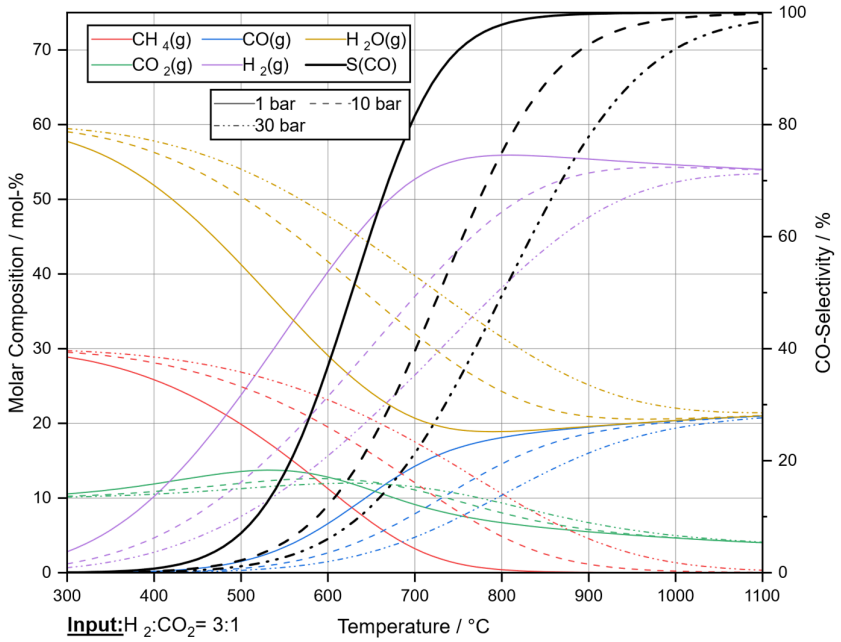

Figure 1: Thermodynamic equilibrium of a feed gas stream (H_2:CO_2=3:1) for a temperature range of 300-1100 °C and pressures of 1, 10 and 30 bara

The evaluation of the thermodynamic equilibrium supports the assumption to consider only the occurring species CO_2, CO, CH_4, H_2 and H_2O. The formation of higher hydrocarbons (e.g., ethane, propane or ethylene) and carbon is not observed in the thermodynamic simulation. Nevertheless, the mass and atom balances (carbon, oxygen, hydrogen) should confirm this assumption.

In the experiments, the amount of the produced water cannot be determined. A mathematical approach is intended to remedy this problem. The first approach is to calculate the mole flow of the feed gas ($\dot{n}_{in}$ in mol/min) with the total inlet mass flow stream ($\dot{m}_{in}$ in kg min^{-1}) divided by the product of the volume fraction of the inlet gas compound i ($x_{i,in}$ in vol.-%) and the molar mass of the compound i (M_i in g mol^{-1}). The volume flow ($\dot{V}_{in}$ in NL min^{-1}) of the feed gas is calculated with the mole flow (assuming ideal gas behavior).

$$\dot{n}_{in} = \frac{\dot{m}_{in}}{\sum_i x_{i,in} * M_i} \qquad \text{Equation 1}$$

$$\dot{V}_{in} = \dot{n}_{in} * 22.414 \frac{NL}{mol} \qquad \text{Equation 2}$$

The wet product gas composition is calculated with the known dry gas composition and the use of the mass and atom balance in the reactor. The calculation is performed in “Matlab 2020b” by applying the “fmincon” function to minimize the deviation of the balances and to obtain the amount of produced water in the product gas. Therefore, the content of water is initially set to 0.1 and the following equations are defined for the wet outlet composition:

$$x_{CO2,out} = x_{CO2,dry} * (1 - x_{H2O,out}) \qquad \text{Equation 3}$$

$$x_{CH4,out} = x_{CH4,dry} * (1 - x_{H2O,out}) \qquad \text{Equation 4}$$

$$x_{CO,out} = x_{CO,dry} * (1 - x_{H2O,out}) \qquad \text{Equation 5}$$

$$x_{H2,out} = x_{H2,dry} * (1 - x_{H2O,out}) \qquad \text{Equation 6}$$

With this approach, the mole outlet flow of the wet gas can be determined (coking is not considered):

$$\dot{n}_{out}=\dot{n}_{in} * \frac{x_{CO2,in}*M_{CO2}+x_{H2,in}*M_{H2}}{x_{CO2,out}*M_{CO2}+x_{CH4,out}*M_{CH4}+x_{CO,out}*M_{CO}+x_{H2,out}*M_{H2}+x_{H2O,out}*M_{H2O}} \quad \text{Equation 7}$$

The atom balances of carbon (CBil), hydrogen (HBil) and oxygen (OBil) are calculated according to the following equations:

$$CBil = \dot{n}_{in} * x_{CO2,in} - \dot{n}_{out} * (x_{CO,out} + x_{CO2,out} + x_{CH4,out}) \quad \text{Equation 8}$$

$$HBil = \dot{n}_{in} * 2 * x_{H2,in} - \dot{n}_{out} * (2 * x_{H2,out} + 4 * x_{CH4,out} + 2 * x_{H2O,out}) \quad \text{Equation 9}$$

$$OBil = \dot{n}_{in} * 2 * x_{CO2,in} - \dot{n}_{out} * (x_{CO,out} + 2 * x_{CO2,out} + x_{H2O,out}) \quad \text{Equation 10}$$

According to the previous defined variables, the mass balance is verified by Equation 11:

$$MBil = \dot{n}_{in} * (x_{CO2,in} * M_{CO2} + x_{H2,in} * M_{H2}) - \dot{n}_{out} * (x_{CO,out} * M_{CO} + x_{CO2,out} * M_{CO2} + x_{CH4,out} * M_{CH4} + x_{H2,out} * M_{H2} + x_{H2O,out} * M_{H2O}) \quad \text{Equation 11}$$

The variable "obj" in Equation 12 represents the deviation in the balances. The value is minimized by the function "fmincon" and the suitable content of water is determined to achieve a representative mass and atom balance. Since all carbon-relevant species are measured in the input stream ($\dot{m}_{CO2,in}$) and the concentrations in the outlet stream ($x_{CO,out}$, $x_{CO2,out}$, $x_{CH4,out}$), the deviation of the carbon and oxygen balance is weighted higher (optimized factor 'a' equal 15) in the minimization process.

$$obj=HBil^2+2*a*CBil^2+a*OBil^2+MBil^2 \quad \text{Equation 12}$$

According to this analysis, the CO_2 conversion (Equation 13), the CO selectivity (Equation 14) and the CO yield (Equation 15) are calculated and depicted in the evaluation diagrams.

$$CO_2 \text{ conversion} = \frac{\dot{n}_{in}*x_{CO2,in}-\dot{n}_{out}*x_{CO2,out}}{\dot{n}_{in}*x_{CO2,in}} \quad \text{Equation 13}$$

$$CO \text{ selectivity} = \frac{\dot{n}_{out}*x_{CO,out}-\dot{n}_{in}*x_{CO,in}}{\dot{n}_{in}*x_{CO2,in}-\dot{n}_{out}*x_{CO2,out}} \quad \text{Equation 14}$$

$$CO \text{ yield} = \frac{\dot{n}_{out}*x_{CO,out}-\dot{n}_{in}*x_{CO,in}}{\dot{n}_{in}*x_{CO2,in}} \quad \text{Equation 15}$$

The relative deviation of the carbon balance can give an evidence of carbon formation in the reaction zone and is calculated as:

$$\text{Relative deviation of C balance in \%} = \left(1 - \frac{\dot{n}_{out}*(x_{CO,out}+x_{CO2,out}+x_{CH4,out})}{\dot{n}_{in}*x_{CO2,in}}\right) * 100 \quad \text{Equation 16}$$

$$\text{Relative deviation of O balance in \%} = \left(1 - \frac{\dot{n}_{out}*(x_{CO,out}+2*x_{CO2,out}+x_{H2O,out})}{\dot{n}_{in}*2*x_{CO2,in}}\right) * 100 \quad \text{Equation 17}$$

$$\text{Relative deviation of H balance in \%} = \left(1 - \frac{\dot{n}_{out}*(2*x_{H2,out}+2*x_{H2O,out}+4*x_{CH4,out})}{\dot{n}_{in}*2*x_{H2,in}}\right) * 100 \quad \text{Equation 18}$$

The accuracy of the gas analysis is also taken into account, whereas the error is calculated for each operating point.

1.1. Results of catalyst 1 – Nickel-based catalyst

The calculated composition of the wet product gas is depicted in Figure 2 for the nickel catalyst at 1, 3, 6 and 8 bara in a temperature range of 550 to 950 °C (GHSV 8,000 h^{-1}). The input composition of the gas mixture is set to a H_2:CO_2 ratio of 3:1 for each catalyst. The ratio was checked with the gas analysis before each experiment and the H_2:CO_2 ratio was reported in the range between 2.8 and 3.1. The selectivity of CO reaches 100 % at 1 bara and temperatures higher than 750 °C. This trend changes for higher pressures, whereas increasing temperatures are required to achieve 100 % CO selectivity. Higher pressures favor the methane formation and this is reflected in lower CO selectivities. Low CO selectivity also affects the CO yield, which approaches the CO_2 conversion only at high temperatures (> 750°C at 1 bara, > 850 °C at 3 bara, 950 °C at 6 bara).

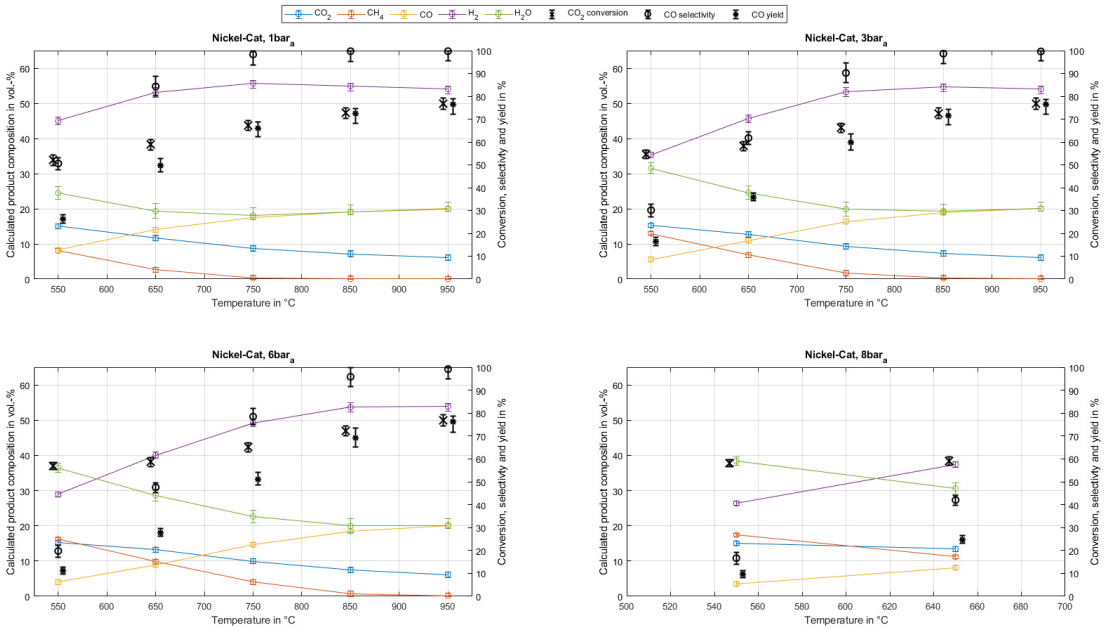

Figure 2: Calculated product gas composition (with error bars), CO_2 conversion, CO selectivity and CO yield at 1, 3, 6 and 8 bara in a temperature range of 550 to 950 °C for catalyst 1

1.2. Results of catalyst 2 – Perovskite 80/20 material

Figure 3 depicts the calculated composition of the wet product gas for the perovskite 80/20 catalyst at 1, 3, 6 and 8 bara in a temperature range of 550 to 850 °C (GHSV 8,000 h^{-1}). The figures show high CO selectivities of approximately 100 % at 1 and 3 bara and the entire temperature range. The CO selectivity slightly decreases with pressures higher than 6 bara due to the formation of methane. As a conclusion, the diagrams for 1 and 3 bara state that only the rWGS reaction takes place in the reactor ($x_{H2O,out} = x_{CO,out}$, $x_{CH4,out} = 0$). This assumption changes for higher pressures of 6 and 8 bara, as a measurable formation of CH_4 is detected. This also explains the higher proportion of water, as the CO_2 methanation reaction (Equation 3 in the manuscript) produces from a stoichiometric perspective more water than the rWGS reaction (Equation 1 in the manuscript) ($x_{H2O,out} > x_{CO,out}$, $x_{CH4,out} > 0$).

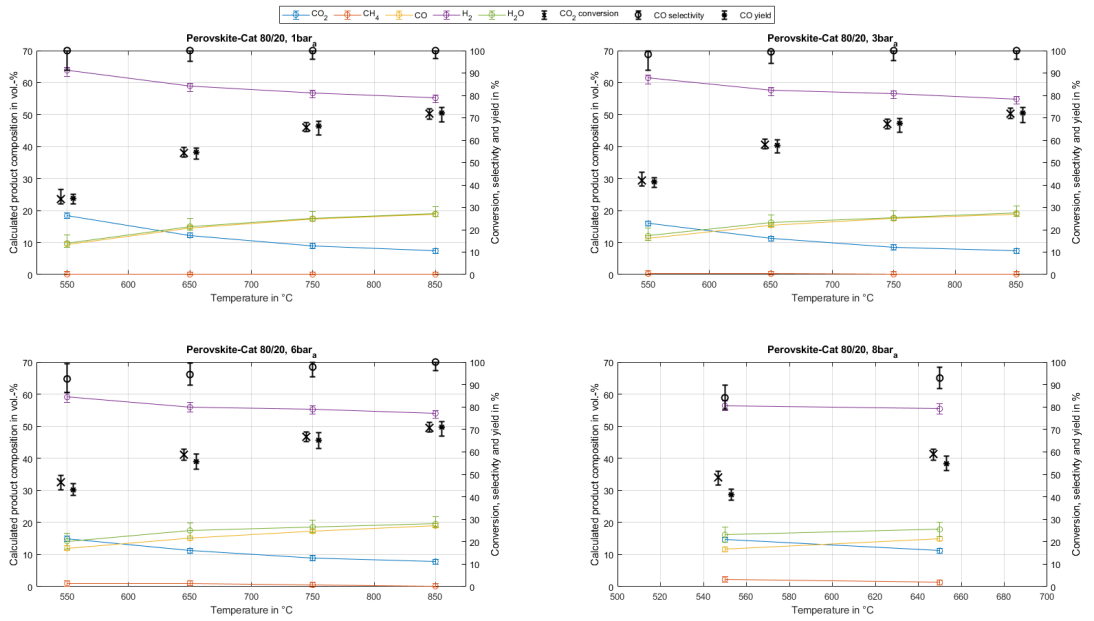

Figure 3: Calculated product gas composition, CO_2 conversion, CO selectivity and CO yield at 1, 3, 6 and 8 bara in a temperature range of 550 to 850 °C for catalyst 2

1.3. Results of catalyst 3 – Perovskite 50/50 material

Figure 4 shows the calculated composition (and error bars) of the wet product gas for the perovskite 50/50 catalyst at 1, 3, 6 and 8 bara in a temperature range of 550 to 850 °C (GHSV 8,000 h^{-1}). The figures show similar results as catalyst 2, with a CO selectivity of approximately 100 % at 1 and 3 bara and the entire temperature range. The CO selectivity is also slightly decreasing at pressures higher than 6 bara, where again methane formation occurs.

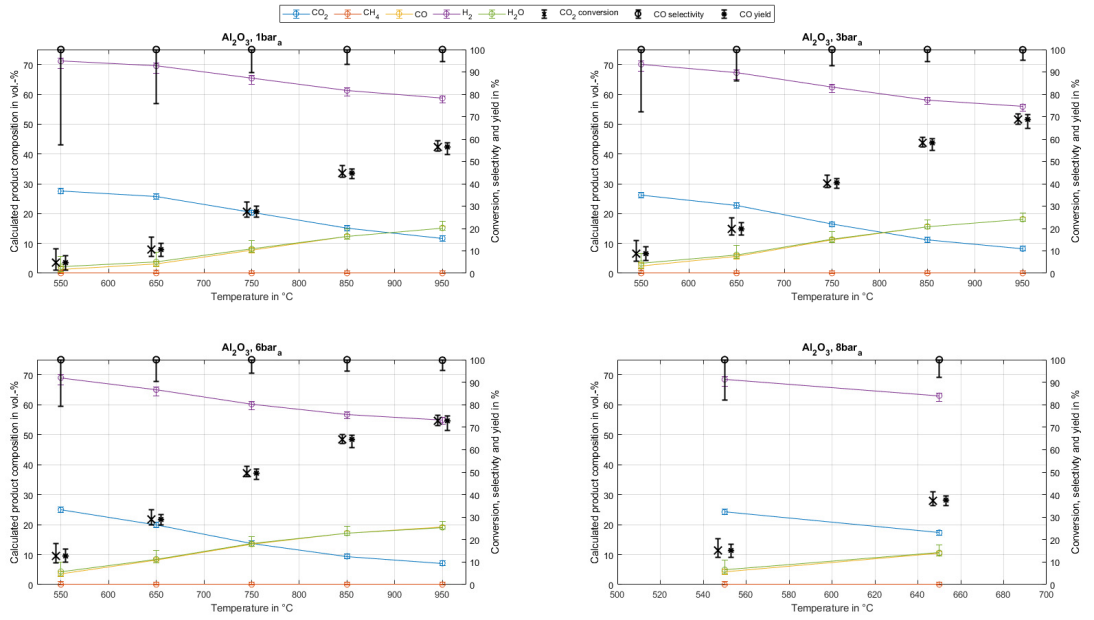

Figure 4: Calculated product gas composition, CO_2 conversion, CO selectivity and CO yield at 1, 3, 6 and 8 bara in a temperature range of 550 to 850 °C for catalyst 3

1.4. Results of catalyst 4 – Al_2O_3 material

Figure 5 depicts the calculated composition of the wet product gas for Al_2O_3 at 1, 3, 6 and 8 bara in a temperature range of 550 to 950 °C (GHSV 8,000 h^{-1}). No methane formation is observed for all operating points. The investigation shows for the operated pressure levels that only the rWGS reaction occurs. This result is again shown by the same H_2O and CO concentration ($x_{H2O,out} = x_{CO,out}$, $x_{CH4,out} = 0$). In contrast to the nickel or perovskite catalysts, the CO concentration does not reach thermodynamic equilibrium when Al_2O_3 is involved.

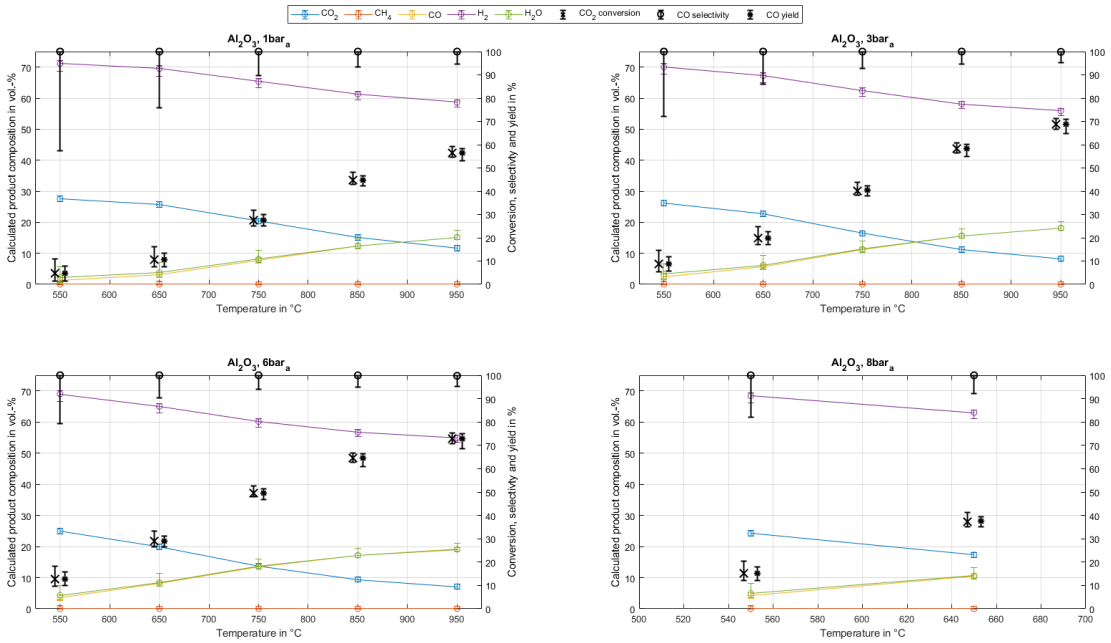

Figure 5: Calculated product gas composition, CO_2 conversion, CO selectivity and CO yield at 1, 3, 6 and 8 bara in a temperature range of 550 to 950 °C for catalyst 4

1.5. Calculation of the deviations in the atom balances

The atom balance is intended to provide proof that the model has been set up correctly and is balanced well. It should be mentioned at the outset that balancing is difficult due to the fact that the water content in the product gas is not measured and must be calculated based on a number of assumptions. The atom balance for carbon is shown in Figure 6, for oxygen in Figure 7 and for hydrogen in Figure 8. The optimization of Equation 12 is carried out using Matlab, which minimizes the deviations. The species CO_2, CH_4, CO, H_2 and H_2O are considered in this study, and these are included in the calculation.

The relative deviation in the carbon balance (Figure 6) is between -0.7 and approx. +1.5 % for all catalysts. A similar picture emerges for the relative deviation in the oxygen balance (Figure 7). The deviation is for catalyst 1 between -0.8 and +0.9 %, for catalyst 2 between -2.05 and +0.3 %, for catalyst 3 between -1.4 and +1.05 % and for catalyst 4 between -2.35 and 0.78 %. In summary, it can also be stated that the trend of the carbon and oxygen deviation for catalysts 1, 2 and 3 correlates. This effect is due to the fact that CO_2 as a feed gas is composed of the two feed atoms C and O. In contrast, the trend is different for catalyst 4, where the oxygen deviation does not follow the carbon deviation.

The atom balance of hydrogen shows different relative deviations, which result in maximum values between -9 and +12.5 %. This can be attributed to the fact that the gas composition is provided with two flow controllers for CO_2 and H_2, respectively, which are calibrated for an operating flow rate of

up to 45 NL/min. In this setup, hydrogen is fed at a rate of approx. 3.5 NL/min for a GHSV value of 8000 h^{-1}. The accuracy of the mass flow controllers is +/-0.5 % which allows a deviation of +/- 0.225 NL/min. The observed deviations in the hydrogen balance can therefore be attributed to a slight and dynamic change of the H_2:CO_2 ratio in the feed gas composition.

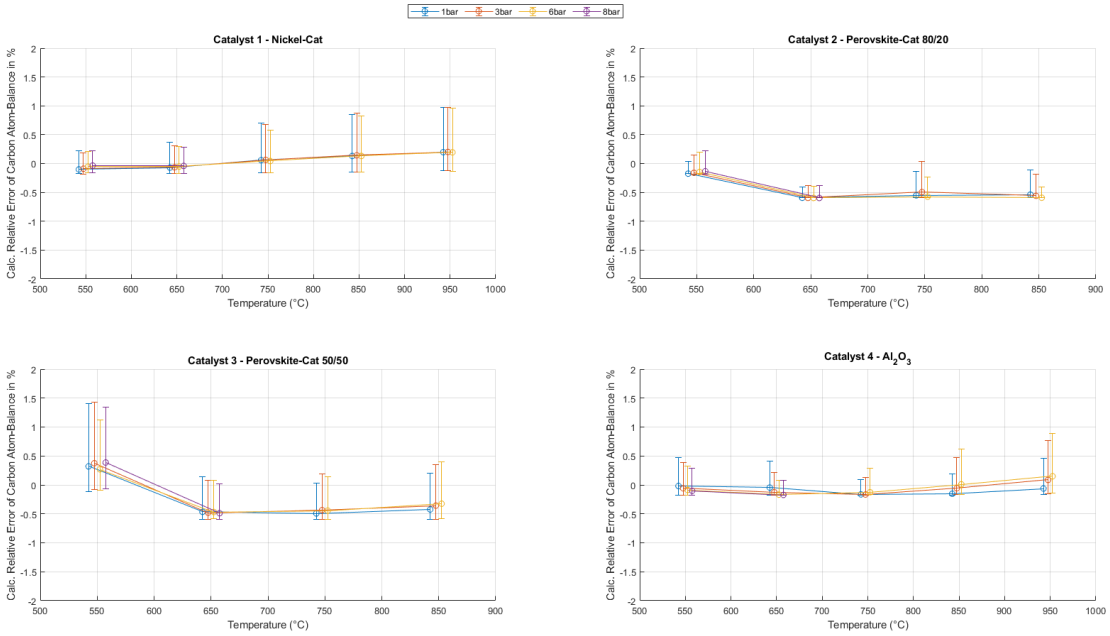

Figure 6: Carbon balance of all four catalysts in the temperature range of 550-950 °C (catalyst 1 and 4) or 550-850 °C (catalyst 2 and 3) and pressure levels of 1, 3, 6 and 8 bara

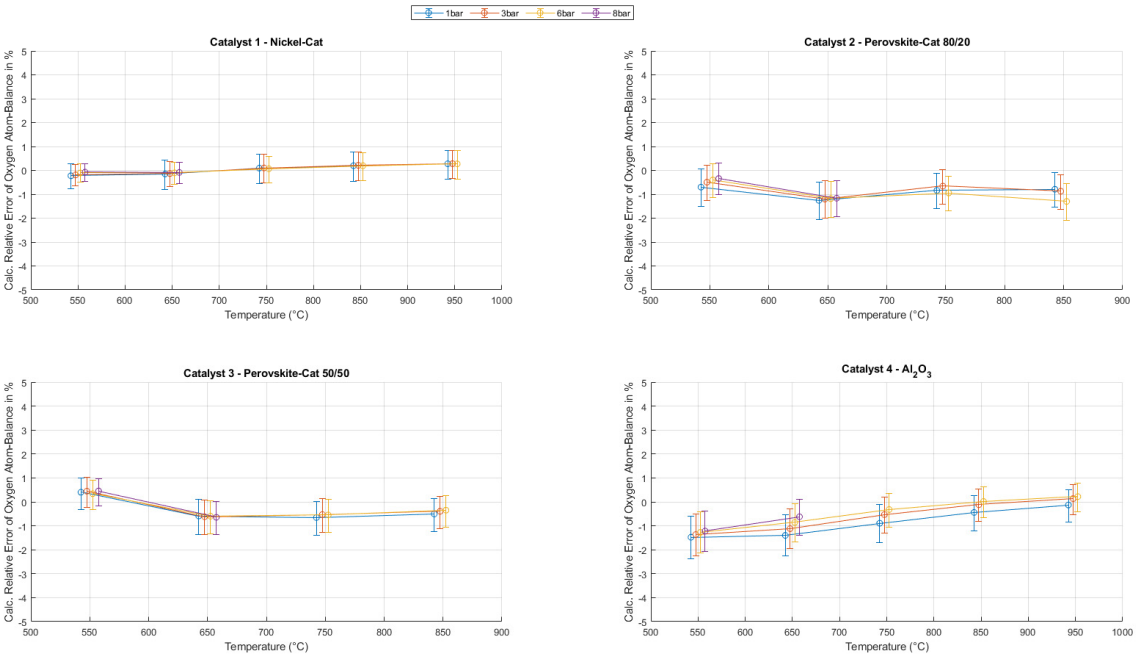

Figure 7: Oxygen balance of all four catalysts in the temperature range of 550-950 °C (catalyst 1 and 4) or 550-850 °C (catalyst 2 and 3) and pressure levels of 1, 3, 6 and 8 bara

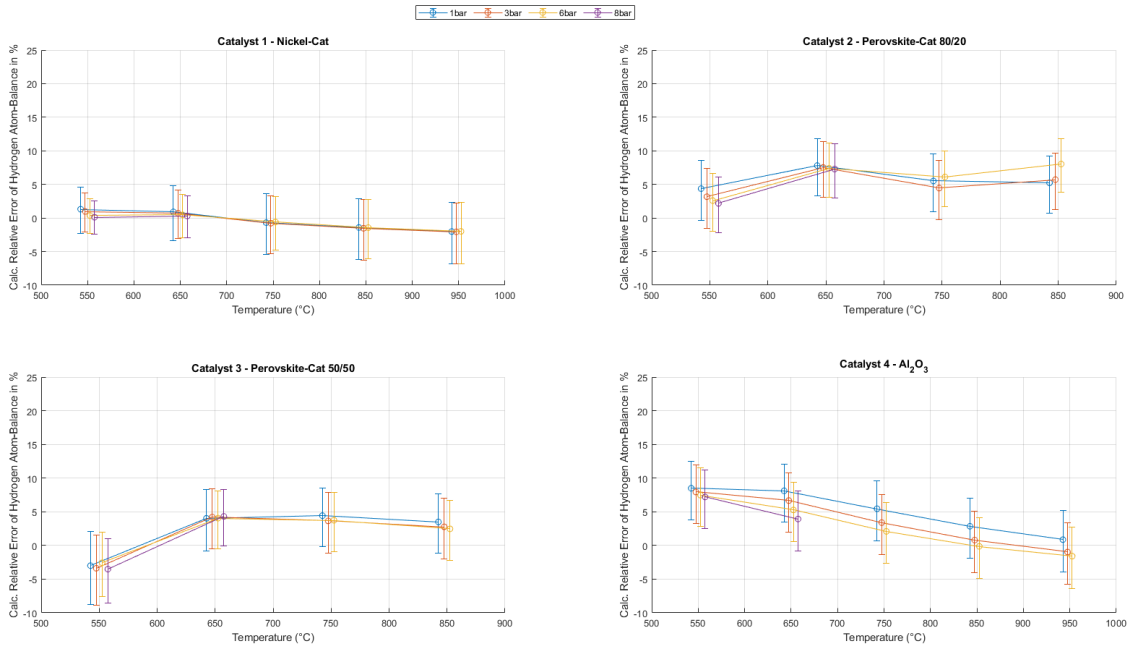

Figure 8: Hydrogen balance of all four catalysts in the temperature range of 550-950 °C (catalyst 1 and 4) or 550-850 °C (catalyst 2 and 3) and pressure levels of 1, 3, 6 and 8 bara

2. Material analysis

The perovskite based catalysts 2 and 3 have been characterized before and after testing. A PANalytical X'Pert Pro diffractometer in Bragg–Brentano geometry (with separated Cu $K\alpha_{1,2}$ radiation) and an X'Celerator linear detector was used to perform X-ray diffraction (XRD) measurements. Data analysis and reflex assignment were performed with the HighScore Plus software (PANalytical) and the PDF-4+ 2023 database (ICDD - International Centre for Diffraction Data). Scanning electron microscopy (SEM) images were recorded with secondary electrons on a Quanta 250 FEGSEM (FEI Company) microscope with an Octane Elite X-ray detector (EDAX Inc). An acceleration voltage of 5 kV was used for satisfactory surface-sensitivity.

For both perovskite based catalysts, XRD (figure 9) confirmed the presence of the perovskite phase. It is partly retained after the catalytic test runs, however, several new phases appear. In both cases a CoFe metallic alloy phase was observed, which can be attributed to the formation of catalytically active metal nanoparticles (exsolution process). Additionally, further phases due to segregation and beginning decomposition appeared. For catalyst 2, a segregation of Ca took place, leading to the formation of carbonate ($CaCO_3$). Catalyst 3 showed stronger decomposition, leading to Nd-oxide and –hydroxide phases. In accordance, also the exsolution phase is more intense in comparison to the retained perovskite phase than for catalyst 2. In terms of stability during operation, the higher amount of Al_2O_3 binder in catalyst seems to be detrimental.

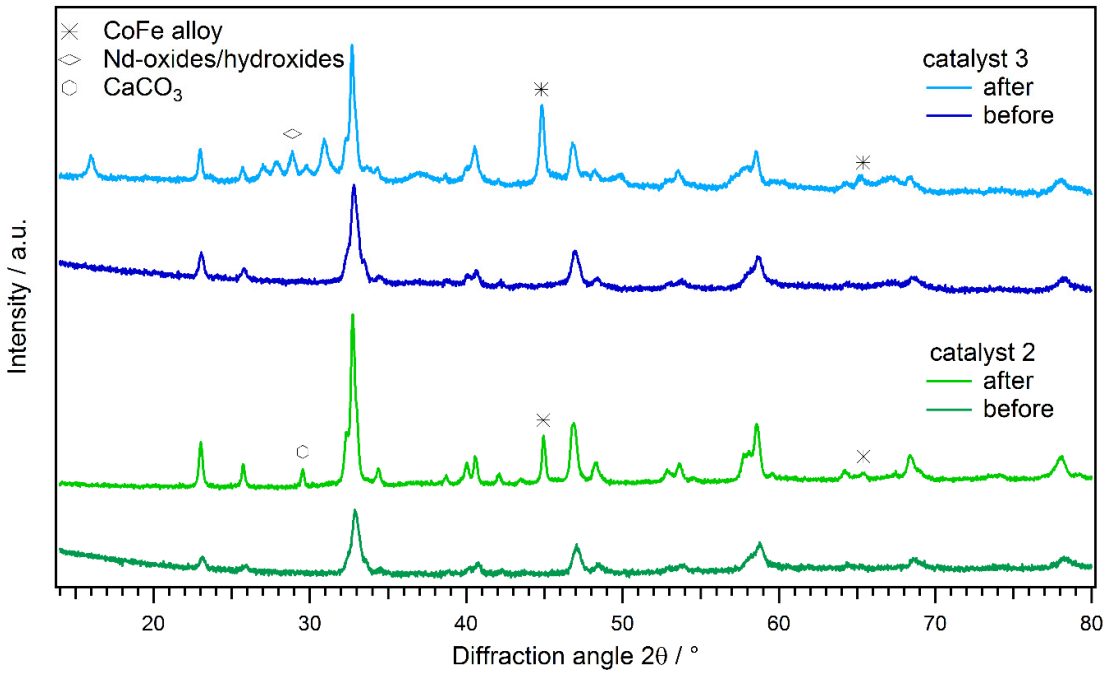

Figure 9: XRD patterns of catalyst 2 and 3 before and after the catalytic testing. For both, exsolution (CoFe alloy) could be observed, as well as a segregation/decomposition phase (Ca/Nd-containing phases).

SEM images go in line with observations from XRD. Figures 10 and 11 compare images of the pristine catalysts (a,b) with the ones after testing (c-f) for catalysts 2 and 3, respectively. Different parts of the used catalysts are shown, which feature different morphological changes related to several processes going on during pretreatment and operation. Exsolved particles with sizes of 80-100 nm are visible as brighter small dots (Figure 10c+d and Figure 11c). For catalyst 2, formation of $CaCO_3$ (Figure 10e, larger smooth crystallites) could be seen, in accordance to the XRD results. In addition, coking was observed in the form of carbon nanotubes (Figure 10f). For catalyst 3, the stronger decomposition as seen with XRD led to a higher degree of surface roughening (Figure 11d).

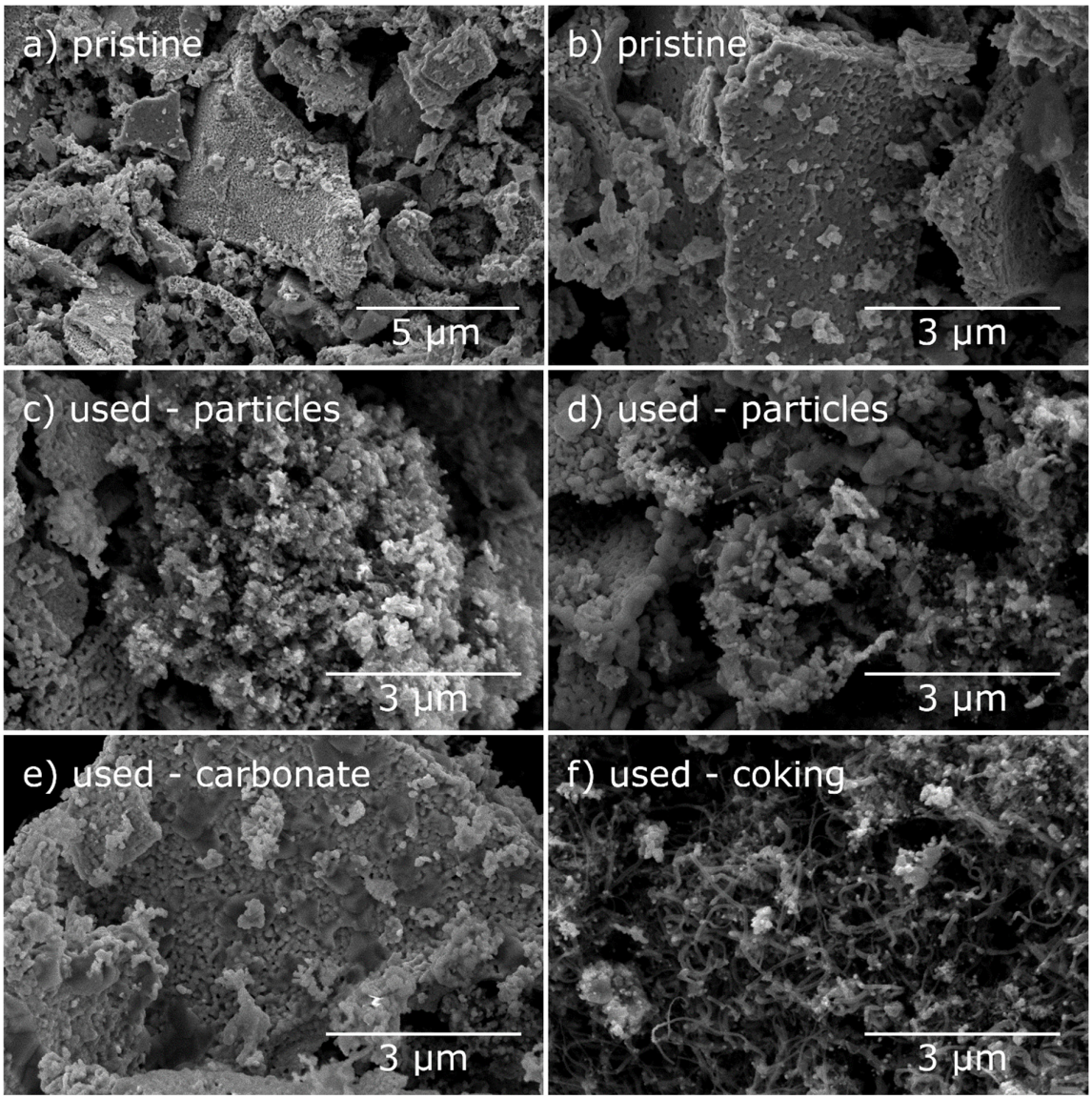

Figure 10: SEM images of catalyst 2 – perovskite 80/20. a, b) Pristine catalyst at different magnifications. c-f) Material after the catalytic testing. Exsolved nanoparticles can be observed (bright spots in c and d), but also formation of carbonate (larger smooth crystallites in e) and coking (carbon nanotubes in f).

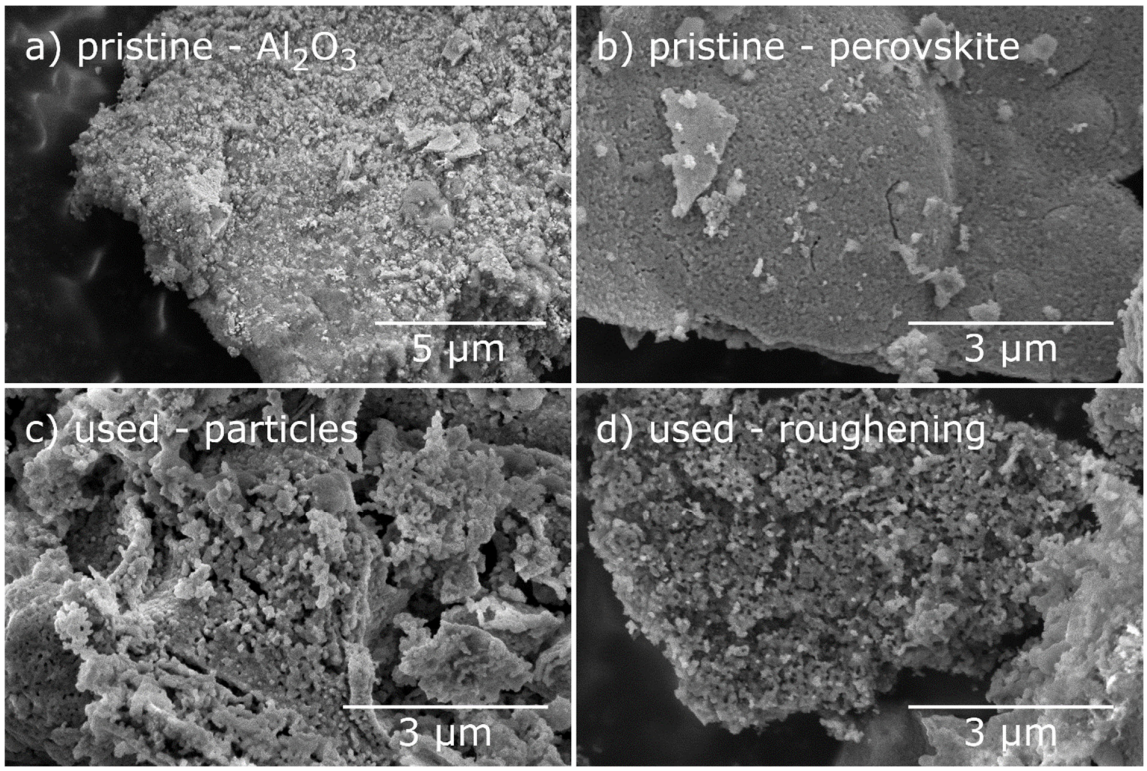

Figure 11: SEM images of catalyst 3 – perovskite 50/50. a, b) Pristine catalyst at different magnifications. The Al_2O_3 (seen in a with chunks of perovskite on top) and the perovskite sheets (b) have a distinguished morphology. c, d) Material after the catalytic testing. Some exsolved particles (c) and surface roughening (d) can be observed.